

ABSTRACT

SCHOELL, RYAN MICHAEL. **Understanding the Mechanisms Involved in Chlorine-Induced Stress Corrosion Cracking of Stainless Steel 304 under a Simulated Marine Environment** (Under the direction of Dr. Djamel Kaoumi).

In situ x-ray tomography and diffraction experiments were conducted at Argonne National Laboratory's Advanced Photon Source to study the mechanisms of Chlorine-Induced Stress Corrosion Cracking in different heats of 304SS. Dry storage canisters made from 304SS near marine environments are at risk of failure due to a combination of corrosive salts and stress leading to chlorine-induced stress corrosion cracking. A custom-made tensile apparatus made it possible to conduct an *in-situ* tomography diffraction experiment in a simulated marine environment. Drops of concentrated MgCl₂ solution were added to the crack and the temperature, stress, and relative humidity were controlled and monitored. Experiments were conducted on three heats of 304SS at different stress intensities and temperatures. Several tomography and diffraction scans were run over the course of each experiment.

Beyond chlorine-induced stress corrosion cracking, initial tomography scans of the fatigue pre-cracked samples revealed the development of microvoids when compared to the tomography of the as-received materials. Electron microscopy showed several types of precipitates in the as-received materials and showed microvoids associated with sulfides in the fatigue pre-cracked materials. Microvoids preferentially formed at sulfides during fatigue due to their lower elastic modulus compared to the matrix. The shape of the precipitates have an influence on the shapes of the microvoids. Fatigue pre-cracking also increased the amount of deformation induced martensite at the crack tip due to the plastic zone.

Diffraction scans revealed chlorine-induced stress corrosion cracking does not lead to a significant increase in deformation induced martensite compared to fatigue pre-cracking and final mechanical failure. Little formation of deformation induced martensite indicates the mechanism of chlorine-induced stress corrosion cracking does not include deformation induced martensite and suggests either a different mechanical deformation mechanism is at play or the mechanisms is not mechanical in nature. Additionally, neither an intrinsic nor extrinsic mechanism as a result of an increase in deformation induced martensite are playing a significant role in crack retardation during chlorine-induced stress corrosion cracking.

Stress intensity was shown to play a role in cracking morphology. Three different cracking morphologies were found at a low, medium, and high initial stress intensities. Low initial stress intensities (above KISCC) led to the propagation of a single crack, medium initial stress intensities showed microbranching, while even initial higher stress intensities led to macrobranching. A single crack phase propagated first before the development of branching. Additionally, crack branching was found to not be a perquisite for steady state crack propagation in stage II.

Temperature was found to play a role in crack growth rate with higher temperatures leading to faster crack growth rates. An increase in temperature increased the rate of the rate limiting step in chlorine-induced stress corrosion cracking. An Arrhenius behavior from the experiments was used to calculate an activation energy which suggested the production of hydrogen. Hydrogen production suggested the mechanisms for chlorine-induced stress corrosion cracking is dissolution.

Chlorine ions were confirmed to be influential in causing cracking under the conditions ran in this experiment. Negatively charged chlorine ions concentrate at the crack

tip and bring along positively charged hydronium ions. Concentrated hydronium ions lower the pH in the region and lead to an active anodic region at the crack tip, leading to dissolution of metals into solution. A passivating, cathodic region forms on the crack wake and prevents crack blunting. Stress works to open the crack and allow chlorine to diffuse to the crack tip while preventing any passivating layer to form. A dissolution-based model was proposed based on the presence of chlorine bearing metal salts (FeCl_2 , CrCl_2 , and $\text{NiCl}_2 \cdot 6\text{H}_2\text{O}$) which indicate metal ions were dissolved into solution and crystallized when the solution dried.

© Copyright 2020 by Ryan Schoell

All Rights Reserved

Understanding the Mechanisms Involved in Chlorine-Induced Stress Corrosion Cracking of
Stainless Steel 304 under a Simulated Marine Environment

by
Ryan Michael Schoell

A Thesis submitted to the Graduate Faculty of
North Carolina State University
in partial fulfillment of the
requirements for the degree of
Doctor of Philosophy in Nuclear Engineering

Raleigh, North Carolina
2020

APPROVED BY:

Dr. Djamel Kaoumi
(Committee Chair)

Dr. Benjamin Beeler

Dr. Korukonda Murty

Dr. Timothy Horn

BIOGRAPHY

Ryan Schoell was born in Lansdale Pennsylvania to John and Kathleen Schoell. Ryan attended school in the North Penn School District and graduated with his high school diploma in June 2013. After high school, Ryan attended college at Ohio State University majoring in chemical and biomolecular engineering. Outside of his studies, Ryan was an undergraduate researcher for Dr. Liang-Shih Fan conducting research on the process of chemical looping to capture carbon dioxide from burning fossil fuels with no exergy lost. Ryan specifically focused on the fabrication and testing of the iron oxide particles used in the process. Ryan graduated from Ohio State in May of 2017 with a bachelor's degree in Chemical and Biomolecular Engineering with a minor in Nuclear Engineering with Magna Cum Laude distinction. After graduation, Ryan moved to North Carolina and attended North Carolina State University in pursuit of a Doctorate in Nuclear Engineering under the direction of Dr. Djamel Kaoumi. Along the way, Ryan received his master's of Material Science and Engineering degree. Ryan's doctorate project was titled Innovative Approach to SCC Inspection and Evaluation of Canisters in Dry Storage.

ACKNOWLEDGMENTS

First, a thanks to both my parents who have given me the opportunity to pursue my doctorate in Nuclear Engineering and have supported me every step of the way. I would not be able to have accomplished finishing my doctorate without your support. I would also like to extend my thanks to all my friends and family for their support.

Special thanks to my PhD advisor, Dr. Djamel Kaoumi for guiding me through my Master's and PhD. Additional thanks for allowing me to participate and assist on other projects. My time under you has expanded my knowledge in both nuclear engineering and material science. I am grateful for the many opportunities to participate in different experiments, especially at the national laboratories.

I would also like to thank all my committee members for their feedback and help during my Ph.D. Thanks to Dr. Ron Scattergood, Dr. Korukonda Murty, Dr. Mohamed Bourham, Dr. Benjamin Beeler, and Dr. Timothy Horn for participating on my committee. A special thanks to those who also served as professors in my classes.

I would also like to recognize the staff at the Analytical Instrument Facility (AIF) and the beamline staff at 1-ID-E at the Advanced Photon Source (APS). My research was made possible by the hard-working staff at both AIF and APS.

Finally, I would like to recognize my colleagues in my group: Dr. Ce Zheng, Dr. Ryan Smith, Dr. Li Xi, Dr. Yuchen Zhao, Dr. Martin Owusu-Mensah, Fu-Yun Tsai, Angelica Lopez, Jacob Cooper, Kai Duemmler, Enguerrand Buckel, Zeinab Alsmadi, and Cody Meeks. It has been a privilege to work with all of you.

TABLE OF CONTENTS

LIST OF TABLES.....	vi
LIST OF FIGURES	vii
Chapter 1: Introduction	1
1.1 Motivation for Studying Stress Corrosion Cracking in Dry Storage Canisters near Coastal United States	1
1.2 Fundamentals of Stress Corrosion Cracking.....	3
1.3 Chlorine Induced Stress Corrosion Cracking	9
1.3.1 Deliquescence Relative Humidity.....	10
1.3.2 Effect of Different Chloride Salts and Effect of Concentration of Salts on Corrosion and Stress Corrosion Cracking.....	11
1.3.3 Types of Experiments Conducted in Literature on Chlorine Induced Stress Corrosion Cracking	14
1.3.4 Proposed Mechanisms for Chlorine Induced Stress Corrosion Cracking.....	16
1.3.5 Crack Branching in General Stress Corrosion Cracking	16
1.4 Remaining Questions about Chlorine Induced Stress Corrosion Cracking in Austenitic 304 Stainless Steels.....	18
Chapter 2: Materials & Methodology.....	21
2.1 Materials	21
2.1.1 As-Received Commercial-304 Characterization	23
2.1.2 As-Received 304H Characterization.....	28
2.1.3 As-Received 304L Characterization	33
2.1.4 Tomography of As-Received and Fatigue Pre-Cracked Materials	38
2.1.5 Synchrotron X-ray Diffraction of As-Received and Fatigue Pre-Cracked Materials	41
2.2 <i>In situ</i> Synchrotron X-ray Tomography and Diffraction	42
2.2.1 Principles of X-ray Tomography	43
2.2.2 <i>In Situ</i> Experimental Setup	46
2.2.3 Sample Fatigue Pre-Cracking	47
2.2.4 Table of Experimental Conditions	48
2.3 Post Experimental Analysis and Characterization	50
2.3.1 Tomography using AVIZO©.....	50
2.3.2 Crack Measurements and Volume Measurements of Microvoids and Precipitates	51
2.3.3 Electron Microscopy Analysis.....	52
2.3.4 Stress Intensity Analysis and Finite Element Analysis.....	54
2.3.5 X-ray Diffraction Volumetric Phase Fraction Analysis.....	56
Chapter 3: Results.....	58
3.1 Tomography, Stress Intensity Analysis, and X-Ray Diffraction Results	59
3.1.1 Commercial-304 Experiments	59
3.1.1.1 304-FE-40K _o -80C-55%	59
a) Tomography	59
b) Stress Intensity Analysis.....	60
c) Phase Fraction Analysis.....	62
3.1.1.2 304-CL-46K _o -50C-55%	65
a) Tomography	65

b) Stress Intensity Analysis.....	65
c) Phase Fraction Analysis	67
3.1.2 304H Experiments	70
3.1.2.1 304H-FE-20K _o -80C-55%	70
a) Tomography.....	70
b) Stress Intensity Analysis.....	70
c) Phase Fraction Analysis	72
3.1.3 304L Experiments	73
3.1.3.1 304L-FE-18K _o -80C-55%	73
a) Tomography.....	73
b) Stress Intensity Analysis.....	74
c) Phase Fraction Analysis	75
3.1.3.2 304L-CL-30K _o -80C-55%	76
a) Tomography.....	76
b) Stress Intensity Analysis.....	78
c) Phase Fraction Analysis	79
3.1.3.3 304L-CL-43K _o -50C-55%	80
a) Tomography.....	80
b) Stress Intensity Analysis.....	81
c) Phase Fraction Analysis	82
3.2 Microstructural Analysis with Optical, Scanning Electron, and Transmission Electron Microscopy	84
3.2.1 Optical and Scanning Electron Microscopy	84
3.2.2 Transmission Electron Microscopy	90
Chapter 4: Discussion	98
4.1 What are the Effects of Fatigue Pre-Cracking on the Initial Microstructure.....	98
4.1.1 Microvoid Formation and Shape	98
4.1.2 Deformation Induced Martensite	105
4.2 What is the Role of Martensite as a Possible Intrinsic and Extrinsic Factor in Crack Retardation.....	107
4.2.1 Intrinsic Factor	107
4.2.2 Extrinsic Factor	112
4.3 How does the Stress Intensity Affect the Rate and Morphology of Cracking.....	114
4.3.1 Stress Intensity Effect on Rate.....	114
4.3.2 Stress Intensity Effect on Morphology	115
4.3.3 How does Crack Branching Influence the Steady State Propagation Rate.....	120
4.4 What Role does Temperature Play on Crack Growth Rates.....	121
4.4.1 Effect of Temperature on Crack Growth Rate	121
4.4.2 Effect of Temperature on Morphology	122
4.5 What is the Role of Chlorine and Chlorine Bearing Compounds.....	123
4.6 What are the Mechanism that are Operating on the Microstructural Level.....	126
Chapter 5: Conclusions	132
Chapter 6: Future Works.....	134
References	135
Appendices.....	139
Appendix A: Grain Size Measurements with ImageJ	140

Appendix B: Precipitate Area Density.....	145
Appendix C: Using AVIZO to Extract Crack from Tomography	148
Appendix D: Tomographs of 304SS Samples which did not Crack.....	163

LIST OF TABLES

Table 1 Concentration of Chloride Bearing Salts in Natural Sea Water.....	9
Table 2 Chemical Composition of 304ss (wt%) used in [4]	13
Table 3 Salt Deposition Parameters used in [4]	13
Table 4 Crack Lengths and Crack Growth Rates in 304SS Samples Tested at 0.1% Strain and 0.2% Strain	13
Table 5 Chemical Compositions for 304L, 304H, and Commercial-304	21
Table 6 Precipitation Found in the As-Received Commercial-304 Microstructure through Scanning Electron Microscopy, Energy Dispersive Spectroscopy, and Transmission Electron Microscopy Observations	27
Table 7 Precipitation Found in the As-Received 304H Microstructure through Scanning Electron Microscopy, Energy Dispersive Spectroscopy, and Transmission Electron Microscopy Observations.....	33
Table 8 Precipitation Found in the As-Received 304L Microstructure through Scanning Electron Microscopy, Energy Dispersive Spectroscopy, and Transmission Electron Microscopy Observations.....	37
Table 9 Tomographs of the As-Received and Fatigue Pre-Cracked Samples Showing Precipitates and Microvoids	39
Table 10 Volumetric Phase Fraction Analysis of As-Received 304SS and Fatigued 304SS	42
Table 11 Experimental Parameters for In Situ Tomography and Diffraction Study of Chlorine Induced Stress Corrosion Cracking	49
Table 12 Summary of Experimental Conditions for the In Situ X-ray Tomography and Diffraction to Study Chlorine-Induced Stress Corrosion Cracking	58
Table 13 Engineering Stress, Crack Length and Stress Intensity for the Initial and Final Tomographs for 304-FE-40Ko-80C-55%	61
Table 14 Phase Fraction of Austenite (γ -Fe), α' -Martensite (α' -Fe), and ε -Martensite (ε -Fe) in the 304-FE-40Ko-80C-55% Sample Before and After Testing	63
Table 15 Engineering Stress, Crack Length and Stress Intensity for the Initial and Final Tomographs for 304-FE-40Ko-80C-55%	66

Table 16 Phase Fraction of Austenite (γ -Fe), α' -Martensite (α' -Fe), and ε -Martensite (ε -Fe) in the 304-CL-46Ko-50C-55% Sample Before and After Testing.....	68
Table 17 Phase Fraction of Austenite (γ -Fe), α' -Martensite (α' -Fe), and ε -Martensite (ε -Fe) in the 304-CL-46Ko-50C-55% Sample After Fracture	68
Table 18 Engineering Stress, Crack Length and Stress Intensity for the Initial and Final Tomographs for 304H-FE-20Ko-80C-55%	71
Table 19 Phase Fraction of Austenite (γ -Fe), α' -Martensite (α' -Fe), and ε -Martensite (ε -Fe) in the 304H-FE-20Ko-80C-55% Sample Before and After Testing	73
Table 20 Engineering Stress, Crack Length and Stress Intensity for the Initial and Final Tomographs for 304L-FE-18Ko-80C-55%	75
Table 21 Phase Fraction of Austenite (γ -Fe), α' -Martensite (α' -Fe), and ε -Martensite (ε -Fe) in the 304L-FE-18Ko-80C-55% Sample Before and After Testing.....	76
Table 22 Engineering Stress, Crack Length and Stress Intensity for the Initial and Final Tomographs for 304L-CL-30Ko-80C-55%	78
Table 23 Phase Fraction of Austenite (γ -Fe), α' -Martensite (α' -Fe), and ε -Martensite (ε -Fe) in the 304L-CL-30Ko-80C-55% Sample Before and After Testing	80
Table 24 Engineering Stress, Crack Length and Stress Intensity for the Initial and Final Tomographs for 304L-CL-46Ko-50C-55%	82
Table 25 Phase Fraction of Austenite (γ -Fe), α' -Martensite (α' -Fe), and ε -Martensite (ε -Fe) in the 304L-CL-46Ko-50C-55% Sample Before and After Testing	83
Table 26 Phase Fraction of Austenite (γ -Fe), α' -Martensite (α' -Fe), and ε -Martensite (ε -Fe) in the 304L-CL-46Ko-50C-55% Sample after Fracture.....	83
Table 27 Tomography Scans of As-Received and Fatigue Pre-Cracked Samples Showing Varying Degrees of Microvoids in Terms of Number and Shape.....	99
Table 28 Comparing Volumetric Density of Microvoids in Fatigue Pre-Cracked Samples to the Area Density of Precipitates in the As-Received Materials	101
Table 29 Elastic Modulus of 304SS and Various Precipitates found in As-Received 304SS Samples	102
Table 30 Calculated Stacking Fault Energies of 304L, 304H, and Commercial-304 using Various Empirical Models	106

Table 31 Phase Fraction Analysis for Commercial-304 Samples during Chlorine-Induced Stress Corrosion Cracking	108
Table 32 Phase Fraction Analysis for the 304H Sample during Chlorine-Induced Stress Corrosion Cracking	109
Table 33 Phase Fraction Analysis for the 304L Samples during Chlorine-Induced Stress Corrosion Cracking	109
Table 34 Phase Fraction Analysis for As-Received and Fatigue Pre-Cracked State of 304SS Samples	111
Table 35 Phase Fraction Analysis for Fractured Samples.....	111

LIST OF FIGURES

Figure 1 Diagram of Dry Storage Casket in both the Vertical (Left) and Horizontal (Right) Configuration. Caskets are made up of an Outer Concrete Casing which is used to House the Stainless Steel Canister Holding the Spent Nuclear Fuel	2
Figure 2 SYSWELD Welding Simulation of Residual Stresses in Heat Affected Zones of a Bolt Used in the Dry Storage Caskets	3
Figure 3 Opening Modes for a Crack Consisting of Mode I (Tension), Mode II (In-Plane Shear) and Mode III (Transverse Shear).....	4
Figure 4 Crack Propagation Rate as a Function of Stress Intensity for Stress Corrosion Cracking consisting of Stage 1 (Crack Initiation and Propagation), Stage 2 (Steady State Crack Propagation), and Stage 3 (Final Fracture)	5
Figure 5 a) (Left) Pourbaix Diagram for a Carbon Steel, and b) (Right) Potentiokinetic Polarization Curve for Stainless Steels Showing Cracking Regions	7
Figure 6 Possible Rate Limiting Steps in Stress Corrosion Cracking which may Lead to Stage 2 Steady State Crack Propagation.....	8
Figure 7 Deliquescence Relative Humidity as a Function of Container Surface Temperature with different Concentrations of Salts Deposited.....	10
Figure 8 Tensile Rig used to Induce Stress on 304SS Tensile Samples	13
Figure 9 Optical Microscopy, Strain Maps, Inverse Pole Figures, and Phase and Grain Boundary Character of Cracks under Drop 3 Showing Crack Branching and Transgranular Cracking	14
Figure 10 Typical Stress Corrosion Cracking Crack Growth Rate as a Function of Stress Intensity Profile with Regions for Microbranching and Macrobranching	18
Figure 11 Optical Microscopy of As-Received Commercial-304 after Etching in a Solution of Aqua Regia showing Grain Sizes of around 20 μm which are Equiaxial and show some Twin Boundaries	23
Figure 12 Synchrotron X-ray Diffraction Spectrum of As-Received Commercial-304 Showing Various Phases Present in the Microstructure with Enough Volume Fraction	24
Figure 13 a) Scanning Electron Micrograph of As-Received Commercial-304 Showing Precipitate Population and b) Energy Dispersive Spectroscopy Spectrum (Red Curve Corresponds to Spot next to Precipitate and the Yellow Curve corresponds to on the Precipitate) and Chemical Maps showing One Elongated Precipitate to be Rich in Silicon and Oxygen	25

Figure 14 a) Low Magnification Transmission Electron Microscopy Micrograph of As-Received Commercial-304 and b) Higher Magnification Micrographs of Dislocations (Red and Yellow Boxes), Grain and Twin Boundaries with no Precipitation (Green) and a Cr23C6 within a Grain (Blue Box)	26
Figure 15 Optical Microscopy of As-Received 304H after Etching in a Solution of Aqua Regia showing Grain Sizes of around 30 μm which are Equiaxial and show some Twin Boundaries	29
Figure 16 Synchrotron X-ray Diffraction Spectrum of As-Received 304H Showing Various Phases Present in the Microstructure with Enough Volume Fraction.....	30
Figure 17 a) Scanning Electron Micrograph of Precipitates in 304H and b) an Energy Dispersive X-ray Spectroscopy Spectrum Showing an Elongated Carbide (Yellow Curve is Scan on the Precipitate and Red Curve is Scan next to Precipitate)	31
Figure 18 Transmission Electron Microscopy Micrograph of 304H As-Received showing a) Tiple Junctions and Grain Boundaries, b) Twin Boundaries, and c) Residual Martensite as Indicated by Selected Area Electron Diffraction shown in d)	32
Figure 19 Optical Microscopy of As-Received 304L after Etching in a Solution of Aqua Regia showing Grain Sizes of around 50 μm which are Equiaxial and show some Twin Boundaries	34
Figure 20 Synchrotron X-ray Diffraction Spectrum of As-Received 304L Showing Various Phases Present in the Microstructure with Enough Volume Fraction.....	35
Figure 21 Scanning Electron Microscopy Micrograph of As-Received 304L Showing Larger Precipitates at 65X Magnification and Many Small Precipitates at 500X Magnification. Some Precipitates are shown in Line with the Rolling Direction....	36
Figure 22 Transmission Electron Microscopy of the As-Received 304L Material Showing a) A Grain of Residual Martensite Confirmed by the Selected Area shown in b), Twin Boundaries, and d) Stacking Faults Indicated by Blue Arrows	36
Figure 23 Histograms of Volumes of Voids in Fatigue Pre-Cracked a) Commerical-304, b) 304H, and c) 304L.....	41
Figure 24 a) Arial View and Schematic of the Advance Photon Source Facility at Argonne National Laboratory and b) Chart of X-ray Sources as a Function of Brilliance and Energy	43
Figure 25 X-ray Tomography Scanning Process Diagram with an X-ray Source, an Object (Red Circle in this Figure), a Scintillator and Detector. The Process is used to Form Sinograms	44

Figure 26 Unfiltered Backprojection (Left), Kernel Function Convolution (Center), and Filtered Backprojection (Right)	45
Figure 27 a) Experimental Setup at the Advanced Photon Source using Beamline 1-ID-E and b) Diagram of the Custom Built Tensile Machine for In Situ Tomography and Diffraction	47
Figure 28 a) Large Notched Samples for Fatigue Pre-Cracking, b) Diagram of Large Notched Sample and EDM Cuts to Obtain c) Pre-Cracked Single Edged Crack Samples	48
Figure 29 AVIZO Process Commercial-304 Sample after Thresholding but before Manual Removal Process (Left) and after (Right)	51
Figure 30 Crack Measurement at Six Equidistant Points Along the Crack (units in μm)	52
Figure 31 Picture of a) ThermoFisher Quanta 3D Dual Focused Ion Beam and Scanning Electron Microscope and b) ThermoFisher Talos F200X Transmission Electron Microscope	53
Figure 32 Abacus \circledcirc Simulation Setup to Map and Quantify Principal Stresses and Strain for the Experimental Conditions	55
Figure 33 Labeled Diffraction Pattern of 304H Sample	56
Figure 34 3-D Tomograph of the Commercial-304-FE-40Ko-80C-55% Sample Before (Left) and After (Right) the Experiment (Units in μm)	60
Figure 35 3-D Tomographs of Commercial-304-FE-40Ko-80C-55% a) over the Progression of the Experiment and b) showing Four Angles relative to the Z-Axis of the Final Tomography Scan.....	60
Figure 36 Crack Growth Rate as a Function of Stress Intensity for 304-FE-40Ko-80C-55% showing an Average Cracking Rate of $2.788 \times 10^{-9} \text{ m/s}$	62
Figure 37 Dynamics of Phase Fraction of γ -Fe, α' -Fe, and ε -Fe for the 304-FE-40Ko-80C-55% Sample above the Crack, at the Crack, below the Crack, and the Total Scanned Volume	64
Figure 38 Detailed Tomography Progression of 304-FE-40Ko-80C-55% Sample over Time ..	64
Figure 39 3-D Tomographs of Commercial-304-CL-46Ko-50C-55% a) over the Progression of the Experiment and b) showing Four Angles relative to the Z-Axis of the Final Tomography Scan.....	65

Figure 40 Crack Growth Rate as a Function of 304-CL-46Ko-50C-55% Sample with an Average Cracking Rate of 1.592×10^{-9} m/s with the Last Data Point and 6.120×10^{-10} m/s without the Last Data Point	67
Figure 41 Dynamics of Phase Fraction of γ -Fe, α' -Fe, and ε -Fe for the 304-CL-46Ko-50C-55% Sample above the Crack, at the Crack, below the Crack, and the Total Scanned Volume	69
Figure 42 Detailed Tomography Progression of 304-CL-46Ko-50C-55% Sample over Time ..	69
Figure 43 3-D Tomographs of 304H-FE-20Ko-80C-55% a) over the Progression of the Experiment and b) showing Four Angles relative to the Z-Axis of the Final Tomography Scan.....	70
Figure 44 Crack Growth Rate as a Function of 304H-FE-20Ko-80C-55% Sample with an Average Cracking Rate of 7.82×10^{-10} m/s.....	72
Figure 45 3-D Tomographs of 304L-FE-18Ko-80C-55% a) over the Progression of the Experiment and b) showing Four Angles relative to the Z-Axis of the Final Tomography Scan.....	74
Figure 46 Crack Growth Rate as a Function of 304L-FE-18Ko-80C-55% Sample with an Average Cracking Rate of 4.934×10^{-10} m/s.....	75
Figure 47 3-D Tomographs of 304L-CL-30Ko-80C-55% a) over the Progression of the Experiment and b) showing Four Angles relative to the Z-Axis of the Final Tomography Scan.....	77
Figure 48 a) Orthoslices in the XZ-Plane in the 304L-CL-30Ko-80C-55% Sample Illustrating the Many Small Branched and Showing How Quickly the Morphology Changes with each Slice (1 slice= $1.17 \mu\text{m}$). b) Shows a Magnified view of one of the Microbranches	77
Figure 49 Crack Growth Rate as a Function of 304L-CL-30Ko-80C-55% Sample with an Average Cracking Rate of 1.776×10^{-9} m/s.....	79
Figure 50 3-D Tomographs of 304L-CL-43Ko-50C-55% a) over the Progression of the Experiment and b) showing Four Angles relative to the Z-Axis of the Final Tomography Scan.....	81
Figure 51 Crack Growth Rate as a Function of 304L-CL-43Ko-50C-55% Sample with an Average Cracking Rate of 1.470×10^{-9} m/s.....	82
Figure 52 a) Optical Microscopy and b) Scanning Electron Microscopy Micrographs with Chemical Maps of 304-FE-40Ko-80C-55% Sample.....	84

Figure 53 Low Magnification Scanning Electron Microscopy Micrograph of the Fractured Surface of 304-FE-40Ko-80C-55% using a) Secondary Electron, and b) Backscatter Electrons	86
Figure 54 Scanning Electron Microscopy Micrograph and Chemical Maps of Branching Crack of 304-FE-40Ko-80C-55% Sample	86
Figure 55 Scanning Electron Microscopy Micrograph and Chemical Maps of Fatigue Region of 304-FE-40Ko-80C-55%	87
Figure 56 Low Magnification Scanning Electron Microscopy Micrograph of the 304H-FE-20Ko-80C-55% Sample using Secondary Electrons	88
Figure 57 Scanning Electron Microscopy Micrograph and Chemical Maps of the Crack Front Region of 304H-FE-20Ko-80C-55% Sample	89
Figure 58 Scanning Electron Microscopy Micrograph and Chemical Maps of the Fatigue Region of 304H-FE-20Ko-80C-55% Sample	89
Figure 59 Scanning Electron Microscopy Micrograph and Chemical Maps of a Vertical Crack in the 304H-FE-20Ko-80C-55% Sample	90
Figure 60 a) Location of Transmission Electron Microscopy Liftout, b) Transmisison Electron Microscopy Bright Field and Selected Area Electron Diffraction of Sample near Branching Crack Showing Evidence of Martensite (Orange Arrow), c) High Angle Annular Dark Field, Chemical Maps, and Selected Area Electron Diffraction Pattern of Sample near Crack Tip.....	92
Figure 61 a) Location of Transmission Electron Microscopy Liftout, b) Bright Field Transmission Electron Microscopy Micrograph of the Sample with Selected Area Electron Diffraction Patterns and c) Chemical Maps of the 304-FE-40Ko-80C-55% at the Crack Wake	93
Figure 62 a) Location of Focused Ion Beam Liftout, b) Bright Field Transmission Electron Microscope Micrograph and Accompanying Selected Area Electron Diffraction Pattern, and c) Chemical Maps of Crack of the 304-FE-40Ko-80C-55% Sample at the Crack Tip showing Chlorine Migrating into Sample	94
Figure 63 a) Scanning Electron Micrograph of Transmission Electron Microscopy Liftout (Red Arrow), b) Low Magnification Transmission Electron Microscopy Micrograph, c) Higher Magnification Transmission Electron Microscopy Micrograph showing Two Phases, and d) Selected Area Electron Diffraction Pattern showing the Presence of Austenite (Blue) and Martensite (Orange)	96
Figure 64 Initial after Loading and Final Tomograph of 304-CL-31Ko-80C-55% Sample showing the Main Crack did not Propagate	97

Figure 65 a) b) Location of Transmission Electron Microscopy Liftout, c) High Angle Annular Dark Field Micrograph of Sample, and d) Chemical Maps of Yellow Region of c) in the 304-CL-31Ko-80C-55% showing the lack of Chlorine	97
Figure 66 a) Bright Field Transmission Electron Microscopy Micrograph of a Void and Precipitate Identified as Cu ₂ S by the Selected Area Electron Diffraction Pattern and the Chemical Maps Shown in b)	100
Figure 67 Synchrotron X-Ray Diffraction Spectrums Showing MnS (111) Peak in a) Commercial-304 and not in the b) 304H or c) 304L Materials	103
Figure 68 Crack Resistance Curve of Two Zirconia based Materials with a Medium Transformability (MT) and a Low Transformability (LT).....	113
Figure 69 Crack Growth Rate as a Function of Stress Intensity for Commerical-304 Samples (Blue Box), the 304H Sample (Red Box), and the 304L Samples (Green Box)....	114
Figure 70 Effect of Apparent Stress Intensity on the Crack Growth Rate of 316SS in Simulated Pressurized Water Reactor Primary Waters Showing an Increase in Crack Growth Rate with Stress Intensity	115
Figure 71 Different Crack Morphologies in Different Samples with a) Low Stress Intensity (Monocrack), b) Medium Stress Intensity (Micobranching), and c) High Stress Intensity (Macrobranching) compared to d) Branching in Literature	116
Figure 72 a) FEA Simulation with a Stress Intensity of about 40 MPa m ^{1/2} , b) 20 MPa m ^{1/2} , and c) Diagram of Plane Stress and Strain on Sample.....	118
Figure 73 Tomography of Final Scan of 304-FE-40Ko-80C-55% at Different a) and b). c) Optical Microscopy of Final State of 304-FE-40Ko-80C-55% Sample showing Possible Pitting on Location of Branching.....	119
Figure 74 Tomographs of Progression of 304-FE-40Ko-80C-55% Sample Showing a Single Crack Until around 5.88 Hours	120
Figure 75 a) Tomographs of 304-CL-31Ko-80C-55% Sample initially after Load and the Final Scan and b) Abaqus Simulation of 304-CL-31Ko-80C-55% Sample.....	124
Figure 76 High Angle Annular Dark Field Micrograph, Selected Area Electron Diffraction Pattern, and Chemical Maps Illustrating the Presents of Chlorine and Oxygen Bearing Compounds around the Crack of 304-FE-40Ko-80C-55%	125
Figure 77 Pouraix Diagram of Iron in a Solution of 0.1 M NaCl showing Active, Passive, and Immune Regions.....	127

Figure 78 Crevice Corrosion of Metal in a NaCl solution..... 128

Figure 79 Possible Mechanisms of Chlorine-Induced Stress Corrosion Cracking 131

CHAPTER 1: Introduction

1.1 Motivation for Studying Stress Corrosion Cracking in Dry Storage Canisters near Coastal United States

After spending approximately 54 months inside nuclear reactors to generate power, fuel rods are placed in cooling pools on-site [1]. Although the fission reaction has halted, the radioactive fission products continue to decay and generate heat which must be removed in order for the fuel rods to remain intact [1]. Over time, the radioactivity decreases as does the heat emitted. Once the level of heat generation reaches below a certain level, the spent fuel rods can be air cooled inside interim dry storage caskets [1]. Although the United States has the technology to reprocess the fuel and separate the long lived fuel elements from the short lived fission products, the United States has not used this route in fear of proliferation [1]. Also, long term storage options such as Yucca Mountain are currently not available due to debates over the site [1]. For the foreseeable future, spent nuclear fuel will spend its lifetime in dry storage caskets until another option comes into fruition. As a result, more studies need to be conducted to ensure the safety and structural integrity of the dry storage caskets. A diagram of a dry storage casket is shown in **Figure 1**. The spent nuclear fuel is placed inside a stainless steel canister filled with helium gas [1]. The canisters are then placed in a vented concrete structure which allows air to passively remove heat from the decay of the spent fuel [1]. The stainless steels used for the canisters are usually austenitic 304 or 316 type stainless steels. These alloys are generally used because of their inherent resistance to corrosion, radiation tolerance, and desired mechanical strength for the application.

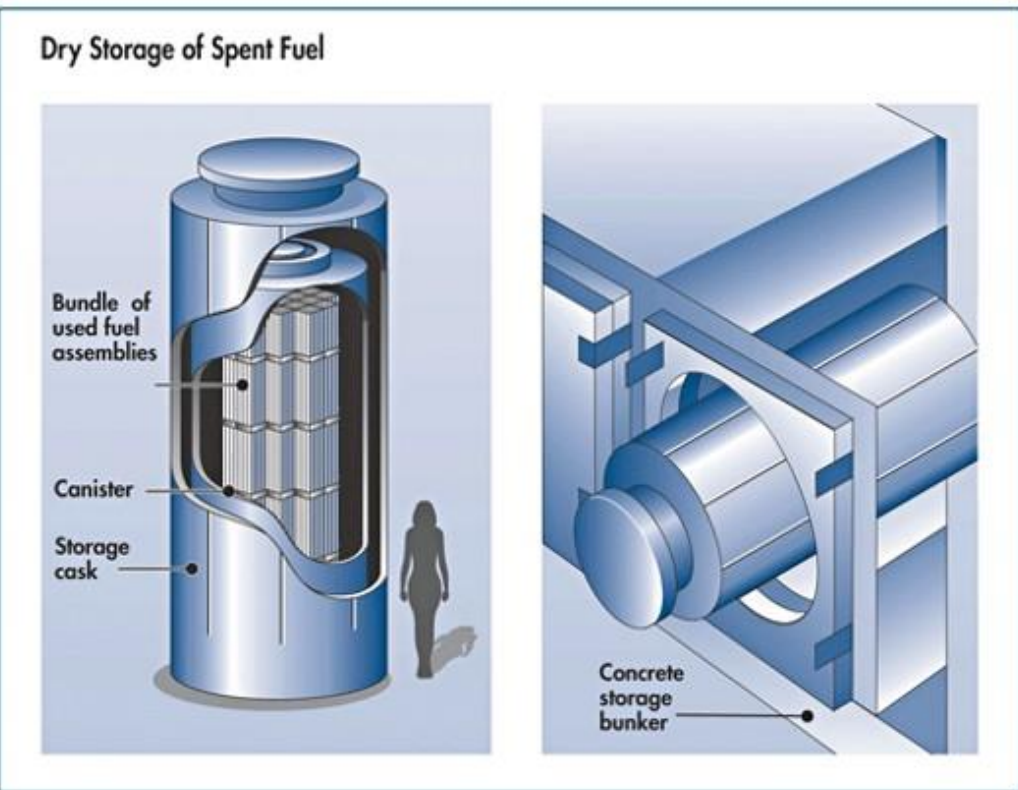


Figure 1: Diagram of Dry Storage Casket in both the Vertical (Left) and Horizontal (Right) Configuration. Caskets are made up of an Outer Concrete Casing which is used to House the Stainless Steel Canister Holding the Spent Nuclear Fuel [2]

One potential issue with regards to these canisters are with those that are stationed near coastal regions of the United States. The Department of Energy (DOE) has identified that the canisters near coastal region are at a possible risk of failure due to Chlorine-Induced Stress Corrosion Cracking (CISCC). It is well known that austenitic stainless steels are vulnerable to CISCC [3]. The concern with the canisters near the coastal regions is the possibility of marine salts depositing on the surface of the canisters since the canisters are air cooled. The deposited salts can turn into an insidious brine above a critical humidity level known as the Deliquescence Relative Humidity (DRH) and can result in pits [4, 5]. Combined with residual stress in the material from fabrication and Heat Affected Zones (HAZ) from welds, a crack can develop from defects like pits and propagate under the synergistic action of both corrosion and stress. The DOE has not found

any evidence of cracking yet in the canisters, but marine salts have been found to have been deposited on the surface of the dry storage canisters. Moreover, the DOE has found evidence through simulations that residual stresses around HAZ are high enough to cause CISCC as shown in **Figure 2**. Although cracking has not been found in the canisters themselves, it is important to have a better understanding of CISCC in the canisters to predict cracking rates as well as develop strategies to reduce the risk of failure due to CISCC. The failure of the canisters could result in the release of radioactive materials into the environment which makes the study of process ever more paramount. The purpose of this thesis is to discuss what is known about CISCC on austenitic stainless steels as well as highlight areas where there is still ambiguity. Furthermore, experimentation of the austenitic stainless-steel material in simulated marine environments will help answer some questions surrounding the process of CISCC.

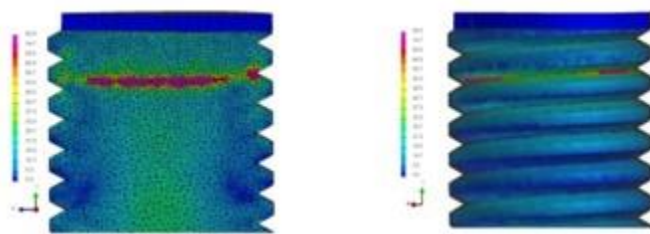


Figure 2: SYSWELD Welding Simulation of Residual Stresses in Heat Affected Zones of a Bolt Used in the Dry Storage Caskets [2]

1.2 Fundamentals of Stress Corrosion Cracking

Before discussing the details of what is known about the process of CISCC, it is important that a basic knowledge of Stress Corrosion Cracking (SCC) be reviewed. SCC is defined as being the slow failure of a material due to the propagation of a subcritical crack influenced by environmental and mechanical factors [3]. The combined effects of both mechanical stress and corrosion are what leads to SCC [3]. To illustrate the detrimental nature of SCC, fracture mechanics must first be explained. For austenitic stainless steels, Linear Elastic Fracture

Mechanics (LEFM) can be used to describe the stresses around a crack tip [6]. Three modes of crack opening are shown in **Figure 3** below. Most SCC experiments are done under type I loading because of its simplistic nature. To describe the stress distribution around the crack, a factor known as the stress intensity factor (K) is used and the general formula for K is shown in **Equation 1** [7].

$$K = Y\sigma\sqrt{\pi a} \quad (1)$$

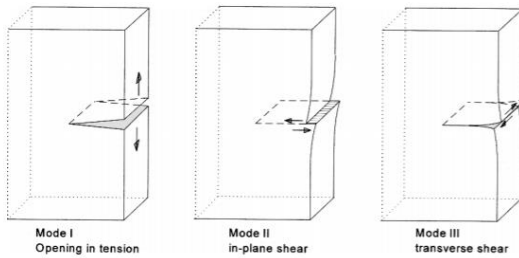


Figure 3: Opening Modes for a Crack Consisting of Mode I (Tension), Mode II (In-Plane Shear) and Mode III (Transverse Shear) [7]

In **Equation 1**, a represents the length of the crack, σ represents the engineering stress applied to the sample, and Y represents the geometric factor that depends on the geometry of the crack relative to the sample's geometry [7]. In LEFM, there exists a stress intensity factor value at which the crack will propagate in an inert environment which is known as the critical stress intensity factor (K_{IC}) where the subscript I is used to specify the mode of crack opening [7]. The thermodynamics behind crack propagation is the release of stored elastic strain energy at the cost of creating two free surfaces and a plastic zone ahead of the crack which leads to a lower Gibbs free energy [7]. Although LEFT was intended for materials that only experience elastic deformation, LEFT can still be used for materials which only have a small plastic zone ahead of the crack relative to the sample size [7]. The critical stress intensity relates to the critical stress intensity involved in stress corrosion cracking by the following: $K_{ISCC} < K_{IC}$ [3]. From this relationship between K_{IC} and K_{ISCC} , the detrimental aspect of stress corrosion cracking appears.

Materials that are originally designed to have stress intensity factors below K_{IC} when a crack appears are now at the risk of SCC if the material is in a corrosive environment with a stress intensity larger than K_{ISCC} . Materials can develop small cracks which can propagate until failure with little to no warning signs. K_{ISCC} is defined as the minimum stress intensity needed in which the combined action of stress and corrosion can cause crack propagation. The stresses generally needed for SCC are usually less than that of the macroscopic yield stress. The stress on the material must be non-compressive in nature and can come from applied loads or from residual stress from processes involved in fabrication or welding. In order for SCC to occur, three criteria must be met which are 1) a susceptible material, 2) a corrosive environment, and 3) some sort of adequate non-compressive stress. A material will not fracture by stress corrosion cracking if the material is corroded first and then taken out of the corrosive environment and put under stress. The corrosive environment can exist as an aqueous solution or as a condensed thin film. Three stages of SCC exist and are shown in **Figure 4** below. [3]

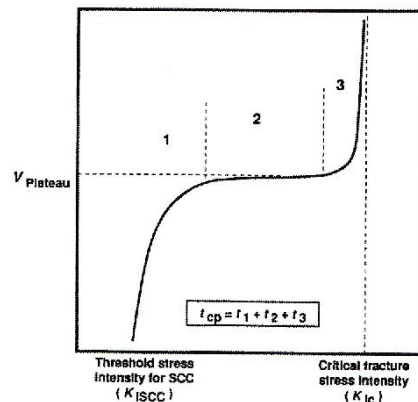


Figure 4: Crack Propagation Rate as a Function of Stress Intensity for Stress Corrosion Cracking consisting of Stage 1 (Crack Initiation and Propagation), Stage 2 (Steady State Crack Propagation), and Stage 3 (Final Fracture) [3]

The first stage shown in **Figure 4** is known as the initiation stage where a defect like a pit grows into a crack that has an increasing rate in propagation with increasing stress

intensity [3]. In order for the pit to grow into a crack, the stress intensity factor must be greater than K_{ISCC} . The second stage is known as the steady state regime where there is little to no changes in crack propagation rate with increasing stress intensity. The cause of the constant rate is thought to be a rate limiting step involved in the SCC mechanism such as mass transfer into the crack. Typical steady state propagation rates can range from micrometers per second to nanometers per second depending on the material and the corrosive environment. The third and final stage of SCC is the crack propagation to failure where the rate of crack propagation increases as the stress intensity factor approaches the critical stress intensity factor. Experiments involving SCC propagation rates generally use fatigued pre-cracked samples and usually involve either a Constant Load (CL) in which the value of K increases with crack length or a Fixed Extension (FE) in which the value of K decreases with crack propagation due to the decrease in load with propagation. Constant load is typically the condition in which SCC failures occur, but fixed extension is useful in determining the value of K_{ISCC} . The value of K_{ISCC} is specific to a material in a specific environment. Varying parameters such as temperature, pressure, oxygen content, and other such parameters can have devastating effects on the crack propagation rates. In general, environments which cause an alloy to develop a protective film are prone to stress corrosion cracking. Austenitic stainless steels are generally used because of their ability to form a protective layer against uniform corrosion attack; however, the ability to protect against uniform corrosion attack makes it susceptible to SCC. Passive films are needed for SCC because a passive film must form on the walls of the crack in order to allow the highest current density to come from the crack tip. The highest current density from the crack tip prevents the crack from blunting which might stop the progression of the crack. The ratio of the current density from the crack tip to the current density of the walls must be more than one in order for the crack to grow. Current density is one of the

factors that influences the kinetics of corrosion and can affect the propagation rate of a crack. Thermodynamically, SCC can only occur if the dissolution of the material is favorable as well as the formation of a protective layer [3]. Tools like Pourbaix diagrams (shown in **Figure 5a**) are very useful in determining the stable species under a certain electrochemical potential and pH. Moreover, potentiokinetic polarization curves (as shown in **Figure 5b**) can be helpful in identifying regions where a protective films form. The mechanism behind SCC is still unknown but many researchers have proposed different mechanisms to explain experiments done on certain materials/environment combinations [3]. Proposed mechanisms must be able to explain region 2 in **Figure 4** where the kinetics of the crack are almost independent of stress intensity in order to be considered. Some possible rate limiting steps are shown in **Figure 6** below.

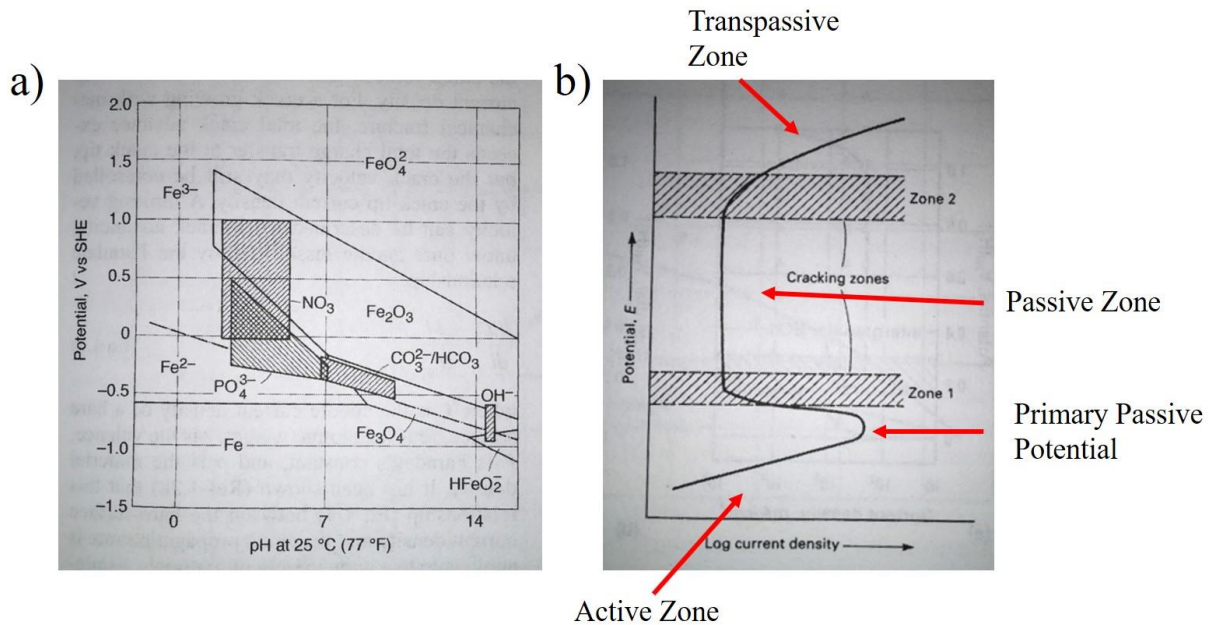


Figure 5: a) (Left) Pourbaix Diagram for a Carbon Steel, and b) (Right) Potentiokinetic Polarization Curve for Stainless Steels Showing Cracking Regions [3]

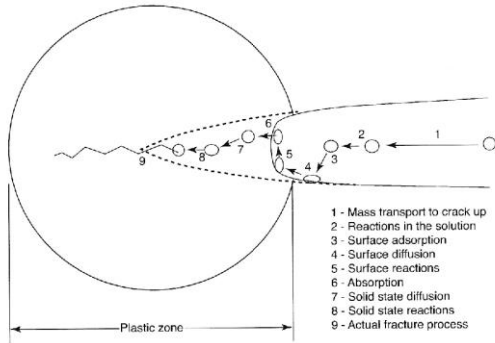


Figure 6: Possible Rate Limiting Steps in Stress Corrosion Cracking which may Lead to Stage 2 Steady State Crack Propagation [3]

It is accepted among researchers that the environment inside the crack can vary differently from the bulk fluid surrounding the material which is why diffusion of chemical species is considered a possible limiting step in SCC [3]. The proposed mechanisms are categorized into two different classifications depending on if the crack advances via dissolution or by mechanical fracture [3]. One proposed mechanism that fits into the dissolution classification describes concentrated stress at the crack tip leading to high strain which might prevent the formation of a protective film and would allow for dissolution of the material at the crack tip (Dissolution Model) [3]. Another proposed mechanism within the classification of dissolution suggests that a passive film at the crack tip fractures due to the concentrated stress at the crack tip (Film Rupture Model) [3]. The fractured passive film exposes new metal surfaces which can be anodically corroded [3]. The process can repeat itself by forming new passive layers after each fracture in the old passive layer [3]. The breaking and reforming of the passive layer may explain the steady state regime for the crack propagation rate with stress intensity [3]. In the mechanical fracture classification, a proposed mechanism known as the corrosion tunneling model theorizes that corrosion into the material creates many tunnels next to each other that are separated by thin pieces of material [3]. The thin materials which separates the tunnels can then be broken by ductile

deformation [3]. In the film induced cleavage mechanism under the mechanical fracture class, a brittle crack can form in the passive film at the crack tip due to concentrated stresses [3]. The crack can then continue into the bare metal leading to propagation [3]. Different material and environment combinations might be explained by different variations of different mechanisms [3].

1.3 Chlorine Induced Stress Corrosion Cracking

To conduct a study to probe the mechanisms involved in chlorine induced stress corrosion cracking, it is important to review what is already known about the process through literature studies. Firstly, the compounds that can be found in sea salt must be analyzed. It has been found that the chlorine bearing salts in sea water consist of NaCl, KCl, MgCl₂, and CaCl₂ [8]. The concentration of each type of salt that is found in natural sea water are shown in **Table 1**. From the table below, NaCl makes up the majority of the chlorine bearing salts followed by MgCl₂ and CaCl₂ with trace amounts of KCl [8]. It is thus important to investigate the possible roles of each type of salt and how they compare in terms of CISCC. Some aspects such as the DRH and the corrosiveness of the salts are detailed here.

Table 1: Concentration of Chloride Bearing Salts in Natural Sea Water [8]

Chloride	Concentration (mol.kg ⁻¹ of sea water)
NaCl	0.41
MgCl ₂ .6H ₂ O	0.05
CaCl ₂ .2H ₂ O	0.01
KCl	0.003

1.3.1 Deliquescence Relative Humidity

One comparison that can be made of the more concentrated salts is the relative humidity needed to lead to the concentrated brine when the salts reach the DRH. **Figure 7** shows a graph that plots the DRH as a function of temperature for both NaCl and MgCl₂. As the figure depicts, NaCl has a high DRH of about 75% and does not appear to vary with temperature. Unlike NaCl, MgCl₂ has a relatively low DRH at around 35% and an increase in temperature leads to a decrease in the DRH. This indicates that MgCl₂ would become a concreted brine before NaCl as the relative humidity increases and that MgCl₂ can be in a brine form for a larger range of relative humidities. For CaCl₂, the DRH is similar to MgCl₂ with a DRH of ~35% at 20 °C down to ~13% at 50 °C [9, 10].

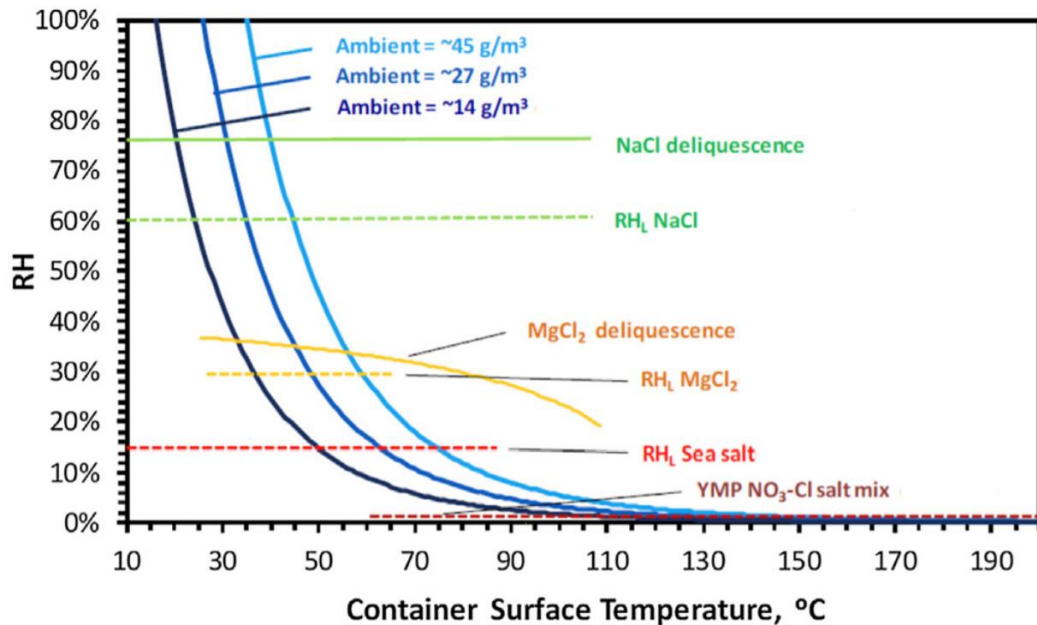


Figure 7: Deliquescence Relative Humidity as a Function of Container Surface Temperature with different Concentrations of Salts Deposited [11]

1.3.2 Effect of Different Chloride Salts and Effect of Concentration of Salts on Corrosion and Stress Corrosion Cracking

To gauge each chlorine bearing salt in sea salts ability to cause corrosion, various studies were examined in literature. One study by Prosek et al. performed CISCC experiments on austenitic stainless steels like 304, 316L, 904L, and S31254 [5]. The experiment utilized U-bend samples which were prepared as described in ASTM G30-94 [5]. Six drops of a concentrated chloride solution were placed on the U-bend samples [5]. The salt solutions included MgCl₂, CaCl₂, and NaCl with concentrations of 350 g/L, 400 g/L, and 190 g/L, respectively [5]. Samples were placed inside a climate controlled chamber and held at temperature of 20 °C, 30 °C, or 40 °C with a relative humidity of 30%, 50%, or 70% for 10 weeks [5]. The results showed that the samples which were deposited with MgCl₂ and CaCl₂ showed cracking at temperatures as low as 30° C and were transgranular in nature [5]. Pitting was found to have occurred which served as a stress concentrator from which a crack could develop [5]. At higher values of relative humidity, cracking was less prevalent which was due to more water being deposited onto the surface and diluting the salts on the surface [5]. Additionally, oxygen transport is also slower due to the increase in thickness of the film [5]. These results suggest that the aggressiveness of the salt relies on the ability to first form a thin brine (above DRH) and is based off the concentration of the solution formed with more concentrated solutions being more aggressive [5]. Finally, the observation of crack branching in the samples was presented but the authors did not discuss the reason other than discussing how it is common for CISCC [5].

Another study conducted by Ornek and Engelberg performed similar experiments with drops of salt solution on 304SS (Composition in **Table 2**) to study the effects of strain and the density of chloride deposition [4]. Small tensile specimens with a gauge thickness length of 20 mm were used. A picture of the tensile rig used to induce various levels of strains is shown in **Figure 8**. Samples were put under a constant load with a strain of either 0.1% or 0.2% which was measured using a strain gauge [4]. Drops of different concentrations of salt were added to the surface of the samples [4]. The specific parameters used are evident in **Table 3**. The test samples were placed inside a KBF Binder Humidity cabinet set to 50° C and a relative humidity of 30% for 6 months. In terms of analysis performed on the samples, a combination of optical microscopy and Scanning Electron Microscopy (SEM) equipped with an Electron Backscatter Diffraction (EBSD) detector were used [4]. SEM analysis was performed to probe the length of each crack along the gauge width (3 mm) and a rough estimate of crack growth rate by dividing the total length by the time. The results of the crack growth depths and rates are presented in **Table 4**. The crack depth and growth rate were only slightly elevated at higher strains. Additionally, the salt density may have had an effect on the crack growth rate of the higher strained material; however, all cracks of different salt densities had cracks that existed the entire 3 mm of the sample. The sample that was strained to only 0.1 % showed that increasing the density of salts increases the crack length and rate. In terms of topology, all the cracks that formed in the 0.1% strained sample were transgranular and branched (Example shown in **Figure 9**). The cracks that formed in the 0.2% strained were also branched but the authors described them as being less branched and having a straighter path (i.e. angle relative to the main crack plane was lower).

Table 2: Chemical Composition of 304ss (wt%) used in [4]

Cr	Ni	Mn	Si	C	N	P	S
18.15	8.6	1.38	0.45	0.055	0.038	0.032	0.005

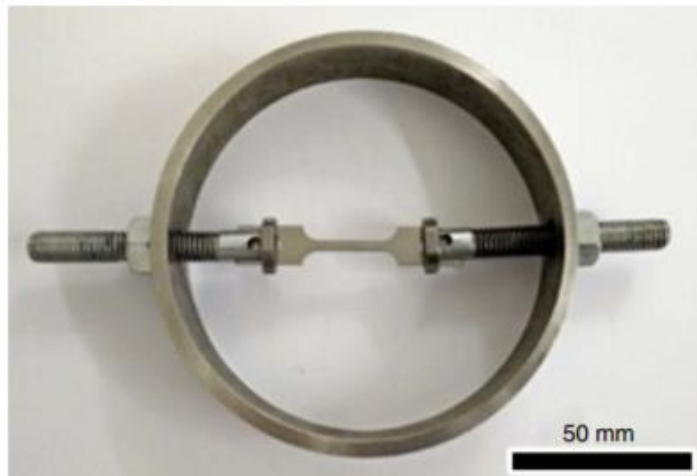


Figure 8: Tensile Rig used to Induce Stress on 304SS Tensile Samples [4]

Table 3: Salt Deposition Parameters used in [4]

No.	Concentration [mol]	Salt	Droplet Volume [μL]	Droplet Diameter [mm]	Deposition Density of Cl^- [$\mu\text{g}/\text{cm}^2$]
1	0.001	MgCl_2	0.5	1.76	1.5
2	0.01	MgCl_2	0.5	1.76	14.5
3	0.035	MgCl_2	0.5	1.76	50.7
4	0.1	MgCl_2	0.5	1.76	145
5	1	MgCl_2	0.5	1.76	1449.8
6	0.2	1 MgCl_2 : 0.68 FeCl_3	0.5	1.76	434.9

Table 4: Crack Lengths and Crack Growth Rates in 304SS Samples Tested at 0.1% Strain and 0.2% Strain [4]

No.	Deposition Density of Cl^- [$\mu\text{g}/\text{cm}^2$]	Low Strain (0.1%)		Low Strain (0.2%)	
		Longest SCC Crack Observed [μm]	Calculated Crack Growth Rate* [m/s]	Longest SCC Crack Observed [μm]	Calculated Crack Growth Rate [m/s] ^(A)
1	1.5	—	—	—	—
2	14.5	400	2.6×10^{-11}	—	—
3	50.7	2,341	1.5×10^{-10}	3,000	1.9×10^{-10}
4	145	2,597	1.7×10^{-10}	3,000	1.9×10^{-10}
5	1449.8	2,800	1.8×10^{-10}	3,000	1.9×10^{-10}
6	434.9	50	3.2×10^{-12}	500	3.2×10^{-11}

(A) Only surface cracks were considered.

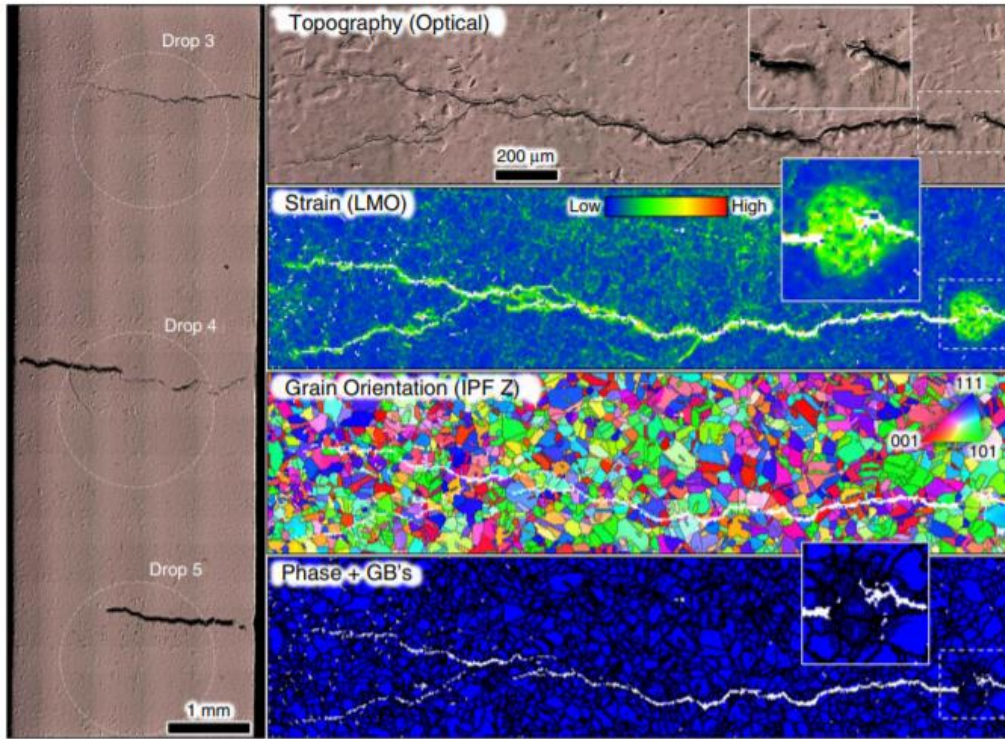


Figure 9: Optical Microscopy , Strain Maps, Inverse Pole Figures, and Phase and Grain Boundary Character of Cracks under Drop 3 Showing Crack Branching and Transgranular Cracking [4]

1.3.3 Types of Experiments Conducted in Literature on Chlorine Induced Stress

Corrosion Cracking

In literature, CISCC on austenitic stainless steel has been studied extensively in boiling solutions of $MgCl_2$ [3]; however, it has been shown elsewhere that cracking rates and even sometimes mechanisms can be different in thin film solutions compared to bulk solutions [4, 11]. The boiling bulk solutions of $MgCl_2$ have been used mostly because of the severity of CISCC on stainless steels giving the ability to do rapid testing [3]. Bulk solutions can contain less oxygen compared to thin films [9]. Oxygen migration into cracks can play a role in stress corrosion cracking in terms of cracking rate and morphology [3]. There have been a few studies that have studied the effects of CISCC in thin films under humid atmospheric environments on austenitic stainless steels like 304SS [4, 5, 9, 12, 13]. These studies confirm that CISCC in

stainless steels is mostly transgranular in nature [4, 5, 9]. In cases where sensitization is evident, cracking has been reported to have switched from transgranular to intergranular [14]. In general, it has been found that when the “corrosiveness” decreases, more selective attacks seems to be more evident and result in an intergranular nature [14]. Studies like those found in [4, 5, 9] tended to just look mostly at the macroscopic properties and effects to parameters like the type of salt, relative humidity and temperature. These examples of studies show that a macroscopic (i.e. cracking susceptibility, crack lengths, and crack growth rates) understanding has been improved; however, these research studies as well as other lack the microstructural information that can be used to better understand the overall mechanisms at play. A mechanistic view of the problem can lead to solutions of prevention and mitigation as well as the development of better materials. In terms of mechanisms, a better understanding of pitting and initiation have been researched while the propagation stage has been slightly neglected. For initiation, it is well known that the chlorine ions can disrupt the passive chromium oxide layer and cause the potential of the metal to be above the pitting potential [11, 15]. The pit acts as the anode while the surrounding material acts as a cathode and can cause the pit to grow further [11]. The pit can serve as a place for stress to concentrate and can develop into a crack [4, 5, 9, 11]. In terms of the propagation stage, there has only been some speculation about cracking due to metal dissolution but it is unclear how stress may play a role in the mechanisms [11]. More research is needed to understand, from a microstructural point of view, the mechanisms at play.

1.3.4 Proposed Mechanisms for Chlorine Induced Stress Corrosion Cracking

For chlorine induced stress corrosion cracking, two models have been proposed based on the role of chlorine [14]. Depending on the concentration, chlorine ions shift both the electrochemical potential as well as the pH of the solution [16]. Solutions that contain 0.5 M to 5 M can have a pH of -0.5 to 0.5 and are shifted to an active passive state [16]. Chlorine ions are known to disrupt the passive chromium oxide films that form [11]. In one set of models, anodic dissolution is believed to be the mechanism where the crack tip is always exposed due to high stresses and the electrochemical potential being in an active-passive state [14, 17]. Dislocation buildups and slip at the crack tip provide preferential dissolution at the crack tip. The disruption of the protective chromium oxide by the chlorine ions also helps dissolution. Another version of the model states that the stress is used to crack any passive layer at the crack tip to allow for more dissolution [3] . Another model states that crack propagation is due to the cleavage and fracture of a corrosion layer that forms at the crack tip [14, 18]. This model would explain the jumps in crack length that were acoustically measured [17].

1.3.5 Crack Branching in General Stress Corrosion Cracking

Many experiments involving CISCC report crack branching but do not specify the reason for branching [4, 5]. Crack branching happens in almost all types of materials including steels, titanium based alloys, aluminum based alloys and many others [19]. In cases with SCC, it has been theorized that crack branching takes place on the surface because the surface is in a state of plane stress and is not as hindered like the bulk material [19]; however, it has been shown the cracks in high strength materials tends to grow faster in the bulk due to a plane strain condition being dominant and keeping the plastic zone small [19]. Additionally, the inside of the crack has been

found to be more acidic in a corrosive environment than the sides due to the limiting diffusion [19]. Sample size might play a role in terms of where branching occurs due to a plane stress condition becoming more dominant with smaller samples. The branching on the surface over time could transverse towards the bulk of the material due to the subjacent layer undergoing plastic deformation [19]. Branching has been separated into two categories. The first category is known as microbranching where the crack front splits into many cracks which are only separated by a distance on the order of a grain [19-21]. The others category is known as macrobranching where the crack separates into two or more large cracks which are separated by many times the grain size [19-21]. Microcracks can transcend into macrocracks when a high enough stress intensity is achieved that selects a subset of cracks to continue while the other arrest [21]. In terms of the role of stress intensity on crack branching, other researchers have shown that branching needs a minimum stress intensity for both microbranching and macrobranching as shown in **Figure 10**. Macrocrack branching has been seen to happen in the second stage or steady state region of the curve. One area of debate amongst researchers is whether macrobranching is a symptom of crack branching or the cause of the steady state regime [20]. Some researcher argue that branching hinders the acceleration of crack propagation, although many researchers do not treat crack as branching in terms of stress intensity which would be reduced due to branching [20]. More research is needed in this area to determine the relationship between branching and the steady state regime of the growth rate as a function of stress intensity curve.

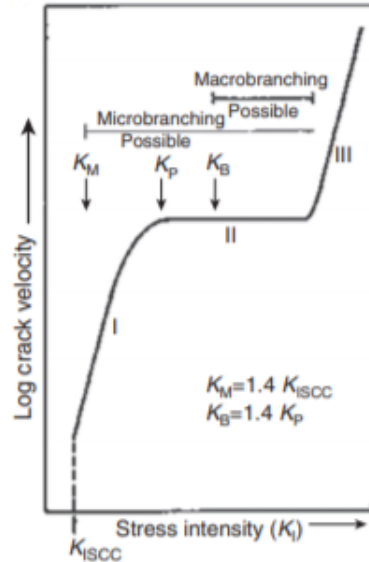


Figure 10: Typical Stress Corrosion Cracking Crack Growth Rate as a Function of Stress Intensity Profile with Regions for Microbranching and Macrobranching [20]

1.4 Remaining Questions about Chlorine Induced Stress Corrosion Cracking in Austenitic 304 Stainless Steels

There are several questions to be asked about the process of chlorine induced stress corrosion cracking in austenitic stainless steels. Additionally, there are question which arise from the experimental results which will be discussed further in chapter. Below is the list of questions which will be answered with this thesis.

(1) What are the effects of fatigue pre-cracking on the initial microstructure?

As will be shown in Chapter 3, fatigue was shown to have altered microstructure of each material in terms of phase transformation and microvoid formation. It is important to consider the possible effects of fatigue pre-cracking on the CISCC behavior. Many researchers who study SCC behavior choose to fatigue pre-crack specimens which may have an undesirable effect on the SCC behavior itself.

(2) What is the role of martensite as a possible intrinsic and extrinsic factor in crack retardation?

There are many crack retardation mechanisms which different material can possess. Retardation mechanisms are broken down into two categories: Intrinsic and Extrinsic. Intrinsic mechanisms are the ones that are altering crack rate at the crack tip. In this study, the act of phase transformation could be taking away energy used to propagate a crack depending on the mechanisms of CISCC. Extrinsic mechanisms are the ones which occur behind the crack tip in the crack wake. In this study, the austenitic matrix can be transformed into deformation induced martensite at the crack tip. The transformed material remains along the crack wake as the crack propagates. Compared to the austenitic matrix, the transformed martensite can lead to an increased strain locally. The resultant dilatation provides a closure stress which effectively shields the crack tip from some stress and decreases the stress intensity. Phase transformation in Partially Stabilized Zirconia (PSZ) is an example of a material which has this extrinsic mechanism known as transformation toughening [22]. Other researchers have looked into using cold worked material with a higher martensite phase fraction as a result of cold working [23, 24]; however, cold working can increase the yield strength of the material due to the increase in dislocation density [25]. Increasing the strength of the material often leads to a decreased plastic zone (Lowering the fracture toughness) so the effects of martensite and increased hardness due to cold working becomes convoluted.

(3) How does the stress intensity affect the rate and morphology of cracks?

From **Figure 4** for general SCC, the stress intensity effects on crack propagation rates can vary depending on which stage of SCC a material is undergoing. Does CISCC follow the

same trends? Additionally, how does stress intensity affect the types of morphology the crack can take with emphasis on how it affects the branching nature the crack can take.

(4) How does crack branching influence the steady state propagation rate?

A question which has been posed by researchers regards the role of crack branching on the steady state propagation rate [20]. Crack branching is a feature which has been seen often in test but does not always occur [20, 21, 23, 26-29]. It is unclear if crack branching causes steady state propagation or vice versa.

(5) What role does temperature play on crack growth rates?

If the rate limiting step is related to temperature, how does it affect the crack propagation rate and by how much.

(6) What is the role of chlorine and chlorine forming compounds?

How does chlorine induce stress corrosion cracking and what specific role does chlorine play?

(7) What are the mechanisms that are operating on the microstructural level?

Overall, the mechanism is the key to understanding the different aspects of CISCC and how different factors can influence cracking rates and morphology.

Chapter 2: Materials & Methodology

2.1 Materials

Cannisters for storage of spent nuclear fuel are usually made of 304SS and 316SS. 316SS is more corrosion resistant compared to 304SS and the 304SS canisters are the ones which have been identified as the most at risk for CISCC [2]. Austenitic 304SS has a face centered cubic crystal structure and the material created by annealing the material around 1200 °C followed by a water quench to keep the metastable austenite phase at room temperature. The alloy is solution strengthened meaning that impurities are intentionally added to strengthen the material by generating lattice strain fields which can restrict dislocation motion [25]. Although 304SS is solution annealed to produce a uniform phase, some precipitates can still form.

For this study three versions of 304SS were used in this study which included a commercial-304, 304H (High Carbon), and 304L (Low Carbon). The compositions of each of the alloys used in this study is shown in **Table 5**. Various heats of 304SS are currently used as canister materials. This experiment used two heats of 304SS material (304H and 304L) which were obtained and fabricated at Sandia National Laboratory (SNL) while the commercial-304SS material was obtained from McMasters. The commercial-304 material was used since it would be the most susceptible to CISCC compared to the other two heats of 304SS

Table 5: Chemical Compositions for 304L, 304H, and Commercial-304

Material	C	Co	Cr	Cu	Mn	Mo	N	Ni	P	S	Si
304L	0.0216	0.198	18.3105	0.3915	1.828	0.2855	0.0889	8.1125	0.0325	0.001	0.251
304H	0.0418	0.1345	18.193	0.4005	1.7495	0.2985	0.0844	8.0725	0.0335	0.001	0.293
304	0.022	0.15	18.1	0.45	1.68	0.30	0.09	8.4	0.037	0.025	0.4

Before conducting experiments, each of the three samples was characterized with optical microscopy, synchrotron x-ray diffraction, scanning electron microscopy, and transmission electron microscopy. Optical microscopy was used to measure grain sizes as well as assess grain morphology. Optical samples were prepared by polishing the samples with SiC paper using 400 grit, 600 grit, 800 grit, and 1200 grit followed by polishing with 1 μm diamond solution followed by 0.05 μm colloidal silica to create a mirror like finish. Samples were then etched using an Aqua Regia solution (60 mL of HCl + 20 mL HNO₃) to reveal the grain structure. ImageJ was then used to calculate the grain sizes by assuming the grains were circular in shape. A detailed guide to grain size measurements can be found in **Appendix A**. Synchrotron x-ray diffraction was conducted on the as-received materials at Argonne National Laboratory's Advanced Photon Source using an x-ray energy of 71.676 keV. Phases with enough volume fractions in the materials were identified using x-ray diffraction. Scanning electron microscopy was used to observe the different phases which were identified from the x-ray diffraction spectra as well as identify new phases which lacked the volume fraction to be detected by x-ray diffraction. The Scanning Electron Microscope (SEM) was equipped with Energy Dispersive Spectroscopy (EDS) to collect chemical information in the form of maps and characteristic x-ray spectrum. Additionally, shapes of precipitates were also observed as well as directionality of groups of precipitates relative to the rolling direction. Area densities of precipitates were calculated for each material with the aid of ImageJ. More detail about the area density calculation is found in **Appendix B**. Samples were prepared for SEM by electropolishing using a Lectopol \circledcirc with a 10% V/V of perchloric acid in methanol at room temperature with a voltage of 14 V. Finally, Transmission Electron Microscopy (TEM) was conducted to identify the phases of precipitates and find new precipitates which might have been too small for scanning electron microscopy. Moreover, precipitates locations in the

microstructure were also identified. Additionally, TEM was also used to identify various microstructural features like stacking faults, grain boundaries, and twin boundaries. TEM were prepared via electropolishing using a twin jet Tenupol[©] with a 10% V/V of perchloric acid in methanol solution at -35 °C using a voltage of 17 V to create electron transparent areas within a 3 mm disc.

2.1.1 As-Received Commercial-304 Characterization

The optical microscopy of the etched as-received commercial-304 is shown below in **Figure 11**. The grains were measured to have an average size of 20 μm and the morphology is equiaxial. Also evident in the optical microscopy is some twin boundaries.

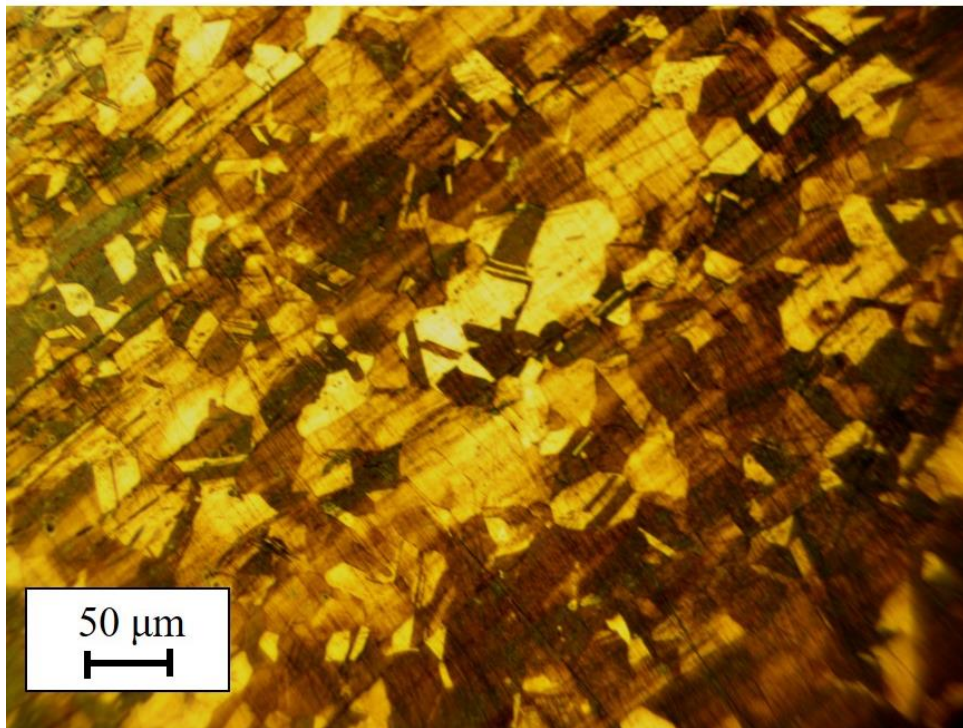


Figure 11: Optical Microscopy of As-Received Commercial-304 after Etching in a Solution of Aqua Regia showing Grain Sizes of around 20 μm which are Equiaxial and show some Twin Boundaries

Synchrotron x-ray diffraction was then employed to identify phases with enough volume fraction in the as-received commercial-304 sample. The x-ray diffraction spectrum is shown in **Figure 12**. The main phase in the spectrum is that of the austenite phase. Some residual martensite in the form of body center cubic α' -martensite and hexagonal closed packed ϵ -martensite is also present. Small intensity peaks for manganese sulfide were also present which is a typical inclusion which can be present in 304SS [3]. A small intensity peak of an $M_{23}C_6$ carbide was also present where M can stand for Fe, Cr, or Mn which have closely related d-spacings.

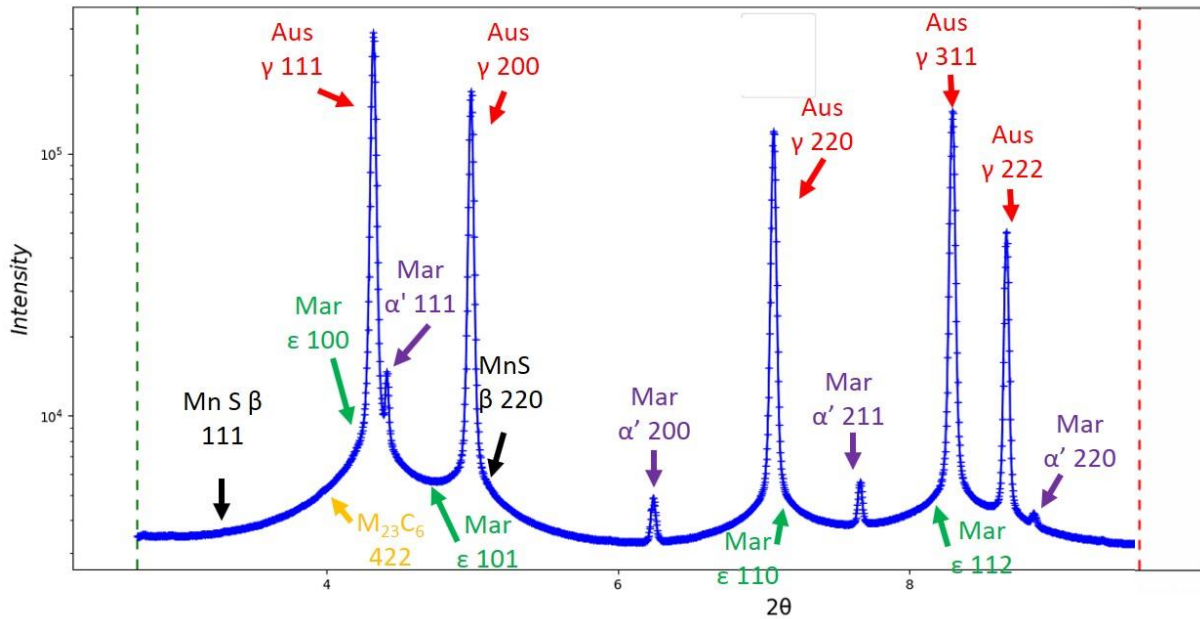


Figure 12: Synchrotron X-ray Diffraction Spectrum of As-Received Commercial-304 Showing Various Phases Present in the Microstructure with Enough Volume Fraction

Scanning electron microscopy was performed on the as-received commercial-304 material to observe the phases which the x-ray diffraction spectrum revealed in the material as well as find other phases which did not have enough volume fraction to be evidenced by synchrotron x-ray diffraction. Additionally, the shapes and density of precipitates

was also observed. **Figure 13a** shows the SEM micrograph of a population of precipitates in the as-received commercial-304 material. There appears to be many precipitates and **Figure 13b** shows the EDS spectrum and chemical maps of one of these precipitates. From the magnified SEM micrograph, the precipitate is elongated in one direction and the EDS spectrum and chemical maps suggest the presence of a silicon and oxygen rich precipitate. The area density of precipitates in this micrograph was calculated to be 0.00646.

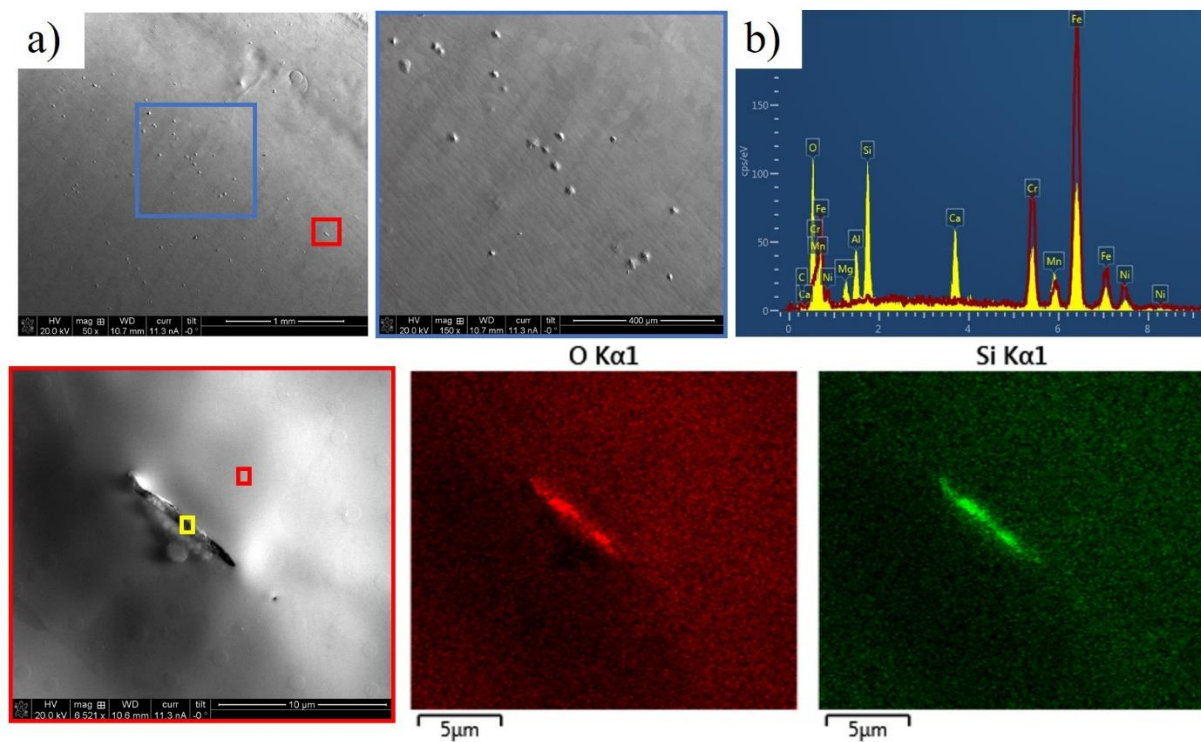


Figure 13: a) Scanning Electron Micrograph of As-Received Commercial-304 Showing Precipitate Population and b) Energy Dispersive Spectroscopy Spectrum (Red Curve Corresponds to Spot next to Precipitate and the Yellow Curve corresponds to on the Precipitate) and Chemical Maps showing One Elongated Precipitate to be Rich in Silicon and Oxygen

Transmission Electron Microscopy was performed to observe microstructural features like dislocations, stacking faults, and grain boundaries as well as observe smaller precipitates. A TEM micrograph of the as-received commercial-304 sample is shown in **Figure 14a**. High Magnification micrographs of commercial-304 are evident in **Figure 14b**. The

red and yellow box depict dislocations within a grain. The green box shows a grain boundary and a twin boundary which appear to be without precipitation. The blue box depicts a Cr₂₃C₆ carbide present within one of the grains.

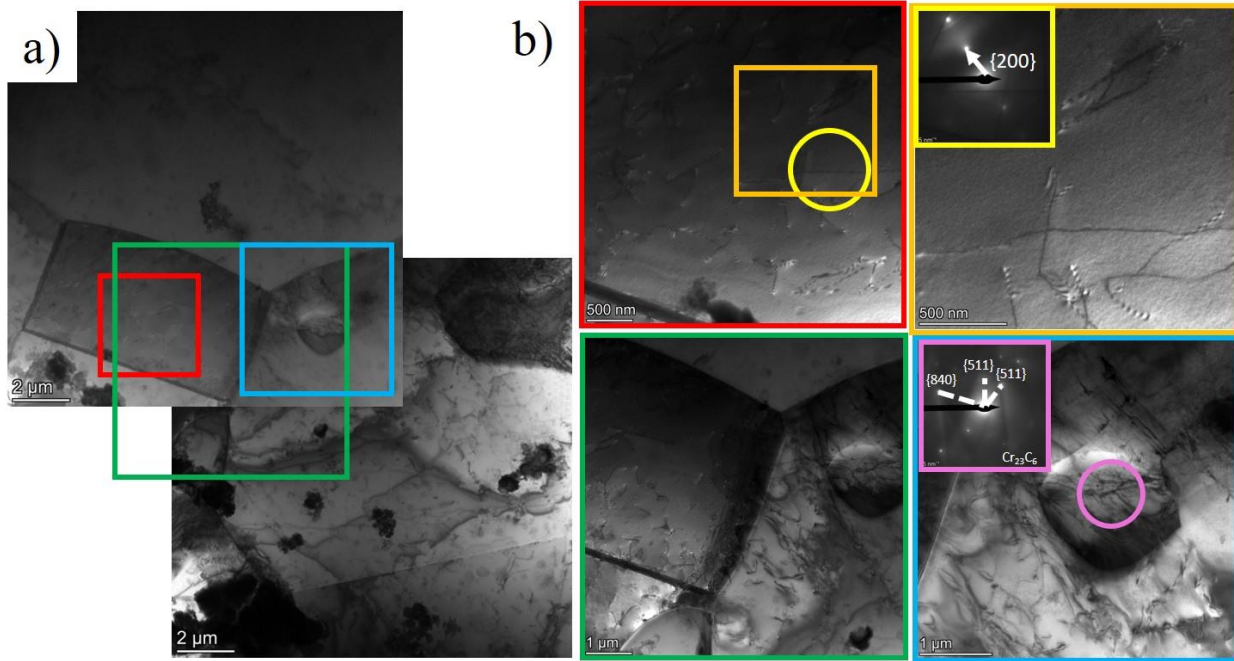
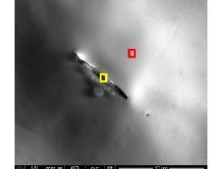
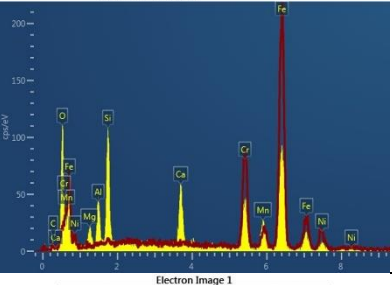
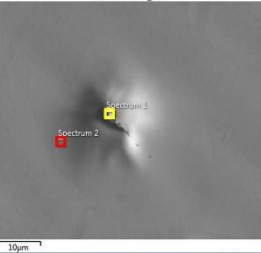
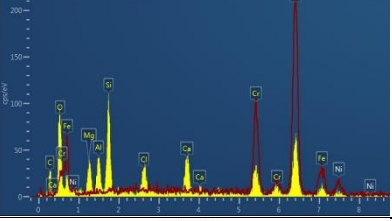
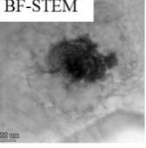
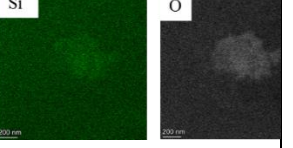
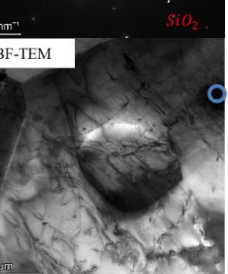
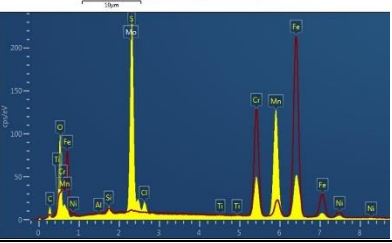
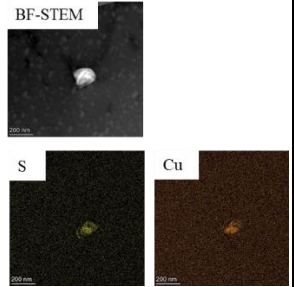
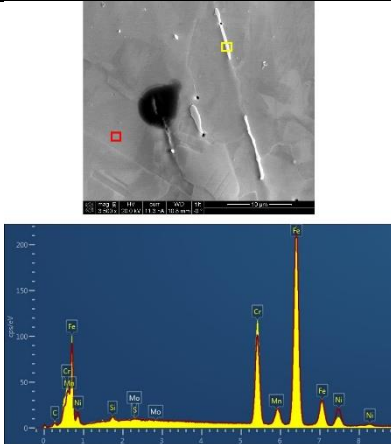
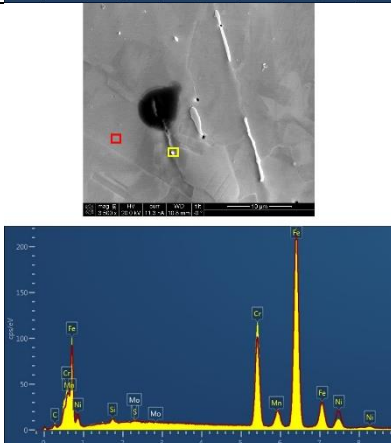
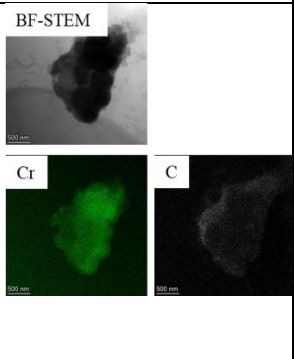
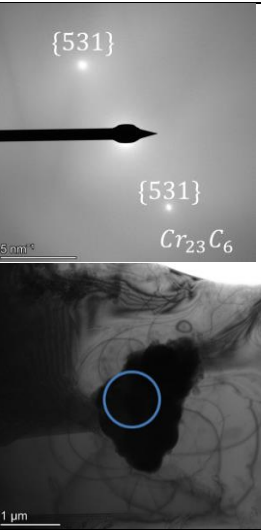


Figure 14: a) Low Magnification Transmission Electron Microscopy Micrograph of As-Received Commercial-304 and b) Higher Magnification Micrographs of Dislocations (Red and Yellow Boxes), Grain and Twin Boundaries with no Precipitation (Green) and a Cr₂₃C₆ within a Grain (Blue Box)

Table 6 shows the rest of the precipitates which were evidence either by SEM and/or TEM observations. Some of the other precipitates which were evidenced include an elongated MnS particle found in SEM and a copper and sulfide rich particle in TEM believed to be Cu₂S

Table 6: Precipitation Found in the As-Received Commercial-304 Microstructure through Scanning Electron Microscopy, Energy Dispersive Spectroscopy, and Transmission Electron Microscopy Observations

Alloy	Precipitate Shape	SEM	TEM	Diffraction
304	Elongated Si and O rich particles (~10 um long)	 	Did not find large Si O Particles	Did not find large Si O Particles
304	Small Si and O rich particles (~5 um)	 	 	 
304	Elongated MnS	 	Elongated MnS feature what not found	Elongated MnS feature what not found

304	Spherical Sulfide	Not Found in SEM	BF-STEM 	No Diffraction Pattern
304	Elongated Carbide		Not found in TEM	Not Found in TEM
304	Smaller Carbides		BF-STEM 	{531}  Cr ₂₃ C ₆

2.1.2 As-Received 304H Characterization

The optical microscopy of the etched as-received 304H is shown below in

Figure 15. The grains were measured to have an average size of 30 μm and the morphology is equiaxial. Also evident in the optical microscopy is some twin boundaries.

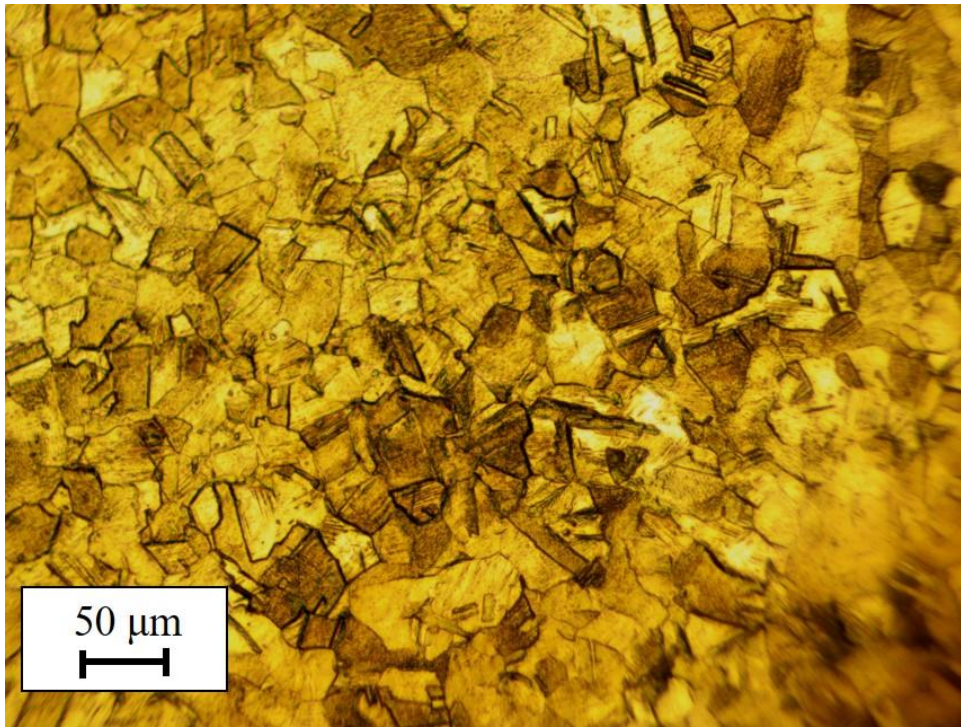


Figure 15: Optical Microscopy of As-Received 304H after Etching in a Solution of Aqua Regia showing Grain Sizes of around $30 \mu\text{m}$ which are Equiaxial and show some Twin Boundaries

The synchrotron x-ray diffraction spectrum for as-received 304H is shown in **Figure 16**. The synchrotron x-ray spectrum shows the major phase is austenite with some residual martensite (Both α' -martensite and ε -martensite). In addition to the main phases, the spectrum shows carbides.

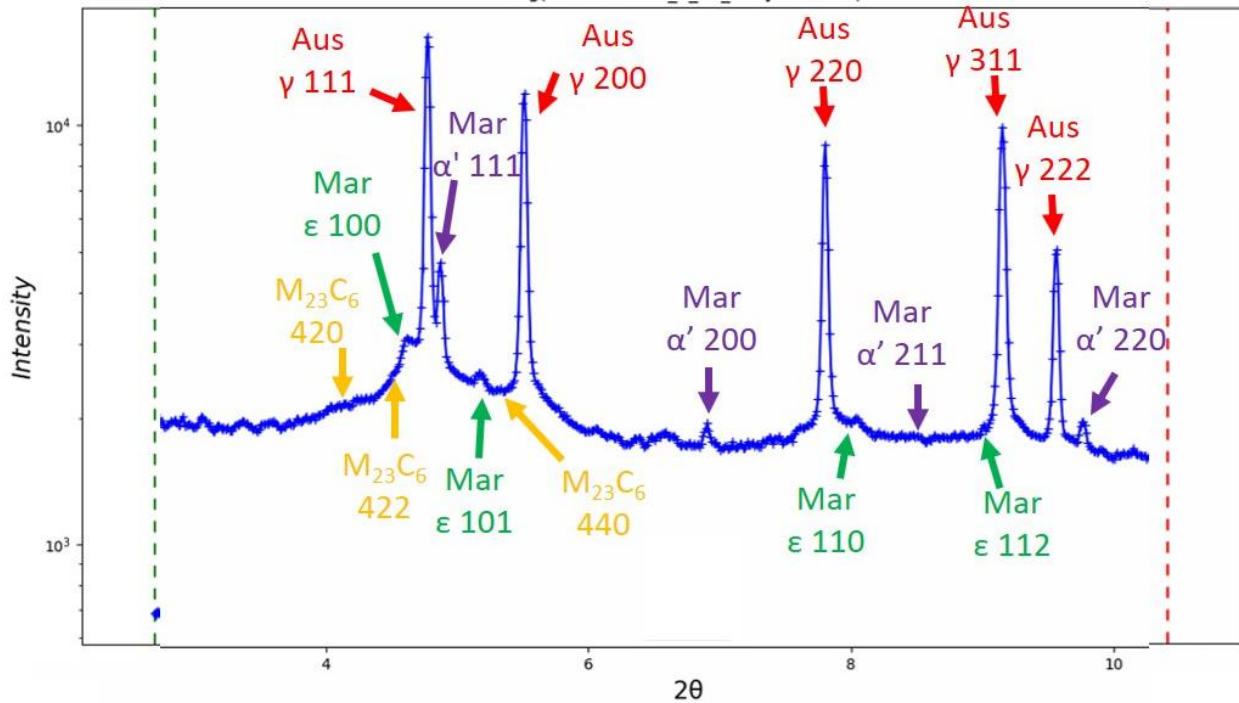


Figure 16: Synchrotron X-ray Diffraction Spectrum of As-Received 304H Showing Various Phases Present in the Microstructure with Enough Volume Fraction

An SEM micrograph of the as-received 304H material is shown below in **Figure 17**. The SEM micrograph shows several precipitates on the surface ranging in size and shape. The precipitate area density calculated for this micrograph was 0.00342 which is smaller than the area density calculated for commercial-304. Several precipitates appear to be in line with the rolling direction of the original plate of material. TEM micrographs and a selected area electron diffraction pattern are shown in **Figure 18**. From the micrograph both a triple junction and a twin boundary can be seen in **Figure 18a** and **b** and there does not appear to be any precipitation at the grain boundaries. **Figure 18c** shows a residual martensite grain which was identified by selected area electron diffraction shown in **Figure 18d**.

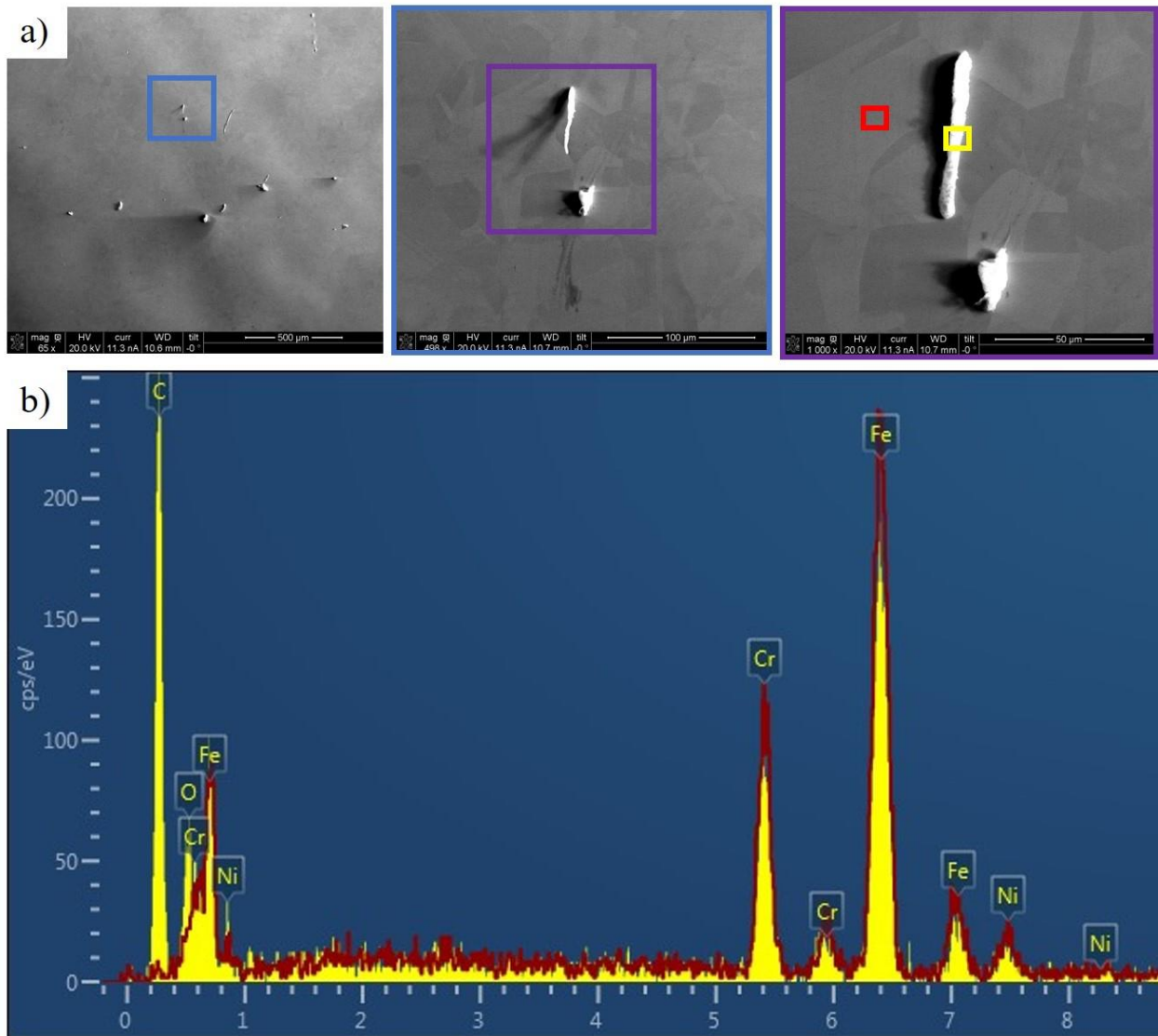


Figure 17: a) Scanning Electron Micrograph of Precipitates in 304H and b) an Energy Dispersive X-ray Spectroscopy Spectrum Showing an Elongated Carbide (Yellow Curve is Scan on the Precipitate and Red Curve is Scan next to Precipitate)

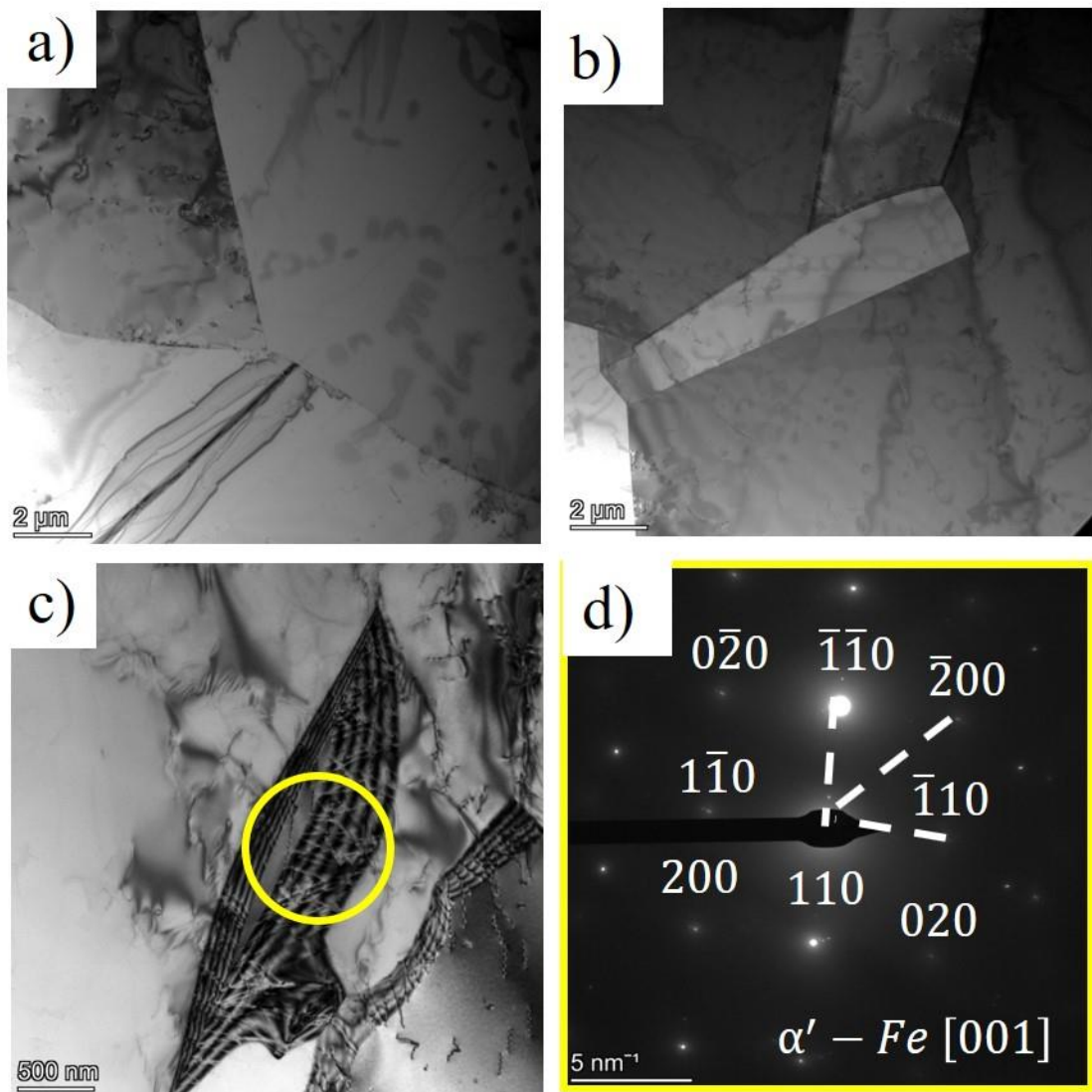
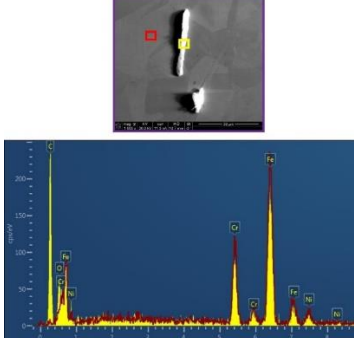
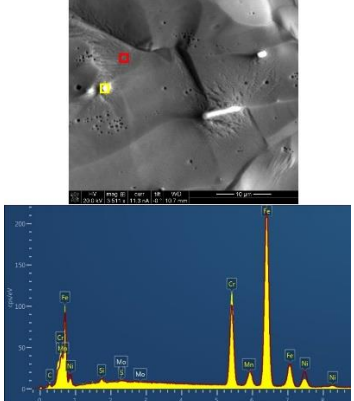
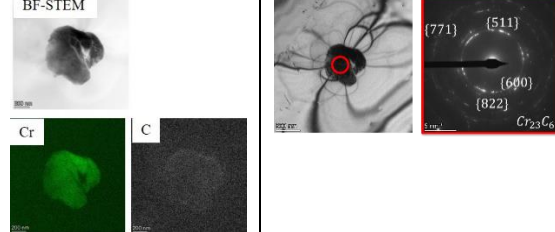
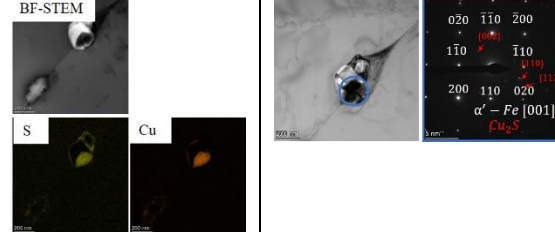


Figure 18: Transmission Electron Microscopy Micrograph of 304H As-Received showing a) Tiple Junctions and Grain Boundaries, b) Twin Boundaries, and c) Residual Martensite as Indicated by Selected Area Electron Diffraction shown in d)

Table 7 shows the precipitates which were observed in the 304H as-received material using SEM and TEM. Precipitates which were found include both elongated and spherical carbides as well as a Cu₂S precipitate.

Table 7: Precipitation Found in the As-Received 304H Microstructure through Scanning Electron Microscopy, Energy Dispersive Spectroscopy, and Transmission Electron Microscopy Observations

Alloy	Precipitate Shape	SEM	TEM	Diffraction
304H	Elongated Carbides		Not Found in TEM	Not Found in TEM
304H	Spherical Carbides			
304H	Sulfide	Not found in SEM		

2.1.3 As-Received 304L Characterization

The optical microscopy of the etched as-received 304L is shown below in **Figure 19**. The grains were measured to have an average size of 50 μm and the morphology is equiaxial. Also evident in the optical microscopy is some twin boundaries.

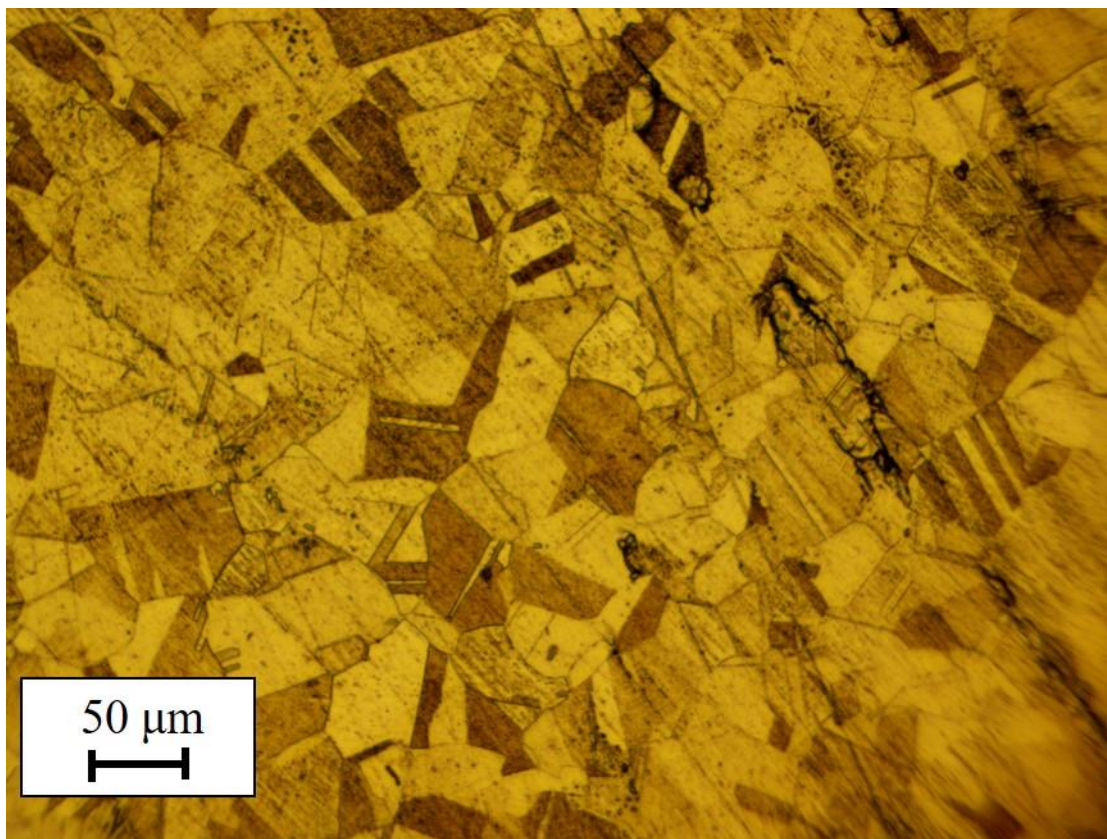


Figure 19: Optical Microscopy of As-Received 304L after Etching in a Solution of Aqua Regia showing Grain Sizes of around 50 μm which are Equiaxial and show some Twin Boundaries

The synchrotron x-ray diffraction spectrum for as-received 304L is shown in **Figure 20**. The synchrotron x-ray spectrum shows the major phase is austenite with some residual martensite (Both α' -martensite and ϵ -martensite). In addition to the main phases, the spectrum shows carbides are also present in the as-received 304L microstructure.

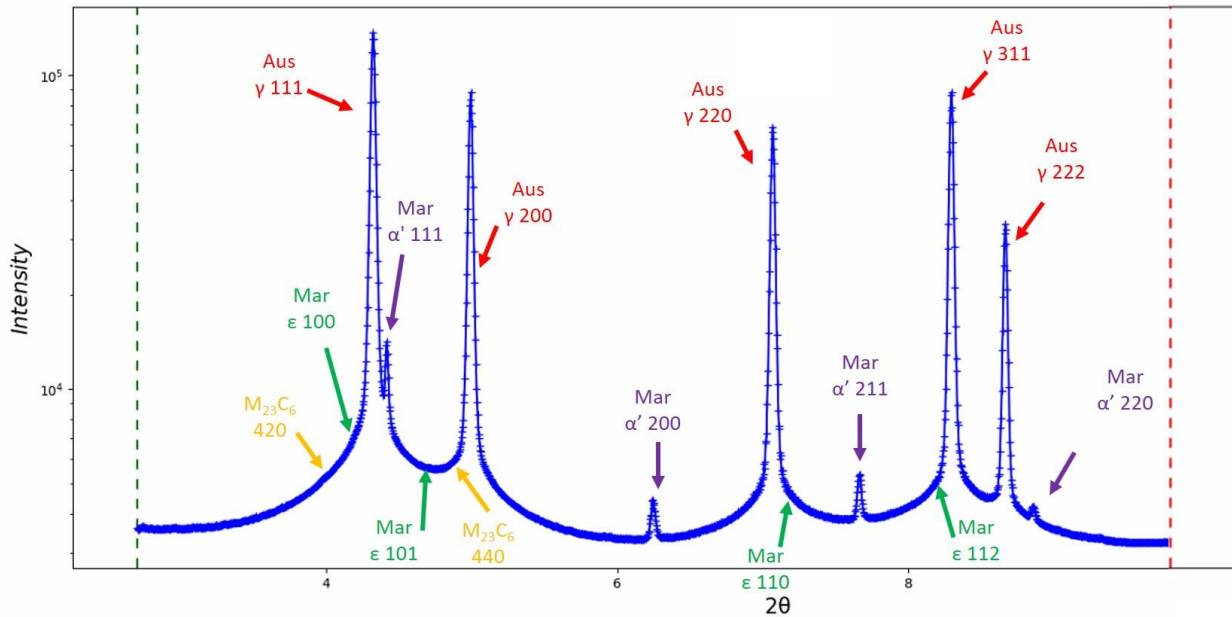


Figure 20: Synchrotron X-ray Diffraction Spectrum of As-Received 304L Showing Various Phases Present in the Microstructure with Enough Volume Fraction

An SEM micrograph of the as-received 304L material is shown below in **Figure 21**. The SEM micrograph shows several precipitates on the surface ranging in size and shape. In fact, the higher magnification micrograph reveals the presence of many small precipitates. Some of these small precipitates appear to form a line in the rolling direction. The precipitate area density calculated for this micrograph was 0.00166 which is the smallest compared to as-received 304H and commercial-304. Several precipitates appear to be in line with the rolling direction of the original plate of material.

The TEM for as-received 304L is shown in **Figure 22**. Residual α' -martensite was found in the as-received 304L as shown in **Figure 22a** and confirmed by the selected area electron diffraction pattern shown in **Figure 22b**. Twin boundaries were also present along with stacking faults as shown by **Figure 22c** and **d**, respectively.

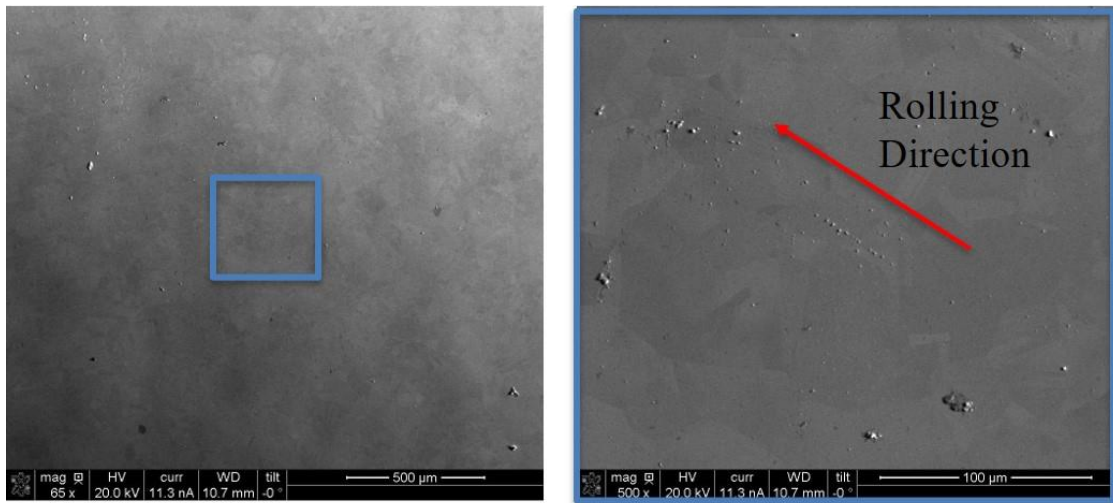


Figure 21: Scanning Electron Microscopy Micrograph of As-Received 304L Showing Larger Precipitates at 65X Magnification and Many Small Precipitates at 500X Magnification. Some Precipitates are shown in Line with the Rolling Direction

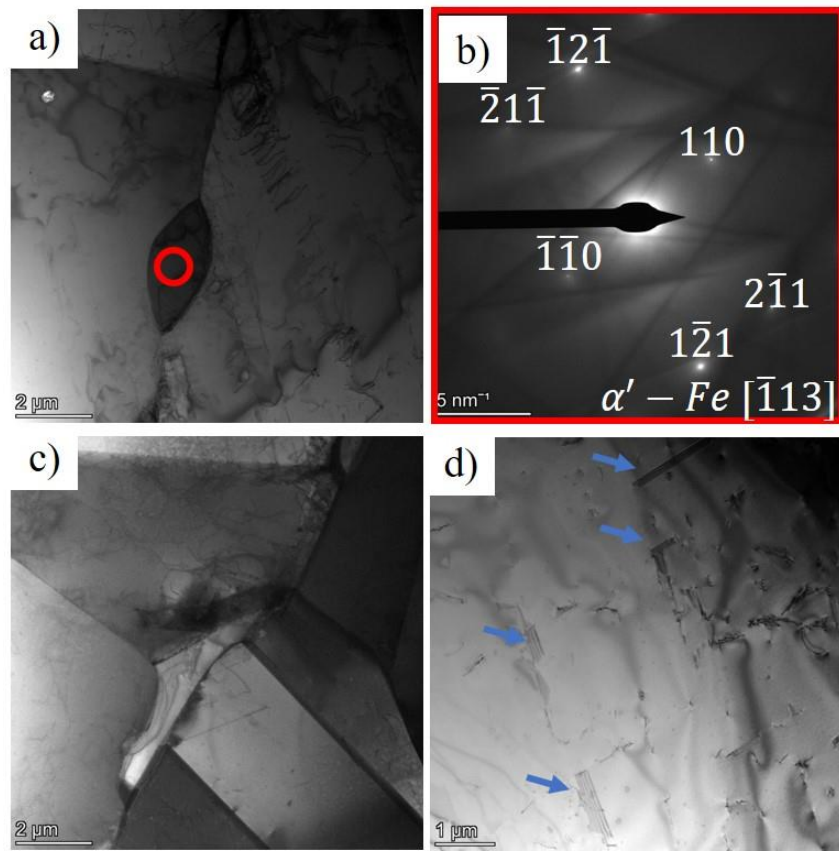
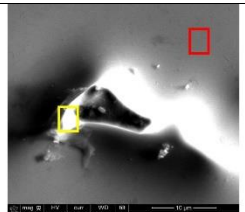
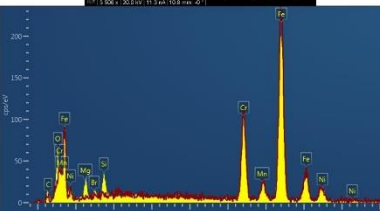
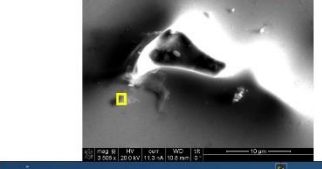
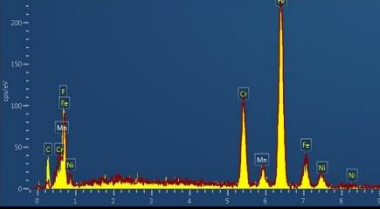
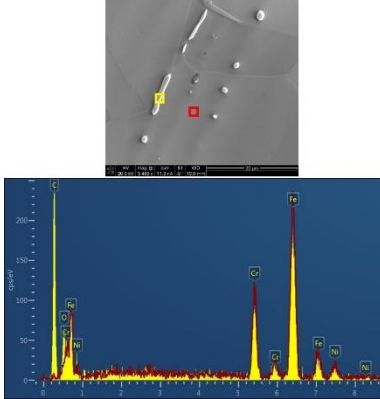
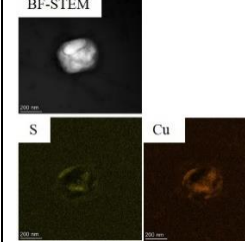
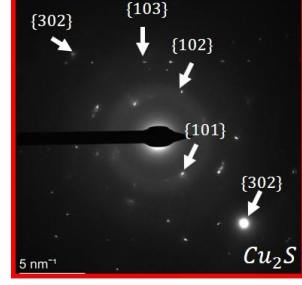
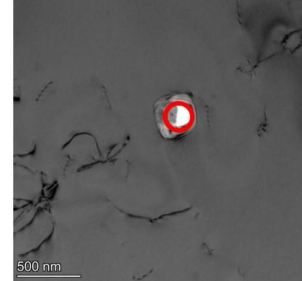


Figure 22: Transmission Electron Microscopy of the As-Received 304L Material Showing a) A Grain of Residual Martensite Confirmed by the Selected Area shown in b), Twin Boundaries, and d) Stacking Faults Indicated by Blue Arrows

Table 8 shows the precipitates that were observed in the as-received 304L material through SEM and TEM observations. Some precipitates which were evidenced include small silicon oxide particles, spherical and elongated carbides, and copper sulfide.

Table 8: Precipitation Found in the As-Received 304L Microstructure through Scanning Electron Microscopy, Energy Dispersive Spectroscopy, and Transmission Electron Microscopy Observations

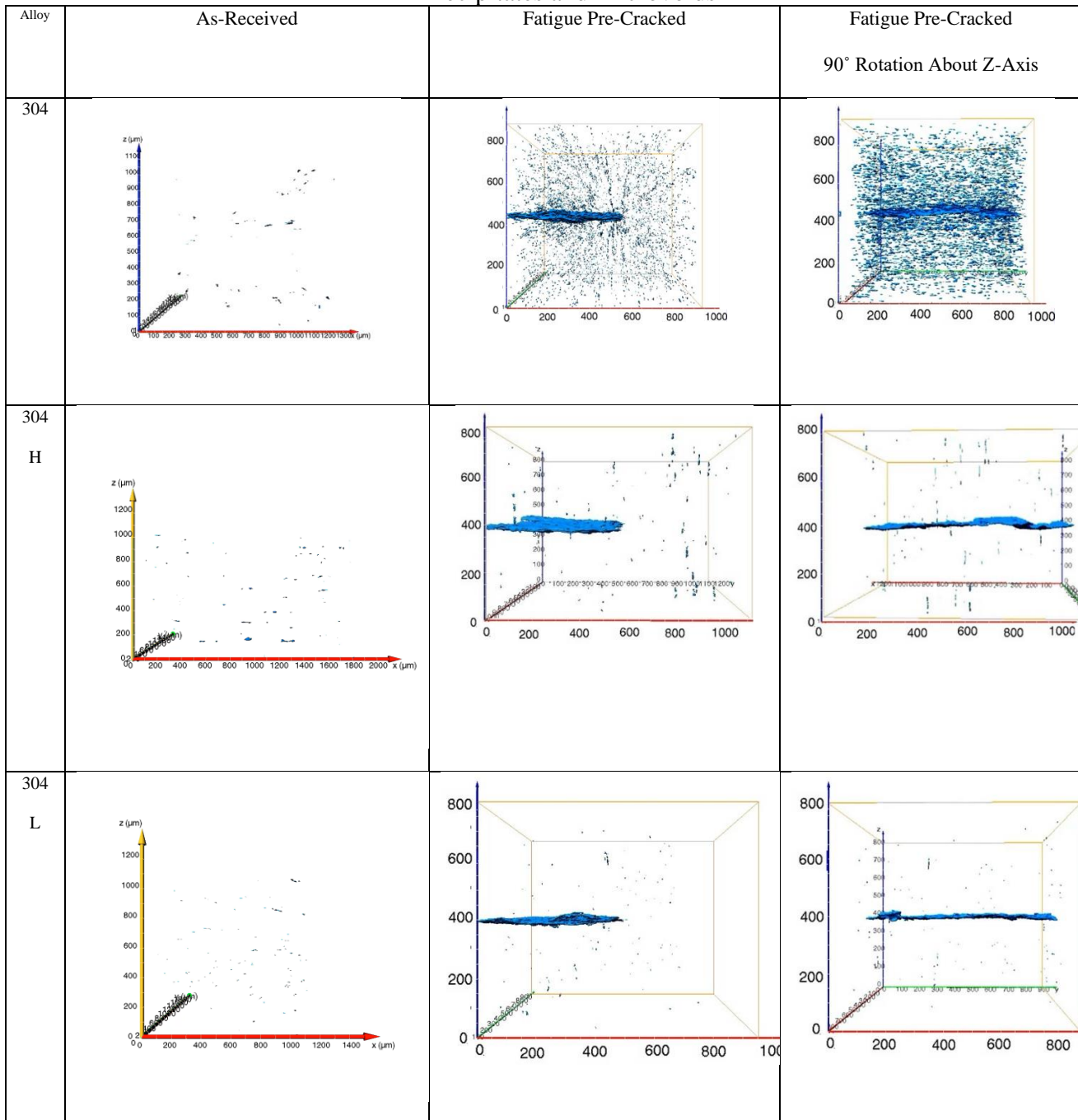
Alloy	Precipitate Shape	SEM	TEM	Diffraction
304L	Spherical Silicon Oxide Particles	 	Not found in TEM	Not Found in TEM
304L	Spherical Carbides	 	Not Found in TEM	Not Found in TEM

304L	Elongated Carbide		Not Found in TEM	Not Found in TEM
304L	Copper Sulfide	Not Found in SEM		 

2.1.4 Tomography of As-Received and Fatigue Pre-Cracked Materials

Since this study involved fatigue pre-cracking the samples, a detailed analysis must be conducted on the pre-cracked samples to see how fatigue may have impacted the microstructure of the material. The materials microstructure is responsible for the mechanical and electrochemical processes that occur on the macroscale [25]. To characterize the changes in the material, tomography scans were conducted at the Advanced Photon Source at Argonne National Laboratory using the 1-ID-E beamline on the as-received materials and the fatigue pre-cracked samples. **Table 9** shows the tomographs of the as-received and fatigue pre-cracked materials for commercial-304, 304H, and 304L.

Table 9: Tomographs of the As-Received and Fatigue Pre-Cracked Samples Showing Precipitates and Microvoids



As a consequence of attenuation contrast, microvoids and some precipitates in the sample also become extracted through the segmentation process. The as-received materials

show mostly precipitates while the fatigue pre-cracked samples show the addition of microvoids into the microstructure. Comparing the microvoids of the different 304 stainless steel samples, two observations were evident. The first is that the higher impurity commercial-304 sample contained the most microvoids followed by 304H and then 304L. The second observation is the overall shape and size of the features. The shape and size are best seen when comparing the fatigue pre-cracked tomographs of **Table 9** in the last two columns which are the same tomographs rotated 90° around the vertical z-axis. The commercial-304 sample has elongated features in the thickness direction (i.e. the direction parallel to the crack front) of the sample. The 304H sample, on the other hand, has elongated features in the loading direction. The 304L sample appears to contain some elongated features but smaller, more spherical features.

The average size and number density of the voids in each of the smaller samples was obtained with the Avizo© tool known as Label Analysis. The Label Analysis tool identifies each of the voids and measures the number of voxels (3-D pixel) it contains. The volume data was plotted in histograms shown in **Figure 23**. The shapes of the histograms all are skewed to the left with the majority of voids being the smaller in size. The average volume of the voids in the commercial-304 sample was 292.07 μm^3 with a number density of 3666.42 voids/mm³ (Volume density of 1.723×10^{-3}). The number density was calculated by assuming a homogenous distribution of voids. The average void volume for the 304H sample and 304L sample single edge crack specimens were 251.92 μm^3 and 188.66 μm^3 , respectively. The number density for the 304H sample and the 304L single edge crack specimens were 234.50 voids/mm³ (Volume

density of 5.907×10^{-5}) and 214.25 voids/mm³ (Volume density of 4.060×10^{-5}), respectively.

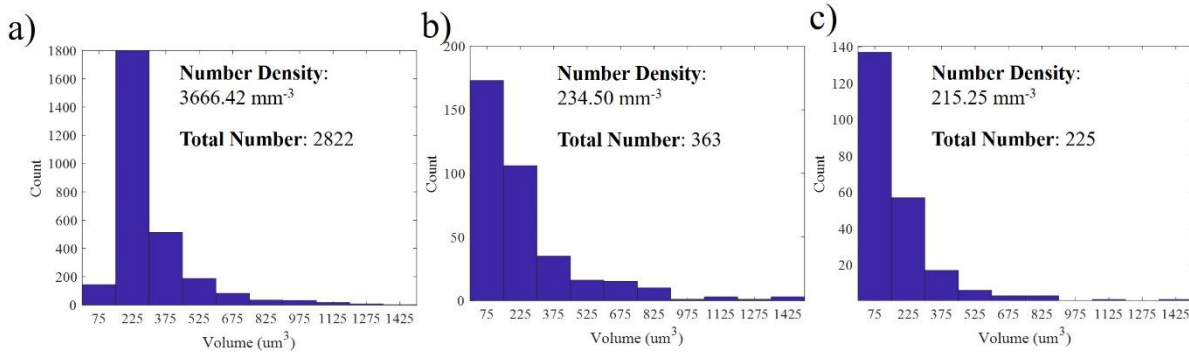


Figure 23: Histograms of Volumes of Voids in Fatigue Pre-Cracked a) Commerical-304, b) 304H, and c) 304L

2.1.5 Synchrotron X-ray Diffraction of As-Received and Fatigue Pre-Cracked Materials

Like the tomography scans of the as-received and fatigue pre-cracked materials, a diffraction scan was conducted on both as-received and fatigue pre-cracked. Diffraction scans of the as-received material were also conducted to determine the effects of fatigue on the volumetric phase fractions of austenite, α' -martensite, and ϵ -martensite. When a crack was present, diffraction scans were taken above the crack, at the crack, and below the crack. The volumetric phase fractions of each sample before and after fatigue are shown in **Table 10**. All materials appear to have increased in both ϵ -Fe and α' -Fe with a larger increase in α' -Fe. In terms of location, the commercial-304 sample has most of the martensite located at the crack, most likely as a result of the deformation within the plastic zone. Similarly, most of the α' -martensite of the 304L sample is located at the crack. The ϵ -martensite of the 304L sample appears to be the most below the crack. Both types of martensite also appear to be the most prevalent at the crack in the 304H sample. The main observation was the increase in the fraction of martensite as a result of deformation induce martensite.

Table 10: Volumetric Phase Fraction Analysis of As-Received 304SS and Fatigued 304SS

	304 As-Received			304H As-Received			304L As-Received		
	γ -Fe	α' -Fe	ε -Fe	γ -Fe	α' -Fe	ε -Fe	γ -Fe	α' -Fe	ε -Fe
	98.62	1.29	0.09	99.16	0.52	0.32	98.02	1.84	0.14
	304 Fatigue Pre-Cracked			304H Fatigue Pre-Cracked			304L Fatigue Pre-Cracked		
	γ -Fe	α' -Fe	ε -Fe	γ -Fe	α' -Fe	ε -Fe	γ -Fe	α' -Fe	ε -Fe
Above Crack	93.43	5.7	0.86	96.91	1.85	1.23	96.62	1.71	1.65
At Crack	86.69	11.62	1.67	94.97	3.89	1.13	93.14	5.29	1.55
Below Crack	91.24	7.85	0.89	89.86	8.87	1.26	94.9	1.75	3.34
Total	91.13	7.81	1.05	94.05	4.73	1.2	94.94	2.85	2.19

2.2 *In situ* Synchrotron X-ray Tomography and Diffraction

To probe the mechanism, cracking rates, and cracking morphology, an *in-situ* study was conducted at Argonne National Laboratory's (ANL) Advanced Photon Source (APS). An aerial view of the facility is shown in **Figure 24a**. APS has the highest brilliance of high energy x-rays in the world (As shown by **Figure 24b**) with 71 beamlines tangent to the x-ray ring and can be used to conduct many different types of experiments. One which was used was an *in situ* CISCC x-ray tomography and diffraction study on samples of 304SS in simulated marine environment to collect 3-D information about the crack and phases present, respectively. *In situ* tomography and diffraction can be conducted only at a synchrotron source like APS due to the high brilliance of high energy x-rays as a result of a particle accelerator exceling electrons to produce synchrotron x-rays. Before discussing the specifics of the experiment, it is important to review the principles of x-ray tomography to understand the type of data which can be obtained. A description of the basics of X-ray Tomography are presented in the next section.

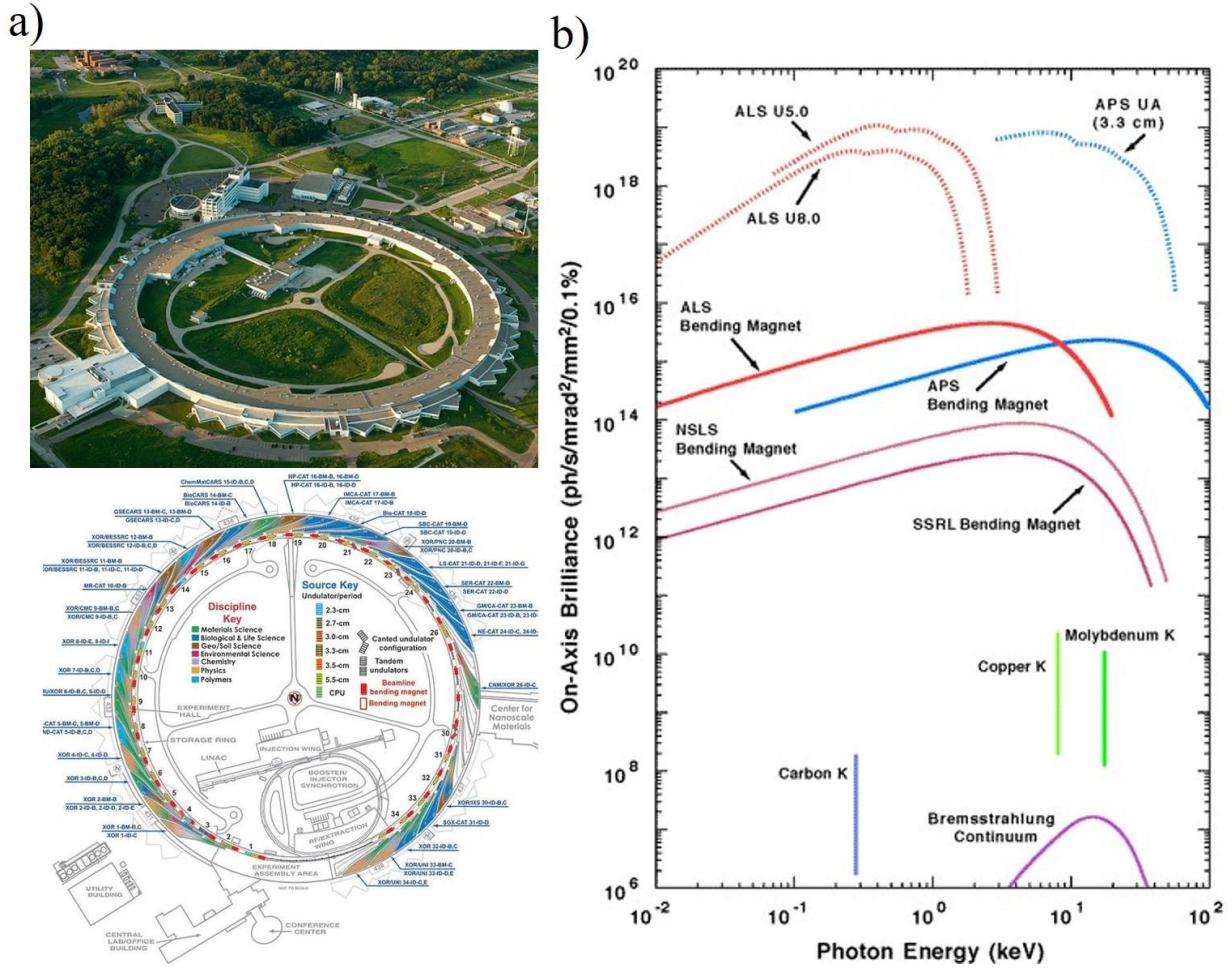


Figure 24: a) Aerial View and Schematic of the Advance Photon Source Facility at Argonne National Laboratory and b) Chart of X-ray Sources as a Function of Brilliance and Energy [30]

2.2.1 Principles of X-ray Tomography

A description of how tomography scans are taken must be investigated before explaining how they were used in this experiment. **Figure 25** serves as a basic drawing of the x-ray tomography scanning process where the red circle is the object being scanned. X-rays come from a source such as a synchrotron or a Cu K- α source [31]. In our experiments, a synchrotron source was used as it provides a flux of x-rays magnitudes higher than Cu K- α sources

which reduces the required exposure time and reduces the total scan time. Reducing total scan time is crucial for conducting *in situ* experiments to have enough temporal resolution to see differences in crack length. A sample is placed between the x-ray source and the scintillator and detectors on a rotating stage. X-ray tomography works off the principle of x-ray attenuation contrast by which matter attenuates x-rays and reduces the number of x-rays [31]. At a single rotation angle, an x-ray beam of a specific size goes through the sample and hits the scintillator [31]. The scintillator converts the x-rays into visible light which a Charged Coupled Device (CCD) camera can detect [31]. The location of the sample will cause a “dark” projection of the samples due to the attenuation while the other places that have not been attenuated will be unaffected. A “white” scan and a “dark” scan are conducted to get the original number of x-rays (to see how many were attenuated by the object) and to remove background levels of x-rays, respectively [31]. White scans are obtained by removing the object and taking a scan with the same exposure time while dark scans are obtained by blocking x-rays from a source using a shield and taking the same scan with the same exposure time [31]. As the sample rotates and images are taken, a graph known as a sinogram (Shown in **Figure 25**) can be created which plots the pixel response as a function of rotation [31]. The sinogram in the example is for the red object as it spins on the rotating stage, leading to a sine wave like graph.

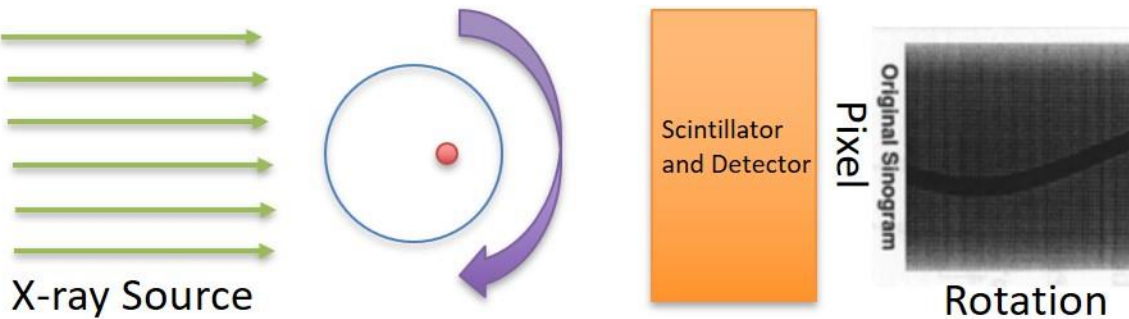


Figure 25: X-ray Tomography Scanning Process Diagram with an X-ray Source, an Object (Red Circle in this Figure), a Scintillator and Detector. The Process is used to Form Sinograms [31]

The next step is to obtain the object back using the information from the sinogram in a process known as filtered back projection [31]. Firstly, back projection is the process by which the scan of an x-ray at a particular angle is inverted so that where the object is generates a positive response while areas where no attenuation occurred generates zero response. **Figure 26** shows an example of backprojection (Left Figure) of the object in **Figure 25**. As is illustrated in the first figure of **Figure 26**, two angles can be used to obtain the position of the object but we can see we require more angles to obtain the real shape of the objects as is shown with more backprojections; however, one problem that arises with more backprojections is the object boundaries becomes blurred as more projections overlap and can be seen in the first image of **Figure 26** with many backprojections. To alleviate the problem, a function known as a kernel (Shown in the middle image of **Figure 26**) can be utilized [31]. The kernel itself is a function that has negative components near the edges of its peak while the peak remains positive. Convolved with each backprojection we can obtain defined boundaries between the object and its surroundings as shown in the last image of **Figure 26**. The use of the kernel improves the contrast of the image at cost of the signal to noise ratio [31].

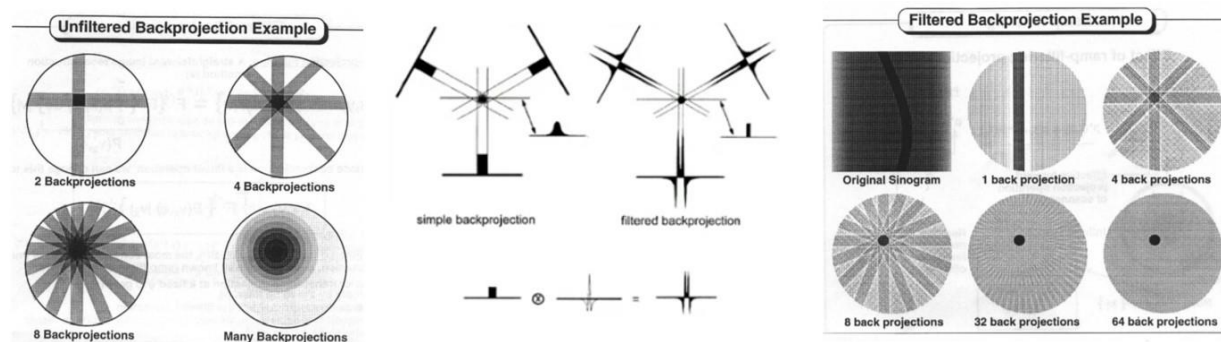


Figure 26: Unfiltered Backprojection (Left), Kernel Function Convolution (Center), and Filtered Backprojection (Right) [31]

After the backprojection algorithm, a fast Fourier transform algorithm can be used to remove artifacts that can arise from the non-linear response of the detectors as well as dust on the optics and detectors as a results of constant bombardment from high energy x-rays [13]. The data is then converted into a stack of 2-D images where each image is a slice of the material. The 2-D slices can then be read by a program known as AVIZO®.

Knowing these basic principles of x-ray tomography, experiments were devised to perform *in situ* CISCC with a custom-made tensile apparatus. The experiments were specifically performed on the 1-ID-E beamline where tomography scans took about 15 minutes. Several tomography scan can be obtained throughout the duration of the experiments to probe the crack shape at different points in time.

2.2.2 *In Situ* Experimental Setup

To conduct the *in situ* SCC experiment, a custom made tensile machine was designed and fabricated to both add a controlled load on samples as well as provide a simulated marine environment. The tensile machine, as depicted in **Figure 27**, is comprised of a stepper motor to induce a load, a load cell to measure the load, a k-type thermocouple to measure the temperature, a relative humidity sensor to measure the humidity, and a Kapton chamber to hold in a simulated marine environment (i.e. humid air) while remaining x-ray transparent. Infrared heaters were added to the side of the tensile machine to control the temperature of the sample. The tensile machine was placed on top of a rotating stage to rotate the sample relative to the x-ray source. Before the start of the experiment, a drop of concentrated MgCl₂ aqueous solution (500 g/L) was added to the crack to simulate the deposition of marine salts. MgCl₂ was chosen as it has been found to be the most detrimental in terms of CISCC in austenitic stainless steels [5]. Throughout the experiment, water was added through a syringe port in order to maintain a relative

humidity around 55% which is above the DRH for MgCl₂ [5]. The temperatures used were up to 80 ° C The surface temperature of dry storage canisters can reach up to temperatures of 80°C [11]. The samples were kept at a Fixed Extension (FE) or a Constant Load (CL). The stepper motor as well as the data collection were controlled by a custom made LabView© program.

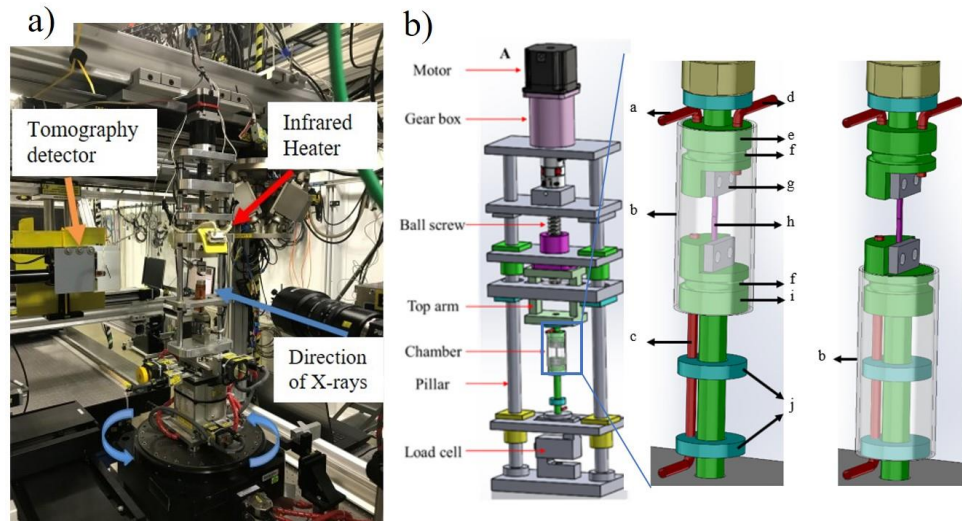


Figure 27: a) Experimental Setup at the Advanced Photon Source using Beamline 1-ID-E and b) Diagram of the Custom Built Tensile Machine for *In Situ* Tomography and Diffraction

2.2.3 Sample Fatigue Pre-Cracking

To probe the cracking behavior in terms of cracking rate and morphology, fatigued pre-cracked samples were used. Samples were fabricated firstly into single edge-notched tension bars with dimensions of 5x5x55 mm as shown in **Figure 28a**. The samples were then fatigued pre-cracked in air using a four-point fatigue machine from Test Resources© until a crack that was about 0.5 mm was detected visually. The aim of the experiment was to study crack propagation and not nucleation which is why samples were pre-cracked. Once a crack of sufficient size was created, smaller samples containing approximately 200 µm of crack with a dimension of

1.2x1.2x35 mm (Shown in **Figure 28c**) were machined out by Electrical Discharge Machining (EDM) according to the diagram shown in **Figure 28b**. Small samples were needed in order to allow enough x-rays to make it through to the detector with a reasonable exposure time that would allow for an *in situ* SCC experiment.

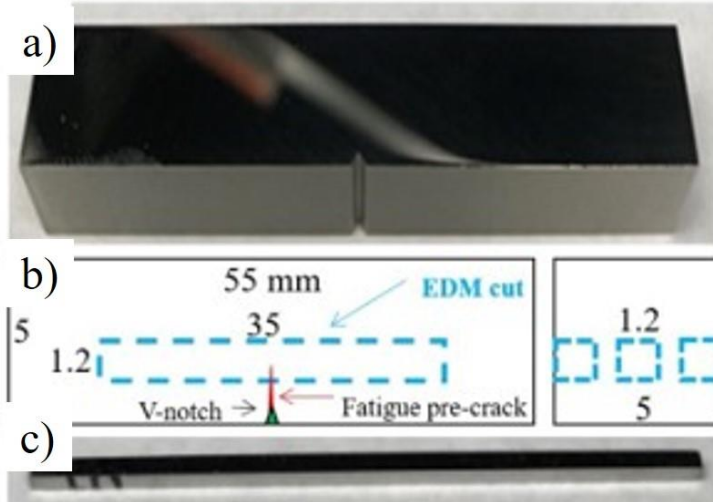


Figure 28: a) Large Notched Samples for Fatigue Pre-Cracking, b) Diagram of Large Notched Sample and EDM Cuts to Obtain c) Pre-Cracked Single Edged Crack Samples

2.2.4 Table of Experimental Conditions

Experiments were conducted on the 1-ID-E beamline using a photon energy of 71.676 keV with a flux on the order of 10^{18} photons/mm² s. For the microtomography, images were taken every 0.2° with an exposure time of 0.1 s for 180° using a beam size of 1.8x1.2 mm. For the diffraction, a beam size of 1.2x0.1 mm was used to conduct diffraction scans above the crack, at the crack, and below the crack. Tomography scans were taken around every 30 min while diffraction scans were taken after every three tomography scans. **Table 11** shows the different samples, initial K_o , temperature, relative humidity, duration, and the loading mode of each experiment.

Since there are samples from the same type of material with different experimental conditions, a nomenclature system for the samples was developed to be able to compare and distinguish samples. The nomenclature is based off of the experimental conditions that the samples underwent with respect to the initial stress intensity, temperature, and relative humidity. Additionally, the nomenclature contains information about whether the sample underwent the experiment at a Fixed Extension (FE) or Constant Load (CL). The initial stress intensity (calculated using the tomographs) was calculated after the experiment and the calculations and results are shown in a later section. For example, one sample of commercial-304 sample which underwent a fixed extension test at 80 °C and 55% relative humidity. It was later calculated that the initial stress intensity was 40 MPa m^{1/2}. As such, the sample would be named 304-FE-40K_o-80C-55%. From this point on, this nomenclature will be used.

Table 11: Experimental Parameters for *In Situ* Tomography and Diffraction Study of Chlorine Induced Stress Corrosion Cracking

Sample	Initial K _o (MPa m ^{1/2})	Temperature (°C)	RH(%)	Time (hrs)	Loading Mode
304	39.89	80	55	15.8	Fixed Extension
304	46.3	50	55	7.85	Constant Load
304	31.5	80	55	12.7	Constant Load
304H	43.5	80	55	11.32	Constant Load
304H	31.5	80	55	10.98	Constant Load
304H	19.83	80	55	21.7	Fixed Extension
304L	43.9	50	55	5.5	Constant Load
304L	28	80	55	2.5	Constant Load
304L	17.7	80	55	13.8	Fixed Extension
304L	30.7	80	55	12.38	Constant Load

2.3 Post Experiment Analysis and Characterization

Various types of characterization and analysis tools were used to process the data taken from APS as well as further probe the tested samples. The next couple sections will detail the tools used to conduct the post experiment analysis and characterization.

2.3.1 Tomography using AVIZO[©]

The output after the reconstruction and fast Fourier filtering of the tomography data in a stack of 2-D tiff images which can be read into AVIZO. The AVIZO program has a function known as segregation where objects in each slice can be separated from each other by taking advantage of the attenuation contrast. The threshold tool can be used to extract out the crack and any objects with the same attenuation contrast (such as voids and some precipitates). Thresholding itself is not enough to extract only the crack from the surrounding material as illustrated in the before image of **Figure 29**. As seen in the before picture, the crack (Shown on the right of **Figure 29**) was extracted but so were the edges of the sample since the empty space next to the edges have the same contrast as the crack. To remove parts that are undesired i.e. the surface, the undesired parts are unselected manually in each slice; however, AVIZO ability to take a stack of 2D images and convert them into a format that allows for slices in the three direction (i.e. xy-plane, xz-plane, and yz-plane) means that only a fraction of the number of slices in each direction need to be corrected (i.e. those close to the surface). In addition to the surfaces needing to be removed, some artifacts which can arise from the optics and experimental setup which are not removed by the Fourier filter, must be removed manually. This includes rings which can appear centered around the sample. Finally, noise in the image can be removed using the “Remove Island” function which deselects any island of voxels (3-D pixels) below a threshold size (i.e. resolution

of detector). The volume rendering can then be conducted to obtain the 3-D shape. More detailed on the exact steps used to develop the 3-D volume using AVIZO is found in **Appendix C**.

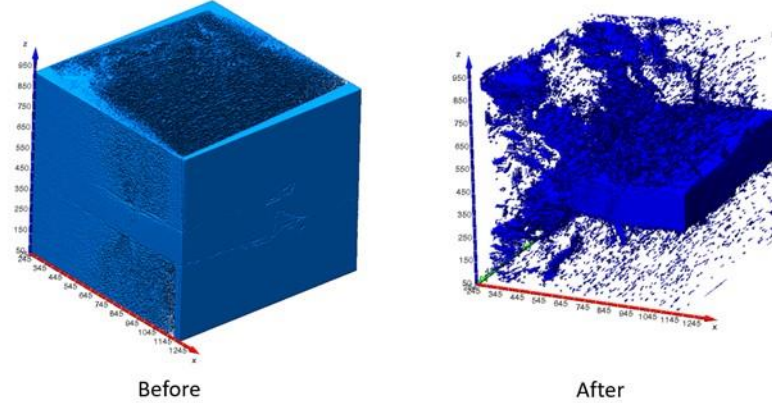


Figure 29: AVIZO Process Commercial-304 Sample after Thresholding but before Manual Removal Process (Left) and after (Right)

2.3.2 Crack Measurements and Volume Measurements of Microvoids and Precipitates

Beyond generating 3-D objects of the scanned sample and extracting images of cracks, the AVIZO program can be utilized to help quantify the object. For example, a measuring function was used to obtain crack length as shown in **Figure 30**. In this study, measurements were made at six equidistant points along the crack opening to get an average crack length since crack fronts are not always uniform in length. Moreover, as seen in **Figure 29**, microvoids are also extracted with the crack. Microvoids can be quantified by using AVIZO“Label Analysis” tool which finds each island of voxels and obtains the volumes of each one. A distribution of volumes as well as number densities of the voids can be calculated.

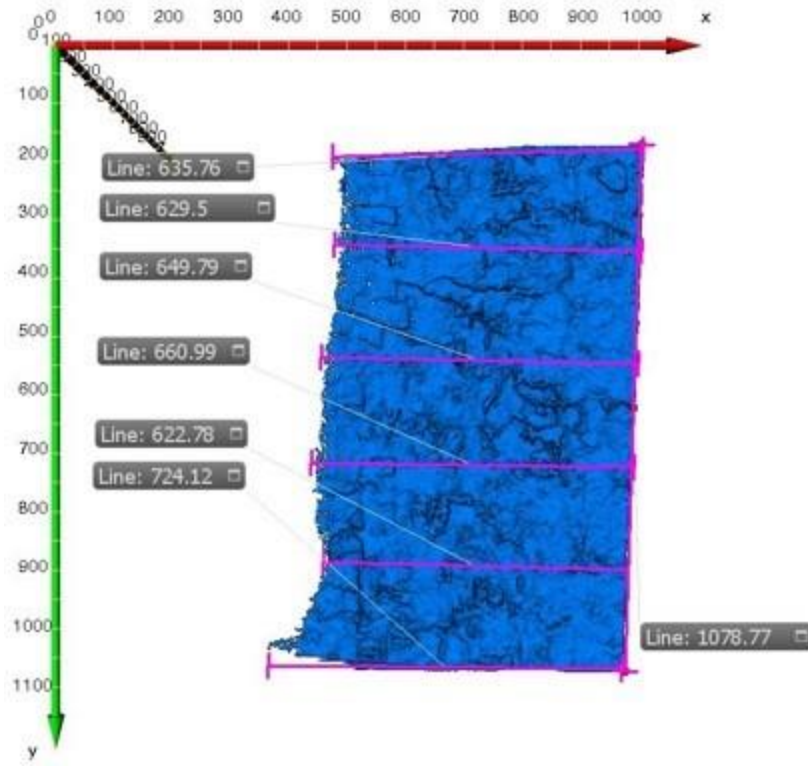


Figure 30: Crack Measurement at Six Equidistant Points Along the Crack (units in μm)

2.3.3 Electron Microscopy Analysis

In order to investigate the underlying mechanisms involved in chlorine induced stress corrosion cracking of austenitic stainless steel 304, various levels of microscopy are needed to observe microstructural features. The microstructure of a material dictates the macroscopic properties such as yield strength and corrosion resistance. Firstly, a ThermoFisher Quanta 3D with a Field Emission Gun (FEG) (Shown in **Figure 31a**) was used to perform Scanning Electron Microscopy (SEM) to observe the crack right after the experiment. Chemical maps were obtained using the equipped Energy Dispersive Spectroscopy (EDS) to collect characteristic x-rays. Some samples were then further fractured using the custom tensile machine to perform fractography under SEM observation and collect chemical maps to view elemental maps of the crack. To probe down further into the microstructure, Transmission Electron

Microscopy (TEM) samples were obtained using the Focused Ion Beam (FIB) on the ThermoFisher Quanta 3D Microscope which uses gallium ions to mill. Samples were obtained from places such as from the edge containing part of a crack, from the edge in front of the crack in the plastic zone, along the crack wake, and at crack tip. TEM analysis was performed using ThermoFisher Talos F200X (Shown in **Figure 31b**) equipped with a FEG and four EDS detectors in a process known as ChemiSTEM. Scanning Transmission Electron Microscopy (STEM) was conducted to acquire the chemical maps of various features such as corrosion products and precipitation. The TEM was operated using 200 keV electrons. Combined with the chemical maps, Selective Area Electron Diffraction (SAED) was performed in TEM mode to obtain structural information about various microstructural features. Specifically, corrosion products were identified using the chemical maps and diffraction information. Likewise, martensite (both the body centered cubic α' -Fe and the hexagonal closed packed ε -Fe) was also identified using electron diffraction. Finally, dislocation imaging was conducted, especially around the crack tip and the plastic zone where plastic deformation is prevalent.

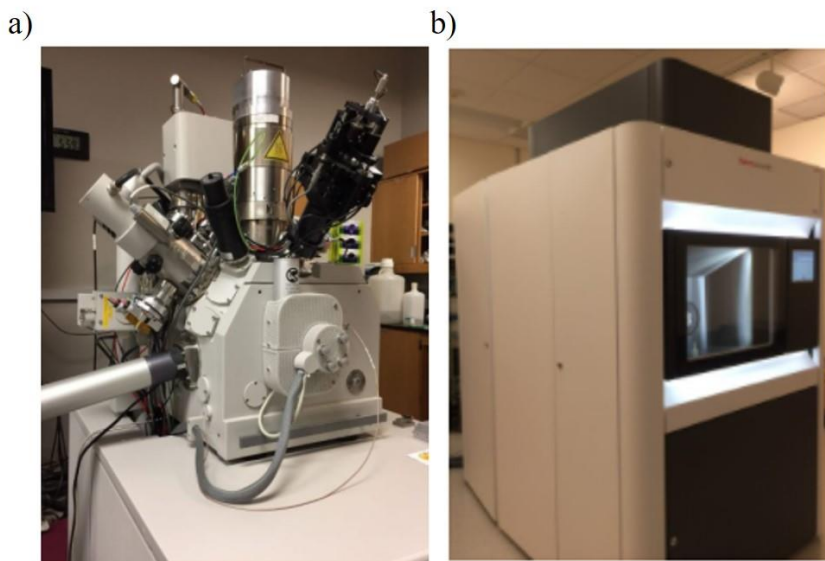


Figure 31: Picture of a) ThermoFisher Quanta 3D Dual Focused Ion Beam and Scanning Electron Microscope and b) ThermoFisher Talos F200X Transmission Electron Microscope

2.3.4 Stress Intensity Analysis and Finite Element Analysis

From the crack lengths using the procedures demonstrated in **Figure 30**, the stress intensity at each scan. To calculate stress intensity for a single-edge crack samples, a mathematical technique discussed in [32] was used. **Equation 1** above shows the formula for the stress intensity factor where K_I is the stress intensity for type I loading, Y is the geometric factor that depends on the geometry of the sample and crack, σ is the far field stress, and a is the crack length. Calculating the geometric factor involved using a dimensionless stress intensity factor knowing the crack length, the sample width in the direction of crack propagation, and the far field engineering stress [32]. Specifically, **Equations 2** and **3** were used to calculate the stress intensity and the dimensionless stress intensity factor (F_I), respectively, where α is the ratio of crack length to sample width along the cracking direction while C_n and t are constants found in [32].

$$F_I = \frac{(1 - \alpha)^{\frac{3}{2}} K}{\sigma \sqrt{\pi a}} \quad (2)$$
$$F_I = 1.1215(1 - \alpha) + \alpha(1 - \alpha) \sum_{n=0}^4 C_n \alpha^n + 1.1215t\alpha \quad (3)$$

The equations used in [32] can only be used on a single edge crack. Some of the samples of 304 scans contained branching which must be taken into account since branching can reduce the effective stress intensity at the crack tip [33]. As such, a different set of equations found in [33] were used to account for the branching.

To support the stress intensity analysis discussed in the Results section, Finite Element Analysis (FEA) simulations were performed using Abacus[©]. These simulations assumed a Young's Modulus of 198.5 GPa, a Poisson's ratio of 0.29, and a yield stress of 265 MPa [34, 35]. Additionally, an overall mesh size of 0.5 mm was used with a local mesh size of 0.04 mm

around the crack for a total of around 130,000 elements. The initial states of the sample were tested and the crack was approximated as a triangle shape. One end of the sample was set to a fixed boundary condition while the other was subjected to an applied load similar to the ones done in the experiment. A diagram of the simulation set up is shown in **Figure 32**. FEA simulations were used to visualize the principle stresses and strains in the sample to see how it might have influenced the cracking under various loading parameters.

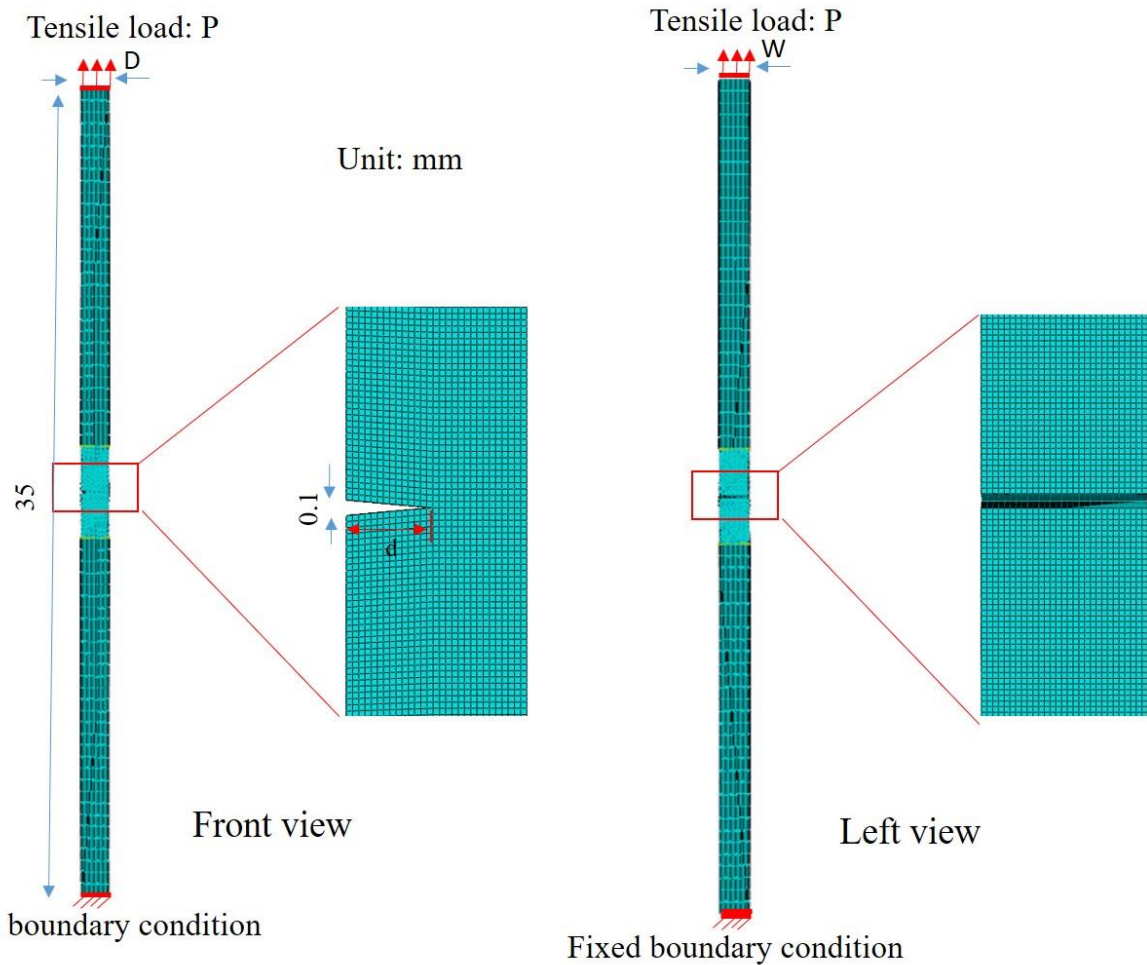


Figure 32: Abacus© Simulation Setup to Map and Quantify Principal Stresses and Strain for the Experimental Conditions

2.3.5 X-ray Diffraction Volumetric Phase Fraction Analysis

X-ray diffraction scans were conducted in order to obtain phase information during the course of the experiment. It is well known that metastable austenite like that of 304SS can undergo a diffusionless phase transformation into martensite due to deformation below a critical temperature (M_t) [36-38]. Factors such as the stacking fault energy of a material can alter the deformation mechanisms into producing either structure of martensite (α' -Fe and ε -Fe) [39]. The deformation around the plastic zone and the crack wake are of particular interests since transformation in those regions can serve as crack growth retardation mechanisms [22]. X-ray diffraction works off the principle that different crystal structures, elements, and d-spacings of different materials leads to different diffraction patterns (i.e. peak locations and intensities) [40]. A typical diffraction pattern for 304SS is shown below in **Figure 33**. The peaks of the figure are labeled with the phase and the reflection responsible for that peak.

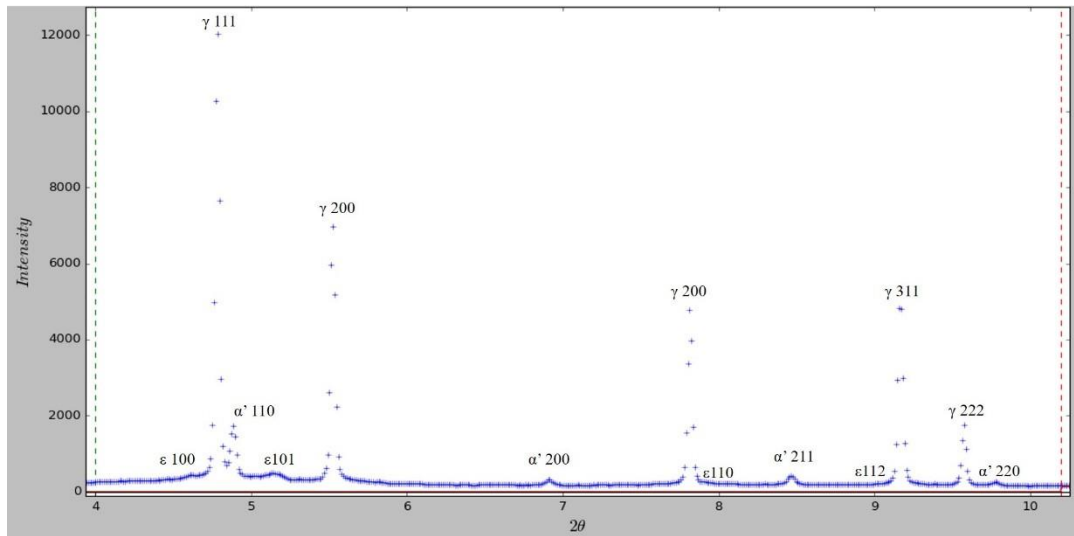


Figure 33: Labeled Diffraction Pattern of 304H Sample

Diffraction scans were analyzed using GSAS II to identify peaks and obtain integrated intensities. The software uses a Rietveld refinement to fit the peaks using both a Gaussian and

Lorentz curves. Phase fractions of austenitic and martensitic phases were obtained by following ASTM E975 [41]. Since the intensity of each diffraction peak is a function of amount of the phase, the multiplicity of the reflection as well as other parameters, the individual peaks need to be normalized to be compared. **Equation 4** which represents the normalization factor (R) was calculated first. Values for the constants such as the atomic scattering factor, multiplicity, and Debye-Waller factor were obtained from [40]. Individual peaks are then selected in GSAS II manually. Integrated intensities were obtained by using GSAS II “Peak Fit” function which uses a σ and γ function to fit each peak. The phase fraction (V) of each phase could then be calculated by taking the integrated intensities of each peak as well as the normalization factor and inputting the values into **Equation 5**.

$$R = \frac{|F|^2 p LP e^{-2M}}{v^2} \quad (4)$$

$|F|^2$: Structure Factor

p: Multiplicity

LP: Lorentz Polarization Factor

e^{-2M} : Debye-Waller Factor

v: Volume of Unit Cell

$$V_i = \frac{\frac{1}{n} \sum_{j=1}^n \frac{I_i^j}{R_i^j}}{\frac{1}{n} \sum_{j=1}^n \frac{I_\gamma^j}{R_\gamma^j} + \frac{1}{n} \sum_{j=1}^n \frac{I_{\alpha'}^j}{R_{\alpha'}^j} + \frac{1}{n} \sum_{j=1}^n \frac{I_\epsilon^j}{R_\epsilon^j}} \quad (5)$$

I: Intensity of Peak

n: Number of Peaks

Chapter 3: Results

As a reminder, the experimental conditions are summarized in **Table 12** below. Observations of each alloy are shown separately in terms of tomography, crack growth rates as a function of stress intensity, and phase fraction. Some of the samples did not show significant crack progression and their tomographs are shown in appendix **D.1**. The samples which showed significant crack growth are shown in this section. This section is separated by alloy to show tomography, stress intensity, and phase fraction analysis. As a reminder, diffraction scans were taken above the crack, at the crack, and below the crack.

Table 12: Summary of Experimental Conditions for the *In Situ* X-ray Tomography and Diffraction to Study Chlorine-Induced Stress Corrosion Cracking

Sample	Initial K_o (MPa $m^{1/2}$)	Temperature (°C)	RH(%)	Time (hrs)	Loading Mode
304	39.89	80	55	15.8	Fixed Extension
304	46.3	50	55	7.85	Constant Load
304	31.5	80	55	12.7	Constant Load
304H	43.5	80	55	11.32	Constant Load
304H	31.5	80	55	10.98	Constant Load
304H	19.83	80	55	21.7	Fixed Extension
304L	43.9	50	55	5.5	Constant Load
304L	28	80	55	2.5	Constant Load
304L	17.7	80	55	13.8	Fixed Extension
304L	30.7	80	55	12.38	Constant Load

3.1 Tomography, Stress Intensity Analysis, and X-ray Diffraction Results

3.1.1 Commercial-304 Experiments

3.1.1.1 304-FE-40K_o-80C-55%

a) Tomography

Figure 34 serves as an example of a reconstructed tomograph of the initial and final scans of the commercial-304-FE-40K_o-80C-55%. One note to mention is that during the reconstruction, the microvoids and precipitates in the sample also were extracted from the sample due to having a similar amount of attenuation giving a similar contrast. In some cases where the microvoids and precipitates obstructed the view of the main crack, they were removed using the Avizo© software.

The progression of the 304-FE-40K_o-80C-55% crack is evident in the reconstructed tomographs shown in **Figure 35a**. Different angles of the final tomograph scan about the z-axis is shown in **Figure 35b**. The 304-FE-40K_o-80C-55% sample, the crack appears to go from a single crack to a branching crack. This commercial-304 sample appears to only have crack branching towards the surface of the sample. The crack was measured to have grown 248 μm .

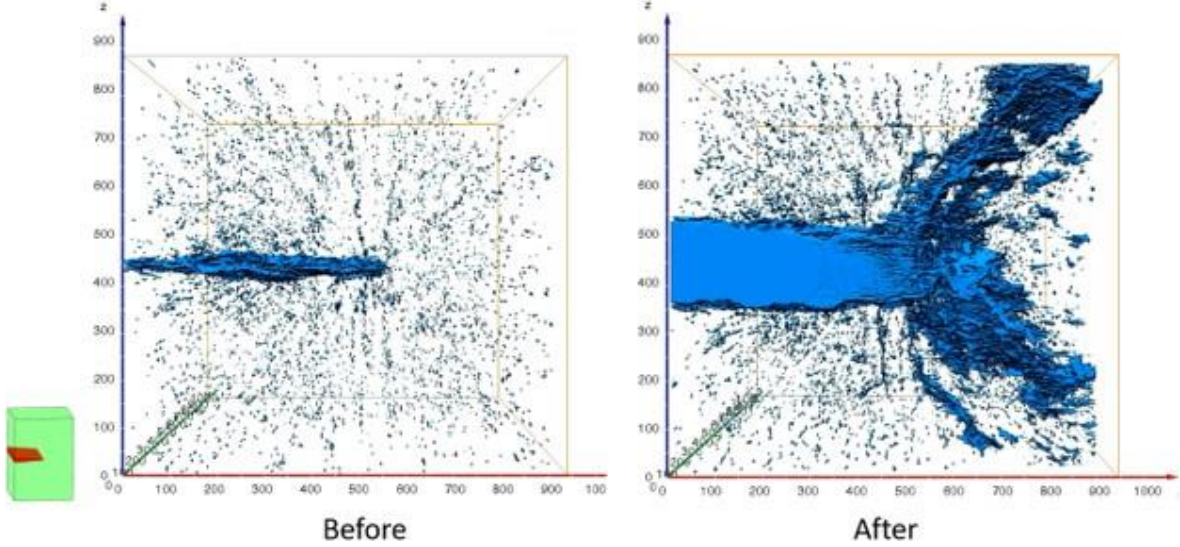


Figure 34: 3-D Tomograph of the Commercial-304-FE-40K_o-80C-55% Sample Before (Left) and After (Right) the Experiment (Units in μm)

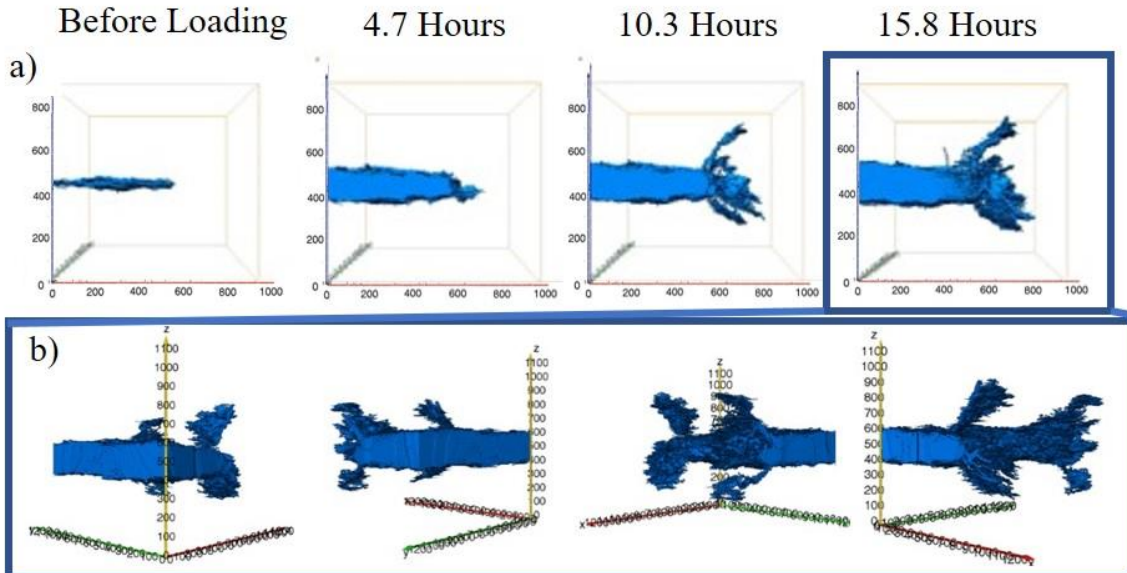


Figure 35: 3-D Tomographs of Commercial-304-FE-40K_o-80C-55% a) over the Progression of the Experiment and b) showing Four Angles relative to the Z-Axis of the Final Tomography Scan

b) Stress Intensity Analysis

To calculate stress intensity for a single-edge crack samples, a mathematical technique discussed in [32] was used. The equations used in [32] can only be used on a single edge crack. Some of the commercial-304-FE-40K_o-80C-55% tomographs contained branching which

must be taken into account since branching can reduce the effective stress intensity at the crack tip [33]. As such, a different set of equations found in [33] were used to account for the branching. The angle of the top branch was found to be around 51.73° relative to the cracking direction while the bottom branch was found to be around 33.47° . The method used in [33] assumes a symmetrically branching crack so the average of the two angles was used which was 42.6° . The dimensionless stress intensity factor was taken from a table found in [33] using the average angle of the crack and α . The calculated crack lengths and stress intensity are shown in **Table 13**. As shown in the table, the branching reduced the stress intensity from the initial $39.89 \text{ MPa m}^{1/2}$ to $3.2 \text{ MPa m}^{1/2}$.

Table 13: Engineering Stress, Crack Length and Stress Intensity for the Initial and Final Tomographs for 304-FE-40K_o-80C-55%

Sample	304-FE-40K _o -80C-55%
Engineering Stress at Beginning (MPa)	209.1
Engineering Stress at End (MPa)	84.3
Average Crack Length at Beginning (μm)	653.8
Average Crack Length at End (μm)	902.3
Difference (μm)	248.5
KI at Beginning ($\text{MPa m}^{1/2}$)	39.89
KI at End ($\text{MPa m}^{1/2}$)	3.2

Plots of the crack growth rate as a function of stress intensity were created and shown in **Figure 36**. Due to the complexity of the crack branching which mostly stayed towards the surface, the crack was treated as a single edge crack and the stress intensity was calculated assuming a single crack. The average crack growth rate was calculated to be $2.788 \times 10^{-9} \text{ m/s}$. There is a degree of scattering in the crack growth rate within an order of magnitude. The plot does not show any significant effect of stress intensity on crack growth rate.

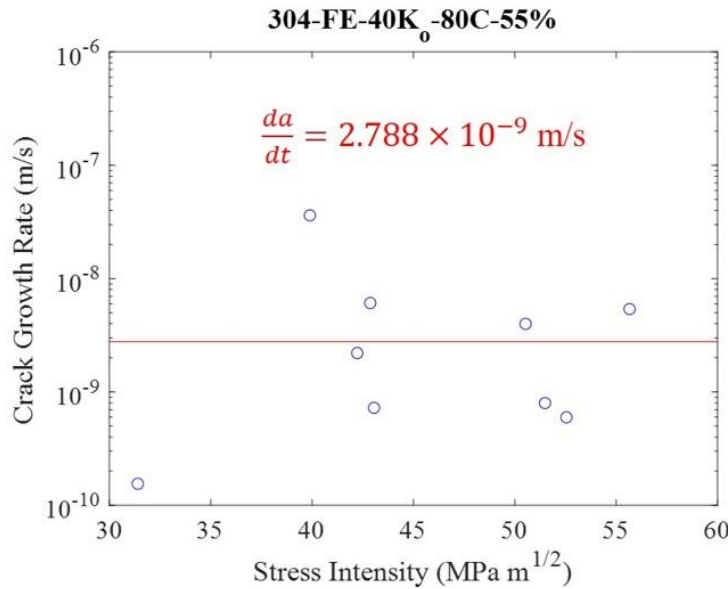


Figure 36: Crack Growth Rate as a Function of Stress Intensity for 304-FE-40K_o-80C-55% showing an Average Cracking Rate of $2.788 \times 10^{-9} \text{ m/s}$

c) Phase Fraction Analysis

Phase fraction analysis for the 304-FE-40K_o-80C-55% sample before the test but after fatigue and after the test is present in **Table 14**. A look at the overall change in phase fraction from the start of the test to the end of the test reveals that not much deformation induced martensite was produced in the overall volume of the scan. A closer look at the location of martensite changes shows an increase above and below the crack while a decrease at the crack. **Figure 35** revealed branching which would shift the plastic zones above and below the crack and could account for the specific changes seen above and below the crack.

Table 14: Phase Fraction of Austenite (γ -Fe), α' -Martensite (α' -Fe), and ε -Martensite (ε -Fe) in the 304-FE-40K_o-80C-55% Sample Before and After Testing

Before Testing After Fatigue			
	304-FE-40K _o -80C-55% (0 hr)		
	γ -Fe	α' -Fe	ε -Fe
Above Crack	93.43	5.7	0.86
At Crack	86.69	11.62	1.67
Below Crack	91.24	7.85	0.89
Total	91.13	7.81	1.05
After Testing			
	304-FE-40K _o -80C-55% (13.26 hr)		
	γ -Fe	α' -Fe	ε -Fe
Above Crack	88.16	10.4	1.42
At Crack	94.07	4.65	1.27
Below Crack	88.46	10.1	1.43
Total	89.66	8.94	1.39

Further analysis was conducted on the 304-FE-40K_o-80C-55% sample to analyze the change in phase fractions over the course of the experiment. The phase fractions above the crack, at the crack, below the crack, and the total scanned volume are shown in **Figure 37**. One observation which can be made is the gradual increase in α' -Fe when branching starts between 4.25 hours and 5.88 hours according to the more detailed tomography progression for 304-FE-40K_o-80C-55% sample shown in **Figure 38**. Below the crack, significant branching does not appear to occur until around 8 hours according to **Figure 38** which appears to have caused in increase in the phase fraction of α' -Fe. These results indicate that the crack tip and the plastic zone are responsible for the deformation induced α' -Fe and the change of crack tip location can change the location of the phase transformation zone.

304-FE-40K_o-80C-55%

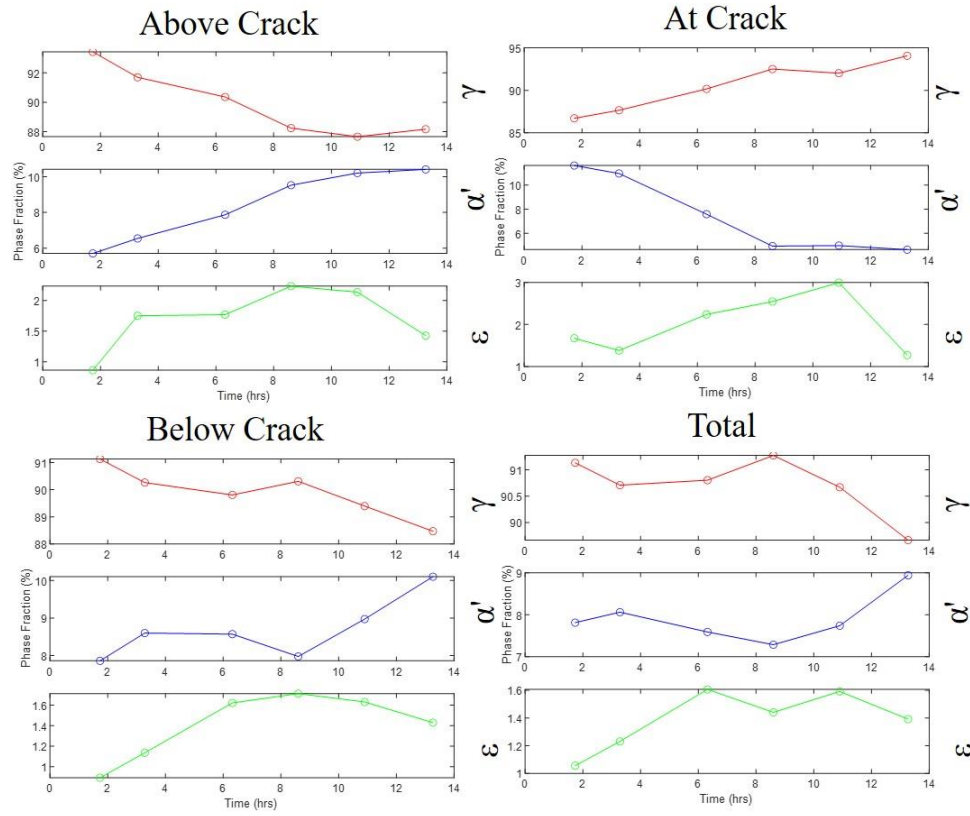


Figure 37: Dynamics of Phase Fraction of γ -Fe, α' -Fe, and ϵ -Fe for the 304-FE-40K_o-80C-55% Sample above the Crack, at the Crack, below the Crack, and the Total Scanned Volume

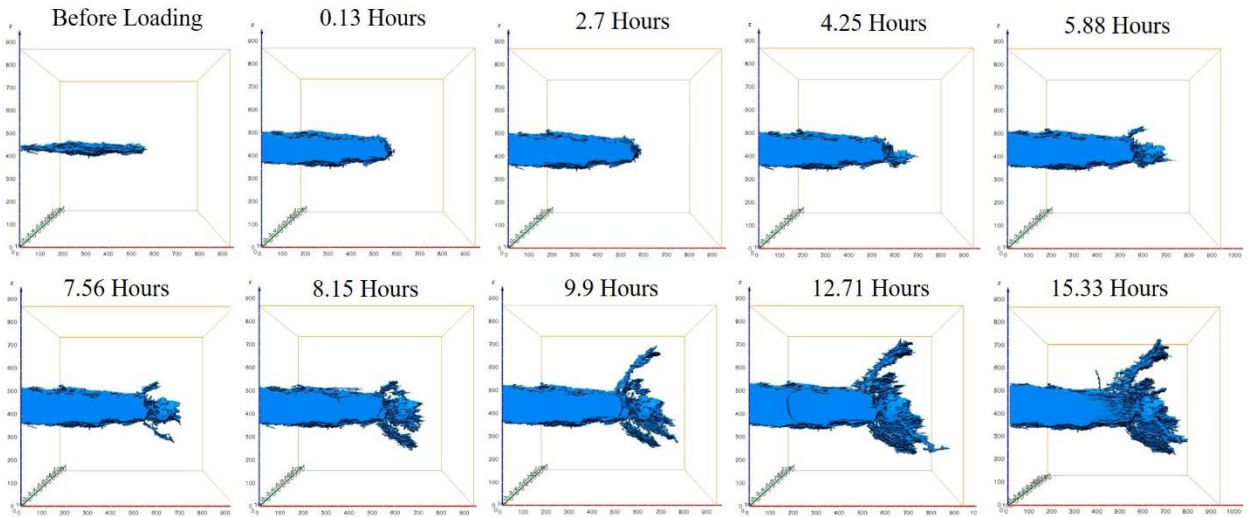


Figure 38: Detailed Tomography Progression of 304-FE-40K_o-80C-55% Sample over Time

3.1.1.2 304-CL-46K_o-50C-55%

a) Tomography

The tomographs over time for 304-CL-46K_o-50C-55% sample is shown in **Figure 39a** with the final scan shown at different angles shown in **Figure 39b**. The 304-CL-46K_o-50C-55% sample fractured to failure during the test with a large crack jump after 6.5 hours as a result of the stress intensity approaching (K_{IC}). Up until the jump in crack growth, the crack appeared to be growing slowly and rather uniformly. The crack was measured to have grown 214 μm before the final fracture.

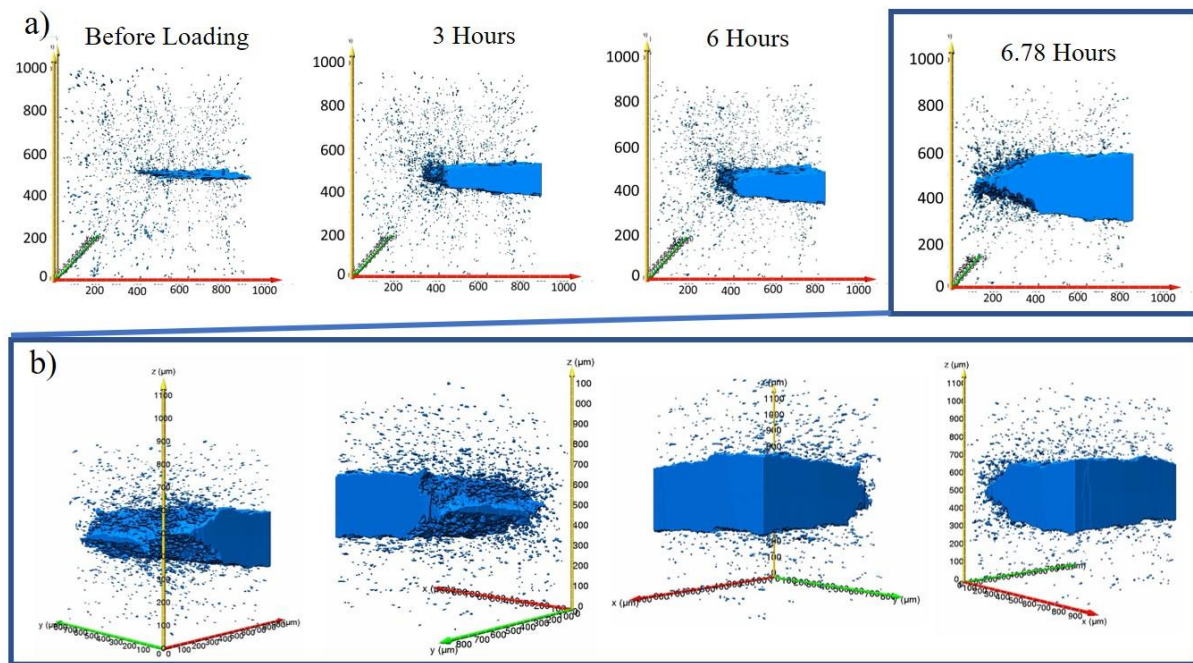


Figure 39: 3-D Tomographs of Commercial-304-CL-46K_o-50C-55% a) over the Progression of the Experiment and b) showing Four Angles relative to the Z-Axis of the Final Tomography Scan

b) Stress Intensity Analysis

The calculated crack lengths and stress intensities for the 304-CL-46K_o-50C-55% are shown in **Table 15**. It should be noted that because the sample fractured, the scan

before fracture was used to obtain the crack length and subsequent stress intensity. The stress intensity was found to have increased from 46.2 to 51.8 as was expected in a constant load experiment.

Table 15: Engineering Stress, Crack Length and Stress Intensity for the Initial and Final Tomographs for 304-FE-40K_o-80C-55%

Sample	304-CL-46K _o -50C-55%
Engineering Stress at Beginning (MPa)	258.4
Engineering Stress at End (MPa)	258.4*
Average Crack Length at Beginning (μm)	572.2
Average Crack Length at End (μm)	786.2*
Difference (μm)	214
KI at Beginning (MPa m^{1/2})	46.2
KI at End (MPa m^{1/2})	51.8*

* Taken Before Fracture

The crack growth rate as a function of stress intensity for the 304-CL-46K_o-50C-55% sample is shown in **Figure 40**. Two average crack growth rates were calculated which were of 1.592×10^{-9} m/s with the last data point and 6.120×10^{-10} m/s without the last data point. The sample fractured and the last data point before fracture can be argued to be apart of stage III as can be seen in the plot where the crack growth rate is orders of magnitude higher than the other data points. As such, the data point was removed to calculate the steady state crack propagation rate. Besides the last data point, the scatter in the data seems to be about an order of magnitude in either direction of the steady state line.

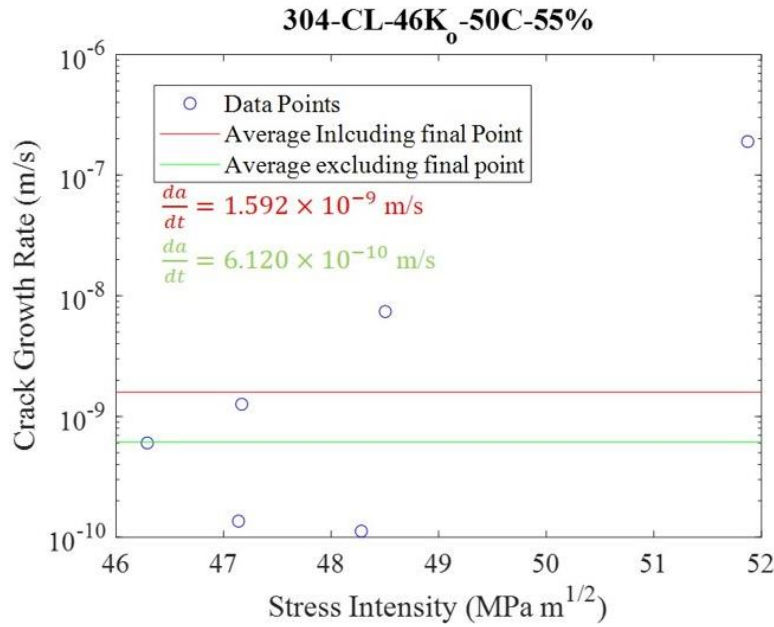


Figure 40: Crack Growth Rate as a Function of 304-CL-46K_o-50C-55% Sample with an Average Cracking Rate of 1.592×10^{-9} m/s with the Last Data Point and 6.120×10^{-10} m/s without the Last Data Point

c) Phase Fraction Analysis

The phase fractions that were calculated from the x-ray diffraction patterns are shown in **Table 16** for the 304-CL-46K_o-50C-55% sample before testing and right before the final fracture. In the total volume, not much martensite was formed with only about a 1.38% increase in α' -Fe and a 0.36% increase in ϵ -Fe. There was a greater change in martensite above and below the crack with a small decrease at the crack. Although the sample fractured, a diffraction scan was able to be conducted on the fractured sample above and below the crack where there was still sample. At the crack, the signal to noise ratio was high and made it difficult to identify and measure any of the peaks. The phase fraction for the 304-CL-46K_o-50C-55% sample after fracture is shown in **Table 17**. The change in martensite (especially α' -Fe) is much greater after the final fracture compared to the during the stress corrosion test.

Table 16: Phase Fraction of Austenite (γ -Fe), α' -Martensite (α' -Fe), and ε -Martensite (ε -Fe) in the 304-CL-46K_o-50C-55% Sample Before and After Testing

Before Testing After Fatigue			
	304-CL-46K _o -50C-55% (0 hr)		
	γ -Fe	α' -Fe	ε -Fe
Above Crack	96.96	2.25	0.79
At Crack	87.9	11.21	0.89
Below Crack	96.82	2.78	0.41
Total	93.89	5.41	0.7
After Testing			
	304-CL-46K-50C-55% (5.63 hr)*		
	γ -Fe	α' -Fe	ε -Fe
Above Crack	90.99	7.54	1.48
At Crack	91.62	7.82	0.56
Below Crack	93.84	5.03	1.13
Total	92.15	6.79	1.06

* Scan Before Fracture

Table 17: Phase Fraction of Austenite (γ -Fe), α' -Martensite (α' -Fe), and ε -Martensite (ε -Fe) in the 304-CL-46K_o-50C-55% Sample After Fracture

304-CL-46K-50C-55% (6.88 hr)	γ -Fe	α' -Fe	ε -Fe
Above Crack	78.83	17.95	3.22
Below Crack Total	82.59	14.67	2.74
Total	80.71	16.31	2.98

A similar detailed analysis like that of the 304-FE-40K_o80C-55% sample was conducted on the 304-CL-46K_o-50C-55% sample. The time evolution of the phase fraction of γ -Fe, α' -Fe, and ε -Fe for the 304-CL-46K_o-50C-55% sample is shown in **Figure 41**. The detailed tomography progression of 304-CL-46K_o-50C-55 sample is shown in **Figure 42**. The sample does not appear to have propagated much during the test and as a result, the martensite fractions do not appear to change much compared to the change when the sample reaches stage three and fractures. The fracture itself causes much more martensite transformation compared to CISCC.

304-CL-46K_o-50C-55%

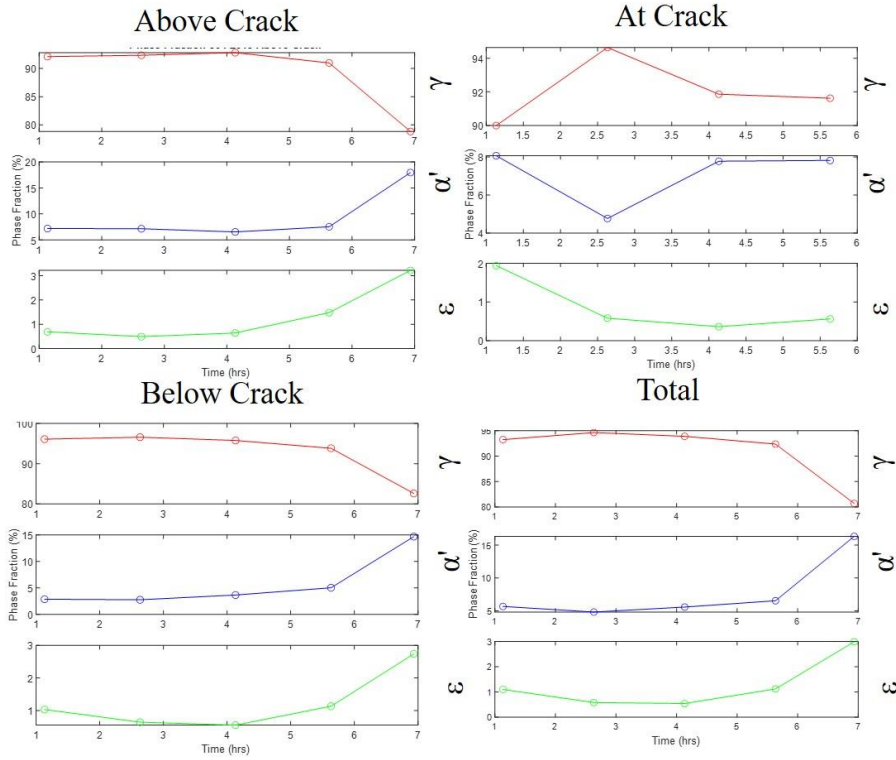


Figure 41: Dynamics of Phase Fraction of γ -Fe, α' -Fe, and ϵ -Fe for the 304-CL-46K_o-50C-55% Sample above the Crack, at the Crack, below the Crack, and the Total Scanned Volume

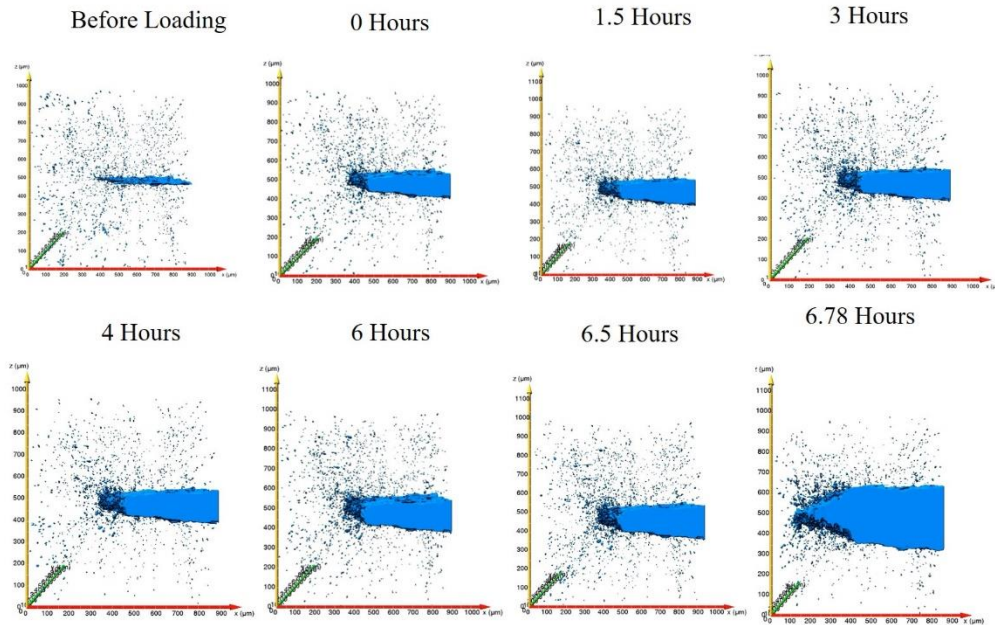


Figure 42: Detailed Tomography Progression of 304-CL-46K_o-50C-55% Sample over Time

3.1.2 304H Experiments

3.1.2.1 304H-FE-20K_o-80C-55%

a) Tomography

The tomographs associated with the 304H-FE-20K_o-80C-55% sample are shown in **Figure 43a**. Interestingly, the 304H-FE-20K_o-80C-55% sample showed the formation of vertical cracks which appear to around the crack tip. **Figure 43b** shows the last scan at different angles which reveals the vertical cracks mostly stayed towards the center of the sample and away from the edges. In terms of crack growth, the sample showed a total growth of about 74 μm .

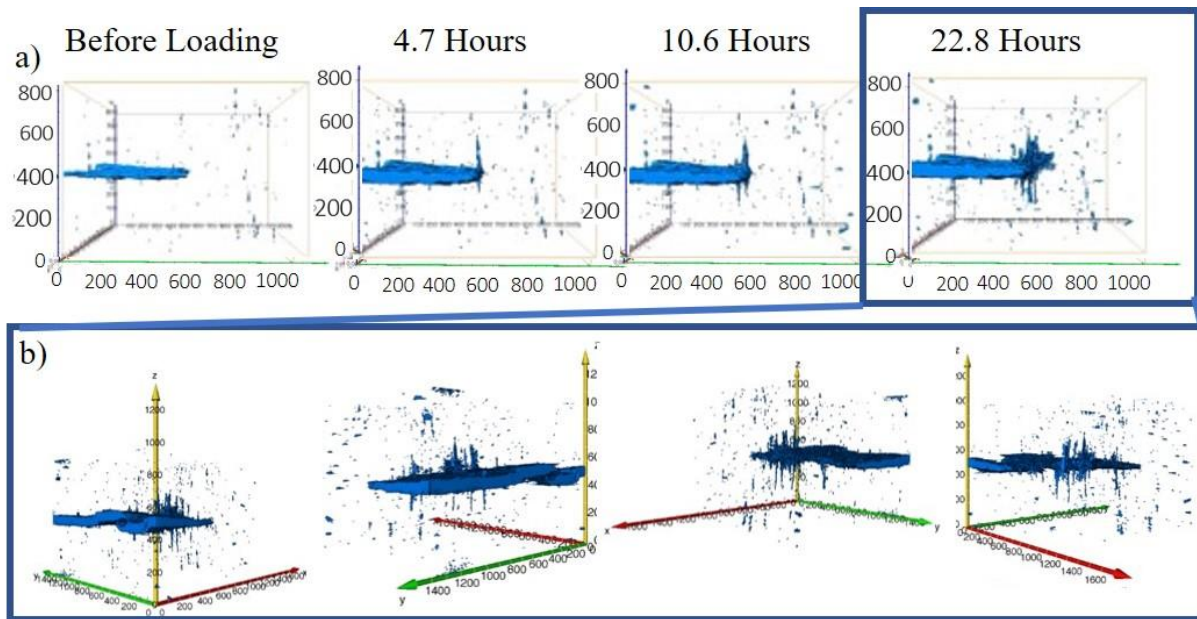


Figure 43: 3-D Tomographs of 304H-FE-20K_o-80C-55% a) over the Progression of the Experiment and b) showing Four Angles relative to the Z-Axis of the Final Tomography Scan

b) Stress Intensity Analysis

Like the other samples, a single edged crack was assumed to calculate the stress intensity, so the vertical cracks were excluded. The stress intensity at the beginning and end

of the experiment can be found in **Table 18**. The stress intensity was found to have increased from $19.83 \text{ MPa m}^{1/2}$ to $26.6 \text{ MPa m}^{1/2}$. An increase in stress intensity is unusual for a fixed extension experiment but the crack growth may not have relieved enough stress for the stress intensity to decrease. A plot of the crack growth rate as a function of stress intensity for the 304H-FE-20K_o-80C-55% sample is shown in **Figure 44**. The average crack growth rate was determined to be $7.82 \times 10^{-10} \text{ m/s}$. In terms of scatter, the data points are relatively close to the average crack growth rate line compared to other samples.

Table 18: Engineering Stress, Crack Length and Stress Intensity for the Initial and Final Tomographs for 304H-FE-20K_o-80C-55%

Sample	304H-FE-20K _o -80C-55%
Engineering Stress at Beginning (MPa)	165.5
Engineering Stress at End (MPa)	150.7
Average Crack Length at Beginning (μm)	620.1
Average Crack Length at End (μm)	694.6
Difference (μm)	74.5
KI at Beginning ($\text{MPa m}^{1/2}$)	19.83
KI at End ($\text{MPa m}^{1/2}$)	26.6

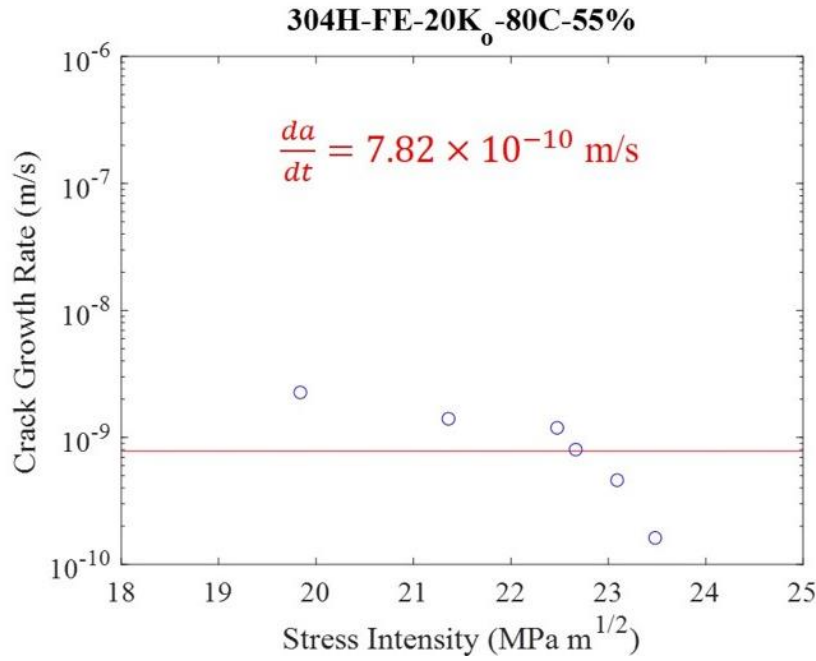


Figure 44: Crack Growth Rate as a Function of 304H-FE-20K_o-80C-55% Sample with an Average Cracking Rate of $7.82 \times 10^{-10} \text{ m/s}$

c) Phase Fraction Analysis

The phase fraction of austenite, α' -martensite, and ε -martensite at the beginning and end of the experiment for the 304H-FE-20K_o-80C-55% sample is shown in **Table 19**. One of the first observations is that the fatigue pre-cracked sample appears to have the majority of the α' -martensite below the crack. From the diffraction scans of a different fatigue pre-cracked 304H, it was found that the majority of the α' -martensite should be at the crack. This observation suggests that the sample may have not been well aligned for the initial scan. The final scan did show the largest amount of α' -martensite at the crack but the overall fraction of α' -martensite decreased by 0.55%. There was an increase in the overall fraction of ε -martensite by 0.73%.

Table 19: Phase Fraction of Austenite (γ -Fe), α' -Martensite (α' -Fe), and ε -Martensite (ε -Fe) in the 304H-FE-20K_o-80C-55% Sample Before and After Testing

Before Testing After Fatigue			
	304H-FE-20K _o -80C-55% (0 hr)		
	γ -Fe	α' -Fe	ε -Fe
Above Crack	96.91	1.85	1.23
At Crack	94.97	3.89	1.13
Below Crack	89.86	8.87	1.26
Total	94.05	4.73	1.2
After Testing			
	304H-FE-20K _o -80C-55% (19.91 hr)		
	γ -Fe	α' -Fe	ε -Fe
Above Crack	97.92	1.86	0.2
At Crack	92.73	6.4	0.85
Below Crack	93.63	4.12	2.23
Total	93.88	4.18	1.93

3.1.3 304L Experiments

3.1.3.1 304L-FE-18K_o-80C-55%

a) Tomography

The tomographs for the 304L-FE-18K_o-80C-55% sample over the duration of the experiment is shown in **Figure 45a**. Like the 304H-FE-20K_o-80C-55% sample, vertical cracks were also present in the 304L-FE-18K_o-80C-55% sample. From the different angles of the final scan shown in **Figure 45b** indicate that the vertical cracks appear to be around the crack wake and crack tip. The crack was measured to have grown about 33 μm throughout the course of the experiment.

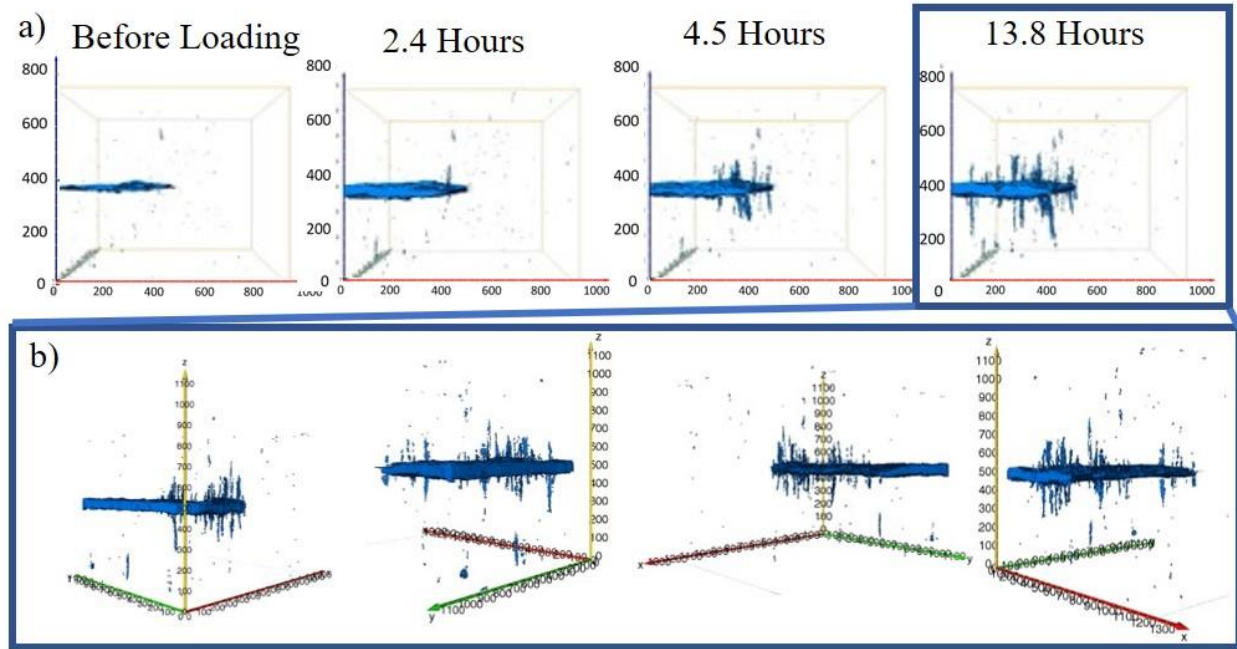


Figure 45: 3-D Tomographs of 304L-FE-18K_o-80C-55% a) over the Progression of the Experiment and b) showing Four Angles relative to the Z-Axis of the Final Tomography Scan

b) Stress Intensity Analysis

The results of the stress intensity analysis for the 304L-FE-18K_o-80C-55% sample is presented in **Table 20**. The stress intensity analysis was conducted ignoring the vertical cracks. The stress intensity was found to have decreased from 17.7 MPa m^{1/2} to 16.1 MPa m^{1/2}. The small decrease is most likely a result of the small increase in the crack length. The crack growth rate as a function of stress intensity for the 304L-FE-18K_o-80C-55% sample is shown in **Figure 46**. The average crack growth rate was found to 4.934×10^{-10} m/s. There does appear to be a similar degree of scattering around the average crack growth rate as other samples.

Table 20: Engineering Stress, Crack Length and Stress Intensity for the Initial and Final Tomographs for 304L-FE-18K_o-80C-55%

Sample	304L-FE-18K _o -80C-55%
Engineering Stress at Beginning (MPa)	164.9
Engineering Stress at End (MPa)	128.5
Average Crack Length at Beginning (μm)	527.9
Average Crack Length at End (μm)	561.2
Difference (μm)	33.3
KI at Beginning (MPa m^{1/2})	17.7
KI at End (MPa m^{1/2})	16.1

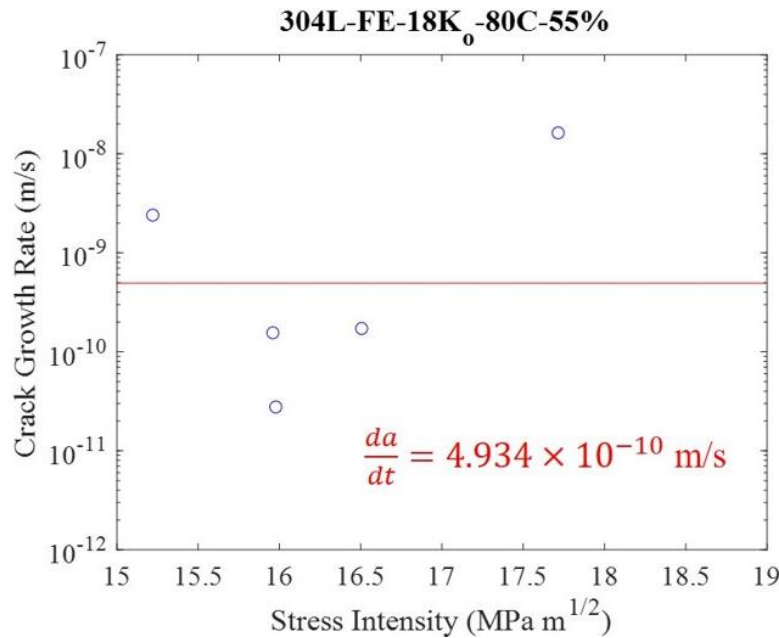


Figure 46: Crack Growth Rate as a Function of 304L-FE-18K_o-80C-55% Sample with an Average Cracking Rate of 4.934×10^{-10} m/s

c) Phase Fraction Analysis

The calculated phase fractions from the x-ray diffraction spectrums for the 304L-FE-18K_o from the initial and final scans from the experiment is listed in **Table 21**. The overall phase fraction in the total scanned volume of both α' -martensite and ϵ -martensite decreased from the start of the experiment to the end. A decrease of 0.9% of α' -martensite and 1.38% ϵ -

martensite occurred in the overall volume phase fraction. In all locations, there was a decrease in both types of martensite.

Table 21: Phase Fraction of Austenite (γ -Fe), α' -Martensite (α' -Fe), and ε -Martensite (ε -Fe) in the 304L-FE-18K_o-80C-55% Sample Before and After Testing

Before Testing After Fatigue			
	304L-FE-18K _o -80C-55% (0 hr)		
	γ -Fe	α' -Fe	ε -Fe
Above Crack	96.62	1.71	1.65
At Crack	93.14	5.29	1.55
Below Crack	94.9	1.75	3.34
Total	94.94	2.85	2.19
After Testing			
	304L-FE-18K _o -80C-55% (11.26 hr)		
	γ -Fe	α' -Fe	ε -Fe
Above Crack	97.22	1.25	0.84
At Crack	95.73	3.47	0.79
Below Crack	97.83	1.35	0.81
Total	97.22	1.95	0.81

3.1.3.2 304L-CL-30K_o-80C-55%

a) Tomography

Tomographs showing the progression of the crack in the 304L-CL-30K_o-80C-55% sample is shown in **Figure 47a**. The 304L-CL-30K_o-80C-55% sample had a total crack growth of 154 μm and the morphology shows evidence of microbranching. Moreover, **Figure 47b** shows that three separate microbranches appear with one towards the middle and two closer to the surface. To better view the microbranching behavior, orthoslices in the XZ-Plane were obtained for one of the microbranches on the surface and is shown in **Figure 48a**. **Figure 48b** shows a close up of the microbranch near the surface. The microbranch towards the center appears to be the largest.

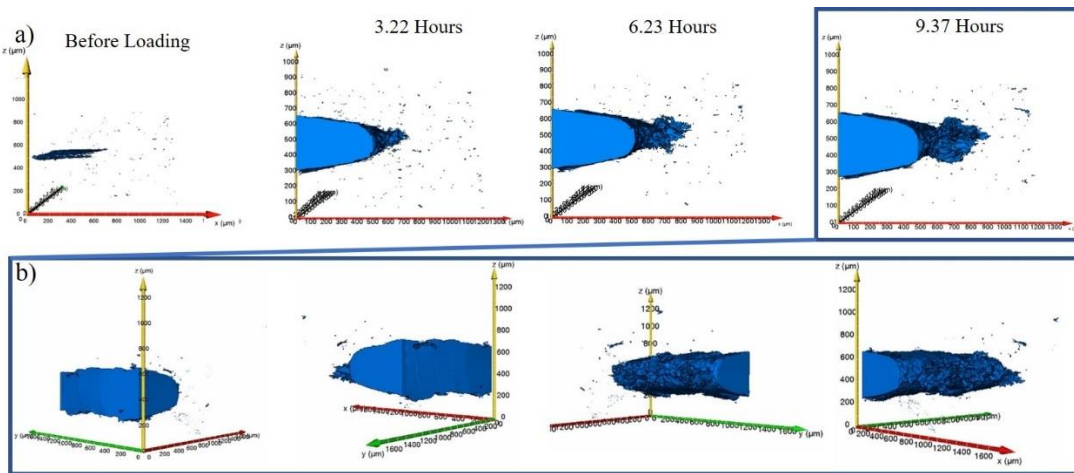


Figure 47: 3-D Tomographs of 304L-CL-30K_o-80C-55% a) over the Progression of the Experiment and b) showing Four Angles relative to the Z-Axis of the Final Tomography Scan

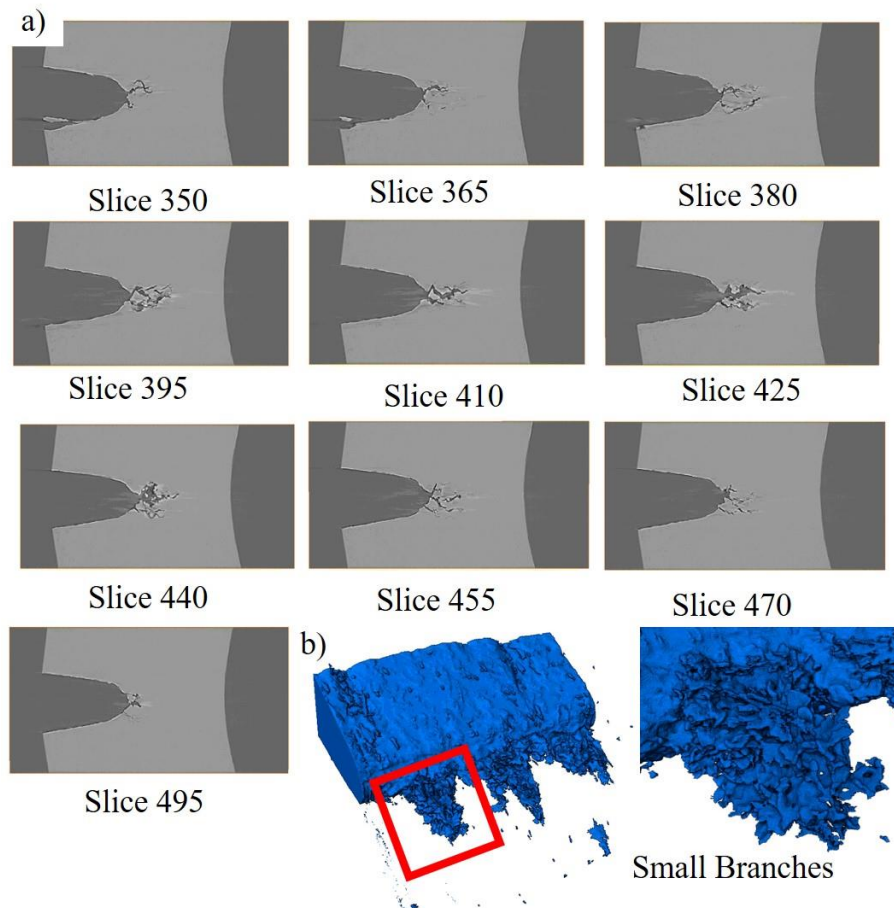


Figure 48: a) Orthoslices in the XZ-Plane in the 304L-CL-30K_o-80C-55% Sample Illustrating the Many Small Branched and Showing How Quickly the Morphology Changes with each Slice (1 slice= 1.17 μm). b) Shows a Magnified view of one of the Microbranches

b) Stress Intensity Analysis

The stress intensity analysis of the initial and final state of the 304L-CL-40K_o-80C-55% sample is listed in **Table 22**. The sample went from a stress intensity of 30.7 MPa m^{1/2} all the way up to around 46.1 MPa m^{1/2}. Because of the non-uniformity of the branching through the thickness of the material, the crack was treated as a single edge crack. A plot of the crack growth rate as a function of stress intensity is shown in **Figure 49**. The average crack growth rate was measured to be 1.776×10^{-9} m/s. The data had a low amount of scatter relative to the average crack growth rate line.

Table 22: Engineering Stress, Crack Length and Stress Intensity for the Initial and Final Tomographs for 304L-CL-30K_o-80C-55%

Table Sample	304L-CL-30K _o -80C-55%
Engineering Stress at Beginning (MPa)	284.7
Engineering Stress at End (MPa)	284.7
Average Crack Length at Beginning (μm)	593.9
Average Crack Length at End (μm)	736.1
Difference (μm)	142.2
KI at Beginning (MPa m ^{1/2})	30.7
KI at End (MPa m ^{1/2})	46.1

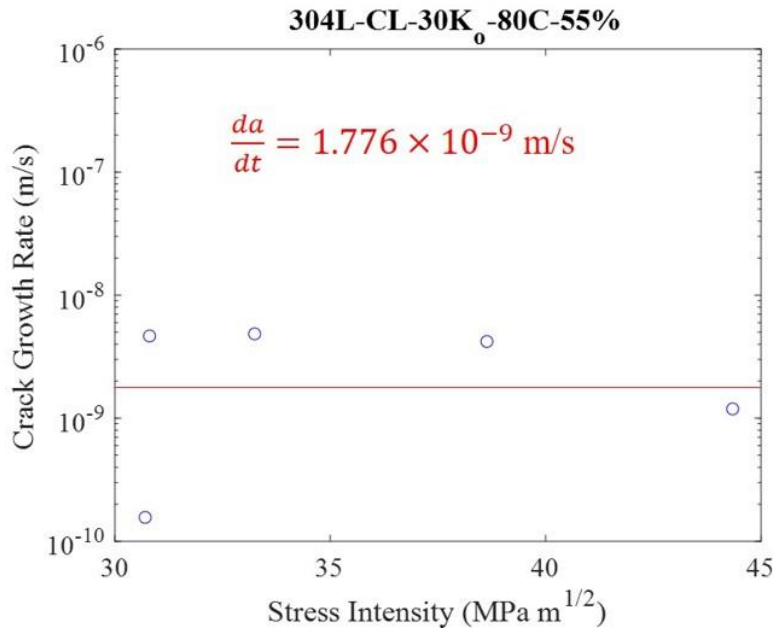


Figure 49: Crack Growth Rate as a Function of 304L-CL-30K_o-80C-55% Sample with an Average Cracking Rate of $1.776 \times 10^{-9} \text{ m/s}$

c) Phase Fraction Analysis

The phase fractions for the 304L-CL-30K_o-80C-55% samples before the experiment but after fatigue and at the end of the experiment are listed in **Table 23**. Like the 304L-FE-18K_o-80C-55% sample, the phase fraction overall decreased for the total scanned volume of α' -martensite in the 304L-CL-30K_o-80C-55% sample. There was a small increase in the phase fraction of ϵ -martensite in the overall volume but only by 0.03%. In terms of location, there was a small increase in the α' -martensite above and below the crack most likely due to branching moving the plastic zones above and below the crack.

Table 23: Phase Fraction of Austenite (γ -Fe), α' -Martensite (α' -Fe), and ε -Martensite (ε -Fe) in the 304L-CL-30K_o-80C-55% Sample Before and After Testing

Before Testing After Fatigue			
	304L-CL-30K-80C-55% (0 hr)		
	γ -Fe	α' -Fe	ε -Fe
Above Crack	98.16	1.75	0.1
At Crack	95.51	4.17	0.31
Below Crack	97.58	2.21	0.21
Total	97.09	2.71	0.21
After Testing			
	304L-CL-30K-80C-55% (11.03 hr)		
	γ -Fe	α' -Fe	ε -Fe
Above Crack	97.7	2.04	0.26
At Crack	97.82	2.12	0.06
Below Crack	96.6	2.99	0.41
Total	97.37	2.38	0.24

3.1.3.2 304L-CL-43K_o-50C-55%

a) Tomography

Figure 50a depicts the progression of the crack over the experiment for the 304L-CL-43K_o-50C-55% sample. Like the 304-CL-46K_o-50C-55% sample, the 304L-CL-43K_o-50C-55% fractured to final failure. The different angles of the 304L-CL-43K_o-50C-55% sample shown in **Figure 50b** reveal the crack progressed rather uniformly and not in sections like other samples. The crack, before the final fracture, was calculated to have grown around 43 μm .

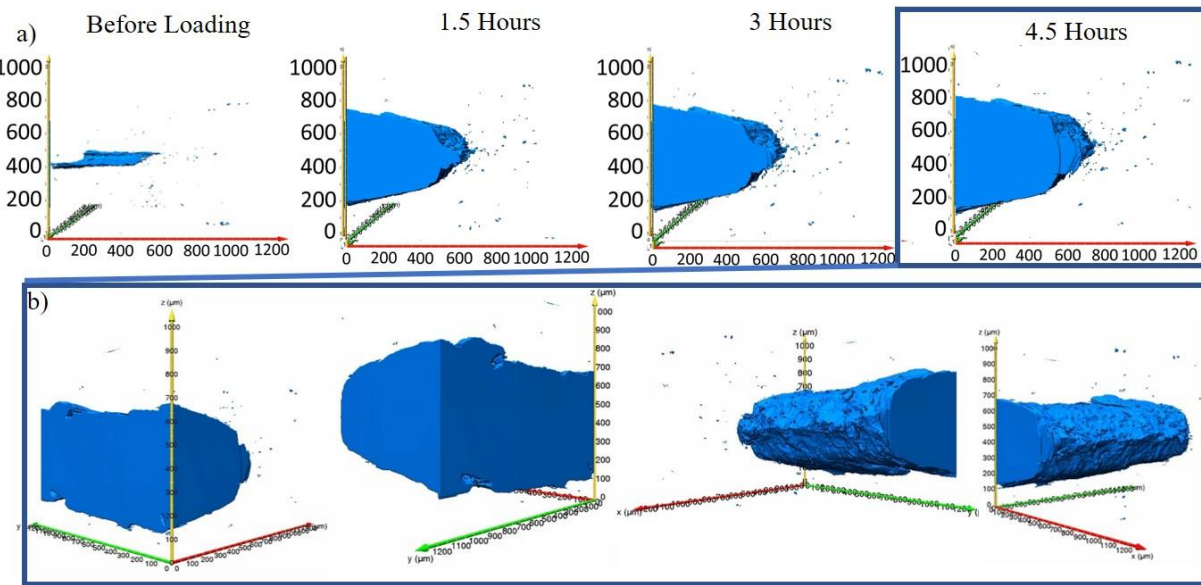


Figure 50: 3-D Tomographs of 304L-CL-43K_o-50C-55% a) over the Progression of the Experiment and b) showing Four Angles relative to the Z-Axis of the Final Tomography Scan

b) Stress Intensity Analysis

The tomographs combined with the load were used to calculate the stress intensity of the 304L-CL-43K_o-50C-55% sample initially and at the end of the experiment and is listed in **Table 24**. The initial stress intensity went from $43.9 \text{ MPa m}^{1/2}$ to $49.9 \text{ MPa m}^{1/2}$ before fracturing. Both samples which fractured were around $50 \text{ MPa m}^{1/2}$ which must be close to the K_{IC} for this sample configuration. The plot of the crack growth rate as a function of stress intensity is shown in **Figure 51**. The average crack growth rate in the 304L-CL-43K_o-50C-55% sample was calculated to be $1.470 \times 10^{-9} \text{ m/s}$. Unlike the 304-CL-46K_o-50C-55% which had its last data point removed, the 304L-CL-43K_o-50C-55% does not appear to have its last data point in the stage III as is evident by the crack growth rate.

Table 24: Engineering Stress, Crack Length and Stress Intensity for the Initial and Final Tomographs for 304L-CL-46K_o-50C-55%

Sample	304L-CL-43K _o -50C-55%
Engineering Stress at Beginning (MPa)	332.3
Engineering Stress at End (MPa)	332.3*
Average Crack Length at Beginning (μm)	651.7
Average Crack Length at End (μm)	694.3*
Difference (μm)	42.6
KI at Beginning (MPa m^{1/2})	43.9
KI at End (MPa m^{1/2})	49.9*

*Scan before Final Fracture

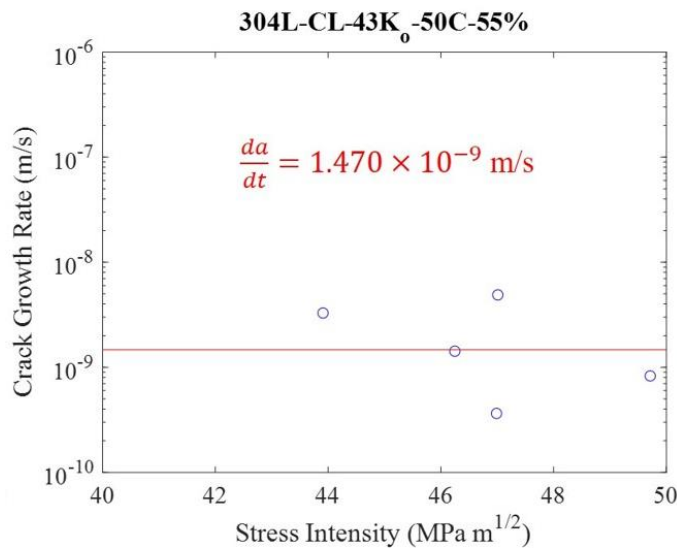


Figure 51: Crack Growth Rate as a Function of 304L-CL-43K_o-50C-55% Sample with an Average Cracking Rate of 1.470×10^{-9} m/s

c) Phase Fraction Analysis

The phase fraction analysis for the initial and final state before fracture of the 304L-CL-43K_o-50C-55% is presented in **Table 25**. Unlike to other 304L samples, this sample had an increase in both types of martensite with a 3.65% increase in α' -martensite and a 0.45% increase in ϵ -martensite. Most of the α' -martensite increase occurred at the crack. After the sample

fractured, scans were taken above and below the crack which reveal a large increase of both types of martensite as shown in **Table 26**. There was an increase of 18.75% in α' -martensite and 2.02% in ε -martensite. Both samples which fractured to final failure showed a much larger increase in martensite as a result of deformation during final fracture compared to during CISCC.

Table 25: Phase Fraction of Austenite (γ -Fe), α' -Martensite (α' -Fe), and ε -Martensite (ε -Fe) in the 304L-CL-46K_o-50C-55% Sample Before and After Testing

Before Testing After Fatigue			
	304L-CL-43K-50C-55% (0 hr)		
	γ -Fe	α' -Fe	ε -Fe
Above Crack	98.7	1.04	0.26
At Crack	95.27	4.44	0.29
Below Crack	98.92	0.92	0.16
Total	97.63	2.13	0.24
After Testing			
	304L-CL-43K-50C-55% (4.13 hr)*		
	γ -Fe	α' -Fe	ε -Fe
Above Crack	94.58	5.02	0.4
At Crack	91.06	8.66	0.28
Below Crack	94.94	3.66	1.39
Total	93.53	5.78	0.69

* Scan Taken Before Fracture

Table 26: Phase Fraction of Austenite (γ -Fe), α' -Martensite (α' -Fe), and ε -Martensite (ε -Fe) in the 304L-CL-46K_o-50C-55% Sample after Fracture

304L-CL-43K-50C-55% (5.63 hr)	γ -Fe	α' -Fe	ε -Fe
Above Crack	75.22	23.32	1.46
Below Crack Total	70.30	25.73	3.97
Total	72.76	24.53	2.71

3.2 Microstructural Analysis with Optical, Scanning Electron, and Transmission Electron Microscopy

3.2.1 Optical and Scanning Electron Microscopy

Post-experimental characterization was conducted using various forms of microscopy from optical, to scanning electron, to transmission electron microscopy. Only a certain set of the samples described above were analyzed further with optical and electron microscopy. Optical microscopy, like that shown in **Figure 52a**, shows the physical appear of the 304-FE-40K_o-80C-55%. The optical microscopy shows the discoloration in and around the crack. The brown discoloration is most likely a corrosion product which formed as a response to the insidious concentrated MgCl₂ solutions. Additionally, the branching crack is show on the surface of the sample. SEM was also performed and shown in **Figure 52b** along with the chemical maps obtained through EDS. The chemical maps suggest that the corrosion products are made up of oxides and chlorine salts.

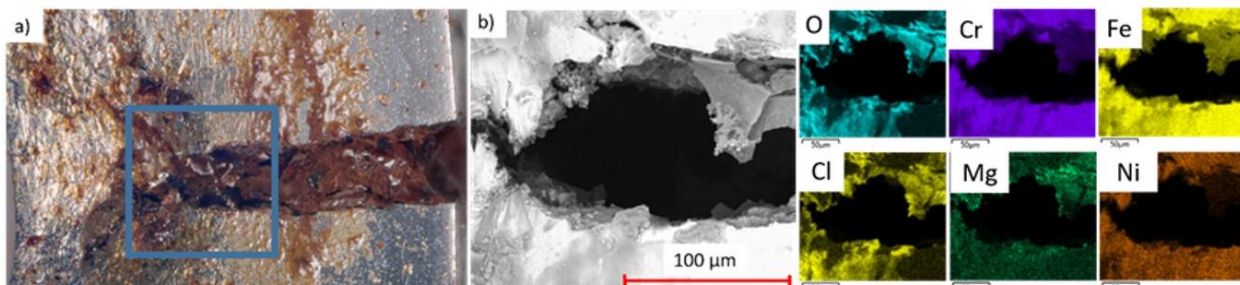


Figure 52: a) Optical Microscopy and b) Scanning Electron Microscopy Micrographs with Chemical Maps of 304-FE-40K_o-80C-55% Sample

Some fractography was conducted on a couple of the samples using SEM equipped with EDS to establish the type of cracking and to visualize locations of specific elements. In order to prevent unnecessary deformation, samples were cut using a diamond saw at a speed of 80 rpm.

One sample of interest was the 304-Fe-40K_o-80C-55% sample. A low magnification SEM micrograph using secondary electrons and backscatter electrons is shown in **Figure 53a** and **b**, respectively. Backscatter electrons were used to obtain micrographs which are Z-contrast meaning that heavier elements appear brighter while lighter elements appear darker. Based on the low magnification SEM micrographs, transgranular cracking appears to be evident from both fatigue and CISCC as evident by the lack of granular looking surfaces. The backscatter micrograph suggests that a low atomic number element is heterogeneously dispersed on the surface of the crack wake. A higher magnification micrograph of the branching crack region of the sample is shown in **Figure 54**. The accompanying elemental maps show a couple of interesting features. First, a look at both the chlorine and magnesium maps shows that they do not overlap. The lack of overlapping maps between chlorine and magnesium suggests that MgCl₂ does not stay together during CISCC and most likely reacts with the metal to form new compounds. Another point to add is that both magnesium and chlorine are found at the crack branch meaning the MgCl₂ was able to diffuse to the crack tip. Additionally, the oxygen map suggests that some kind of oxide did form. Finally, various precipitates appear to be evident on the crack wake which include those rich in carbon, silicon, sulfur, and copper. On the fatigue region of the 304-FE-40K_o-80C-55% sample, shown in **Figure 55**, shows a similar result in terms of the magnesium and chlorine maps as the branching region. In fact, the oxygen map does appear to overlay with the magnesium spots which suggest a magnesium oxide may have formed. The magnesium appears to be in concentrated spots whereas the chlorine appears more diffuse.

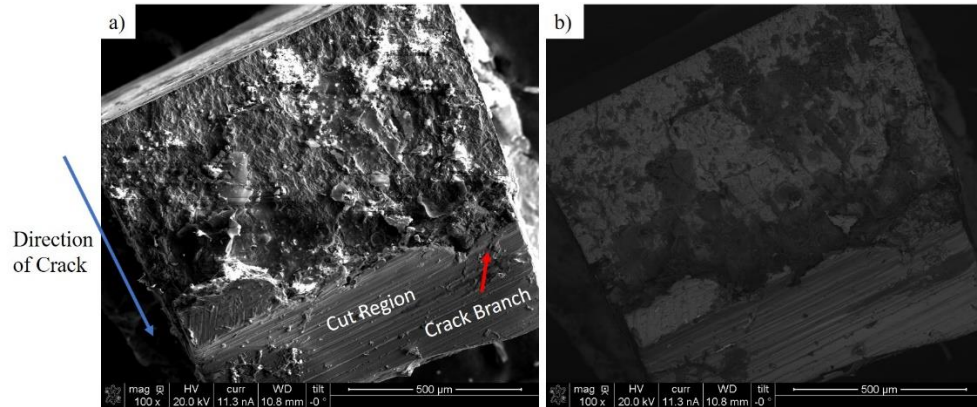


Figure 53: Low Magnification Scanning Electron Microscopy Micrograph of the Fractured Surface of 304-FE-40K_o-80C-55% using a) Secondary Electron, and b) Backscatter Electrons

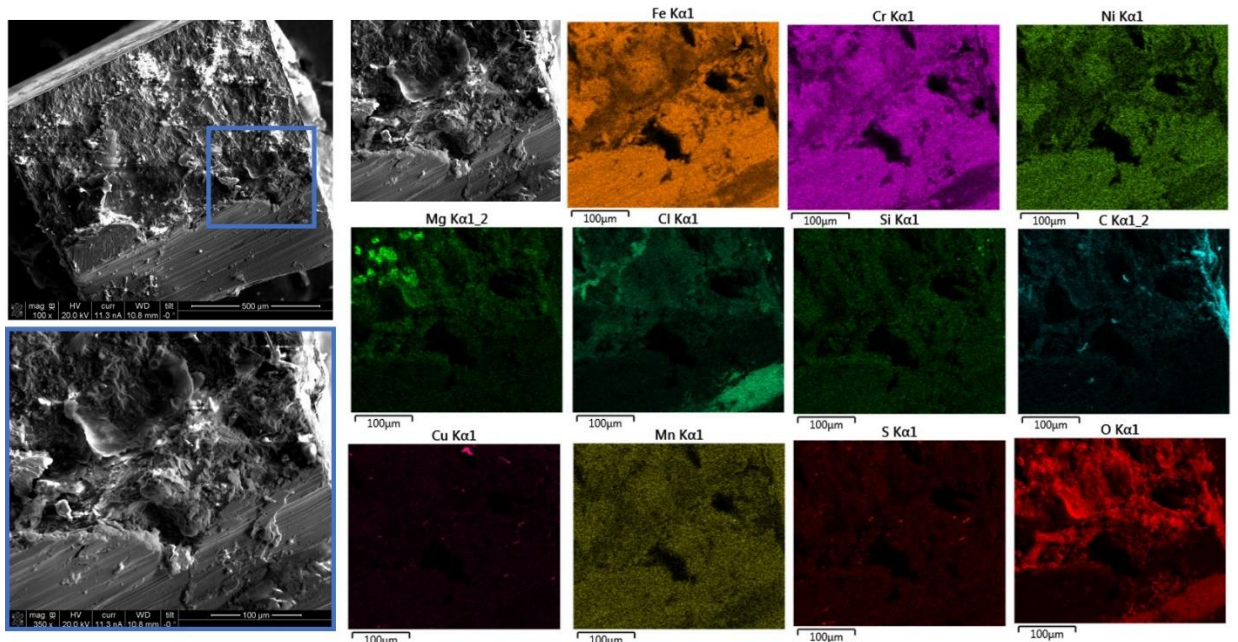


Figure 54: Scanning Electron Microscopy Micrograph and Chemical Maps of Branching Crack of 304-FE-40K_o-80C-55% Sample

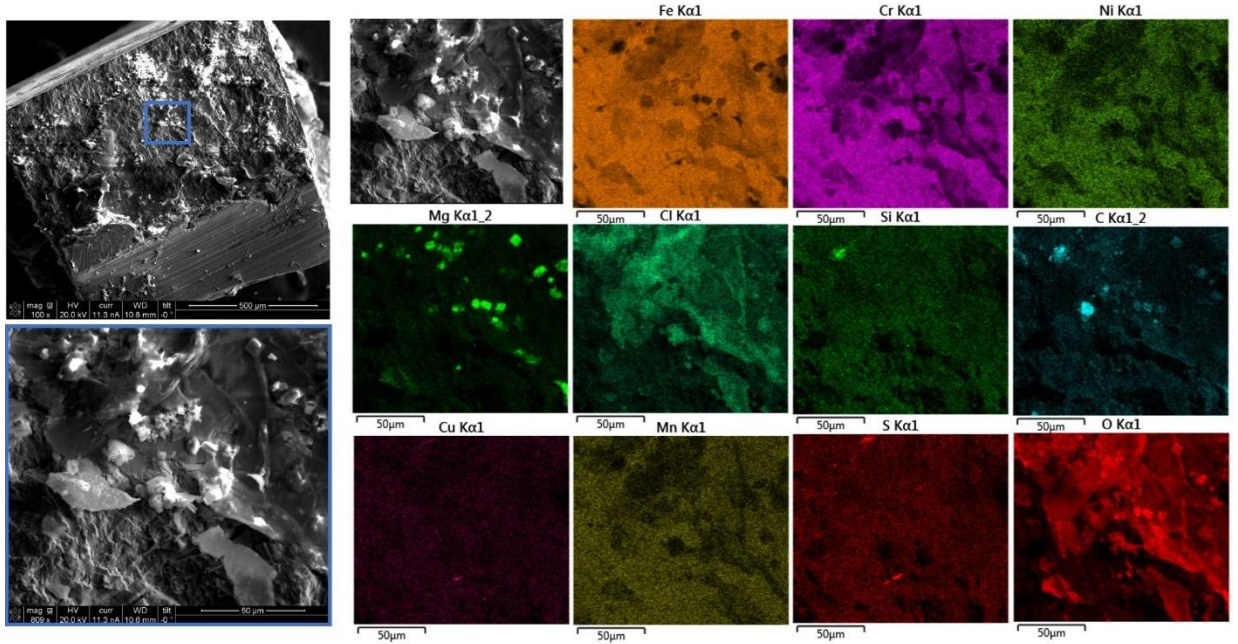


Figure 55: Scanning Electron Microscopy Micrograph and Chemical Maps of Fatigue Region of 304-FE-40K_o-80C-55%

Fractography of the 304H-FE-20K_o-80C-55% was conducted using the SEM and a low magnification SEM micrograph is shown in **Figure 56**. As was evident in the 304-FE-40K_o-80C-55% sample, the 304H-FE-20K_o-80C-55% also showed transgranular cracking in both the fatigue and CISCC regions. **Figure 57** shows a higher magnification of a part of the crack front with some chemical maps. Like the 304-FE-40K_o-80-55% sample, the magnesium and chlorine appear to have been able to diffuse to the crack tip region and the maps do not overlap. The micrograph shows significantly less precipitates on the crack wake as the 304-FE-40K_o-80C-55% sample with only a small copper enrichment and one silicon enrichment. The micrograph and associated chemical maps of the fatigued region are evident in **Figure 58**. Like the crack tip region, the fatigued region has few chemical enrichments. Some chromium carbides do appear evident in the fatigued region. Unlike the crack tip, the chlorine and magnesium map do not look very different compared to the crack tip region. From **Figure 43**, the tomographs of the 304H-FE-20K_o-80C-

55% sample appeared to have vertical cracks. **Figure 59** shows one of these vertical cracks. The hole itself appears to be around $10 \mu\text{m}$ in diameter which matches the measurements on the tomograph. The chemical maps in **Figure 59** indicates the hole has enrichments of carbon around it. Like the fatigued regions, the chlorine and magnesium appear to be not too different in terms of location.

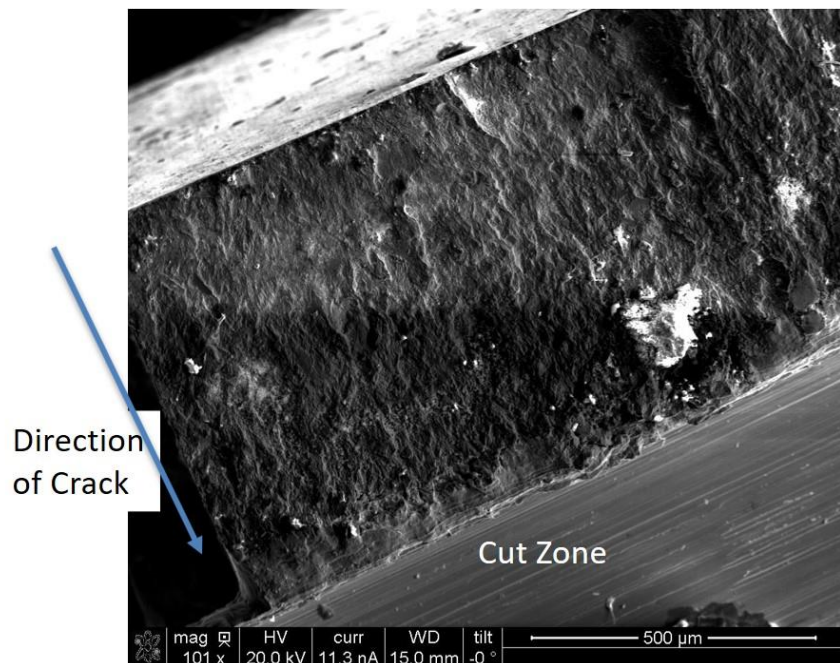


Figure 56: Low Magnification Scanning Electron Microscopy Micrograph of the 304H-FE-20K_o-80C-55% Sample using Secondary Electrons

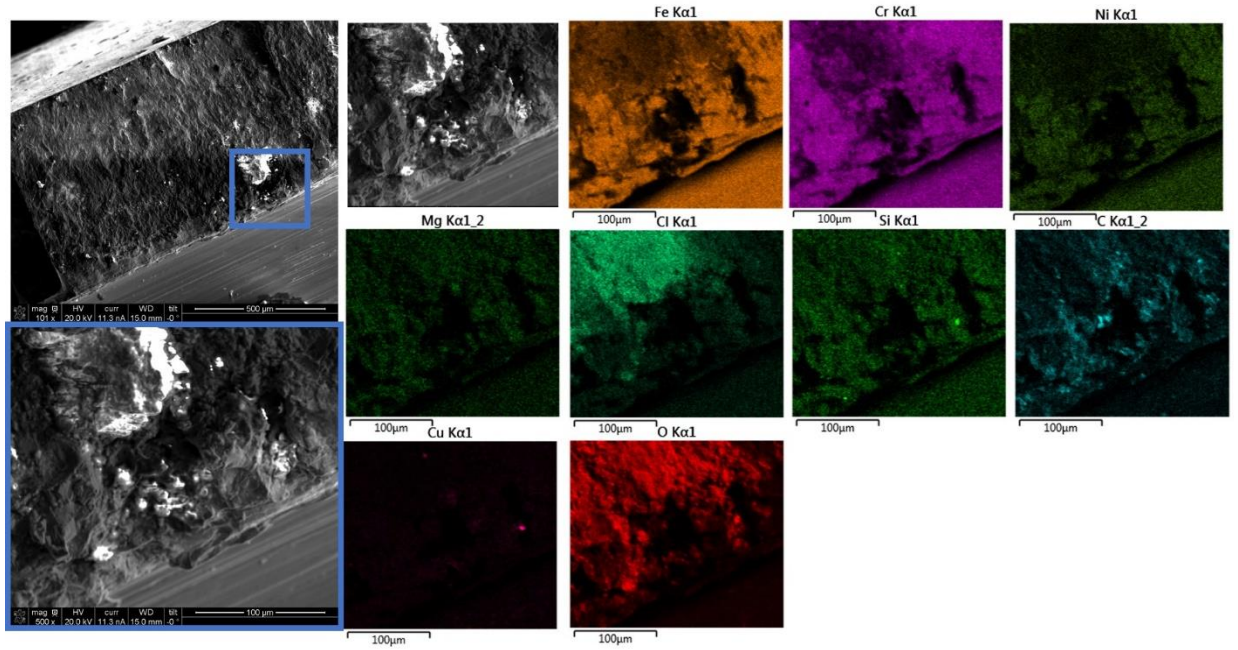


Figure 57: Scanning Electron Microscopy Micrograph and Chemical Maps of the Crack Front Region of 304H-FE-20K_o-80C-55% Sample

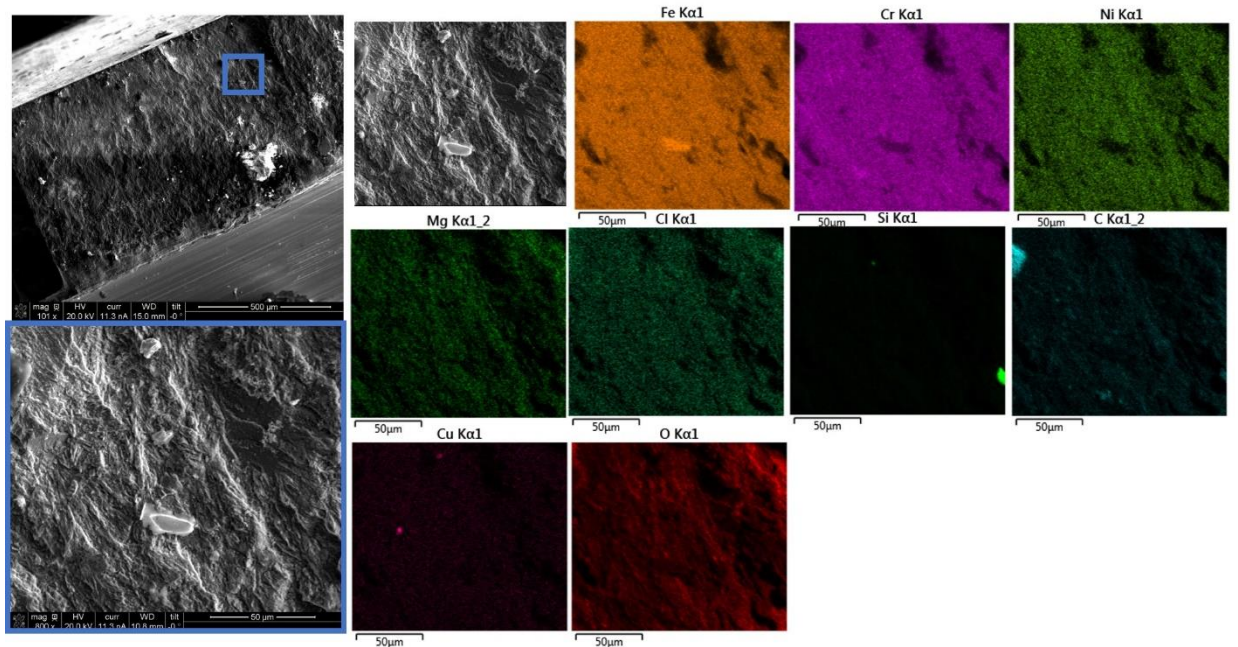


Figure 58: Scanning Electron Microscopy Micrograph and Chemical Maps of the Fatigue Region of 304H-FE-20K_o-80C-55% Sample

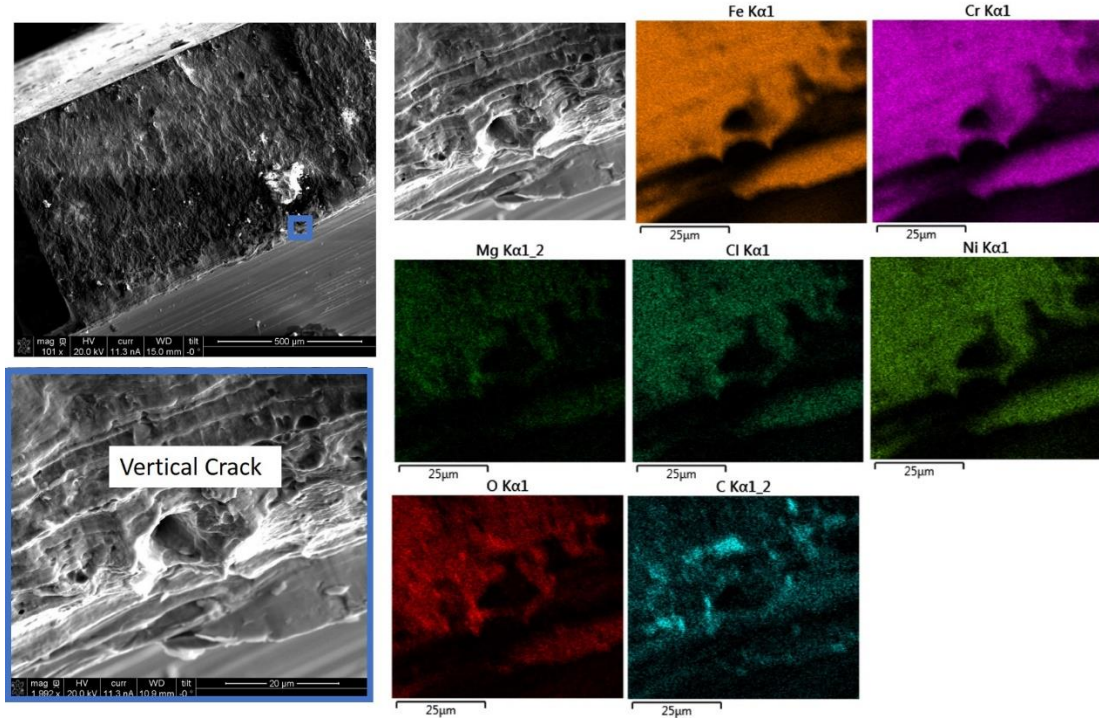


Figure 59: Scanning Electron Microscopy Micrograph and Chemical Maps of a Vertical Crack in the 304H-FE-20K_o-80C-55% Sample

3.2.2 Transmission Electron Microscopy

To answer some of the questions posed in Chapter 1, TEM analysis is needed to analyze the microstructure, especially in different regions of these samples. A study conducted by Shen et al. [42] performed a similar TEM analysis on samples subjected to pressurized water reactor primary water where samples were taken from various positions to develop a timeline which can be used to infer the mechanism at play. Regions such as the crack wake, crack tip, and ahead of the crack tip can be useful.

The first sample which was analyzed was the 304-FE-40K_o-80C-55% where samples were extracted near the crack tip (containing part of the crack) and in front of one of the crack branches (not containing part of the crack) as shown in **Figure 60a**. **Figure 60b** shows TEM micrographs

of the sample in front of one of the crack branch which show regions that contain martensite as indicated by the diffraction pattern that shows reflections belonging to α' -Fe. The martensite appears to exist as laths inside the austenite grains which is typical of 304ss [38]. The other TEM sample that was extracted out of commercial-304-FE-40K_o-80C-55% sample near the crack tip that contains the crack was observed in TEM mode as well as Scanning Transmission Electron Microscopy (STEM) mode. A High Angle Annular Dark Field (HAADF) image of the sample near the crack is shown in **Figure 60c**. Additionally, chemical maps were taken in STEM mode using a SuperX EDS system in a process known as ChemiSTEM (Shown in **Figure 60c**). From the chemical maps near the crack, the development of an oxide appears to be evident. Interestingly, a look at the chlorine and magnesium maps shows areas where chlorine does not overlap with magnesium. This indicates that some of the MgCl₂ salt that was deposited into the crack broke down and the chlorine ingresses inward from the crack surface while magnesium was left behind. To determine the possible compounds that were formed with chlorine and to determine the oxide structure, electron diffraction using a small Selected Area Electron Diffraction (SAED) aperture was conducted in the area. The diffraction pattern from the SAED aperture (Location shown in the HAADF image as a blue circle) is shown in the bottom left corner of **Figure 60c**. The diffraction pattern shows a ring like structure which indicates the presence of nanosized grains. Combined with the information from the chemical maps, the diffraction pattern indicates the presence of salt containing compounds like NiCl₂·6H₂O, CrCl₂, and FeCl₂. Additionally, Fe₃O₄, Fe₂O₃ and Cr₂O₃ were also found with the latter compound known to give stainless steels its high corrosion resistance.

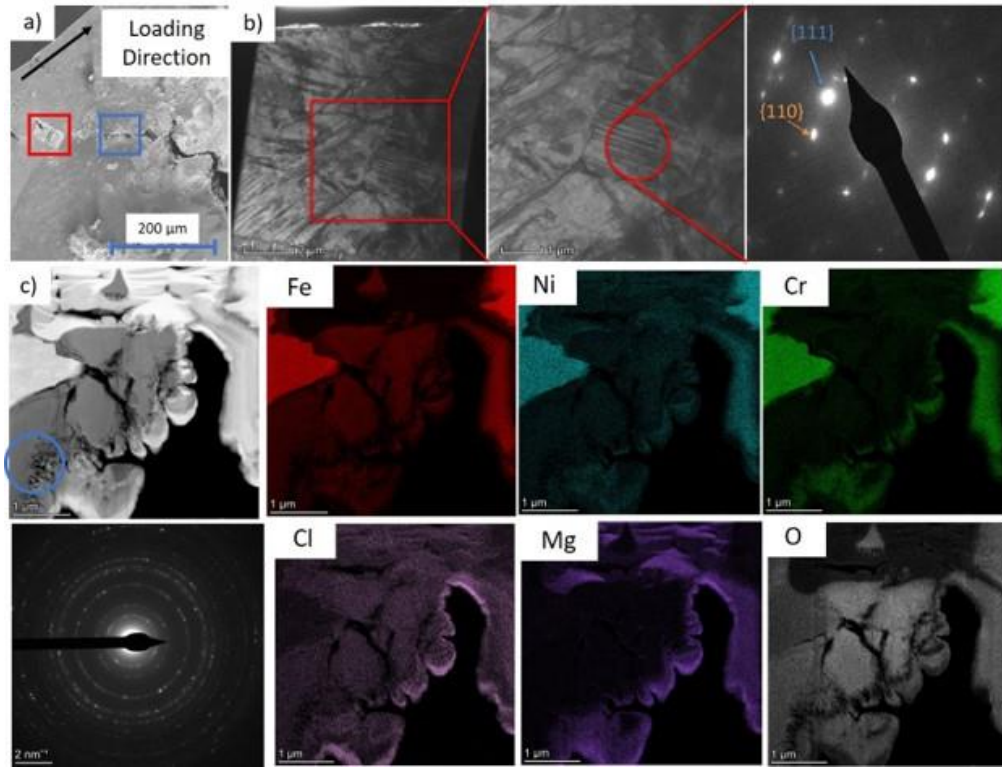


Figure 60: a) Location of Transmission Electron Microscopy Liftout, b) Transmisison Electron Microscopy Bright Field and Selected Area Electron Diffraction of Sample near Branching Crack Showing Evidence of Martensite (Orange Arrow), c) High Angle Annular Dark Field, Chemical Maps, and Selected Area Electron Diffraction Pattern of Sample near Crack Tip

After using the diamond saw to open the 304-FE-40K_o-80C-55% sample, a liftout was taken from the crack wake as shown in **Figure 61a**. Before taking a liftout, a protective platinum strip was placed using the electron beam before using the ion beam to prevent sputtering of the surface. **Figure 61b** shows the BF TEM sample and the SEAD patterns which show the presence of austenite (γ -Fe) and martensite (α' -Fe and ϵ -Fe). Fatigue must have caused deformation induced martensite to form during the pre-cracking of the sample. Chemical maps of the green region of **Figure 61b** is shown in **Figure 61c** indicate that an oxide had formed. Close inspection reveals chromium to match some of the oxygen locations. It should be noted that chromium and oxygen share a common characteristic x-ray; however, the maps do not match completely which would indicate that the chromium signal is authentic. According to the chemical maps of the magnesium

and chlorine, there appears to be a slight enrichment in both at the top of the sample; however, it does not appear to be as distinct compared to maps in **Figure 61c**.

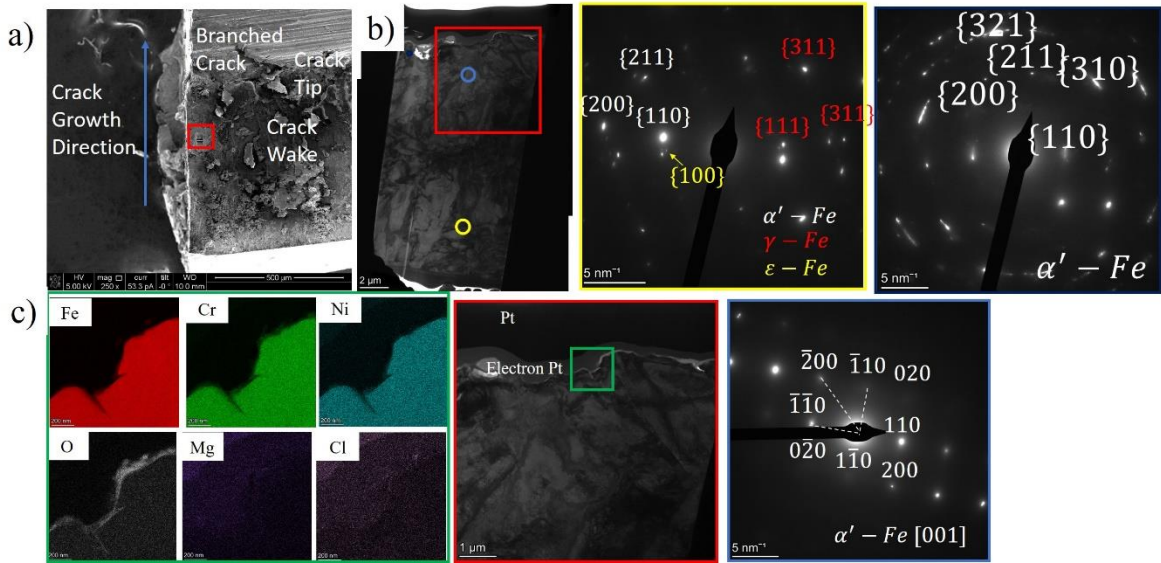


Figure 61: a) Location of Transmission Electron Microscopy Liftout, b) Bright Field Transmission Electron Microscopy Micrograph of the Sample with Selected Area Electron Diffraction Patterns and c) Chemical Maps of the 304-FE-40K_o-80C-55% at the Crack Wake

The next sample for 304-FE-40K_o-80C-55% was taken around the crack tip of the sample.

Figure 62a shows the location of the FIB liftout and **Figure 62b** shows the BF TEM of the sample. The sample was very large and the bottom was preferentially thinned down first. The sample contained a crack which was not evident on the surface. The two magnified BF TEM images shown in the yellow and purple show the matrix. The yellow box shows elongated grain structure while the purple box shows smaller equiaxed grains. Both of these grain structures indicate deformation compared to the as-received equiaxed grains. The SAED of the matrix, shown in the green box of **Figure 62b** indicates the presence of both austenite and α' -martensite most likely brought on by the plastic zone of the crack. Chemical maps of the pink area in **Figure 62b**, shown in **Figure 62c**, again show that magnesium stays on the surface while the chlorine appears to have diffused

inward. The oxygen map suggests an oxide has formed on the outer parts of the crack as well. The elements which are rich in that area include iron, chromium, and nickel which is similar to what was observed when a sample was taken from the side of the crack.

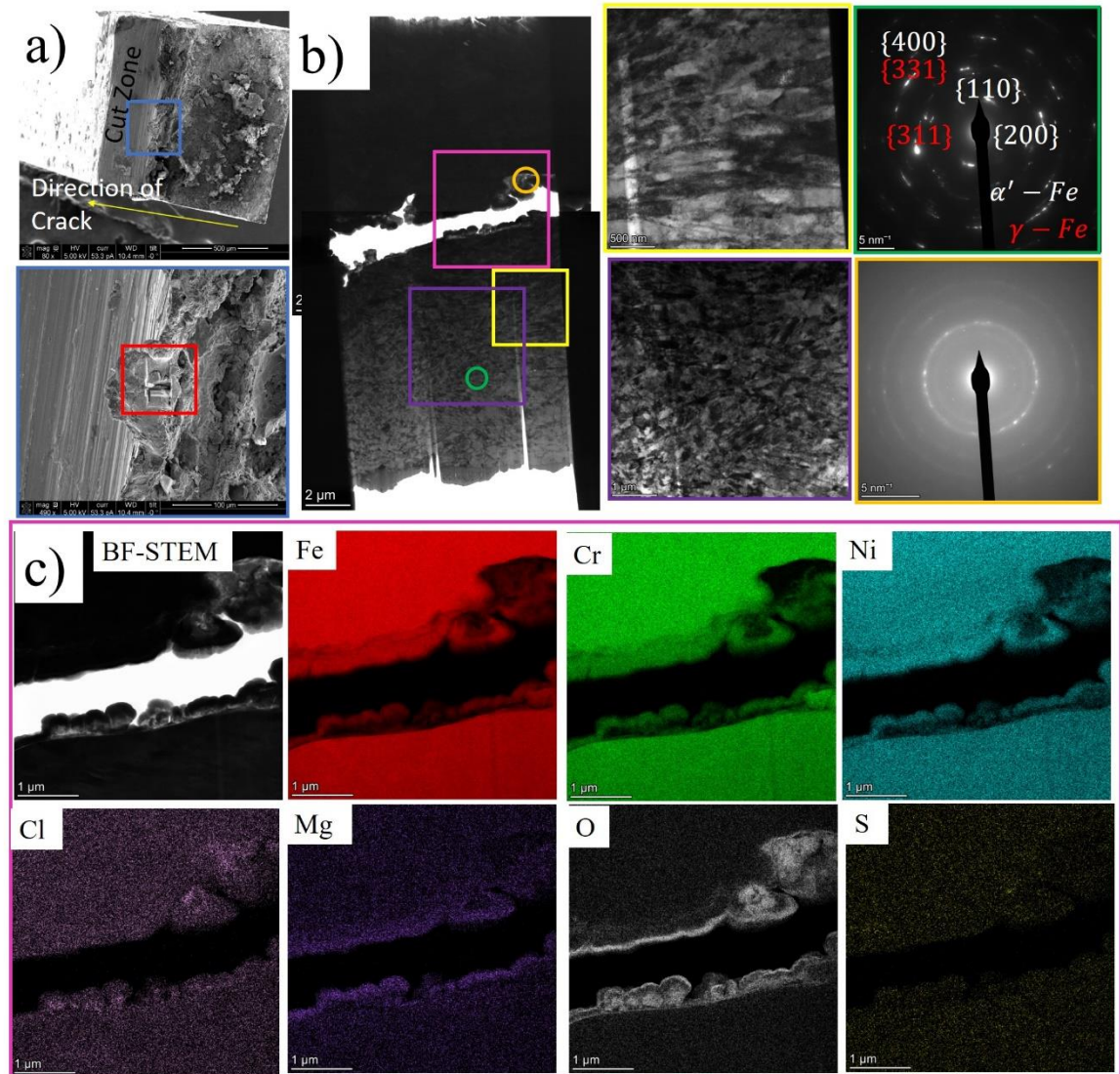


Figure 62: a) Location of Focused Ion Beam Liftout, b) Bright Field Transmission Electron Microscope Micrograph and Accompanying Selected Area Electron Diffraction Pattern, and c) Chemical Maps of Crack of the 304-FE-40K_o-80C-55% Sample at the Crack Tip showing Chlorine Migrating into Sample

The next sample which was analyzed under TEM observations was the 304H-FE-20K_o-80C-55% sample where a liftout was taken out from the side of the sample as shown in the SEM

micrograph in **Figure 63a**). As can be seen in the TEM micrograph in **Figure 63b**), there does not appear to be as much obvious deformation in the microstructure like that found in the plastic zone of the 304-FE-40K_o-80C-55% sample. The liftout was taken close to the crack tip so this region would have been subjected to either the plastic zone of the stress during the SCC experiment or the plastic zone during fatigue pre-cracking. There does appear to be some evidence of α' -Fe as shown in **Figure 63c** and **d**). The diffraction pattern shows that both phases in the sample are in a two-beam condition. An interesting observation that can be made is about the form in which the α' -Fe appears. In the 304-FE-40K_o-80C-55%, the α' -Fe is more lathe-like while the α' -Fe in the 304H-FE-20K_o-80C-55% appears more block-like. According to Pegues et al. the pathway of the phase transformation from metastable austenite into body centered cubic martensite [36]. For example, Pegues discussed how through the pathway of $\gamma \rightarrow \varepsilon \rightarrow \alpha'$ the α' -Fe appears more lathe like in structure while more block-like and irregular through the direct formation from γ -Fe [36].

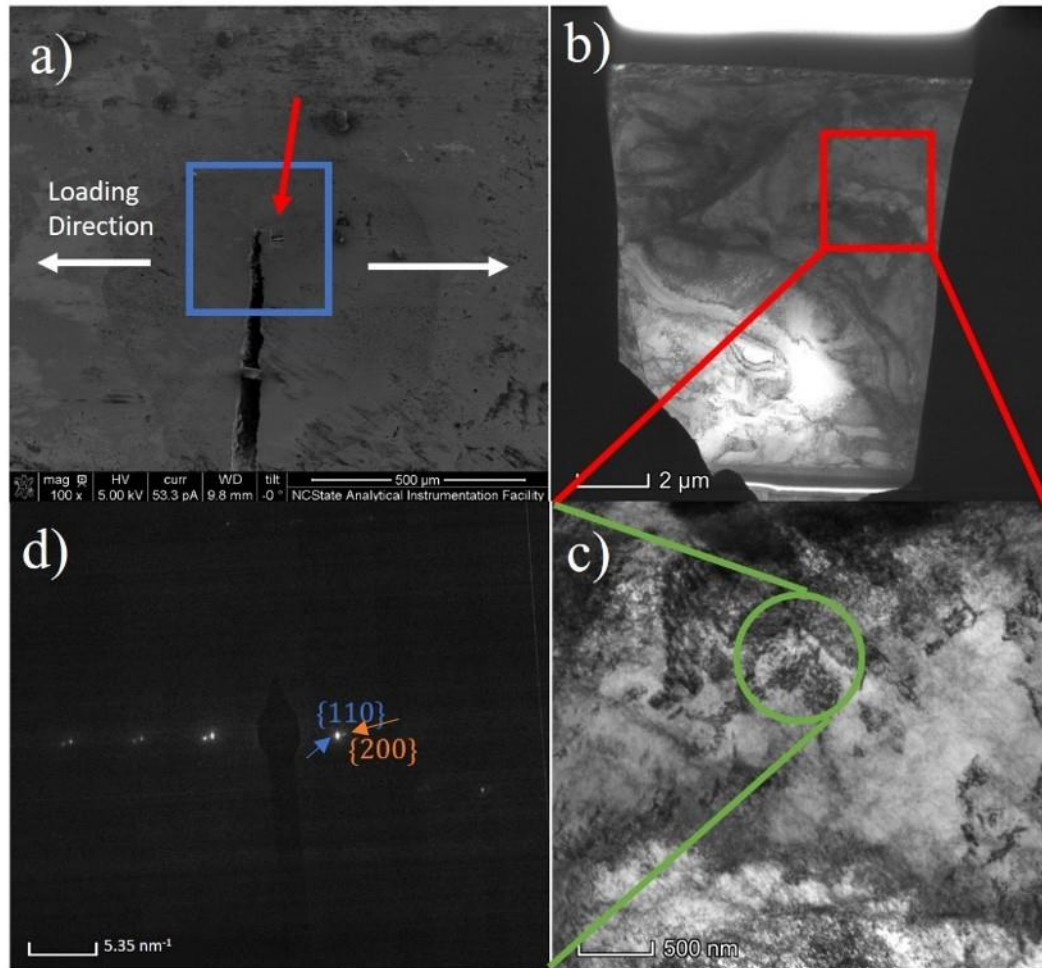


Figure 63: a) Scanning Electron Micrograph of Transmission Electron Microscopy Liftout (Red Arrow), b) Low Magnification Transmission Electron Microscopy Micrograph, c) Higher Magnification Transmission Electron Microscopy Micrograph showing Two Phases, and d) Selected Area Electron Diffraction Pattern showing the Presence of Austenite (Blue) and Martensite (Orange)

The above liftouts were from samples which showed some degree of cracking over the course to the experiment. To further probe why a crack might not propagate, a liftout was obtained from 304-CL-31K_o-80C-55% at the crack tip. As shown in **Figure 64**, the sample did not propagate much with a measured crack growth of 1.84 μm which is very close to the limit of resolution of the tomography detector. Interestingly, there did appear to be some cracking from the other side of the sample opposite the crack opening. The main crack did propagate so the sample was cut

open and a liftout was taken as shown in **Figure 65a** and **b**. Due to the thickness of the sample, conventional TEM was not performed. Instead, STEM was conducted to obtain chemical maps of the surface. As indicated in **Figure 65d**, the chemical maps do not show any significant amount of chlorine or magnesium between the protective electron platinum and the metal. These results show that chlorine is essential for CISCC.

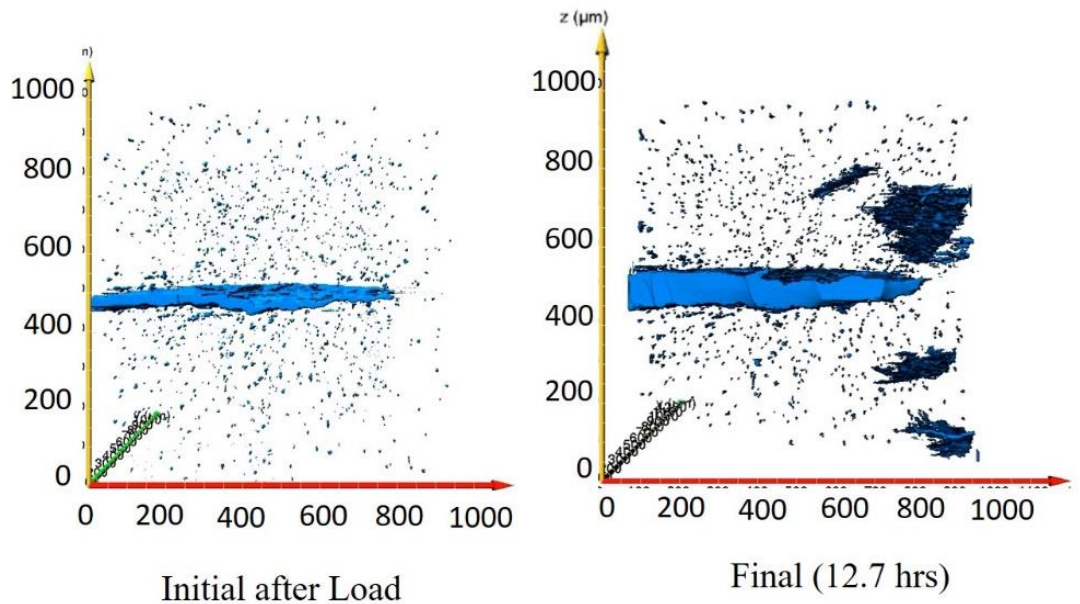


Figure 64: Initial after Loading and Final Tomograph of 304-CL-31K_o-80C-55% Sample showing the Main Crack did not Propagate

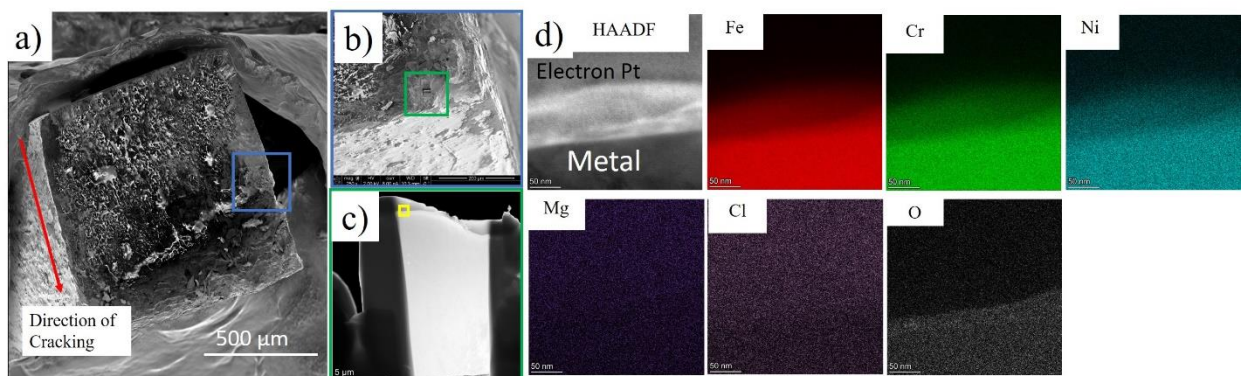


Figure 65: a) b) Location of Transmission Electron Microscopy Liftout, c) High Angle Annular Dark Field Micrograph of Sample, and d) Chemical Maps of Yellow Region of c) in the 304-CL-31K_o-80C-55% showing the lack of Chlorine

Chapter 4: Discussion

Based on the results discussed in the previous chapter, we hereby discuss several questions that were brought up in chapter 1. The questions are listed below.¹

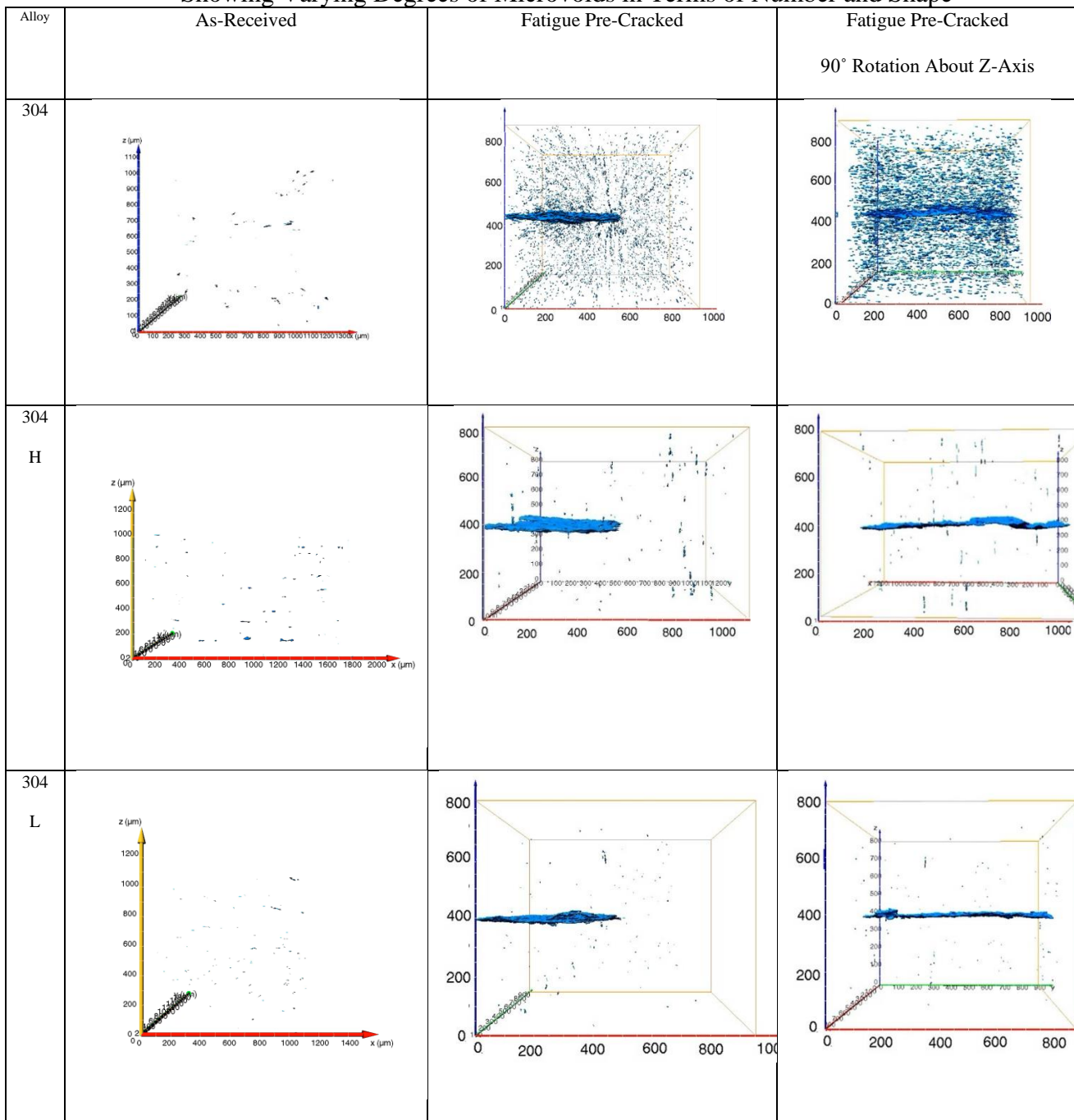
- (1) What are the effects of fatigue pre-cracking on the initial microstructure?**
- (2) What is the role of martensite as a possible intrinsic and extrinsic factor in crack retardation?**
- (3) How does the stress intensity affect the rate and morphology of cracks?**
- (4) How does crack branching influence the steady state propagation rate?**
- (5) What role does temperature play on crack growth rates?**
- (6) What is the role of chlorine and chlorine forming compounds?**
- (7) What are the mechanisms that are operating on the microstructural level?**

4.1 What are the Effects of Fatigue Pre-Cracking on the Initial Microstructure?

4.1.1 Microvoid Formation and Shape

The tomography scans of the fatigue pre-cracked samples clearly showed evidence of voids to varying degrees as shown in **Table 27**. These voids must have originated as the result of the fatigue as suggested by differences found in the as-received state and the fatigue pre-cracked state of each alloy. In fact, a microvoid associated with a sulfide precipitate in the 304H sample was observed under TEM observation after electropolishing a 3 mm disc of fatigue pre-cracked 304H. The TEM micrograph and chemical maps, shown in **Figure 66**, depict a microvoid which had nucleated at a precipitate identified as Cu₂S.

Table 27: Tomography Scans of As-Received and Fatigue Pre-Cracked Samples Showing Varying Degrees of Microvoids in Terms of Number and Shape



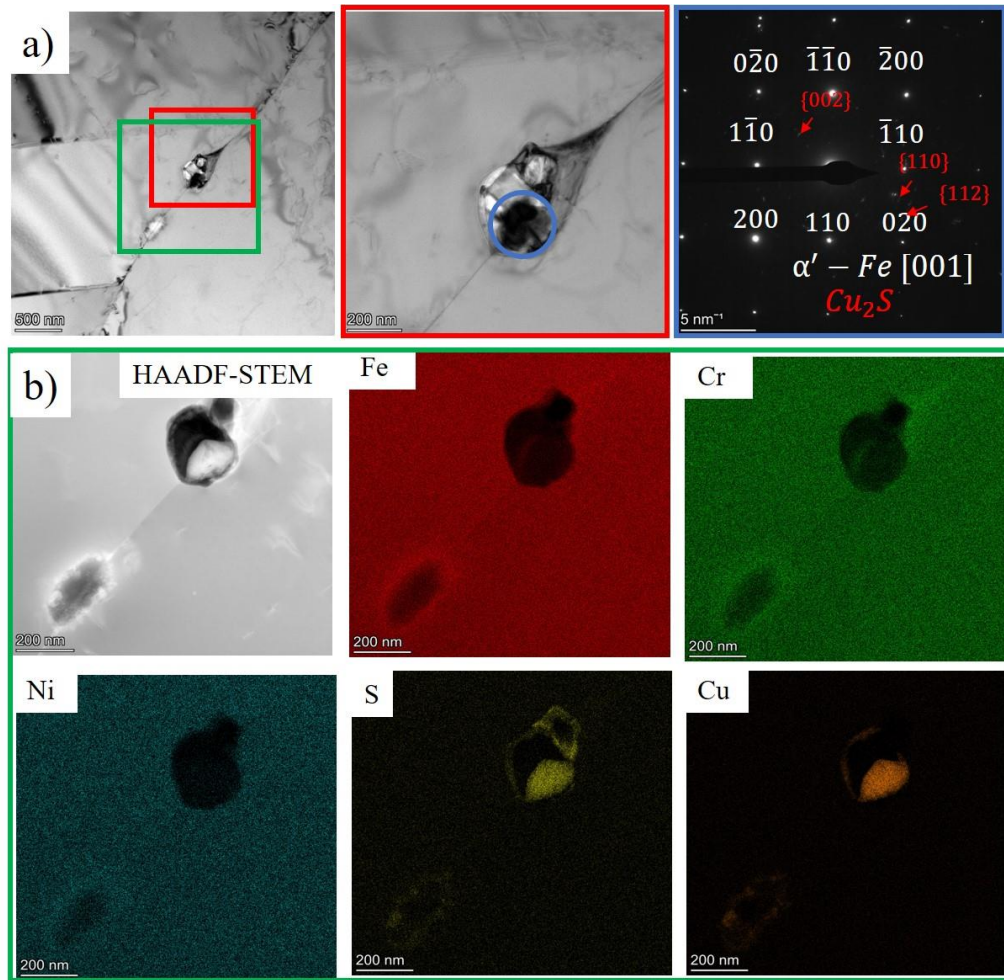


Figure 66: a) Bright Field Transmission Electron Microscopy Micrograph of a Void and Precipitate Identified as Cu_2S by the Selected Area Electron Diffraction Pattern and the Chemical Maps Shown in b)

Comparing the area density of the precipitates in the as-received materials to the volume density of microvoids found in the fatigue pre-cracked samples as shown in **Table 28** reveals that area density is larger than the volume density. Additionally, the volumetric density is an order magnitude higher in the commercial-304 sample compared to 304H even though each sample has a similar area density of precipitates. This inconsistency points to the fact that some types of precipitates are preferentially making more of the microvoids.

Table 28: Comparing Volumetric Density of Microvoids in Fatigue Pre-Cracked Samples to the Area Density of Precipitates in the As-Received Materials

Sample	Volumetric Density (mm ³ /mm ³)
304 Fatigue	0.00107
304H Fatigue	0.0000590
304L Fatigue	0.0000406
Sample	Area Density (mm ² /mm ²)
304 As-Received	0.00646
304H As-Received	0.00342
304L As-Received	0.00166

Other researchers have found void formation in aluminum based alloys and copper as a result of fatigue [43-46]. In the case of the aluminum alloys, void formation was found at the interfaces between incoherent precipitates and the matrix [44, 45]. In fact, Chen et al. found in their *in situ* SEM fatigue experiment on an aluminum alloy known as 2523-T3 that the voids became larger with an increase in the fatigue crack [45]. Chen theorized that debonding occurs between the incoherent precipitates and the matrix which leads to void nucleation [45]. The differences in the elastic modulus between the matrix and the incoherent particles can indeed lead to debonding [46]. These voids can continue to grow until a crack passes through them and causes them to stop growing as a result of stress relaxation from the crack [45]. Sunder et al. found that the microvoids, in an aluminum alloy known as 2014-T6511 and 2024-T3, were preferentially found when the stress intensity (ΔK) was higher [46].

In the case of the 304 samples, nucleation of voids at the interfaces of precipitates is possible due to the inclusions that form in austenitic stainless steels. Inclusions such as manganese sulfide as well as $M_{23}C_6$ carbides are since they were observed in the as-received matrix in chapter 2. A factors that could be contributing to the microvoid formation is the differences in elastic modulus between the precipitate and the matrix. **Table 29** shows values for the elastic modulus of 304SS and some of the precipitates. The table shows that the sulfide-based precipitates have a lower elastic modulus compared to the that of the matrix while $Cr_{23}C_6$ has an elastic modulus which is higher compared to the matrix. The lower elastic modulus indicates that these precipitates strain more under an applied stress compared to both the matrix and $Cr_{23}C_6$. The extra strain could lead to more debonding at the interfaces and lead to void formation.

Table 29: Elastic Modulus of 304SS and Various Precipitates found in As-Received 304SS Samples

Precipitate/Sample	Elastic Modulus (GPa)	Source
Commercial 304	193	[47]
$Cr_{23}C_6$	355	[48]
MnS	95	[48]
Cu_2S	62	[48]

To prove that more sulfides were present in the commercial-304 sample compared to the 304H and 304L, the x-ray diffraction spectrum of the as-received materials can be used. For MnS, the highest intensity peak is the (111) reflection which would have a peak at a 2θ of 3.05° . **Figure 67** shows the x-ray diffraction spectrums from 2.8° to 3.2° to evidence the peak at 3.05° . Only the commercial-304 sample contained a large enough peak to be visible above the background. Although this peak is not clearly evident in the 304H and 304L samples, these samples which

showed sulfur containing precipitates in the as-received state just have a lower volume fraction of MnS in the matrix.

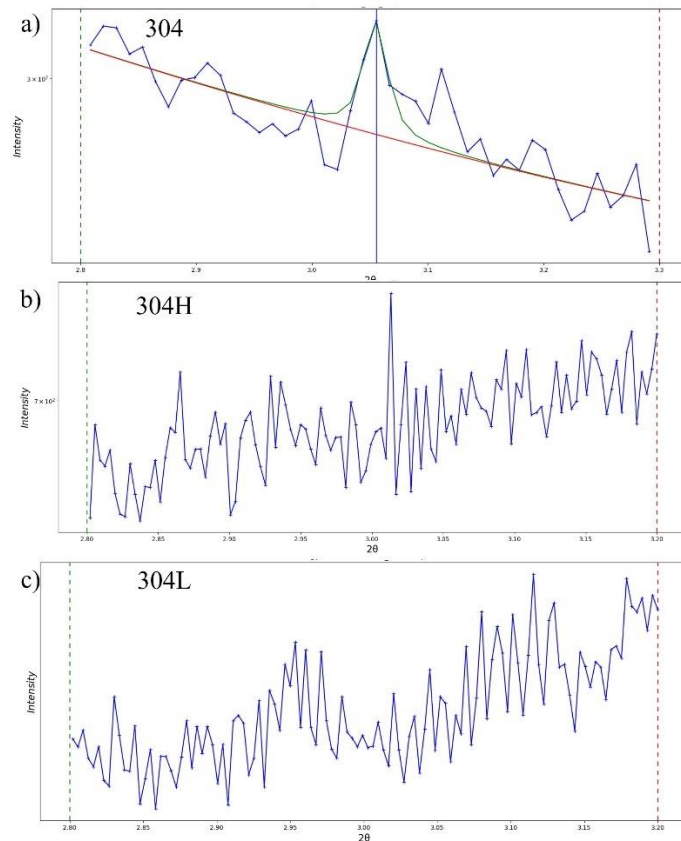


Figure 67: Synchrotron X-Ray Diffraction Spectrums Showing MnS (111) Peak in a) Commercial-304 and not in the b) 304H or c) 304L Materials

The shape of the inclusion also have an impact on the type of voids that formed. From the SEM images in **Table 7**, elongated precipitates were evident in the 304H sample. The elongated precipitates could explain the elongated voids that were seen in the tomograph of the 304H sample. Likewise, elongated precipitates that are most likely located in the commercial-304 sample could have resulted in the horizontal voids. The precipitates in these two samples were most likely elongated along two different directions.

The role of the micro voids in the propagation of a fatigue crack has been known to affect the earlier fatigue crack life [44, 45, 49]. These voids act as smaller cracks which can concentrate stress [44]. Chen et al. was able to show that the cracks followed the voids early in the crack life and would split into multiple cracks to transverse the local voids in the immediate area [45]. The growth of a crack by the growth and coalescence of microvoids has been thought to be the mechanism of crack growth in aluminum alloys which show microvoids interacting with cracks [44]. Understanding the role of microvoid on the overall materials fatigue life is also an important consideration. Researchers such as Guerchais et al. have found that defects such as voids can lower the fatigue limit of the material [49]. In fact, the researchers found that increasing the size of the voids led to an even lower fatigue limit [49]. In testing the effects of void size, Guerchais did not find any critical void size in which the presence of the void did not impact the fatigue limit; although, the smallest void size that was tested had a diameter of 95 μm which is much larger than the voids that were encountered in this study [49].

The formation of these voids in the 304H-FE-20K_o-80C-55% and the 304L-FE-18K_o-80C-55% may have influenced the formation of the vertical cracking which was evident in both tomographs. The act of fatigue pre-cracking generated some microvoids at the interfaces of precipitates and the matrix. The individual voids which formed initially were most likely smaller than the resolution of the scan i.e. around 10 μm . Putting these samples under load generated a stress field within the material to which microvoids may have combined to become larger and thus could be evidenced using the tomography setup. The directionality of the pre-existing precipitates in the loading direction influenced the directionality of the voids and thus lead to the appearance of vertical cracks. Had the pre-existing precipitates in the commercial-304 sample been in the

loading direction instead of the thickness direction, vertical cracks may have appeared in the commercial-304 samples.

4.1.2 Deformation Induced Martensite

From the diffraction scans of the as-received materials and the fatigued materials, fatigue appeared to have induced some martensitic transformation as indicated by the decrease in the austenitic phase. Both the ϵ -Fe phase and the α' -Fe phase increased with a larger increase in the α' -Fe phase. Other researchers have shown an increase in martensite but differ in the type of martensite that is formed [36, 39, 50]. Pegues et al. performed cyclic strain based fatigue on samples of 304L and found an increase in α' -Fe and did not find any indication of ϵ -Fe [36]. Meanwhile, Nikulin et al. performed similar studies on other austenitic steels with varying compositions [39, 50]. Specifically, Nikulin studied Transformation Induced Plasticity (TRIP) and Twinning Induced Plasticity (TWIP) alloys with compositions of Fe-30Mn-(6-x)Si-xAl and Fe-15Mn-10Cr-8Ni-xSi [39, 50]. In both alloys, ϵ -Fe was found to have formed after fatigue with varying amounts depending on the amount of aluminum and silicon in the alloys [39, 50]. The obvious difference between the materials studied by Pegues and Nikulin was the composition of the alloy. Varying the concentration of specific elements like aluminum and silicon can alter the Stacking Fault Energy (SFE) [39, 50]. SFE is one of the factors that has been found to play a crucial role in terms of the deformation mechanisms that a material will undergo [39]. A SFE between 18-20 mJ/m² leads to more ϵ -Fe transformation while a SFE between 18-45 mJ/m² shows mechanical twinning [39]. Above a SFE of 45 mJ/m², dislocation slip is more prevalent while ϵ -Fe transformation is hindered by the high energy cost to change the stacking order from the austenitic FCC structure to the ϵ martensite HCP structure [39].

Several empirical equations found in literature [51-55] can be used to estimate the stacking fault energy of an alloy based on its chemical composition. **Table 30** shows the results of the estimated stacking fault energies of the commercial-304 and the higher purity 304H and 304L alloys using the empirical equations. The SFE present in **Table 30** show a wide range of energies from the low estimations of the Ojima model to the high estimation of Rhodes model while the other models fall somewhere between. From the phase fraction analysis of the 304H sample, the increase in the amount of ε -martensite which would suggest that the STE would most likely be slightly above 20 mJ/m² since both types of structures formed. In terms of α' -Fe formation, two pathways have been suggested including the $\gamma \rightarrow \varepsilon \rightarrow \alpha'$ and the $\gamma \rightarrow \alpha'$ [36]. Pegues discussed how the pathway can dictate the way α' -Fe appears in the austenitic grains under TEM observations [36]. Through the pathway of $\gamma \rightarrow \varepsilon \rightarrow \alpha'$ the α' -Fe appears more lathe-like in structure while more block-like and irregular through the direct formation from γ -Fe. It is more likely that a combination of both mechanisms led to the increase in α' -Fe. Moreover, the reversible reaction of $\varepsilon \rightarrow \gamma$ is also possible; however, this tends to happen at lower SFE [50].

Table 30: Calculated Stacking Fault Energies of 304L, 304H, and Commercial-304 using Various Empirical Models

Model	Material		
	304L (mJ/m ²)	304H (mJ/m ²)	304 (mJ/m ²)
Schramm	18.61	18.15	19.91
Rhodes	44.67	41.28	35.67
Pickering	21.14	29.00	20.31
Ojima	15.47	15.363	15.93
Yonezawa	23.77	23.47	24.06

Looking closer into the location of martensite in the cracked single edge crack specimens reveals the possible roles of martensite as a retardation mechanism. For all the samples, most of the α' -Fe is found at the crack. The plastic deformation at the crack tip inside the plastic zone is most likely the cause of the increase in martensite in the area. The energy to cause phase transformation is an intrinsic mechanism which could reduce cracking rates [56]. The increase of martensite above and below the crack may also be working to retard crack growth. In materials like yttria stabilized zirconia, transformation from a monoclinic structure to a tetragonal structure occurs at the crack tip [56]. The crack then moves through the newly transformed material and the transformed material stays present along the crack wake [56]. The transformed tetragonal phase has a ~4% dilatation compared to the monoclinic phase and, as a result, provides a closure stress on the crack wake and effectively reduces the stress intensity [56]. The process of transformation toughening could be occurring in all three materials. Other studies have shown that the presence of α' -Fe actually decreases the fatigue life of the material during low cycle fatigue [50, 57]. Baudry and Pineau actually found the crack initiation and growth were accelerated when more α' -Fe was present [57], although more ductile materials tend to have a better low cycle fatigue and the transformation into a more brittle material such as α' -Fe would be expected to have negative effects [36, 39, 50]. High cycle fatigue is generally better for materials with a higher strength which the α' -Fe can provide [39].

4.2 What is the Role of Martensite as a Possible Intrinsic and Extrinsic Factor in Crack Retardation?

4.2.1 Intrinsic Factor

As discussed earlier, deformation induced martensite can form in 304SS and the amount of deformation induced martensite and the location of the martensite can play a

role in retarding crack growth. Mechanical cracking requires energy to create two new exposed surfaces and the plastic zone ahead of the crack. Phase transformation from metastable austenite to martensite would require extra energy and would thus increase the amount of energy needed to cause cracking mechanically [22]. The amount of deformation induced martensite can give some insight into the mode of cracking during CISCC (Mechanical or dissolution based). **Table 31, 32, and 33** shows the amount of deformation induced martensite formed during CISCC for the commercial-304 samples, the 304H sample, and the 304L samples, respectively.

Table 31: Phase Fraction Analysis for Commercial-304 Samples during Chlorine-Induced Stress Corrosion Cracking

Before						
	304-FE-40K ₀ -80C-55% (0 hr)			304-CL-46K-50C-55% (0 hr)		
	γ-Fe	α'-Fe	ε-Fe	γ-Fe	α'-Fe	ε-Fe
Above Crack	93.43	5.7	0.86	96.96	2.25	0.79
At Crack	86.69	11.62	1.67	87.9	11.21	0.89
Below Crack	91.24	7.85	0.89	96.82	2.78	0.41
Total	91.13	7.81	1.05	93.89	5.41	0.7
End						
	304-FE-40K ₀ -80C-55% (13.26 hr)			304-CL-46K-50C-55% (5.63 hr)*		
	γ-Fe	α'-Fe	ε-Fe	γ-Fe	α'-Fe	ε-Fe
Above Crack	88.16	10.4	1.42	90.99	7.54	1.48
At Crack	94.07	4.65	1.27	91.62	7.82	0.56
Below Crack	88.46	10.1	1.43	93.84	5.03	1.13
Total	89.66	8.94	1.39	92.15	6.79	1.06

*Scan before Fracture

Table 32: Phase Fraction Analysis for the 304H Sample during Chlorine-Induced Stress Corrosion Cracking

Before			
	304H-FE-20K _o -80C-55% (0 hr)		
	γ -Fe	α' -Fe	ε -Fe
Above Crack	96.91	1.85	1.23
At Crack	94.97	3.89	1.13
Below Crack	89.86	8.87	1.26
Total	94.05	4.73	1.2
End			
	304H-FE-20K _o -80C-55% (19.91 hr)		
	γ -Fe	α' -Fe	ε -Fe
Above Crack	97.92	1.86	0.2
At Crack	92.73	6.4	0.85
Below Crack	93.63	4.12	2.23
Total	93.88	4.18	1.93

Table 33: Phase Fraction Analysis for the 304L Samples during Chlorine-Induced Stress Corrosion Cracking

Before									
	304L-CL-30K-80C-55% (0 hr)			304L-FE-18K _o -80C-55% (0 hr)			304L-CL-43K-50C-55% (0 hr)		
	γ -Fe	α' -Fe	ε -Fe	γ -Fe	α' -Fe	ε -Fe	γ -Fe	α' -Fe	ε -Fe
Above Crack	98.16	1.75	0.1	96.62	1.71	1.65	98.7	1.04	0.26
At Crack	95.51	4.17	0.31	93.14	5.29	1.55	95.27	4.44	0.29
Below Crack	97.58	2.21	0.21	94.9	1.75	3.34	98.92	0.92	0.16
Total	97.09	2.71	0.21	94.94	2.85	2.19	97.63	2.13	0.24
End									
	304L-CL-30K-80C-55% (11.03 hr)			304L-FE-18K _o -80C-55% (11.26 hr)			304L-CL-43K-50C-55% (4.13 hr)*		
	γ -Fe	α' -Fe	ε -Fe	γ -Fe	α' -Fe	ε -Fe	γ -Fe	α' -Fe	ε -Fe
Above Crack	97.7	2.04	0.26	97.22	1.25	0.84	94.58	5.02	0.4
At Crack	97.82	2.12	0.06	95.73	3.47	0.79	91.06	8.66	0.28
Below Crack	96.6	2.99	0.41	97.83	1.35	0.81	94.94	3.66	1.39
Total	97.37	2.38	0.24	97.22	1.95	0.81	93.53	5.78	0.69

*Scan before Fracture

As a reference, the phase fraction analysis for the as-received and fatigue pre-cracked samples is shown in **Table 34** while the final scan before and after final fracture for the two samples which experienced final fracture is shown in **Table 35**. Both the fatigue pre-cracked samples and the final fracture samples are examples of mechanical fracturing and thus can serve as a reference to the type of deformation induced martensite changes that could be expected. For the process of fatigue, the change in the amount of deformation induced martensite (α' -Fe + ε -Fe) was around 7.48%, 4.07%, and 3.06% for the commercial-304, 304H, and 304L materials, respectively. Likewise, both 304-CL-46K_o-50C-55% and 304L-CL-43K_o-50C-55% samples did reach the final stage of SCC in which mechanical cracking caused a large portion of phase transformation. In fact, the difference was around 11.44% and 20.77% for the 304-CL-46K_o-50C-55% and 304L-CL-43K_o-50C-55% samples, respectively. It should be noted that the majority of the transformed material was in the form of α' -Fe which may have come from the direct transformation from austenite ($\gamma \rightarrow \alpha'$) or from epsilon martensite ($\gamma \rightarrow \varepsilon \rightarrow \alpha'$) as was discussed in the previous section. During CISCC, the amount of transformed material between all samples was around 1.67%. The highest amount of transformed material was in the 304L-CL-43K_o-50C-55% with a total of around 4.1%; however, this was the difference between the fatigued pre-cracked state and the scan right before final fracture. In some cases, the amount of martensite went down like in the 304L-FE-18K_o-80C-55% and the 304L-CL-80C-55%. It should be noted that more martensite forms at lower temperatures [58] which could be used to explain the more martensite forming due to the room temperature fatigue. Additionally, the higher rate of martensite transformation in the samples tested at 50 °C compared to 80 °C is explained by the temperature effect on transformation. The small changes in the amount of deformation martensite produced during CISCC compared to the fatigue pre-cracking and final fracture suggest that the mechanism

for CISCC may either be deforming in other ways i.e. dislocation motion or the mechanism may not involve mechanical cracking at all. Additionally, deformation induce martensite would not be serving as an intrinsic factor in slowing the crack growth rate.

Table 34: Phase Fraction Analysis for As-Received and Fatigue Pre-Cracked State of 304SS Samples

	304 As-Received			304H As-Received			304L As-Received		
	γ -Fe	α' -Fe	ε -Fe	γ -Fe	α' -Fe	ε -Fe	γ -Fe	α' -Fe	ε -Fe
	98.62	1.29	0.09	99.16	0.52	0.32	98.02	1.84	0.14
	304 Fatigue Pre-Cracked			304H Fatigue Pre-Cracked			304L Fatigue Pre-Cracked		
	γ -Fe	α' -Fe	ε -Fe	γ -Fe	α' -Fe	ε -Fe	γ -Fe	α' -Fe	ε -Fe
Above Crack	93.43	5.7	0.86	96.91	1.85	1.23	96.62	1.71	1.65
At Crack	86.69	11.62	1.67	94.97	3.89	1.13	93.14	5.29	1.55
Below Crack	91.24	7.85	0.89	89.86	8.87	1.26	94.9	1.75	3.34
Total	91.13	7.81	1.05	94.05	4.73	1.2	94.94	2.85	2.19

Table 35: Phase Fraction Analysis for Fractured Samples

	Before Final Fracture					
	304-CL-46K-50C-55% (5.63 hr)			304L-CL-43K-50C-55% (4.13 hr)		
	γ -Fe	α' -Fe	ε -Fe	γ -Fe	α' -Fe	ε -Fe
Above Crack	90.99	7.54	1.48	94.58	5.02	0.4
At Crack	91.62	7.82	0.56	91.06	8.66	0.28
Below Crack	93.84	5.03	1.13	94.94	3.66	1.39
Total	92.15	6.79	1.06	93.53	5.78	0.69
	After Fracture					
	304-CL-46K-50C-55% (6.88 hr)			304L-CL-43K-50C-55% (5.63 hr)		
	γ -Fe	α' -Fe	ε -Fe	γ -Fe	α' -Fe	ε -Fe
Above Crack	78.83	17.95	3.22	75.22	23.32	1.46
Below Crack Total	82.59	14.67	2.74	70.3	25.73	3.97
Total	80.71	16.31	2.98	72.76	24.53	2.71

4.2.2 Extrinsic Factor

Like the intrinsic factor that deformation induced martensite may have played, the extrinsic factor also serves to retard crack growth. The extrinsic mechanism, known as transformation toughening, works behind the crack at the crack wake [22]. Deformation induced martensite, formed at the crack tip due to the high tension, has a slight elation compare to austenite. As the crack propagates, the deformation induced martensite stays behind in the crack wake where it can close the crack (since the material is now dilated) and reduce the stress intensity at the crack tip. Determining the possibility of transformation toughening occurring during this experiment requires a look into the literature to define the characteristics of this mechanism.

For transformation toughening, it is mostly observed in ceramics like zirconia [22, 59]. A study by Touaiher et. al on different types of zirconia ceramics with various amounts of impurities found that a larger transformed zone could give the material more resistance to cracking [59]. A Vickers hardness test using a load of 300 N was conducted and the size of the transformed zone was measured. **Figure 68** shows a resistance curve with crack length for a composite with a larger transformation zone (MT for medium transformability) and a smaller transformation zone (LT for low transformability). Intuitively, this observation makes sense since more transformed material will provide more strain in the material and will lower the stress on the crack wake and tip. This observation indicates that the more deformation induced martensite created, the higher the resistance is to cracking.

A high percent (nearly 100%) of transformed material has been found experimentally in a zone in the crack wake of about 20 μm for partially stabilized zirconia [22]. The scans we conducted were 100 μm above the crack which would mean a 20% by volume transformation into deformation induced martensite would give similar resistance to those materials known for

transformation toughening. The amount of deformation induced martensite in this experiment only got up to those values of 20% when complete fracture occurred as shown in **Table 35**. This information would indicate that deforming induced martensite during CISCC may not be playing a very dominant role in the mechanism of crack retardation. A remaining question regarding transformation toughening would be to determine if performing the experiment without fatigue pre-cracking would impact the degree of transformation caused by CISCC.

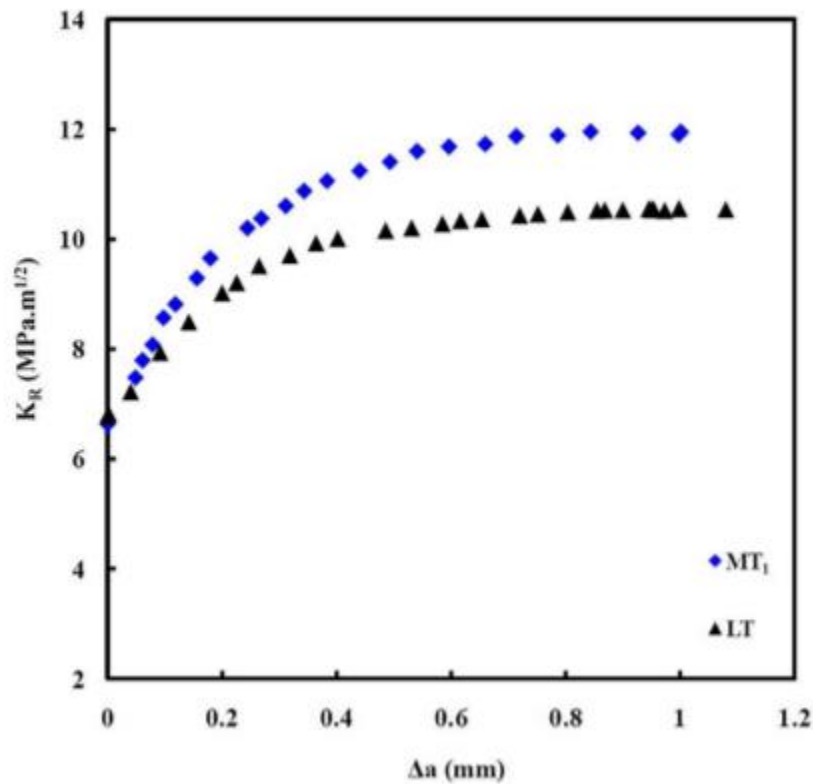


Figure 68: Crack Resistance Curve of Two Zirconia based Materials with a Medium Transformability (MT) and a Low Transformability (LT) [59]

4.3 How does the Stress Intensity Affect the Rate and Morphology of Cracks?

4.3.1 Stress Intensity Effect on Rate

According to the literature, stress intensity can play a varying role in the crack growth rates of CISCC depending on the stage of cracking [3]. Stress intensity has a large impact on early and late stages of cracking whereas the effect is almost negligible in the steady state regime as was shown in **Figure 4**. The crack growth rate plots as a function of stress intensity are all shown in **Figure 69**. In general, our data showed a certain degree of scattering with increasing stress intensity with about an order of magnitude in cracking rates above and below the average. Increasing the stress intensity did not show an upward or downward trend in the data.

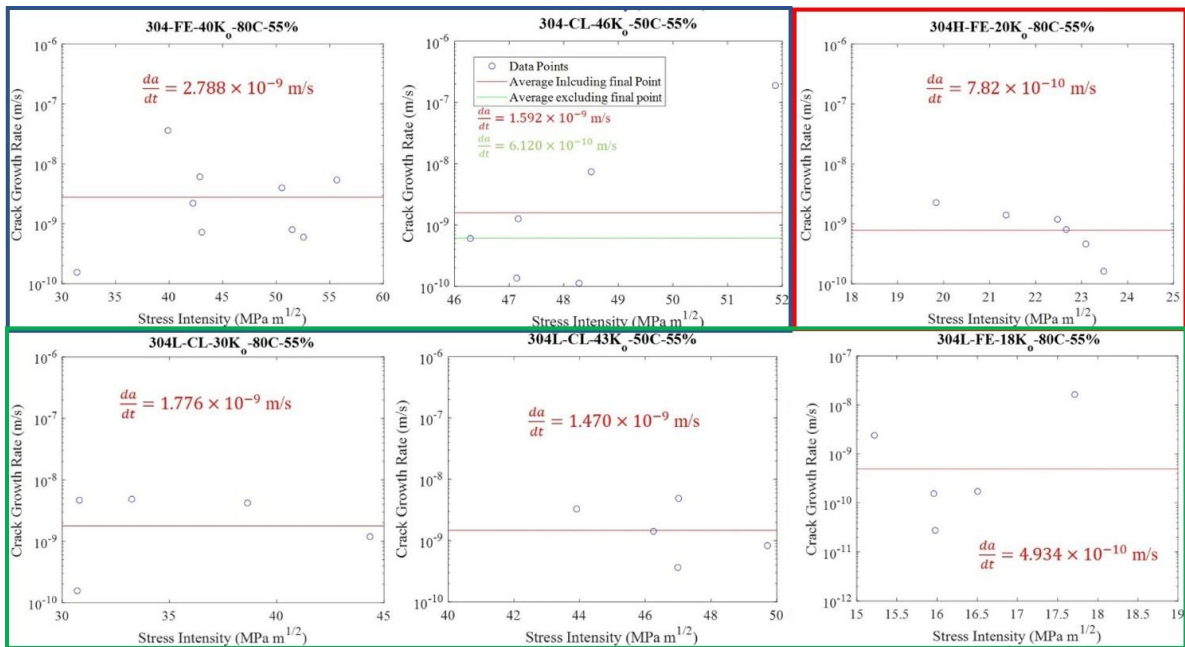


Figure 69: Crack Growth Rate as a Function of Stress Intensity for Commerical-304 Samples (Blue Box), the 304H Sample (Red Box), and the 304L Samples (Green Box)

Regardless of the 304 heat, the cracking growth rate at 80 °C was found to consistently have an average cracking rate on the order of 10^{-9} m/s except for when the stress intensity was too

low like for the cases of 304H-FE-20K_o-80C-55% and 304L-FE-18K_o-80C-55%. The low stress intensity may be in the first stage of SCC and the stress intensity was in a fixed extension loading scheme meaning the stress intensity would decrease with increasing crack growth. These results appear to be consistent with the notion that crack growth rate is relatively constant as a function of stress intensity [3]. However, there are some environments which some authors have found have a dependence of crack growth rate on stress. For example, Terachi et al found 316SS in simulated pressurized water reactor primary water shows a slightly higher crack growth rate at higher stress intensities as shown in **Figure 70**.

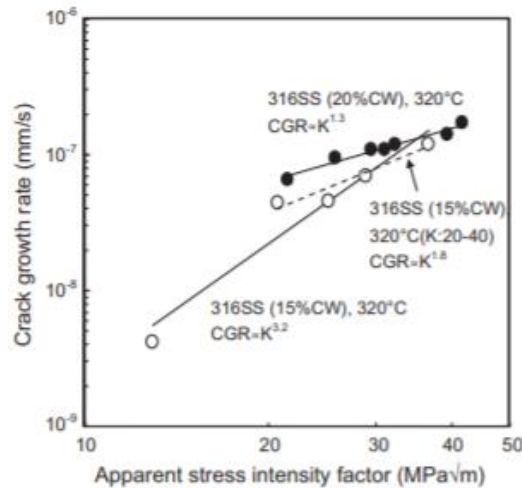


Figure 70: Effect of Apparent Stress Intensity on the Crack Growth Rate of 316SS in Simulated Pressurized Water Reactor Primary Waters Showing an Increase in Crack Growth Rate with Stress Intensity [23]

4.3.2 Stress Intensity Effect on Morphology

In terms of cracking morphology, experiments showed a range of morphologies as shown in **Figure 71**. For example, the 304-FE-40K_o-80C-55% sample shown in **Figure 71c** showed macrobranching where the crack towards the surface of the material was split into two distinct

directions. Microbranching was evident in the 304L-CL-30K_o-80C-55% sample as evident in **Figure 71b**. All other samples appeared to remain as one crack notably the 304H-FE-20K_o-80C-55% and 304L-FE-20K_o-80C-55% sample showed vertical cracking which was explained as a result of fatigue voids combining along the precipitates with directionality to the loading direction.

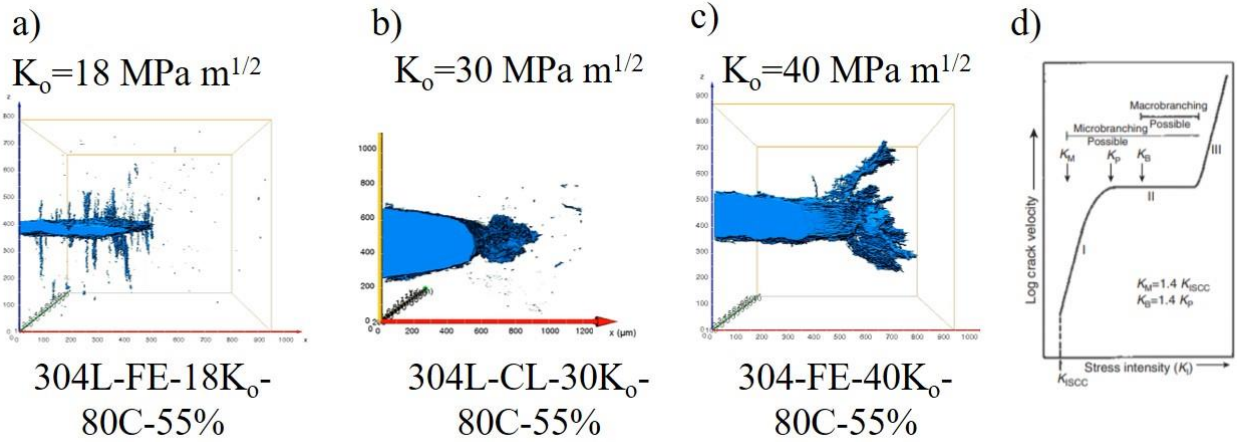


Figure 71: Different Crack Morphologies in Different Samples with a) Low Stress Intensity (Monocrack), b) Medium Stress Intensity (Micobranching), and c) High Stress Intensity (Macrobranching) compared to d) Branching in Literature [20]

These cracking behaviors show a relation to the stress intensity. To explain why branching occurred, fracture mechanics was used to visualize the principal stresses and strains around the crack tip. One factor that was investigated in terms of causing crack branching was the initial stress intensity that the sample was subject to at the beginning of the experiment. As stated earlier, the sample was brought up to a specific load and left in constant extension so that the stress on the sample would decrease with crack growth. To ascertain the shape and relative magnitudes of the stresses and strains around the crack tip, finite element analysis was performed. Plugging in the initial conditions into ABAQUS software resulted in the branching shape that the principal stress took as evident in **Figure 72a**. Comparing this result when a stress intensity of 40 MPa m^{1/2} is used to a similar simulation with a stress intensity of 20 MPa m^{1/2} illustrates the roles of the stress

intensity in the shapes of the principal stresses and strains as shown in **Figure 72b**. The lower stress intensity has a more confined maximum principle stress shape whereas doubling the stress intensity gives more of a branching shape. It has been discussed in [60] that a higher initial stress intensity before a crack starts propagating can often lead to branching. In fact, different types of branching have been found to occur based on the stress intensity where lower stress intensities can undergo microbranching (smaller than average grain size) and higher stress intensities can give way to macrobranching (larger than average grain size) as shown in **Figure 71d** [20]. The observations of macrobranching in 304-FE-40K_o-80C-55% at a higher stress intensity and microbranching seen on the 304L-CL-30K_o-80C-55% at a lower stress intensity is supported in literature [20].

It should be pointed out that due to the small geometry of the sample (Thickness b in the direction of the crack front), a plane stress condition is more valid than a plane strain condition as illustrated by **Figure 72c**. A plane stress condition increases the K_{IC} and K_{ISCC} values due to the increases plastic zone size [61]. To be in a plain strain condition according to the stress intensity approach and the J-integral approach, a sample would need to be about 504 mm and 63.4 mm in thickness, respectively [61-63]. This means that the material might behave differently depending on the conditions of plane stress and strain acting on the sample. Towards the edges of the sample, the stress normal to the surface must be zero which gives a plane stress condition as shown in **Figure 72c**. Towards the middle of the crack, a plane strain condition arises and there must be a transition from plane stress to plane strain [7]. Reducing the thickness of the material ultimately reduces the area of the plane strain condition which results in the increase toughness of the sample [6]. It has been theorized elsewhere [19] that crack branching could happen on the surface compared to the hindered bulk material.

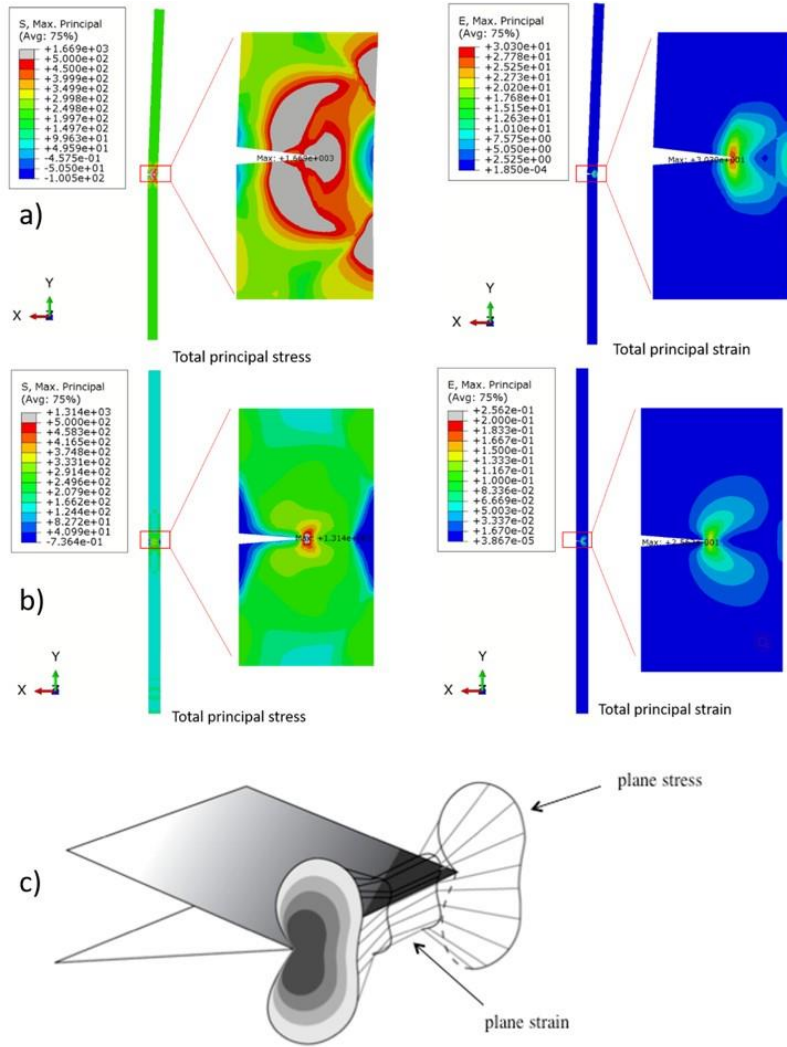


Figure 72) a) FEA Simulation with a Stress Intensity of about $40 \text{ MPa m}^{1/2}$, b) $20 \text{ MPa m}^{1/2}$, and c) Diagram of Plane Stress and Strain on Sample [61]

On the surface, the plane stress condition is present and leads to a larger plastic zone. Another factor that might have played a role in branching towards the surface of the 304-FE-40K_o-80C-55% sample is pitting from the MgCl₂ salt. Pitting on the surface combined with the stress in the plastic zone of the crack could have made it easier for cracking to occur along the surface. **Figure 73** shows optical microscopy of the surface of the materials and discoloration from corrosion is clearly evident around the areas where branching occurred.

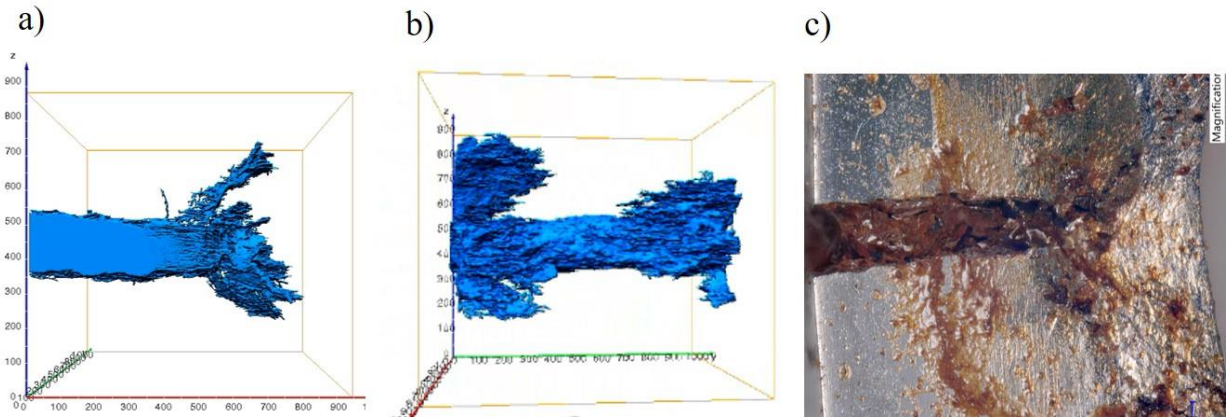


Figure 73: Tomography of Final Scan of 304-FE-40K_o-80C-55% at Different a) and b). c) Optical Microscopy of Final State of 304-FE-40K_o-80C-55% Sample showing Possible Pitting on Location of Branching

Although micro- and macrobranching were apparent at initial stress intensities of $30 \text{ MPa m}^{1/2}$ and $40 \text{ MPa m}^{1/2}$, no branching was evident for the 304L-CL-43K_o-50C-55% and the 304-CL-46K_o-50C-55% samples. Although these samples were tested at a lower temperature, it is more likely that the samples themselves did not have enough time to branch due to a combination of the large cracks and the stress intensity reaching K_{IC} before branching could occur. As seen in **Figure 74**, there was a duration of time where the 304-FE-40K_o-80C-55% sample was a single crack. The 304-FE-40K_o-80C-55% sample only started branching around 5.88 hours. The 304L-CL-43K_o-50C-55% and the 304-CL-46K_o-50C-55% samples only lasted around 4.5 hours and 6.78 hours, respectively, and it's unclear if temperature plays a role in the duration of a single crack. It was noted by Burnett et al. that branching is possible but does not always occur [20].

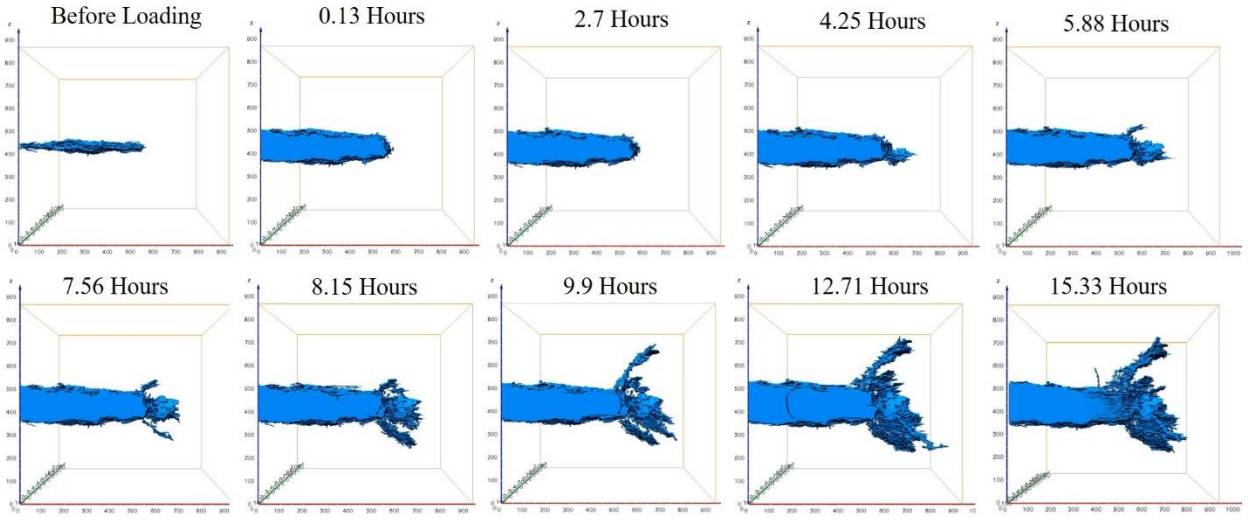


Figure 74: Tomographs of Progression of 304-FE-40K_o-80C-55% Sample Showing a Single Crack Until around 5.88 Hours

4.3.3 How does Crack Branching Influence the Steady State Propagation Rate?

With sample with and without branching, an important question regarding its role on steady state propagation rates can be assessed. From the crack growth rate plots in **Figure 69**. There does not appear to be an upward or downward trend in the data when branching was not evident and evident as can be seen looking at 304L-CL-43K_o-50C-55%, 304-CL-46K_o-50C-55%, 304-FE-40K_o-80C-55%, and 304L-CL-30K_o-80C-55% samples. These result would appear to suggest that the steady state cracking rate does not depend on crack branching. This would indicate that something else in the mechanism of CISCC is the rate limiting step in causing the steady state regime.

4.4 What Role does Temperature Play on Crack Growth Rates?

4.4.1 Effect of Temperature on Crack Growth Rate

Performing the experiments at both 50 °C and 80 °C gave some insight into the possible effect of temperature in CISCC on the cracking rates and morphology. According to literature, temperature can increase the crack growth rate since it can alter the rate of the limiting step [3, 23]. In atmospheric corrosion cases, temperature can increase or decrease stress corrosion cracking rates because the temperature relies also on the relative humidity to create a thin film of brine. For example, increasing the temperature can cause the rates of corrosion, diffusion, etc. to increase but doing so reduces the amount of liquid in the thin film as more water can exist in the air. To combat this issue, our experiment was done at a constant relative humidity so that the equilibrium between the water in the thin film and in the air were the same regardless of temperature. From **Figure 69**, the effect of temperature on the crack growth rate is apparent. In the 304L samples comparing 304L-CL-30K_o-80C-55% with 304L-CL-43K_o-80C-55%, a decrease in the crack growth rate by a factor of 20% was found when dropping the temperature from 80 °C to 50 °C. Likewise, the 304 commercial samples (304-FE-40K_o-80C-55% and 304-CL-46K_o-80C-55%) a decrease in the crack growth rate of 75% times (excluding the last data point due to being in the third stage of cracking) was found. An Arrhenius equation shown in **Equation 6** shows the relationship between temperature and crack growth rate.

$$\frac{da}{dt} = C e^{-\frac{Q}{RT}} \quad (6)$$

Crack growth rate ($\frac{da}{dt}$), is related to temperature (T) by this Arrhenius relationship where

C is a constant, Q is the activation energy, and R is the ideal gas constant. The activation energy was calculated for commercial-304 and 304L since both temperatures of 80 °C and 50 °C were tested. It should be noted that the 304L-FE-18K_o-80C-55% case was not used since there was

reason to believe that sample was still within stage 1 of cracking and the Arrhenius equation is for the steady state regime. With two data points each for commercial-304 and 304L, a large degree of error is expected in the calculation. The activation energy calculated for 304L was 5.97 kJ/mol. For the commercial-304, an activation energy of 47.91 kJ/mol was calculated and the last data point for the 304-CL-46K_o-55% was ignored for the reason it represents a point in stage 3. From the literature, Tjayadi et. al who performed an experiment on sensitized 304H in simulated sea water from 22 °C – 60 °C found an activation energy of 60.9 kJ/mol [64]. Tjayadi related this activation energy to the diffusion of hydrogen into austenitic stainless steel as a result of dissolution by anodic and cathodic coupled reaction. The activation energy calculated for commercial-304 is close to this value while the one for 304L is very low. More data points would be needed in this study to have a better idea of what the activation energy is in this experiment. Terachi noted that activation energies tend to have some degree of error due to the variability in crack growth rate measurements [23]. If the commercial-304 activation energy is close to the actual activation energy, this activation energy would point to a dissolution-based model.

4.4.2 Effect of Temperature on Crack Morphology

The effect on temperature on the morphology of the crack can also be studied through these experiments. These experiments found branching at 80 °C for both commercial-304 and 304L with high enough stress intensity. At 50 °C, both the samples had sufficient stress intensity but did not branch and went into final fracture. The lack of branching at 50 °C might suggest that temperature has an effect on the crack morphology; however, it is more likely, as was explained in the effect of the stress intensity, that the samples simply broke before they had time to cause branching. In cases of branching in these experiments, there was a duration of initial time where the crack was

a single crack and after some time, started to branch. From the temperature effect on crack growth rate, it is reasonable to believe that branching could happen at lower temperatures if a long enough time is given for the sample to propagate. More experiments would need to be conducted to confirm this hypothesis. Although it's not stress corrosion cracking, an experiment performed by Sameljuk et. al did find that temperature can have an effect on the branching since temperature can ultimately alter the fracture toughness of the sample. Although it should be noted the experiment was a tensile test conducted on a chromium metal alloyed with 0.5% La_2O_3 with temperature ranging from -196 °C to 150 °C [65].

4.5 What is the Role of Chlorine and Chlorine Forming Compounds?

The experiment used MgCl_2 to “induce” or “assist” stress corrosion cracking as has been suggested by different studies [3-5, 9, 11, 18, 64]. The presence of chlorine does appear to be influential for the process of SCC in these conditions. In fact, the 304-CL-31K_o-80C-55% sample is the best example of the importance of chlorine. **Figure 75a** shows the tomograph of 304-CL-31K_o-80C-55%. From the tomograph, the crack was measured to only have grown about 1.84 μm which is very close to the resolution limit of the tomography detector. From the TEM of the crack tip, no chlorine was able to be found at the crack tip as was shown in chapter 3. This suggests that the crack may not have been opened enough to allow a sufficient amount of chloride solution to the crack tip region. Interestingly, pitting and to a certain extent, cracking did occur in this sample but on the other end of the specimen opposite the crack opening where salt deposition was observed. **Figure 75b** shows the results of the finite element analysis which was performed to simulate the 304-CL-31K_o-80C-55% sample. With a sufficient stress intensity, tension and compression regions appear on the opposite side of the crack opening. The compression region,

indicated with a green arrow, is right in line with the main crack. The regions above and below, marked with red arrows, show regions of tension. Salt on the surface of the 304-CL-31K_o-80C-55% sample caused pitting to occur since the entire sample was subjected to the simulated marine environment. The tensile stress present in the sample caused cracking in these regions. This sample illustrates that cracking can not occur under these conditions without chlorine i.e. Tensile stress + chlorine presence promotes crack growth; tensile stress without chlorine was not enough (in these experimental conditions) to induce cracking.

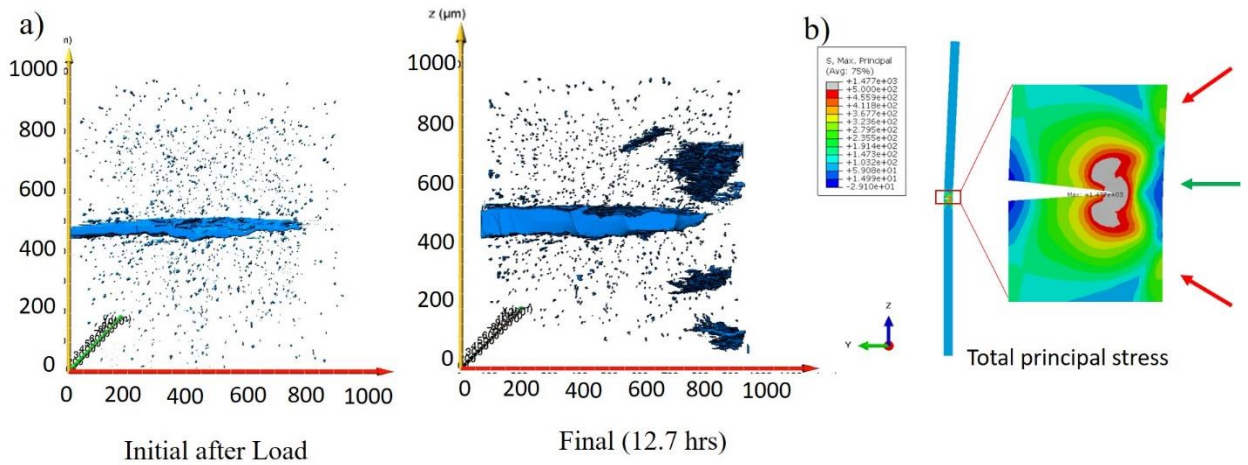


Figure 75: a) Tomographs of 304-CL-31K_o-80C-55% Sample initially after Load and the Final Scan and b) Abaqus Simulation of 304-CL-31K_o-80C-55% Sample

From the diffraction patterns and chemical maps taken of the 304-FE-40K_o-80C-55% which included the crack shown in **Figure 76**, various chlorine bearing compounds were found along with some oxides. The chlorine compounds include FeCl₂, CrCl₂, and NiCl₂·6H₂O. The formation of these chlorine compounds and the magnesium staying only on the surface of the crack and note overlapping with chlorine suggest that a reaction must have occurred.

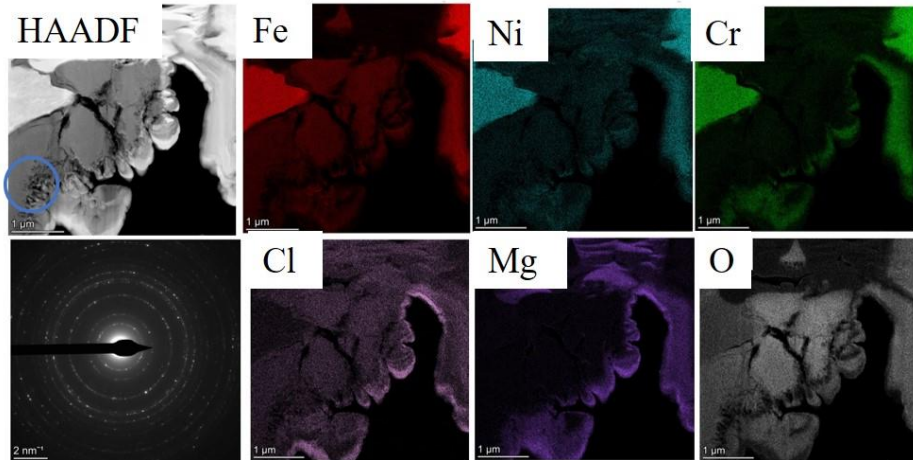


Figure 76: High Angle Annular Dark Field Micrograph, Selected Area Electron Diffraction Pattern, and Chemical Maps Illustrating the Presents of Chlorine and Oxygen Bearing Compounds around the Crack of 304-FE-40K_x-80C-55%

One question which may be raised is the effect the chloride salts have on the corrosion rate and whether they might be passivating like some types of oxide scales. A crude way to determine the possible protectiveness of the chlorine bearing compounds would be to obtain the Pillings-Bedworth ratio which looks at the volume mismatch between the oxide and the “possible protective layer” and determines if there is just the right amount of compression to be protective. Tension in the protective layer can result in cracks which would leave the metal exposed. Similarly, too much compression can result in cracks. Just the right amount of compression may indicate a protective layer has formed. A ratio between 1 and 2 is found to be ideal for a protective layer.

Equation 7 below shows the Pillings-Bedworth (PB) ratio equation.

$$R_{PB} = \frac{V_{Corrosion\ Layer}}{V_{Metal}} = \frac{M_{Corroion\ Layer}\rho_{metal}}{nM_{Metal}\rho_{Corrosion\ Layer}} \quad (7)$$

R_{PB} is the Pillings-Bedworth Ratio, $V_{Corrosion\ Layer}$ is the volume of the corrosion layer, V_{Metal} is the volume of metal, $M_{Corroion\ Layer}$ is the molar mass of the corrosion layer, ρ_{metal} is the density of the metal, n is the number of metal atoms in the corrosion layer formula (i.e. Fe_3O_4 has an $n=3$), M_{Metal} is the molar mass of the metal, and $\rho_{Corrosion\ Layer}$ is the density of the

corrosion layers. Putting in the values for 304SS and the chlorine bearing corrosion layer products, it was calculated that a PB ratio for FeCl_2 , CrCl_2 , and $\text{NiCl}_2 \cdot 6\text{H}_2\text{O}$ is 6.07, 5.71, and 17.64, respectively. These values suggest a large degree of compression which would have cracks in them to allow for additional corrosion of the metal.

One drawback to the ex situ characterization that was performed under the TEM is the change in the environment in which the sample exists. In the *in situ* setup, the sample was subjected to both elevated temperature (above 50 °C) and, most importantly, a relative humidity of 55-65%. A relative humidity of 55-65% is above the critical relative humidity (around 30%) to cause the salts to form a brine on the surface [11]. Taking the sample out of the corrosion chamber and subjecting it to the vacuum of the SEM and TEM chambers most likely caused the salt brines to disappear and leave behind the salt crystals which were observed under TEM observation. To try and explain the role of the chlorine based on the observations that were uncovered in this experiment, a look into the literature was conducted. Firstly, it has been established that the environment inside a crack can differ widely compared to the bulk solution [3]. As a result, the buildup of chlorine ions and other species may occur at the crack tip. A Pourbaix diagram can be used to predict the species which will be evident under different conditions of electrochemical potential and pH. **Figure 77** shows the Pourbaix diagram for iron in a solution of 0.1 M NaCl. Although this is not for the exact environment in this experiment, it can still be useful. According to Donahue and Burns, the crevice and crack like areas can have a pH as low as 1 in NaCl based solutions even as low as 10^{-6} M Cl^- [66]. The solution used in this experiment was a 500 g/L solution of MgCl_2 with a pH of 6.4 which is a 10.5 M Cl^- (enough chlorine to cause an acidic crack tip to form). Using the Pourbaix diagram at a pH of 1, the solution can either be in an active (corrosion occurs) or immune (no corrosion occurs) region depending on the electrochemical

potential. Since cracking did occur and iron bearing corrosion products were found, the setup was most likely in an active region inside the crack. A diagram of crevice corrosion in a Cl^- solution is shown in **Figure 78** could explain the environment seen at the crack.

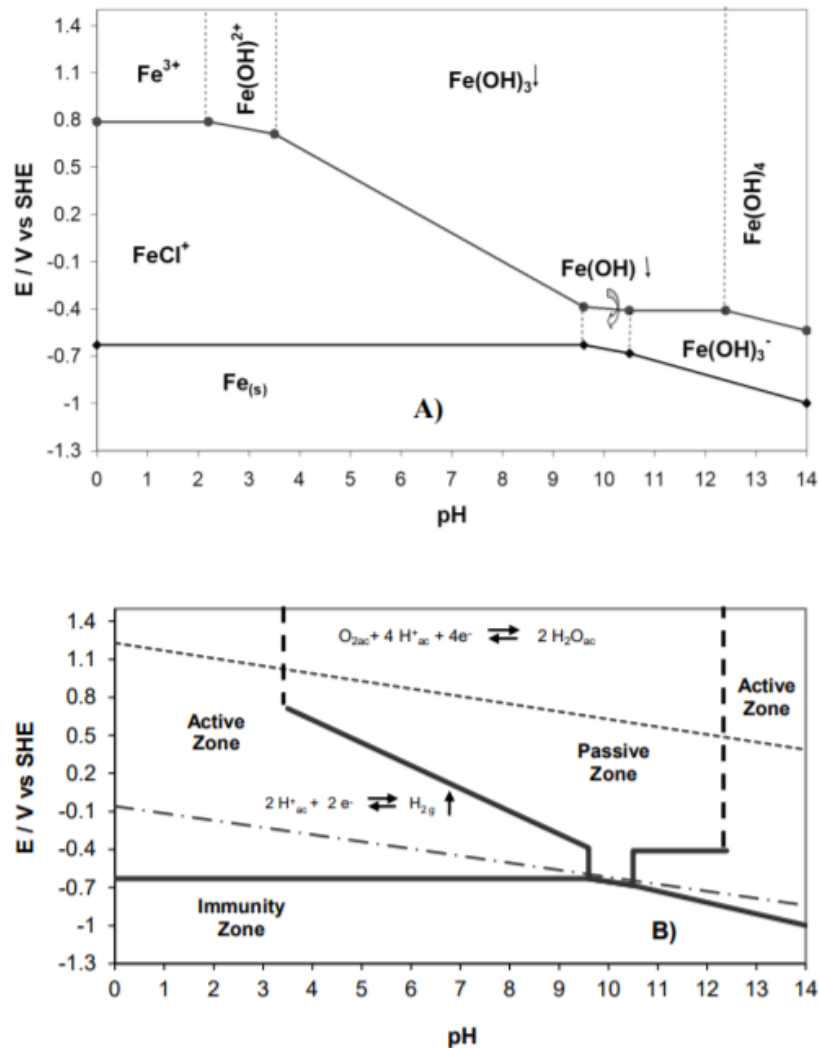


Figure 77: Pourbaix Diagram of Iron in a Solution of 0.1 M NaCl showing Active, Passive, and Immune Regions [67]

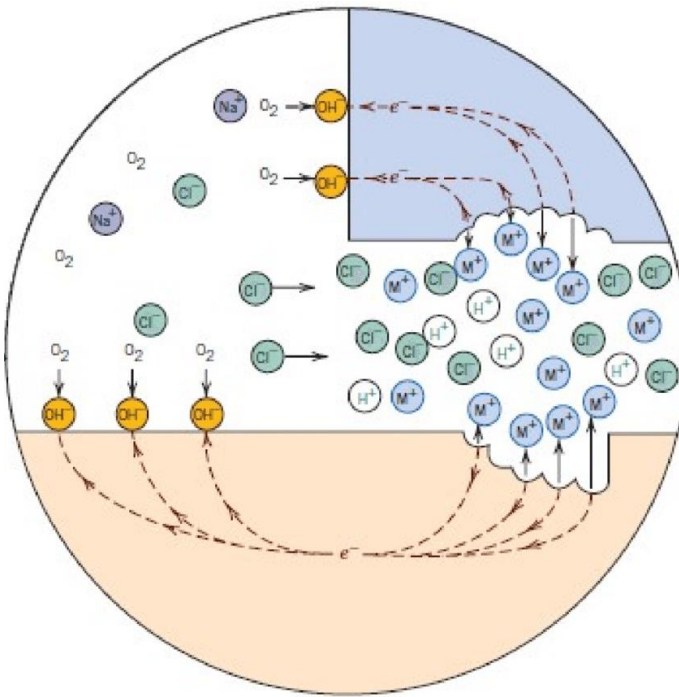
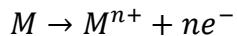
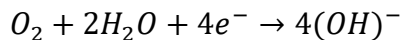


Figure 78: Crevice Corrosion of Metal in a NaCl solution [3]

The electrochemical diagram consists of two half-cell reactions. The anode portion (i.e. portion on the right side of **Figure 57**) has a reaction as follows:



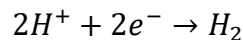
The cathode portion (Left portion of **Figure 57**) has the following reaction:



The concentration of chlorine ions in the crevice attracts positively charged H⁺ so there is no charge imbalance inside the crevice. It is known that both H⁺ and Cl⁻ can destroy protective films on metals [66].

Dissolution would be the mechanism that would most likely occur when chlorine ions are involved, especially since double the concentration of chloride ions is available with one molecule

of MgCl_2 . Another cathodic reaction which could be occurring would be the following according to Sipila et. al [68]

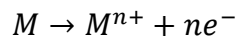


These electrochemical reactions could explain the dissolution of iron, chromium and nickel. These species fall into solution and will combine with the chlorine when the relative humidity drops below the critical relative humidity for deliquescence as seen in **Figure 76**. Meanwhile, the magnesium will combine with the forming hydroxide ions. Mg(OH)_2 is insoluble in water and thus precipitates out. When water is removed i.e. by the addition of heat or put into a vacuum chamber, Mg(OH)_2 breaks down into MgO which could explain the presence of the MgO on the outside of the crack.

4.6 What are the Mechanisms that are Operating on the Microstructural Level?

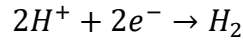
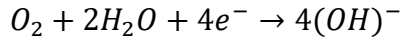
Based on all the experiments that were performed and the analysis, the following **Figure 79** is a depiction of the proposed mechanism of CISCC in 304SS. Salts first deposit on the material. Below a critical relative humidity to form a brine the salt remains solid. Above the critical relative humidity, water begins to deposit on the walls of the canister and mix with the salt to become a brine. Once the pitting potential is achieved, a pit starts to form, and the electrochemical reactions listed being to occur:

Anode:



Where M stands for metal ions like Fe, Cr, and Ni

Cathode:



The flux of positively charged metal ions attracts negative chlorine ions. The increasing concentration of chlorine acidifies the small area causing the anode to form at the base of the pit while the cathode remains the surface. With the addition of a non-compressive stress, the pit can form into a crack above K_{ICSCC} . A protective oxide starts to form on the walls of the crack wake while combination of the acidic crack tip and anodic potential leave the crack tip bare. The stress on the crack tip is used to hold the tip open for enough solution to contact the bare metal and to prevent any oxide layer from forming. Hydrogen is also formed and is able to ingress into the metal. As the crack propagates and opens, the material which used to be the crack tip now grows an oxide. Without the protective oxide, the current density would be the same everywhere and cause the crack to blunt. Once a stress intensity above that for microbranching (K_{Mi}) there is some stress to hold multiple short crack tips open. Crack branching is favorable at higher stress intensities since it reduces the stress at each crack. Above a higher stress intensity for macrobranching (K_{Ma}), two longer distinct crack direction become apparent while the rest are closed or blunted. The process continues until the stress intensity goes critical and mechanical fracture occurs. The process is controlled by a rate limiting step like diffusion of chlorine or the dissolution of metals into solution. The driving force is the differences in electrochemical potential. The concentrated positively charged metal ions will diffuse away from the crack tip while chlorine and hydronium ions diffuse towards the crack tip.

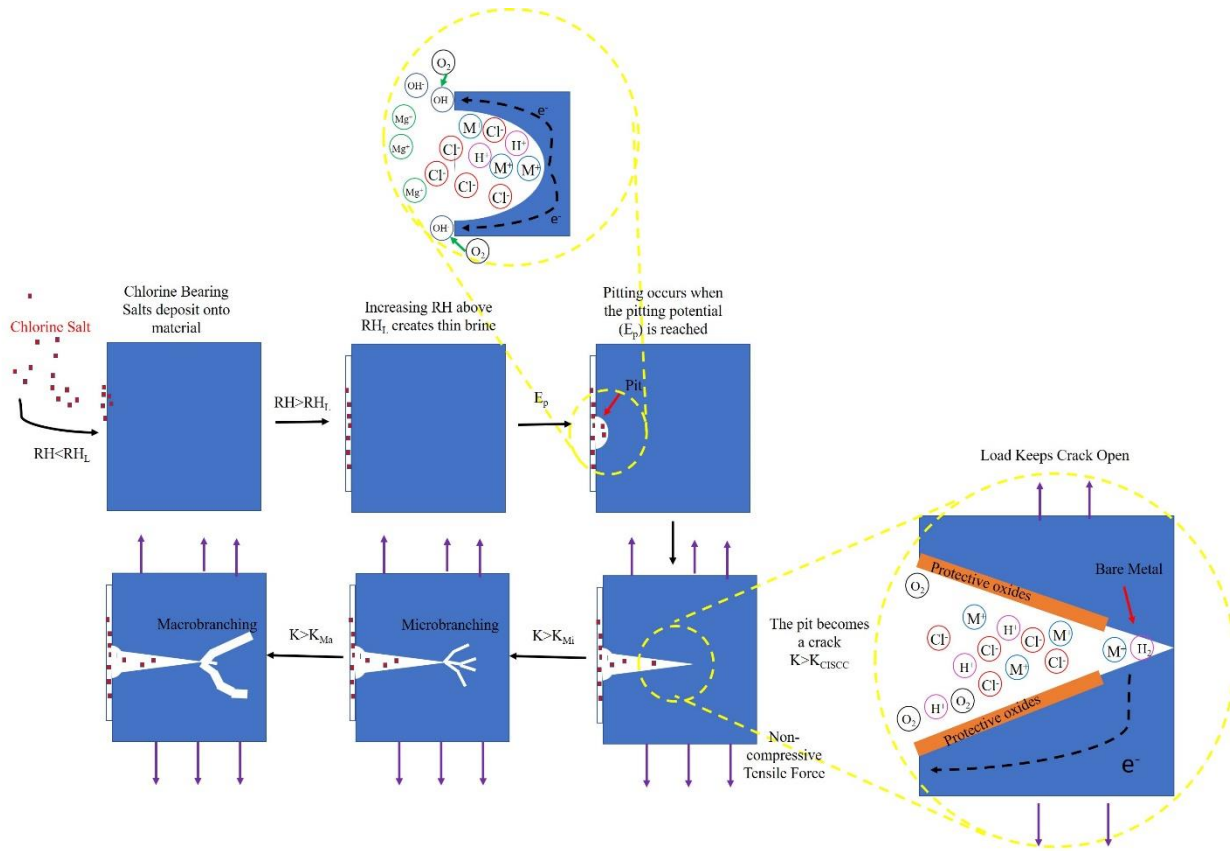


Figure 79: Possible Mechanisms of Chlorine-Induced Stress Corrosion Cracking

Chapter 5: Conclusions

The purpose of this study was to conduct experiments to gain a better understanding of the inner workings of chlorine-induced stress corrosion cracking. The main features and findings of this study are presented below:

- A novel *in situ* synchrotron x-ray tomography and diffraction study on chlorine-induced stress corrosion cracking on 304SS was devised with the aid of a custom-built tensile apparatus with a controlled environmental chamber to simulate a marine environment
- Beyond chlorine-induced stress corrosion cracking since the samples were fatigued pre-cracked, this study enabled to gain new insight into fatigue failure i.e. fatigue induced crack propagation and the role of precipitates/inclusions thanks to tomography data combined with electron microscopy observations. Fatigue pre-cracking was observed to cause the formation of microvoids, preferentially at the interfaces of sulfides due to its lower elastic modulus compared to that of the matrix. Fatigue pre-cracking also increased the amount of deformation induced martensite, especially at the crack tip due to the plastic zone. Fatigue microvoid coalescence was thought to be responsible for “vertical cracks” in some instances
- As far as chlorine-induced stress corrosion cracking it was observed to lead only to a small fraction of deformation induced martensite, indicating that the mechanism does not rely on deformation induced martensite. Intrinsic and extrinsic mechanisms for crack retardation from an increase in the phase fraction of deformation induced martensite are not likely significant factors in chlorine-induced stress corrosion cracking
- Stress intensity has been shown to play a role in crack morphology. Lower stress intensity led to single crack growth, higher stress intensities led to microbranching, and even higher

stress intensities showed macrobranching. There was found to be a duration of single crack phase regardless of stress intensity. Crack Branching was found to be not a prerequisite for steady state propagation rate in stage II

- Temperature was found to increase crack growth rates most likely as a result of an increased rate limiting step like diffusion
- Chlorine was found to be influential in causing cracking under the conditions ran in this experiment. Chlorine ions concentrate at the crack tip and brings along hydronium ions which acidifies the crack tip. The low pH region leads to dissolution of the material at the crack tip
- A dissolution-based model was proposed based on the characterization of the tested samples showing FeCl_2 , CrCl_2 , and $\text{NiCl}_2 \cdot 6\text{H}_2\text{O}$ indicating that Fe, Cr, and Ni dissolve into solution and crystallized out when the solution dried out

Chapter 7: Future Works

Future experimental and simulations work that would complement and further our understanding of CISCC would include the following:

- 1) Testing the three alloys in the same condition after sensitization of the alloys to varying degrees via heat treatments to produce chromium carbides at the grain boundaries while depleting chromium from the surrounding area. Sensitizing these alloys is expected to lead to intergranular cracking as opposed to the transgranular cracking [64]. How does the degree of sensitization effect cracking rates and morphology. Differences in the local chemistry at grain boundaries compared to towards the center of the grain will lead to grain boundary attack. We expect sensitization increases the cracking rate compared to the transgranular rates of non-sensitized 304SS. Additionally, is crack branching evident at higher stress intensities or can it occur at lower stress intensities.
- 2) A simulation based study on the effects of stress intensity on the small materials cracking behavior would be interesting. At what stress intensity does the distribution of . At what stress intensity does the tension zones on the other side of the sample disappear.

REFERENCES

- [1] K.E.H. Raymond L. Murray, Nuclear Energy: An Introduction to the Concepts, Systems, and Applications of Nuclear Processes, Seventh ed., Elsevier, 2015.
- [2] U.S. NRC, Dry Spent Fuel Storage Designs: NRC Approved for General Use, in, 2019.
- [3] R.H. Jones, Stress-Corrosion Cracking: Material Performance and Evaluation Second ed., 2017.
- [4] C. Örnek, D.L. Engelberg, Toward Understanding the Effects of Strain and Chloride Deposition Density on Atmospheric Chloride-Induced Stress Corrosion Cracking of Type 304 Austenitic Stainless Steel Under $MgCl_{sub 2}^{2+}$ and $FeCl_{sub 3}^{3+}:MgCl_{sub 2}^{2+}$ Droplets, *Corrosion*, 75 (2019) 167-182.
- [5] T. Prosek, A. Iversen, C. Taxén, D. Thierry, Low-Temperature Stress Corrosion Cracking of Stainless Steels in the Atmosphere in the Presence of Chloride Deposits, *Corrosion*, 65 (2009) 105-117.
- [6] J. Schijve, Fatigue of Structures and Materials, in: J. Schijve (Ed.), Springer, Springer Netherlands, 2009, pp. 622.
- [7] J. Schijve, I. ebrary, Fatigue of structures and materials, Dordrecht ; London : Springer, c2009., 2009.
- [8] D.R. Kester, I.W. Duedall, D.N. Connors, R.M. Pytkowicz, Preparation of Artificial Seawater, *Limnology and Oceanography*, 12 (1967) 176-179.
- [9] T. Prosek, A.L. Gac, D. Thierry, S.L. Manchet, C. Lojewski, A. Fanica, E. Johansson, C. Canderyd, F. Dupoiron, T. Snauwaert, F. Maas, B. Drolesbeke, Low-Temperature Stress Corrosion Cracking of Austenitic and Duplex Stainless Steels Under Chloride Deposits, *Corrosion*, 70 (2014) 1052-1063.
- [10] S. Shoji, N. Ohnaka, Y. Furutani, T. Saito, Effects of relative humidity on atmospheric stress corrosion cracking of stainless steels, *Corrosion Engineering*, 35 (1986) 559-565.
- [11] Y. Xie, J. Zhang, Chloride-induced stress corrosion cracking of used nuclear fuel welded stainless steel canisters: A review, *Journal of Nuclear Materials*, 466 (2015) 85-93.
- [12] M.F. Chiang, H.H. Hsu, M.C. Young, J.Y. Huang, Mechanical degradation of cold-worked 304 stainless steel in salt spray environments, *Journal of Nuclear Materials*, 422 (2012) 58-68.
- [13] M.C. Remillieux, D. Kaoumi, Y. Ohara, M.A. Stuber Geesey, L. Xi, R. Schoell, C.R. Bryan, D.G. Enos, D.A. Summa, T.J. Ulrich, B.E. Anderson, Z. Shayer, Detecting and imaging stress corrosion cracking in stainless steel, with application to inspecting storage canisters for spent nuclear fuel, *NDT & E International*, 109 (2020) 102180.
- [14] H.S.K.a.B. Raj, Corrosion of Austenitic Stainless Steels: Mechanism, Mitigation, and Monitoring, Narosa Publishing House, 2002.
- [15] S. Feliu, M. Morcillo, S. Feliu, The prediction of atmospheric corrosion from meteorological and pollution parameters—I. Annual corrosion, *Corrosion Science*, 34 (1993) 403-414.
- [16] J. Lieberzeit, T. Prošek, A. Jarvis, L. Kiener, Atmospheric Stress Corrosion Cracking of Stainless Steel Rock Climbing Anchors, Part 1, *Corrosion*, 75 (2019) 1255-1271.
- [17] W.F. Flanagan, B.D. Licher, A mechanism for transgranular stress-corrosion cracking, *International Journal of Fracture*, 79 (1996) 121-135.
- [18] S. Torchio, Stress corrosion cracking of type aisi 304 stainless steel at room temperature; influence of chloride content and acidity, *Corrosion Science*, 20 (1980) 555-561.

- [19] V.A. Marichev, Crack branching during stress corrosion cracking of high-strength materials, Soviet materials science : a transl. of Fiziko-khimicheskaya mekhanika materialov / Academy of Sciences of the Ukrainian SSR, 11 (1975) 139-142.
- [20] L. Burnett Timothy, N.J.H. Holroyd, M. Scamans Geoffrey, X. Zhou, E. Thompson George, J. Withers Philip, The role of crack branching in stress corrosion cracking of aluminium alloys, in: Corrosion Reviews, 2015, pp. 443.
- [21] Y. Hirose, T. Mura, Crack branching behavior in stress corrosion cracking of high strength steel, Engineering Fracture Mechanics, 34 (1989) 729-742.
- [22] P.J. Withers, Fracture mechanics by three-dimensional crack-tip synchrotron X-ray microscopy, Philosophical Transactions of the Royal Society A: Mathematical, Physical and Engineering Sciences, 373 (2015) 20130157.
- [23] T. Terachi, T. Yamada, T. Miyamoto, K. Arioka, SCC growth behaviors of austenitic stainless steels in simulated PWR primary water, Journal of Nuclear Materials, 426 (2012) 59-70.
- [24] J. Hou, Q.J. Peng, T. Shoji, J.Q. Wang, E.H. Han, W. Ke, Effects of cold working path on strain concentration, grain boundary microstructure and stress corrosion cracking in Alloy 600, Corrosion Science, 53 (2011) 2956-2962.
- [25] J.a.D.G.R. William D. Callister, Materials Science and Engineering: An Introduction, 9th ed., 2014.
- [26] J. Ding, L. Zhang, D. Li, M. Lu, J. Xue, W. Zhong, Corrosion and stress corrosion cracking behavior of 316L austenitic stainless steel in high H₂S–CO₂–Cl⁻ environment, Journal of Materials Science, 48 (2013) 3708-3715.
- [27] R. Zhu, J. Wang, L. Zhang, Z. Zhang, E.-h. Han, Stress corrosion cracking of 316L HAZ for 316L stainless steel/Inconel 52M dissimilar metal weld joint in simulated primary water, Corrosion Science, 112 (2016) 373-384.
- [28] D. Du, K. Chen, L. Yu, L. Zhang, X. Shi, X. Xu, SCC crack growth rate of cold worked 316L stainless steel in PWR environment, Journal of Nuclear Materials, 456 (2015) 228-234.
- [29] Z. Lu, T. Shoji, F. Meng, Y. Qiu, T. Dan, H. Xue, Effects of water chemistry and loading conditions on stress corrosion cracking of cold-rolled 316NG stainless steel in high temperature water, Corrosion Science, 53 (2011) 247-262.
- [30] J. Hill, APS Upgrade, in, Tigerhill Studio, 2010.
- [31] P. Willmott, An introduction to synchrotron radiation: techniques and applications, John Wiley & Sons, 2019.
- [32] C.E. Freese, F.I. Baratta, Single edge-crack stress intensity factor solutions, Engineering Fracture Mechanics, 73 (2006) 616-625.
- [33] X. Yan, An Efficient and Accurate Numerical Method of Stress Intensity Factors Calculation of a Branched Crack, Journal of Applied Mechanics, 72 (2005) 330-340.
- [34] D. Deng, H. Murakawa, Numerical simulation of temperature field and residual stress in multi-pass welds in stainless steel pipe and comparison with experimental measurements, Computational materials science, 37 (2006) 269-277.
- [35] X. Wu, Z. Yu, S. Gordon, D. Olson, S. Liu, C.R. Bryan, E.J. Schindelholz, D. Enos, Z. Shayer, Finite Element Analysis of Weld Residual Stresses in Austenitic Stainless Steel Canisters in Dry Storage of Spent Fuel, in, Sandia National Lab.(SNL-NM), Albuquerque, NM (United States), 2017.

- [36] J. Pegues, S. Shao, N. Shamsaei, J. Schneider, R. Moser, Cyclic strain rate effect on martensitic transformation and fatigue behaviour of an austenitic stainless steel, *Fatigue & Fracture of Engineering Materials & Structures*, 40 (2017) 2080-2091.
- [37] J. Liu, D. Kaoumi, Use of in-situ TEM to characterize the deformation-induced martensitic transformation in 304 stainless steel at cryogenic temperature, *Materials Characterization*, 136 (2018) 331-336.
- [38] D. Kaoumi, J. Liu, Deformation induced martensitic transformation in 304 austenitic stainless steel: In-situ vs. ex-situ transmission electron microscopy characterization, *Materials Science and Engineering: A*, 715 (2018) 73-82.
- [39] I. Nikulin, T. Sawaguchi, K. Tsuzaki, Effect of alloying composition on low-cycle fatigue properties and microstructure of Fe–30Mn–(6–x) Si–xAl TRIP/TWIP alloys, *Materials Science and Engineering: A*, 587 (2013) 192-200.
- [40] M. De Graef, M.E. McHenry, Structure of materials: an introduction to crystallography, diffraction and symmetry, Cambridge University Press, 2012.
- [41] A. International, ASTM E975-03, in: Standard Practice for X-Ray Determination of Retained Austenite in Steel with Near Random Crystallographic Orientation, West Conshohocken PA, 2003.
- [42] Z. Shen, D. Du, L. Zhang, S. Lozano-Perez, An insight into PWR primary water SCC mechanisms by comparing surface and crack oxidation, *Corrosion Science*, 148 (2019) 213-227.
- [43] R. Page, J. Weertman, M. Roth, Small angle neutron scattering study of fatigue Induced grain boundary cavities, *Acta Metallurgica*, 30 (1982) 1357-1366.
- [44] Q. Wang, N. Kawagoishi, Q. Chen, Fatigue voids in structural Al-alloys under high-frequency cyclic loading, *Journal of materials science*, 39 (2004) 365-367.
- [45] Y. Chen, S. Pan, M. Zhou, D. Yi, D. Xu, Y. Xu, Effects of inclusions, grain boundaries and grain orientations on the fatigue crack initiation and propagation behavior of 2524-T3 Al alloy, *Materials Science and Engineering: A*, 580 (2013) 150-158.
- [46] R. SUNDER, W.J. PORTER, N.E. ASHBAUGH, Fatigue voids and their significance, *Fatigue & Fracture of Engineering Materials & Structures*, 25 (2002) 1015-1024.
- [47] M.-g. Yin, Z.-b. Cai, Y.-q. Yu, M.-h. Zhu, Impact-sliding wear behaviors of 304SS influenced by different impact kinetic energy and sliding velocity, *Tribology International*, 143 (2020) 106057.
- [48] R. Gaillac, P. Pullumbi, F.-X. Coudert, ELATE: an open-source online application for analysis and visualization of elastic tensors, *Journal of Physics: Condensed Matter*, 28 (2016) 275201.
- [49] R. Guerchais, F. Morel, N. Saintier, C. Robert, Influence of the microstructure and voids on the high-cycle fatigue strength of 316L stainless steel under multiaxial loading, *Fatigue & Fracture of Engineering Materials & Structures*, 38 (2015) 1087-1104.
- [50] I. Nikulin, T. Sawaguchi, K. Ogawa, K. Tsuzaki, Effect of γ to ϵ martensitic transformation on low-cycle fatigue behaviour and fatigue microstructure of Fe–15Mn–10Cr–8Ni–xSi austenitic alloys, *Acta Materialia*, 105 (2016) 207-218.
- [51] M. Ojima, Y. Adachi, Y. Tomota, Y. Katada, Y. Kaneko, K. Kuroda, H. Saka, Weak beam TEM study on stacking fault energy of high nitrogen steels, *steel research international*, 80 (2009) 477-481.
- [52] J. Lu, L. Hultman, E. Holmström, K.H. Antonsson, M. Grehk, W. Li, L. Vitos, A. Golpayegani, Stacking fault energies in austenitic stainless steels, *Acta Materialia*, 111 (2016) 39-46.

- [53] T. Yonezawa, K. Suzuki, S. Ooki, A. Hashimoto, The Effect of Chemical Composition and Heat Treatment Conditions on Stacking Fault Energy for Fe-Cr-Ni Austenitic Stainless Steel, Metallurgical and Materials Transactions A, 44 (2013) 5884-5896.
- [54] G.M. de Bellefon, J. van Duysen, K. Sridharan, Composition-dependence of stacking fault energy in austenitic stainless steels through linear regression with random intercepts, Journal of Nuclear Materials, 492 (2017) 227-230.
- [55] C.G. Rhodes, A.W. Thompson, The composition dependence of stacking fault energy in austenitic stainless steels, Metallurgical Transactions A, 8 (1977) 1901-1906.
- [56] P. Withers, Fracture mechanics by three-dimensional crack-tip synchrotron X-ray microscopy, Philosophical Transactions of the Royal Society A: Mathematical, Physical and Engineering Sciences, 373 (2015) 20130157.
- [57] G. Baudry, A. Pineau, Influence of strain-induced martensitic transformation on the low-cycle fatigue behavior of a stainless steel, Materials Science and Engineering, 28 (1977) 229-242.
- [58] Y. Lv, H. Luo, J. Tang, J. Guo, J. Pi, K. Ye, Corrosion properties of phase reversion induced nano/ultrafine grained AISI 304 metastable austenite stainless steel, Materials Research Bulletin, 107 (2018) 421-429.
- [59] I. Touaiher, M. Saâdaoui, J. Chevalier, L. Preiss, H. Reveron, Fracture behavior of Ce-TZP/alumina/aluminate composites with different amounts of transformation toughening. Influence of the testing methods, Journal of the European Ceramic Society, 38 (2018) 1778-1789.
- [60] Y.D. Ha, F. Bobaru, Studies of dynamic crack propagation and crack branching with peridynamics, International Journal of Fracture, 162 (2010) 229-244.
- [61] C. Bathias, A. Pineau, Fatigue of materials and structures : fundamentals, London : Iste ; Hoboken, NJ : John Wiley, 2010., 2010.
- [62] A. Materials, Stainless Steel - Grade 304, in.
- [63] W.J. Mills, Fracture toughness of type 304 and 316 stainless steels and their welds, International Materials Reviews, 42 (1997) 45-82.
- [64] L. Tjayadi, N. Kumar, K.L. Murty, Accelerated crack growth experiments of SS304H for dry storage canister in substitute ocean water – Effect of temperature, Materials Today Communications, 23 (2020) 100929.
- [65] A.V. Sameljuk, A.D. Vasilev, S.A. Firstov, Temperature dependences of the branching stress intensity factor and the branching crack length in chromium 0.5La₂O₃, International Journal of Refractory Metals and Hard Materials, 15 (1997) 215-218.
- [66] J.R. Donahue, J.T. Burns, Effect of chloride concentration on the corrosion-fatigue crack behavior of an age-hardenable martensitic stainless steel, International Journal of Fatigue, 91 (2016) 79-99.
- [67] P.M. Gil, M. Palomar-Pardavé, M.G.M. de Oca-Yemha, M.T. Ramírez-Silva, C. Ángeles-Chávez, M. Romero-Romo, Effect of Carbonate and Chloride Ions on the Corrosion Susceptibility of Pipeline Steel Samples Artificially Aged, Int. J. Electrochem. Sci, 13 (2018) 1844-1858.
- [68] K. Sipilä, M. Bojinov, W. Mayinger, T. Saario, M. Stanislawski, Effect of chloride and sulfate additions on corrosion of low alloy steel in high-temperature water, Electrochimica Acta, 173 (2015) 757-770.

APPENDICES

Appendix A: Grain Size Measurements with ImageJ

- 1) Grain size measurements are an important microstructural feature which can alter the mechanical properties of a material of the same composition. Measuring the grain sizes first starts with imaging the grain either with a well-polished surface (using 0.05 µm colloidal silica or electropolishing) or by etching the grain boundaries with a chemical or an electrolytic etchant. For example **Figure A.1** shows the grains which have been etched by electropolishing using a 5% perchloric acid solution in methanol

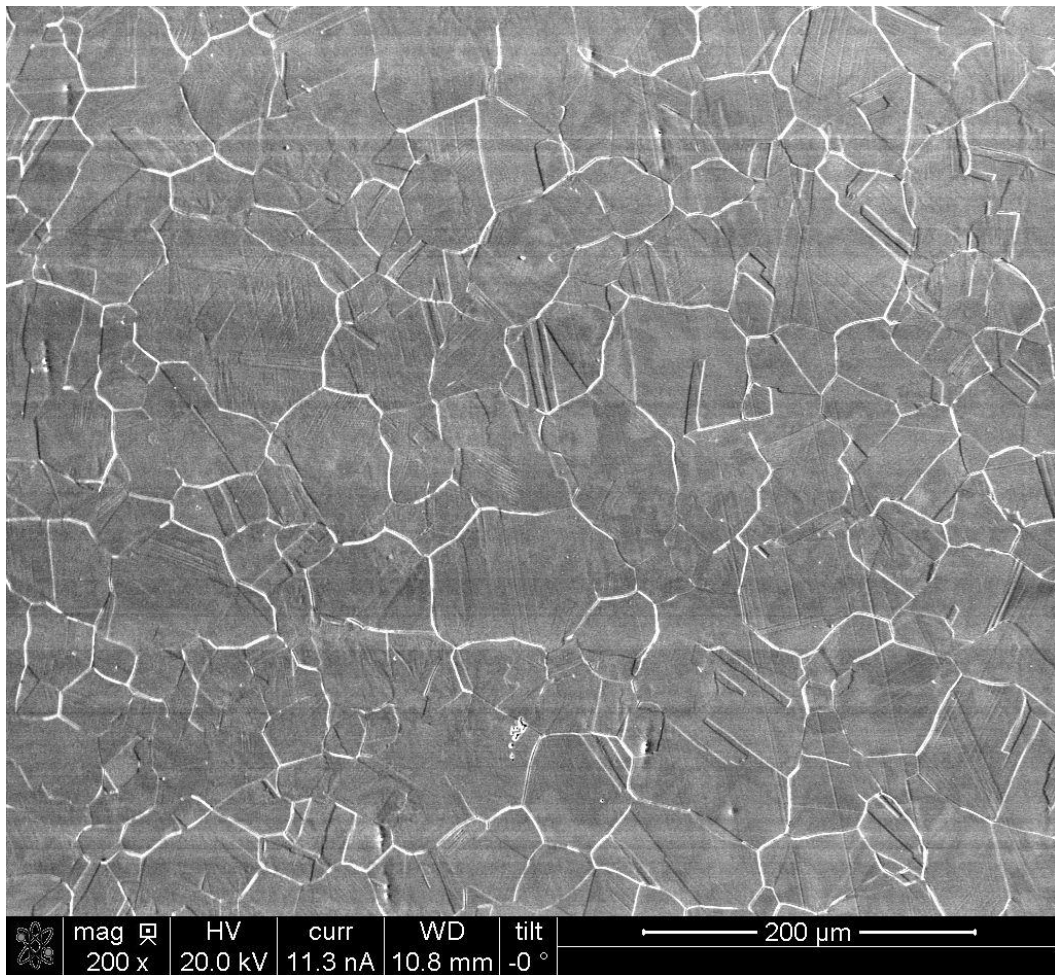


Figure A.1: Scanning Electron Microscopy of Etched Grain Boundaries of 304L by Electropolishing with a 5% Perchloric Acid in Methanol

- 2) ImageJ is a program which is used to calculate the grain areas. For the program to recognize the grain boundaries, a trace of the grains needs to be conducted on transparent paper as shown in **Figure A.2**.

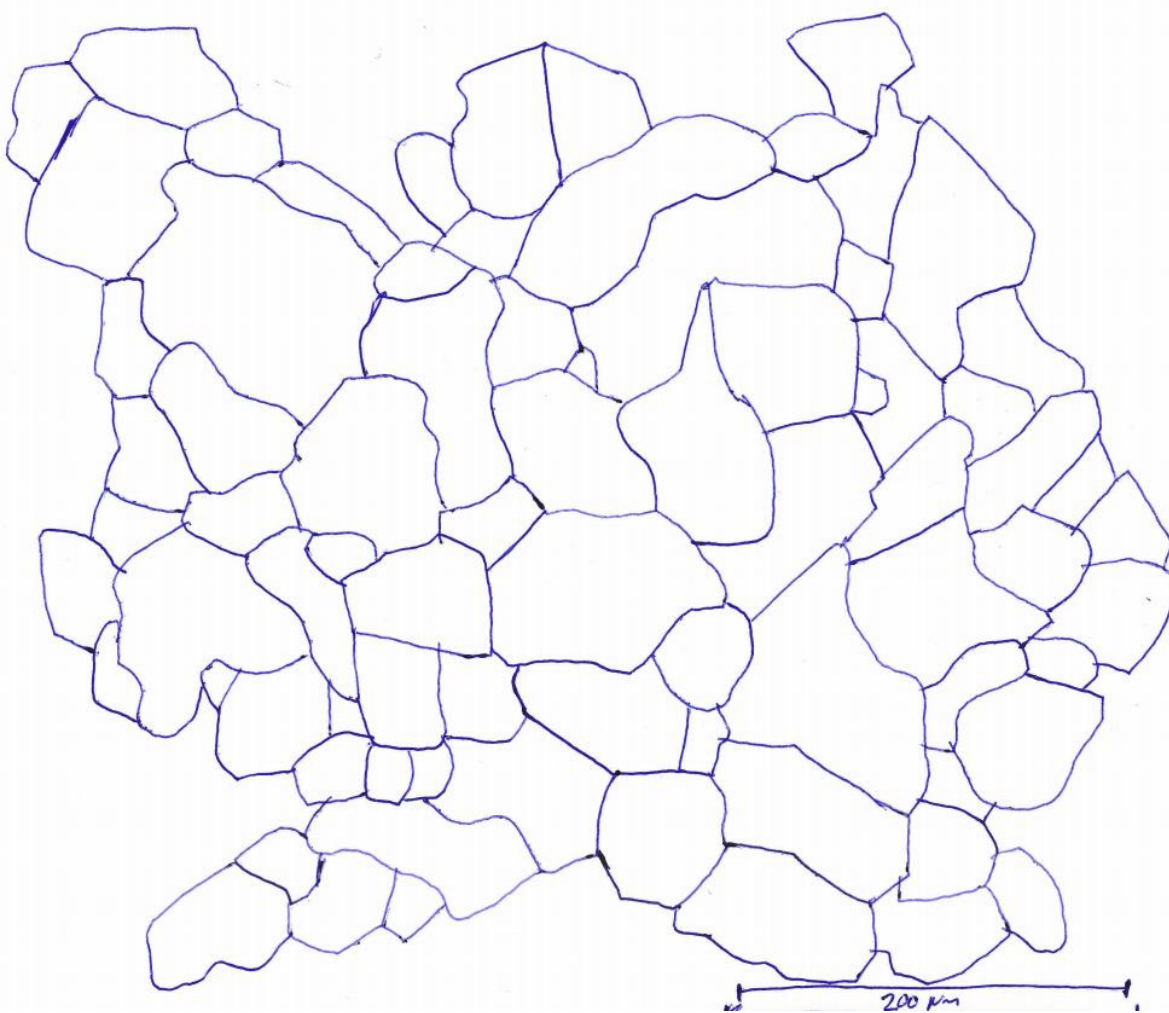


Figure A.2: Trace of the Grain Boundaries of 304L Image of **Figure A.1**

- 3) Once a trace has been created with the scale bar included, ImageJ can be opened and the trace of the grain boundaries can be opened. From there, the scale bar needs to be considered by drawing a line on the scale bar and then going to Analyze > Set Scale. Enter in the length of the scale as shown in **Figure A.3** so the program can convert between pixels and the scale of choice (microns in this example)

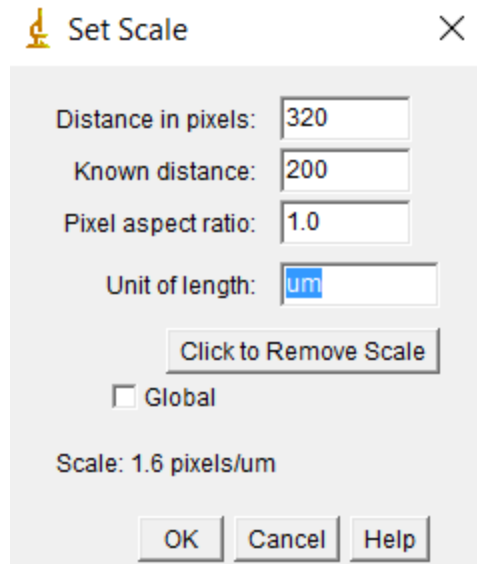


Figure A.3: Setting Scale in ImageJ to Convert Pixels to Microns in Example

- 4) After adding the scale, the rectangle tool can be used to crop the image to remove the scale bar by drawing a rectangle around just the grain and then selecting Image>Crop
- 5) The image then needs to be converted into an 8-bit image for the software to recognize the boundaries. This can be done by going to Image>Type>8-Bit
- 6) Then the image needs to be inverted to make the background black and the boundaries white as shown in **Figure A.4**. This process is done by going to Edit>Invert

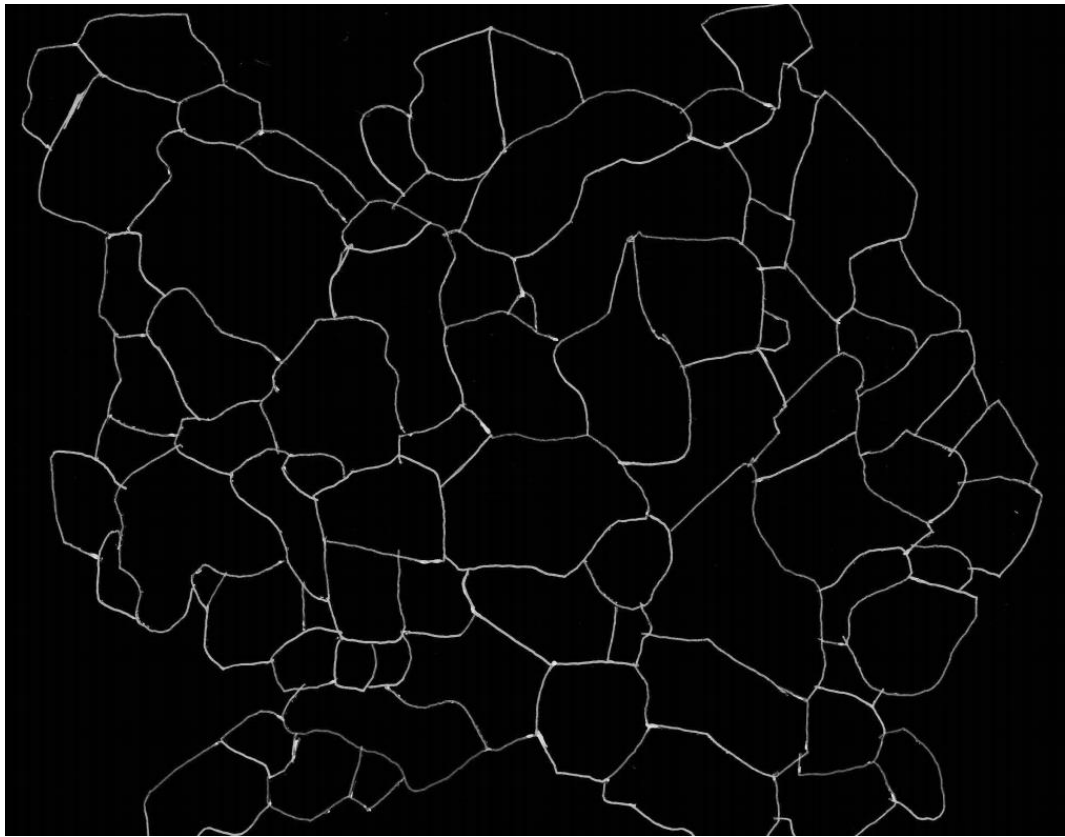


Figure A.4: Inverted 8-Bit Image of Grain Boundaries of 304L

- 7) Thresholding is then used to make grain boundaries a little thicker and better differentiate it from the inside of the grains. This is done by going to Image>Adjust>Threshold and clicking Auto followed by apply
- 8) Each grain area can then be measured using the analyze tool by going to Analyze>Analyze Particles which will bring up the dialogue box shown in **Figure A.5**. Select Exclude on edges to only get the grains and not the area around the grains (i.e. black spaces which surround all the grains)

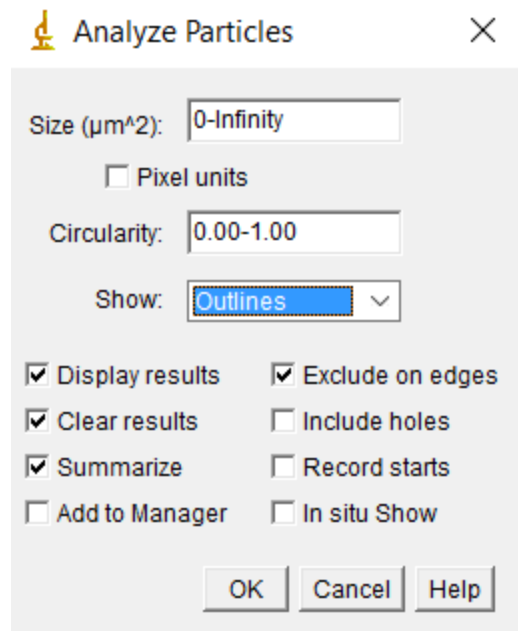


Figure A.5: Analyze Particles Tool

- 9) The software then calculates the number of pixels in each grain and converts this to an area in microns. The average grain size can then be calculated by first calculating the diameter of each grain assuming a circle ($A = \frac{\pi D^2}{4}$). The average diameter is then calculated which represents the average grain size

Appendix B: Precipitate Area Density

- 1) The area density of precipitates is calculated with the assistance of ImageJ. First open the scanning electron micrograph containing precipitates. For this example, a micrograph from the as-received commercial-304 was used and is shown in **Figure B.1**. Both the higher magnification and lower magnification were used to calculate the area density since some precipitates can only be observed at higher magnifications. For now, the lower magnification image will be used first.

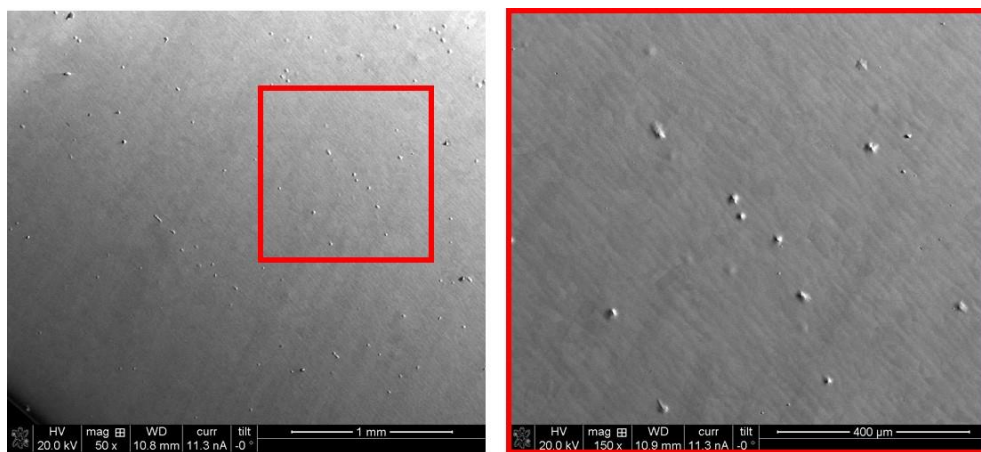


Figure B.1: Scanning Electron Micrograph of Commercial-304 Showing Precipitates

- 2) After opening the lower magnification image in ImageJ, set the scale by using the line tool to draw a line that matched the scan and then go to Analyze>Set Scale and fill in the known distance so the program can convert pixels to the known distance units (in this example, μm).
- 3) After setting the scale, the precipitates can be measured. Approximating the precipitates as ellipses, a major and minor axis can be measured as shown in **Figure B.2**. Each number represents a measurement, and the area of the micrograph was also measured (measurements 177 and 178)

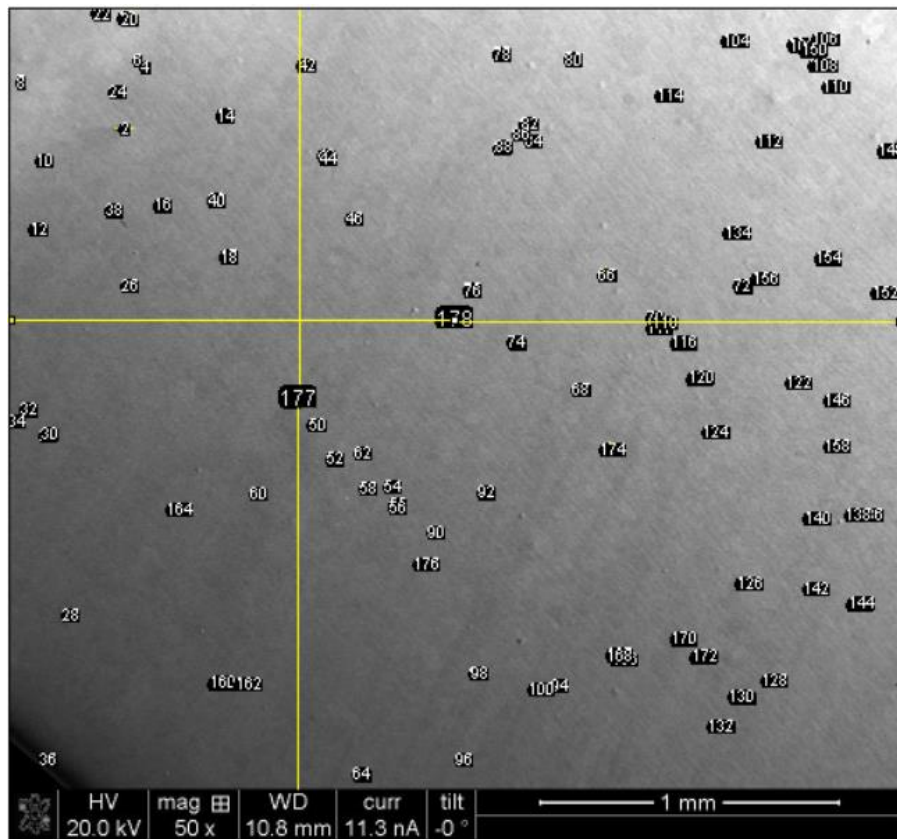


Figure B.2: Low Magnification Micrograph of As-Received Commercial-304 Showing Precipitates Measurements in Major and Minor Directions and Measurements for Micrograph Area

- 4) The area of each precipitate can then be measured using the equation for an area of an ellipse ($Area = AB\pi$ where A is the major radius and B is the minor radius)
- 5) The same procedures can then be used to calculate the area of precipitates in the higher magnification image as shown in **Figure B.3**

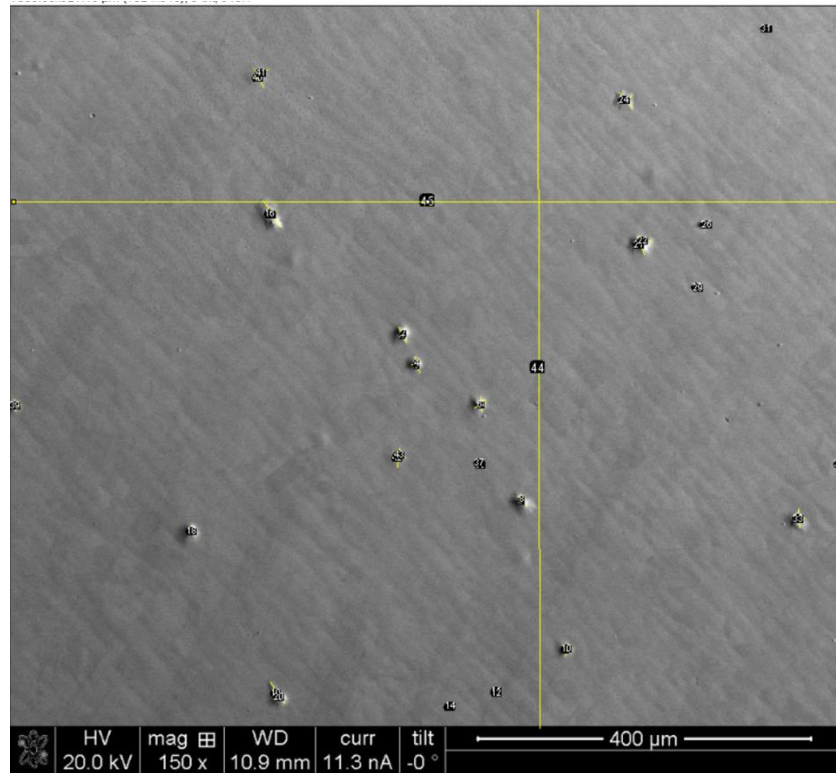


Figure B.3: Higher Magnification Micrograph of As-Received Commercial-304 Showing Precipitates Measurements in Major and Minor Directions and Measurements for Micrograph Area

- 6) The precipitates found in both the higher and low magnification images are accounted for by removing their measurements from the higher magnification image. Then an average area of precipitates in the higher magnification is calculated. To account for the possible small precipitates in the lower magnification image, the number of higher magnification images in the lower magnification image and is multiplied by the number of new measurements found at the higher magnification and the average area in the higher magnification image. This is then combined with the area of precipitates in the lower magnification image and divided by the area of the lower magnification micrograph

Appendix C: Using AVIZO to Extract Crack from Tomographs

- 1) Open up Avizo Software
- 2) The picture below in **Figure C.1** shows the opening screen. If starting a new tomography analysis, click “OPEN DATA” (circled in red). If continuing a project, click “OPEN PROJECT” and find the saved project file to continue

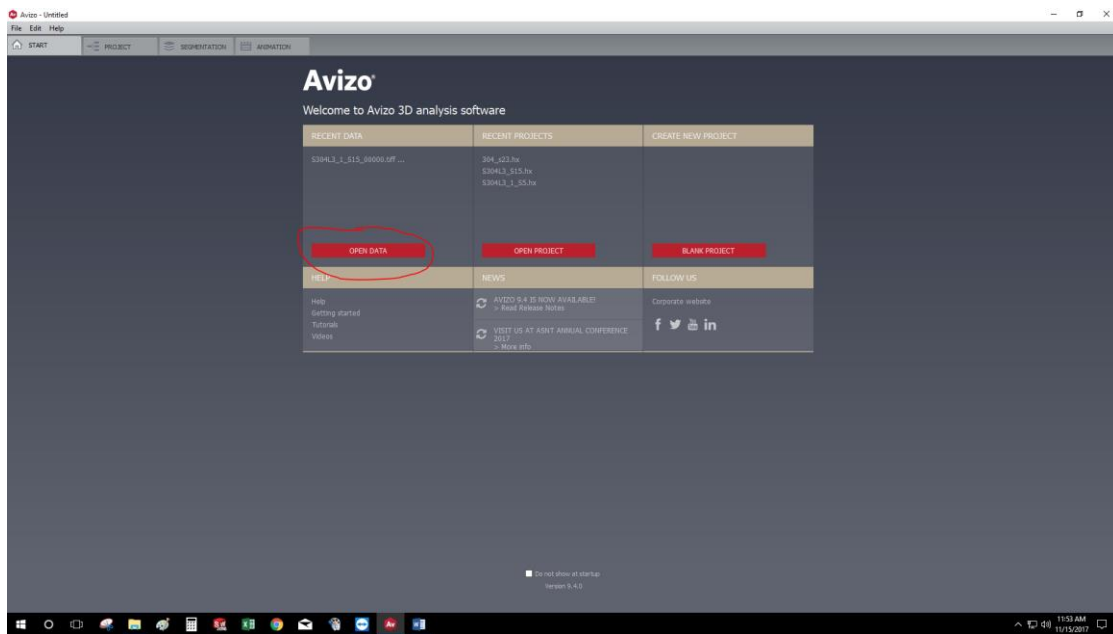


Figure C.1: Avizo Home Page

- 3) Once you have found the data set you want to analyze. Select all the pictures in the file and click open. An easy way to select all the pictures is to select the first picture and then scroll down to the last picture. Then while holding the shift key, select the last picture. This should highlight all the pictures and should look similar to **Figure C.2**. Note: These images should be tiff images

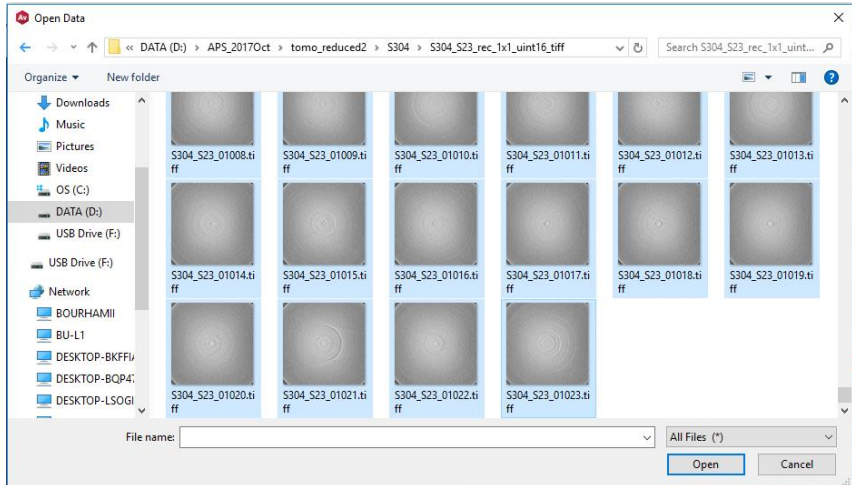


Figure C.2: Selecting Pictures from File

- 4) A message should appear similar to the one below in **Figure C.3**. Select “Read complete volume into memory” (circled in Red) and then click OK

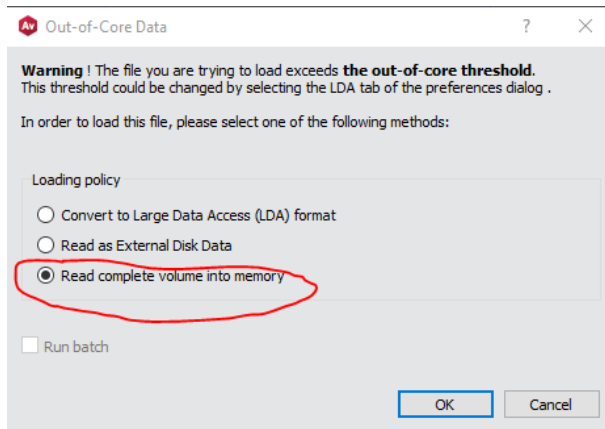


Figure C.3: Out-of-Core Data Message

- 5) The next message that will appear is the “Image Read Parameter” which is shown below in **Figure C.4**. Nothing needs to be changed here so click “OK”

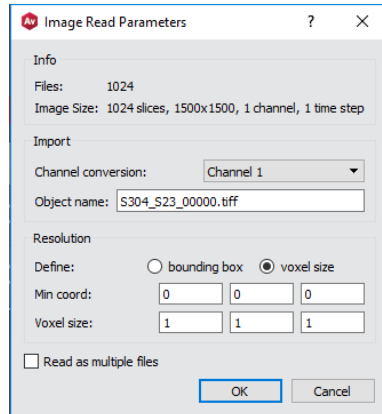


Figure C.4: Image Read Parameters Message Box

- 6) The file may take a little bit of time (5-10 minutes) to upload the pictures into the file.

The next screen you should see is shown below in **Figure C.5**. The next step is to crop the images so that just the sample is showing

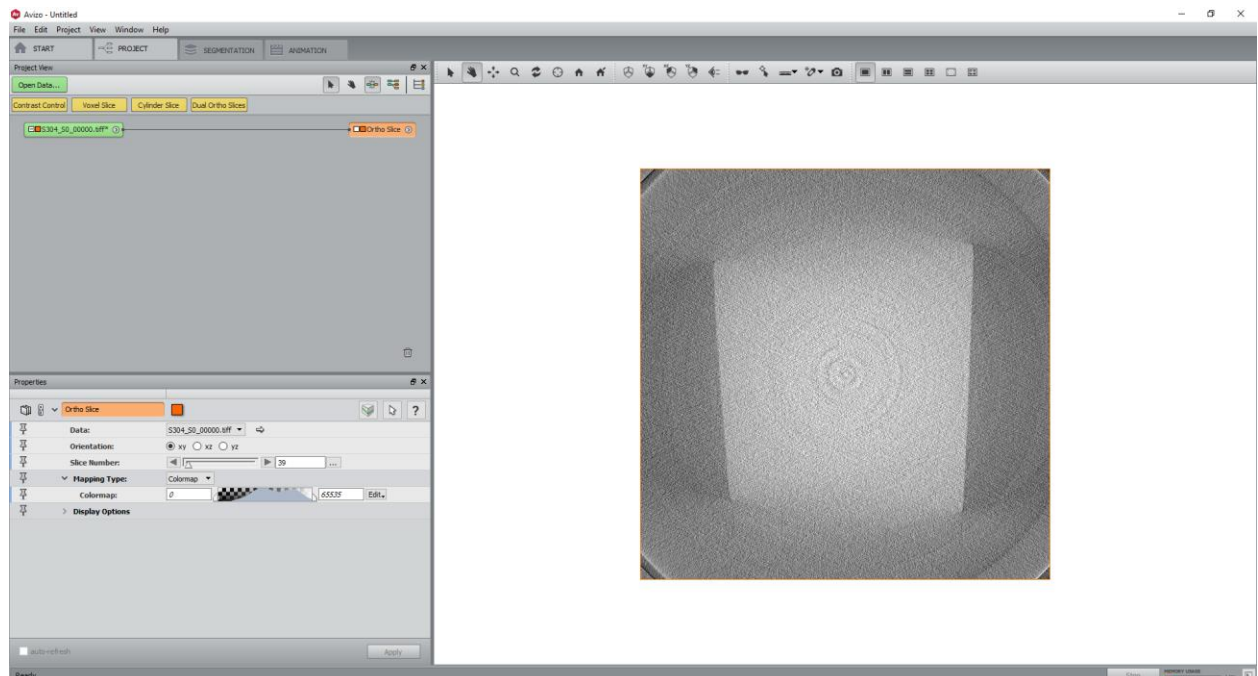


Figure C.5: Loaded Avizo Screen

- 7) For each plane (xy, yz, and xz), you need to find the lower limit (Image 41 for xy in **Figure C.6**) and the upper limit (Image 931 for xy in **Figure C.7**) when the surface of the sample comes into screen. Not all of the sample surface needs to be showing. You can

tell by surface defects. The image in **Figure C.5** shows an example of a picture with no surface defects meaning that it can be excluded

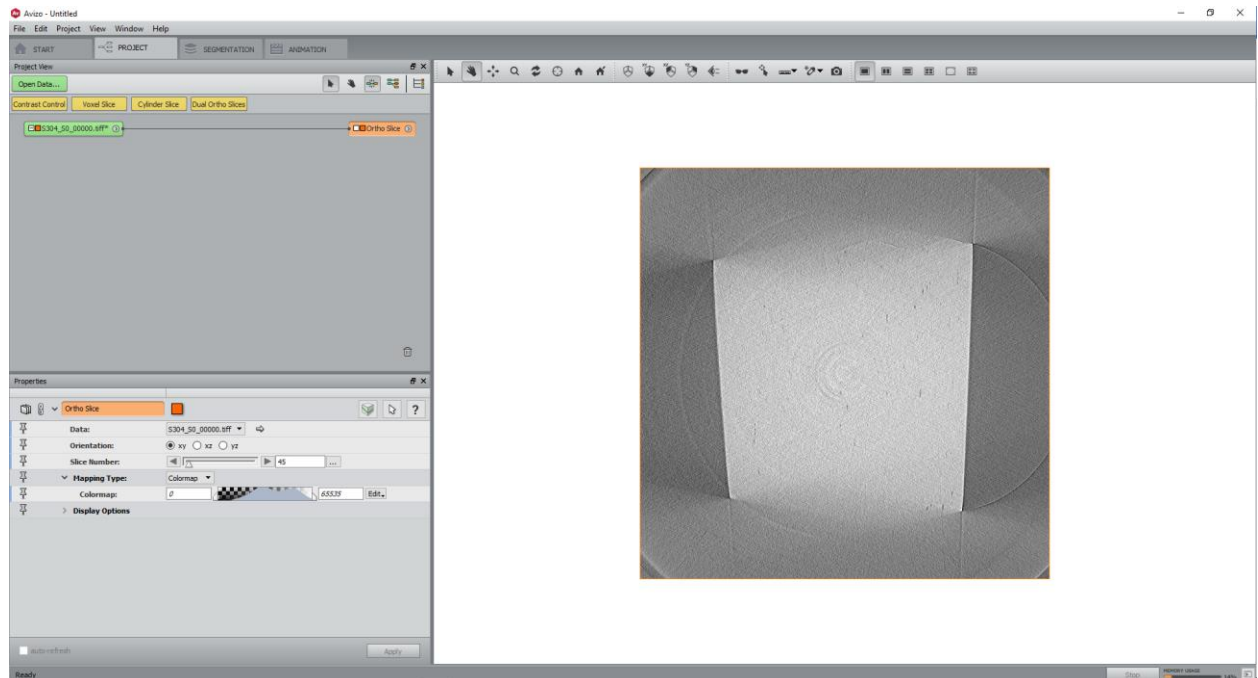


Figure C.6: Lower Limit Crop

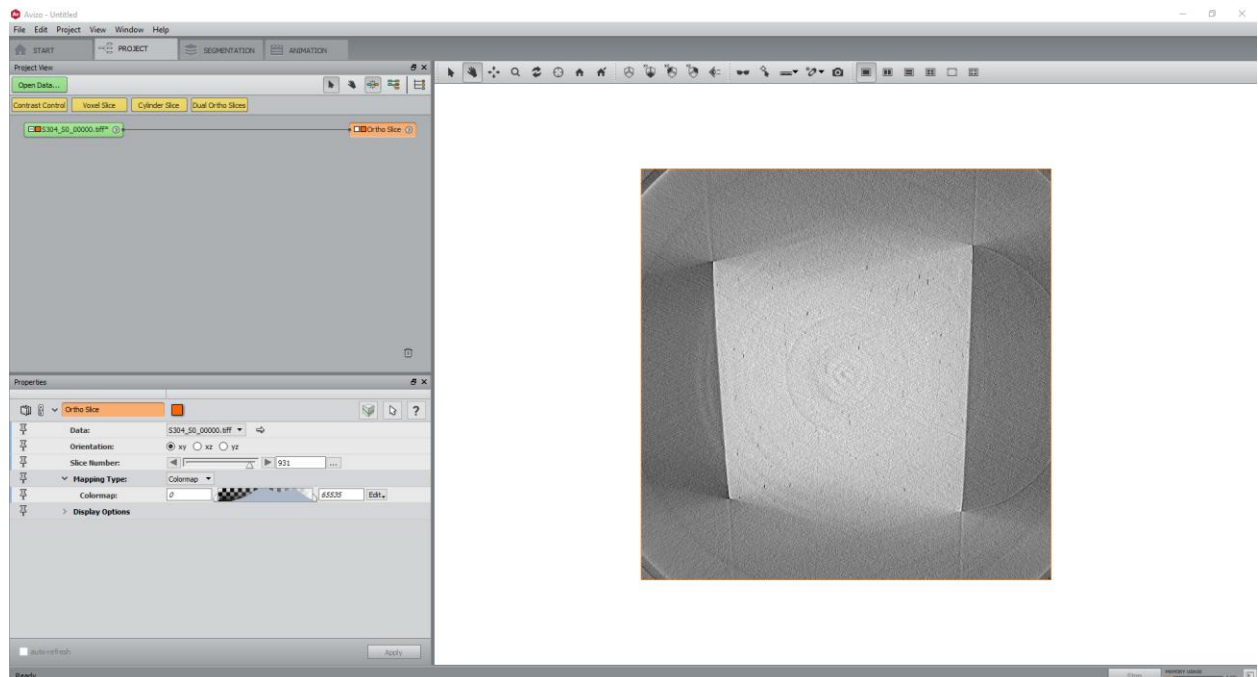


Figure C.7: Upper Limit Crop

- 8) **Figure C.8** shows the process of cropping. To crop the images, select the file in the project view (Circled in Blue) and then click on the crop button in the properties tab (Circled in Red)

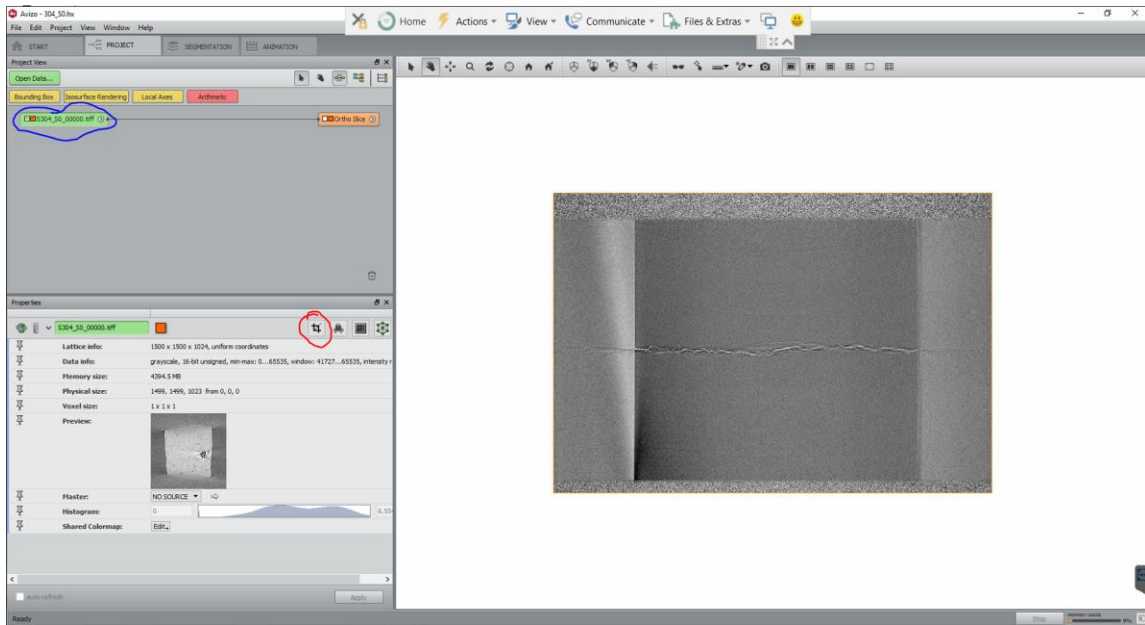


Figure C.8: How to Crop

- 9) The cropping prompt will show up and is shown in **Figure C.9**. The boxes that need to be changed are the “Min index” and the “Max index” for x, y, and z. Each plane corresponds with a direction (xy-plane is the z direction, yz-plane is the x direction, and the xz-plane is the y direction). The limits from the example above for the xy-plane are [41 931] so for the third column (z-direction), the lower limit would be 41 and the upper limit would be 931. After entering in the numbers put zero in to the “Min cord” boxes for x, y, and z so that the lower limit will become the 0 image

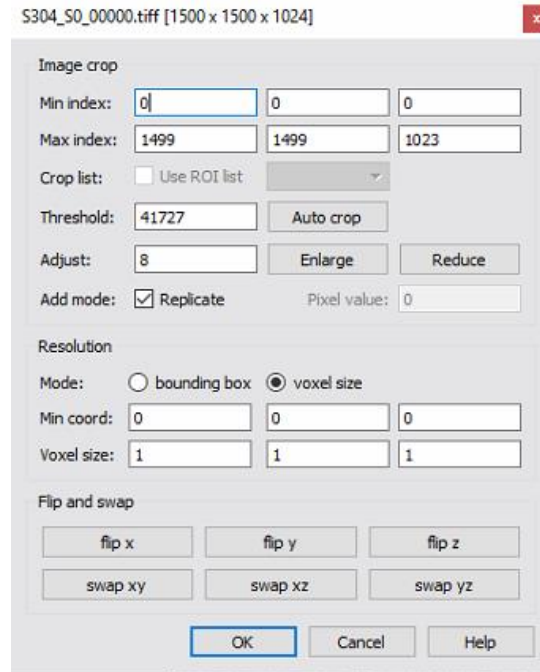


Figure C.9: Cropping Prompt

- 10) The next step is to use the segmentation tab which has tools which allow the user to select and deselect features in an image. **Figure C.10** shows where to find the segmentation tab (circled in blue). To see all three views at once, click the 4 view button (circled in red).

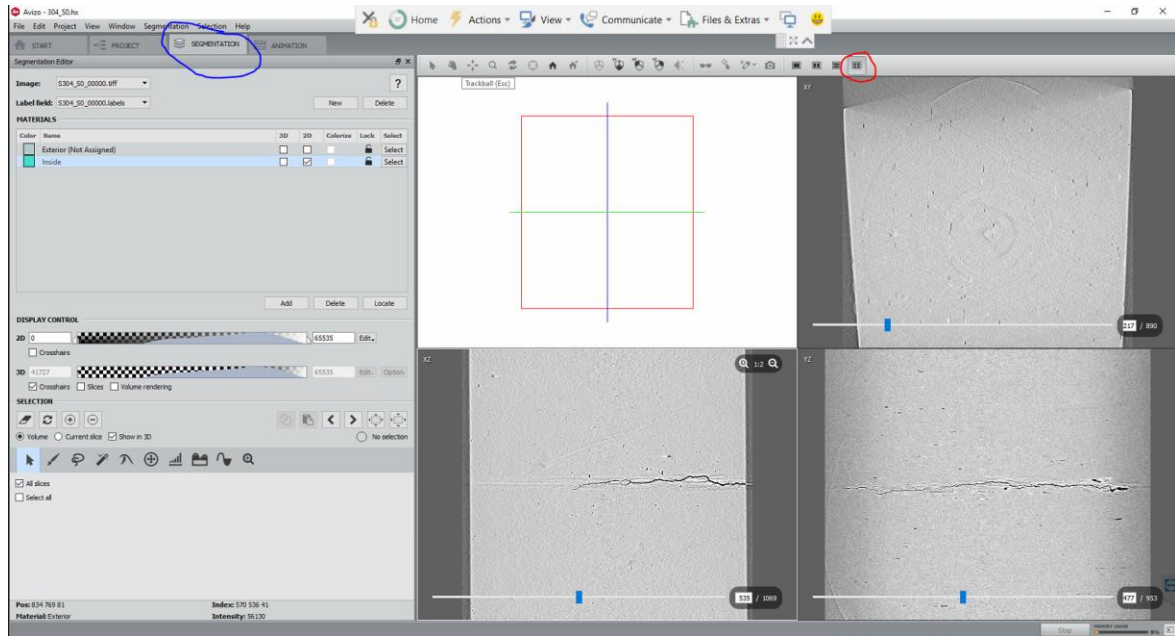


Figure C.10: Segmentation

- 11) In the segmentation tab, the threshold tool should be used to select the crack and voids.

Figure C.11 shows where the threshold tool is located (circled in blue). The limits of the threshold can be changed by moving the bars or plugging in numbers (circled in red). The lower limit should always be zero but the upper limit can vary. The upper limit should be high enough so that as much detail in the crack gets highlighted as well as the voids; however, the upper limit should be low enough so that not a lot of noise is being selected. This upper limit is usually around 38000. After setting the limits, hit “Select Masked Voxels” and then click the addition button (both circled in black). The threshold tool will select more (highlighted in purple) than just the crack and voids so these features need to be deselected.

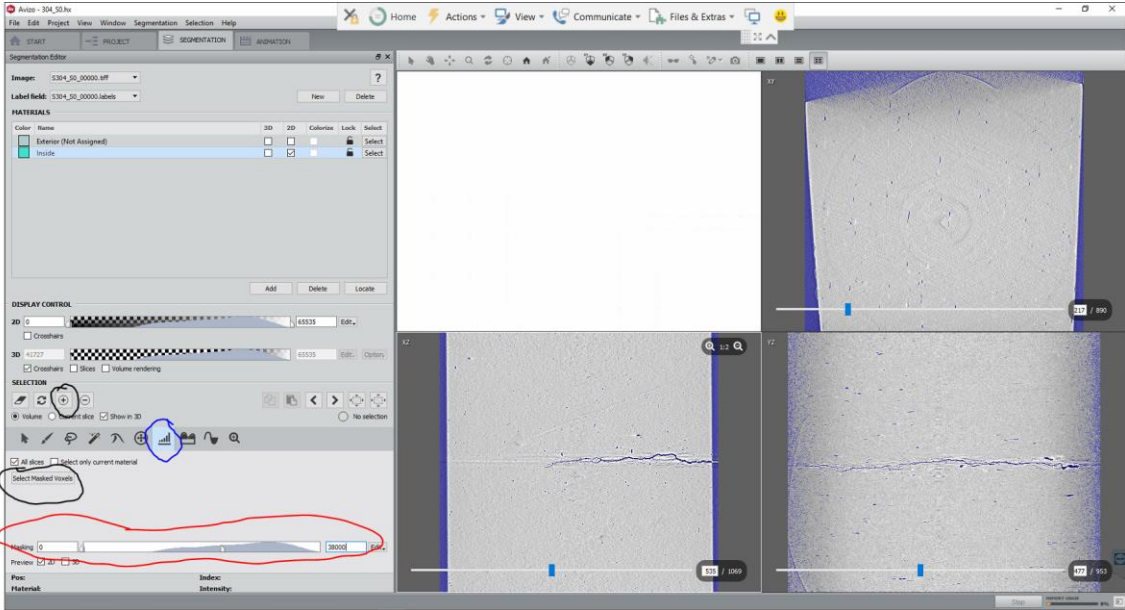


Figure C.11: Threshold Tool

- 12) Without removing the parts of the image that are not really there, a volume rendering would look like **Figure C.12**. You can check the progress after deselecting the parts of the image that are unwanted by doing a volume rendering. **Figure C.13** shows where you can go to perform a volume rendering. After going to the project tab, right click the file label (circled in blue) and select volume rendering (circled in red) and click “create”.
Note: A new volume rendering will need to be created when changes are made so remove old volume renderings first.

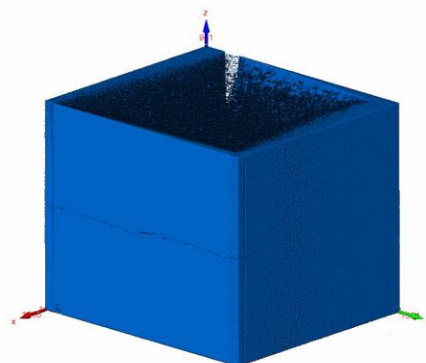


Figure C.12: Volume Rendering of Unselected Features

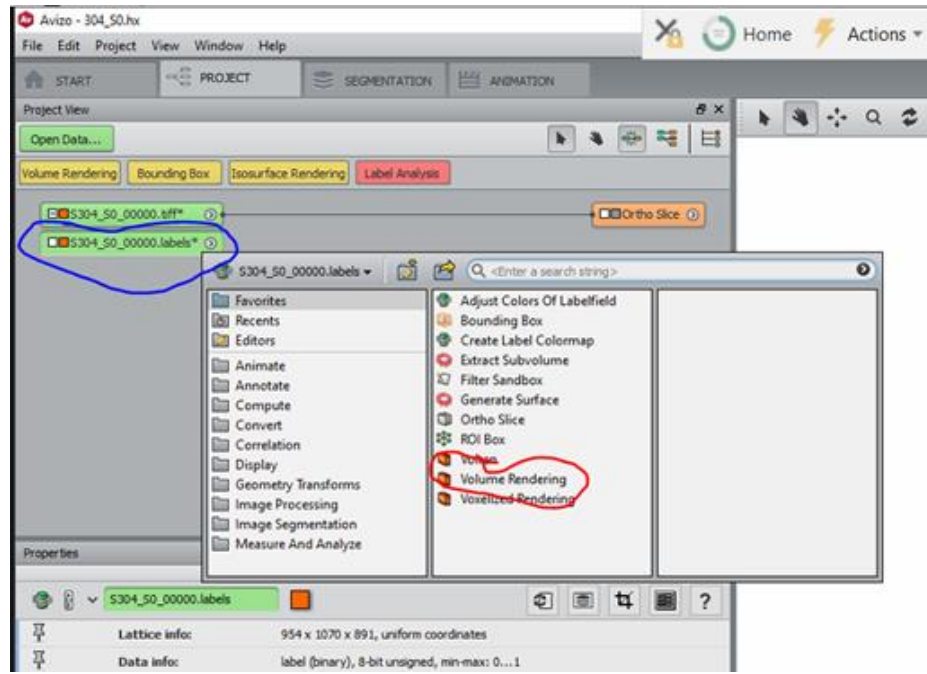


Figure C.13: How to do a Volume Rendering

13) To remove unwanted features, go back to the segmentation tab. You then need to go through each image (slide bar circled in red in **Figure C.14**) in one of the plane view orthoslices and deselect anything that is not a crack or a void. Some common objects that need to be unselected are shown in **Figure C.15**. The best way to remove all the unwanted selections is to remove an unwanted area in the least number of images. For example, **Figure C.16** shows a 10X10X10 cube. If the goal is to remove the yellow highlighted regions, I could go in the negative x direction (yz-plane) and go through 10 blocks of material or I could go in the y direction (xz-plane) and go through one block of material. Obviously, it is less time consuming to do the latter. Similarly, you could go through about 100 images removing the blue shown in the xz-plane instead of going through around 1000 images in the xy-plane (The blue area in the xz-plane corresponds to the top blue area in the xy-plane)

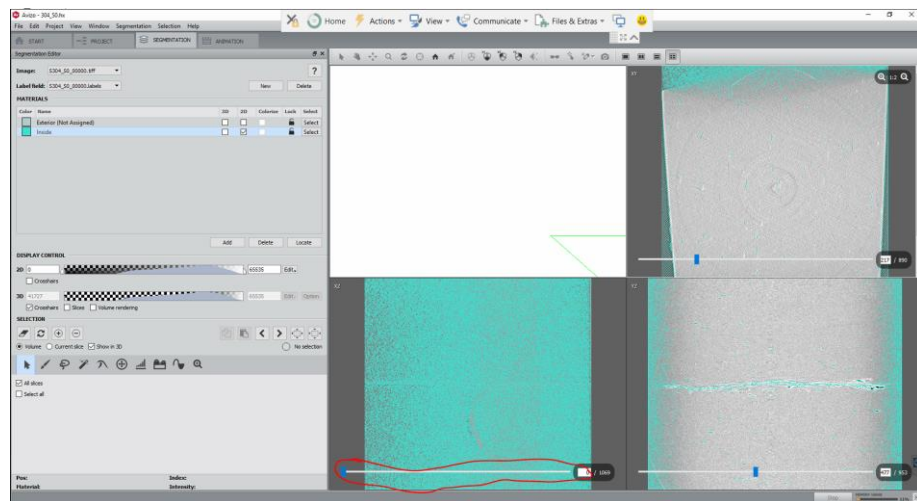


Figure C.14: Navigating through each Orthoslice

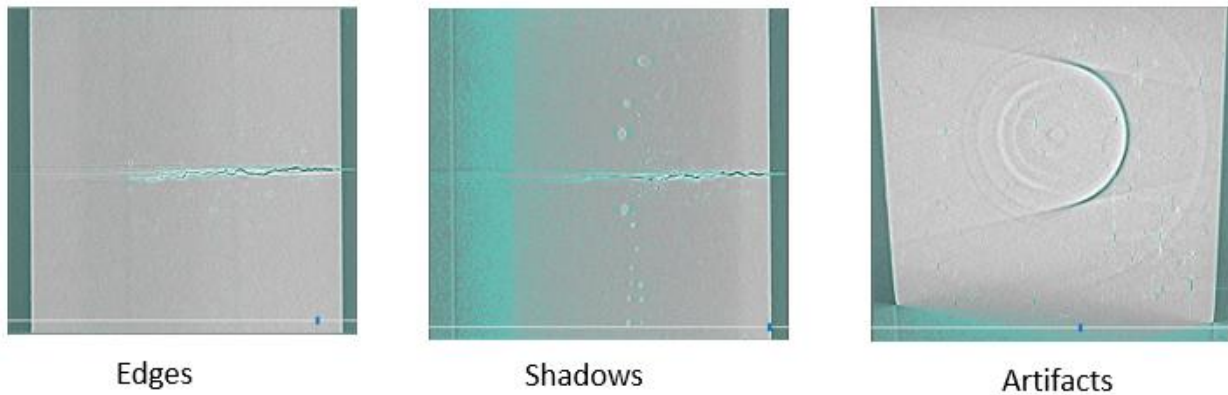


Figure C.15: Common Unwanted Selections

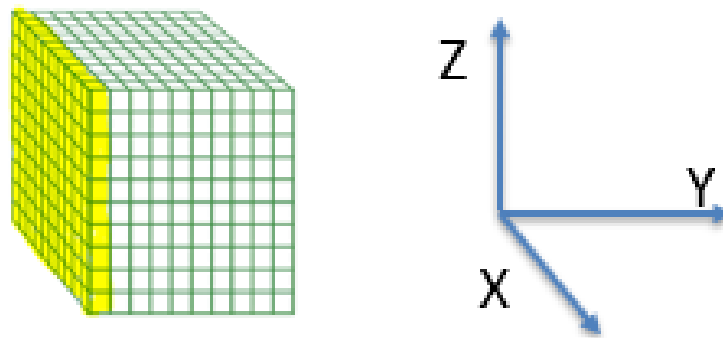


Figure C.16: Example Problem

14) **Figure C.17** shows how to highlight the unwanted area using the brush tool (circled in blue). You can control the pen size using the scale bar (circled in red). Anything that is blue and is covered by the red highlight from the brush is considered selected. You would want to only select the blue regions which are unwanted area and not select the blue areas that are considered cracks or voids.

If a mistake is made, just click “Ctrl+z” and this will undo your last task. After the area that is unwanted is selected, the minus button (circled in black) can be pushed. To make the task easier, you can select one of the three plane screens that you want to work on and click the one screen button near the 4 screen button. The results are shown in **Figure C.18**.

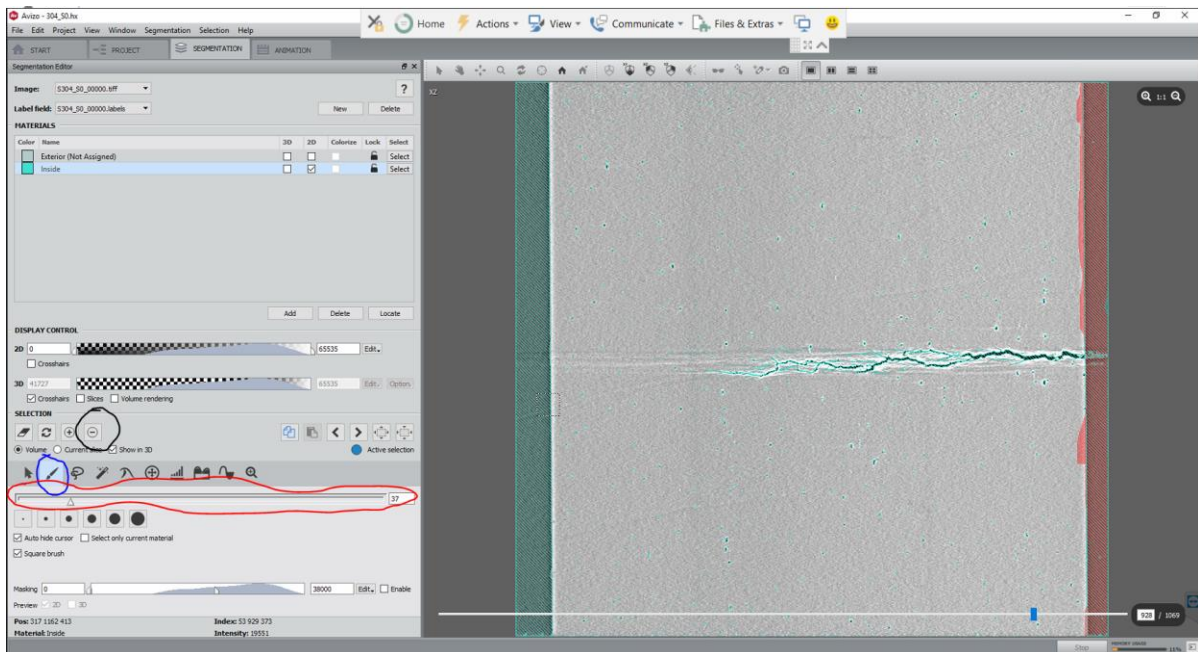


Figure A.17: Brush Tool

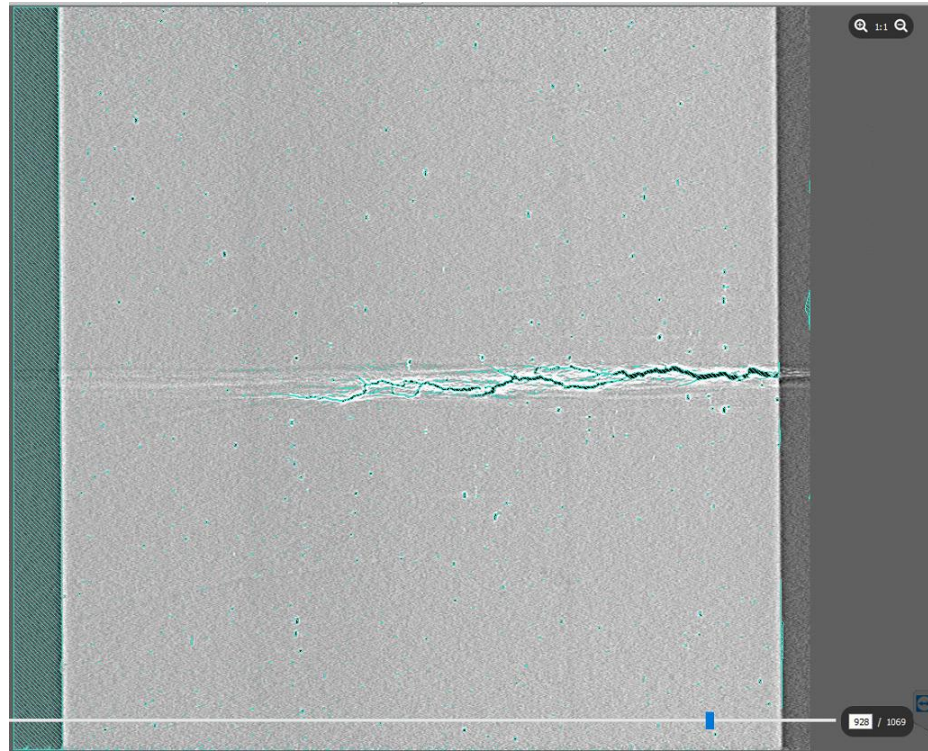


Figure C.18: Unselected Area

Note: Intentionally did bad job to show how missing blue areas by not highlighting in red can leave blue area (right side)

15) Instead of going through all these images one by one and deselecting unwanted areas, the interpolation tool can be used. If there is an unwanted area that is constant through many images in the same direction or if the blue area increases or decreases in a predictable way, you can utilize the interpolation tool. You can start with one image and highlight the common area, then you can skip forward (shouldn't do more than about 10 images) to a further image (2 or more images away) and highlight the same area. You can then select the interpolation tool shown in **Figure C.19** (circled in black) and all the images between the two images that were drawn on will highlight the same area. You can then hit the subtraction key to remove the common selected area. You should always go back to verify that no mistakes were made by the tool.

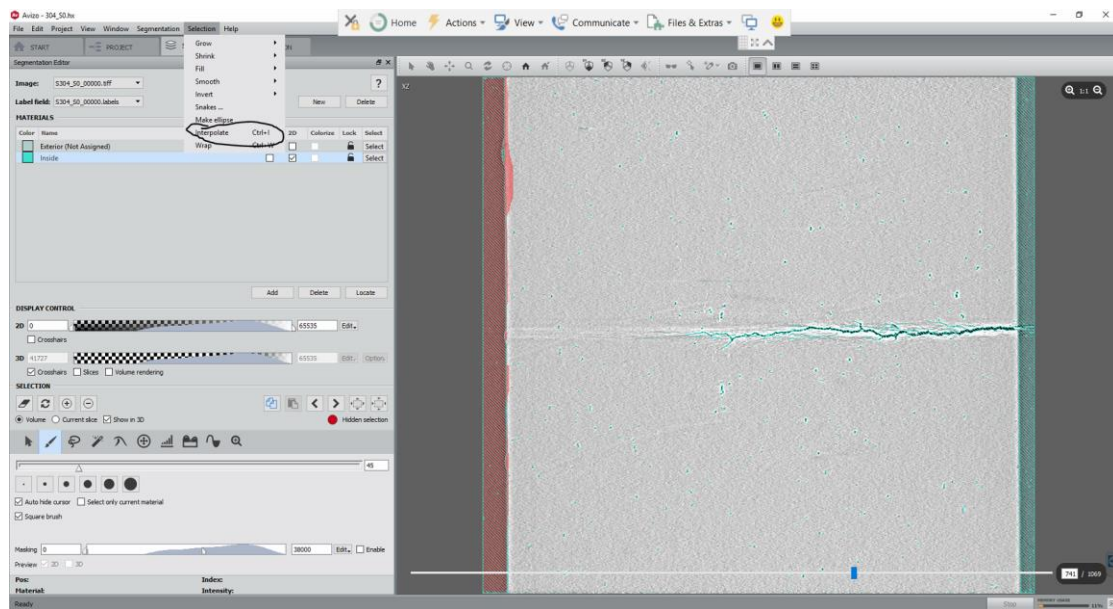


Figure C.19: Interpolation Tool

- 16) Finally, there are going to be spots where there are tiny blue selected areas that are unwanted, and they are going to be hard to remove if they are close to the crack or voids. Instead of going through each image and using a small brush, you can use the Remove Island tool. **Figure C.20** shows how to find the island tool (circled in black). You will then be prompted with a window like the one shown in **Figure C.21**. Make sure to select 3-D volume at the bottom of this window. You can then enter in a number in the upper most box. This tool will remove any islands that are smaller than the number of voxels (volume of 1 um^3) that you choose. This value is usually around 50-90 voxels. You want this number to be big enough so that it gets rid of most of the noise but not too big that it deselects the voids.

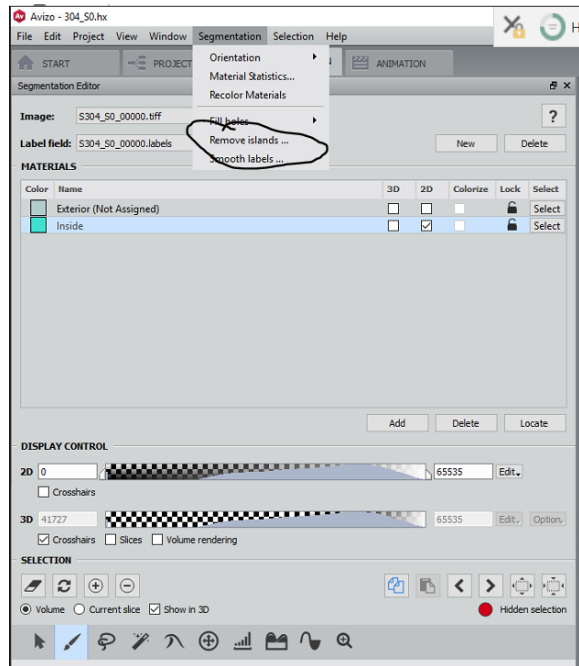


Figure A.20: Remove Island Location

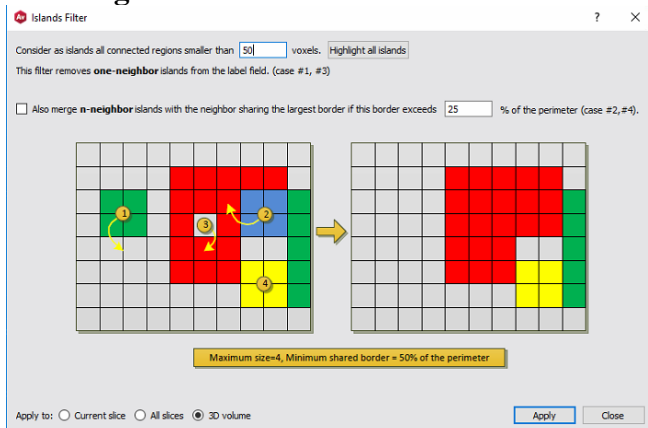


Figure C.21: Remove Island Window

17) Finally, you can check your work by doing a volume rendering which was already discussed earlier. If one desires to just see the crack and no voids, you can use the tool called the “Magic Wand” and select the crack in one of the orthslice views. This tool is similar to the threshold tool except it only highlights areas between the threshold numbers that are connected. An example of a final image (crack and voids) versus an initial image is shown in **Figure C.22**.

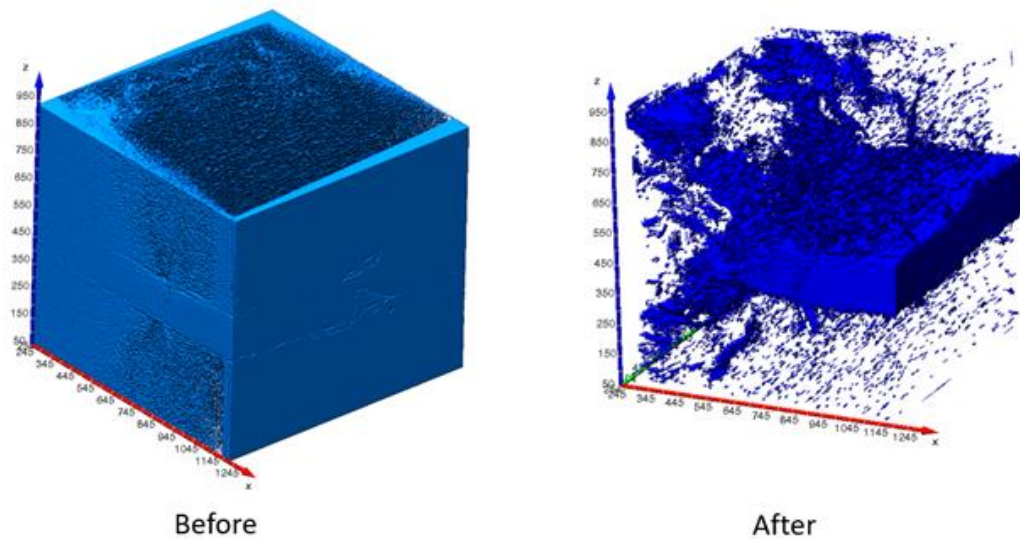


Figure C.22: Final Volume Rendering of a Crack Propagating through

Appendix D: Tomographs of 304SS Samples which did not Crack

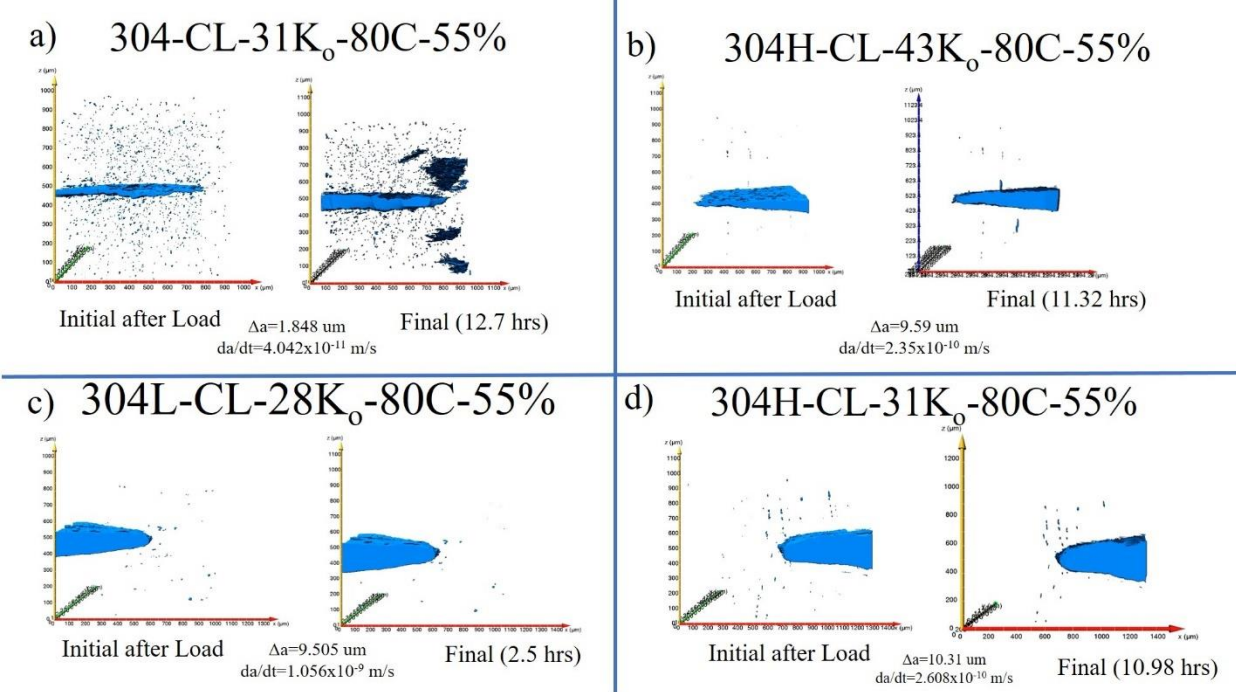


Figure D.1) Tomographs of Samples which did not have Significant Cracking in the Main Crack
of a) 304-CL-31K_o-80C-55%, b) 304H-CL-43K_o-80C-55%, c) 304L-CL-28K_o-80C-55%, and d)

304H-CL-31K_o-80C-55%